UNIVERSITY OF CALIFORNIA SAN DIEGO

From electron transfer to isomerization: chemical dynamics on the ultrafast timescale

A dissertation submitted in partial satisfaction of the
requirements for the degree of Doctor of Philosophy

in

Chemistry

by

Tyler Matthew Porter

Committee in Charge

Professor Clifford P. Kubiak, Chair
Professor Katherine A. Barbeau
Professor Jeffrey D. Rinehart
Professor Akif F.Tezcan
Professor Wei Xiong

2019

This dissertation of Tyler Matthew Porter is approved, and is acceptable in quality and form for publication on microfilm and electronically:

_____

_____

_____

_____

_____

Chair

University of California San Diego

2019

DEDICATION

to Karisa, for all of her love, compassion, and unwavering support

to my parents, for their unending encouragement and assistance

to Dakota, for reminding me what's important in life

to my friends and family, for making life fun

EPIGRAPH

“no one appreciates the very special genius of your conversation as the dog does.”

-Christopher Morley

TABLE OF CONTENTS

LIST OF FIGURES

LIST OF TABLES

ACKNOWLEDGMENTS

Looking back on my PhD. career I am truly blessed to have crossed paths with so many wonderful people. It is not often that one gets to thank those around him, and while words may not convey all of my gratitude, I hope in some way this is a start.

Cliff! I cannot adequately thank you enough for being the best advisor any student could have asked for. You allowed me to forge my own path, develop my own ideas, and become a truly independent researcher. When I first started working in the Kubiak lab, I had no clue who Rudy Marcus was nor what a mixed valent molecule is. All I knew was that Cliff studied molecules that exchanged electrons fast – *really fast*, and that was cool. Working and studying under his guidance has been one of the most rewarding experiences I have ever had as I was able learned more than I ever could have imagined. I have not me a person more passionate and knowledgeable about chemistry than Cliff, and I want to thank you for sharing that with me. You encouraged me to think independently, would never settle for anything less than excellent, and most importantly instilled confidence in my abilities as a scientist. Without your guidance, I would not be who I am today. Thank you for being an inspiration and a mentor whom anyone would aspire to be.

I would also like to thank my undergraduate advisor, Ryan Trovitch. Without his patience, kindness, and guidance I would not have even made it to graduate school. I started in Ryan's lab as a wide-eyed transfer student and from day one was treated just like a graduate student. Under Ryan's direction I had the opportunity to work on my own independent project studying nickel hydrosilylation catalysts. I vividly remember isolating a catalyst I had made while Ryan was giving a lab tour and in passing, he made a comment that has stuck with me since: "In Tyler's flask is a new complex that has never existed before and he is the only person in the world to have it." This ignited a spark in myself and while I did not know it at the time,

every lesson Ryan taught me would ultimately prepare me to forge my own path, develop my own ideas, and most importantly question everything. Thank you for taking a chance on me and instilling in me your passion, love, and knowledge of chemistry. Words cannot express how grateful I am to both Cliff and Ryan, they both showed what it meant to be a great mentor and friend.

To my lab mates and friends, you made this long, strange trip an absolute blast. I will always remember each and every one of one for all of the good times and memories we have shared. Thank you to Steven, for being an amazing lab mate and even better friend. You were like a brother too me and were always there to support me in any endeavor. I was able to learn so much from you both inside and outside of lab. Thank you, Andy, for all of our insightful discussions, your eloquent vocabulary and all of your stories – all of them. It was fun to watch you grow, learn, and mature as a scientist…keep it up! Felix, I'm going to miss your humor, sarcasm, and most importantly your criticism. I could always count on you to give me a straight answer. You always made group meetings entertaining, but most importantly, you showed where a little hard work can get you. Your project has not been easy, but I'll be damned if you're not going to make it work. Joseph "The Kid" Palasz, some of my fondest memories have been with you in my last two years of graduate school. You have brought back the fun loving spirt of the Kubiak lab that I remember when I first joined. You're a smart kid who is incredibly passionate about chemistry and while you may get a little over ambitious at times, your curiosity will never let you down. Thank you to Gavin, my truly remarkable undergrad. You were the best undergraduate researcher any graduate student (and lab) could have asked for. Your passion for chemistry made my job fun and easy, all I had to do was guide you.

While probably the most removed from my studies physically, I could not have done any of this without my family. Mom and Dad, you made it possible for me to chase my dreams. While our initial move to Phoenix may was not met without risk, your love, compassion, and

determination made it one of the best opportunities I have had. You prioritized your family above all else and made sure that we (your kids) would always excel. Thank you, dad, for showing us where a little “elbow grease” and hard work can take us in life. You never settled for anything less than excellent. Mom thank you for your unending compassion and love, you were always my biggest cheerleader and have been the rock of our family. You both have provided for me in ways that I don’t think I could ever repay, and I can say without a doubt that I am the man I am today because of your love, support, and guidance. Thank you for everything! To Teran and Trey, the two best brothers that anyone could have asked for. You two were always there for me to unwind and relax. Teran, I am going to miss our weekly get together and unwinding after a long week of work. Karisa and I were so fortunate to have you and Carli live so close over these last three years. You made the weekends fun!

To Karisa, there are very few people in this world who know and understand me the way you do. There are not enough words to describe my love and appreciation for you. Your unending love, compassion, and support allowed me to shoot for the stars untethered as you’d always be there to catch me. We have grown so much together over these last several years and have taught me so much about life, love, and happiness. While we enter a new chapter of our lives together with lots of unknowns, I do know that I have never loved someone the way I love you. You are my soulmate and I know that any endeavors we embark on, we will always have each other.

Chapter 2: The majority of the material in this chapter comes directly from a manuscript entitled “Tuning electron delocalization and transfer rates in mixed-valent Ru_3O complexes through ‘push–pull’ effects,” by Tyler M. Porter, Gabriele C. Canzi, Steven A. Chabolla, and Clifford P. Kubiak, is published in *The Journal of Physical Chemistry A*, **2016**, *120 (32)*, 6309–6316. The dissertation author is the primary author.

Chapter 3: The majority of the material in this chapter comes directly from a manuscript entitled “Effects of electron on hydrogen bonds,” by Tyler M. Porter, Gavin P. Heim, and Clifford P. Kubiak, is published in *Chemical Science*, **2017**, *8*, 7324–7329. The dissertation author is the primary author.

Chapter 4: Some of the material in this chapter is unpublished. The majority of the material comes directly from a manuscript entitled “Stable mixed-valent complexes formed by electron delocalization across hydrogen bonds of pyrimidinone-linked metal clusters,” by Tyler M. Porter, Gavin P. Heim, and Clifford P. Kubiak, is published in *The Journal of the American Chemical Society*, **2018**, *140*, 12756–12759. The dissertation author is the primary author.

Chapter 5: The majority of the material in this chapter comes directly from a manuscript entitled “Direct observation of the intermediate in an ultrafast isomerization,” by Tyler M. Porter, Jiaxi Wang, Yingmin Li, Bo Xiang, Catherine Salsman, Joel S. Miller, Wei Xiong, and Clifford P. Kubiak, is published in *Chemical Science*, **2019**, *10*, 113–117. The dissertation author is a primary author.

Chapter 6: This chapter is currently being prepared for submission for publication. “Phosphine Steric-Electronic Effects of an Ultrafast Isomerization,” by Tyler M. Porter, Andrew L. Osterircher, and Clifford P. Kubiak. The dissertation author is the primary author.

VITA

2019	Doctor of Philosophy, University of California San Diego
2016	Master of Science, University of California San Diego
2014	Bachelor of Science, Arizona State University, Phoenix

PUBLICATIONS

Taylor J. Aubry, Jonathan C. Axtell, Victoria M. Basile, K. J. Winchell, Jeffery R. Lindmuth, **Tyler M. Porter**, Jiyuan Liu, Anastassia N. Alexandrova, Clifford P. Kubiak, Sarah H. Tolbert, Alexander Spokoyny & Benjamin J. Schwartz, "Dodecaborane-based Dopants Desgined to Shield Anion Electrostatics Lead to Increased Carrier Mobility in a Doped Conjugated Polymer." *Advanced Materials*, **Accepted.**

Tyler M. Porter, Jiaxi Wang, Yingmin Li, Bo Xiang, Catherine Salsman, Joel S. Miller, Wei Xiong, and Clifford P. Kubiak. "Direct Observation of the Intermedeate in an Ultrafast Isomerization." *Chemical Science*, **2019**, *10*, 113–117.

Tyler M. Porter, Gavin P. Heim, and Clifford P. Kubiak, "Stable Mixed-Valent Complexes Formed by Electron Transfer Across Hydrogen Bonds of Pyrimidinone-Linked Metal Clusters." *Journal of the American Chemical Society*, **2018**, *140*, 12756–12759.

Mark H. Reineke, **Tyler M. Porter**, Andrew L. Ostericher, and Clifford P. Kubiak, "Synthesis and Characterization of Heteroleptic Ni(II) Bipyridine Complexes Bearing(N-hetercyclic carbene) Ligands. *Organometallics*, **2018**, *37*, 448–453.

Jessica H. Golden, Laura Estergreen, **Tyler M. Porter**, Abegail C. Tadle, Daniel Sylyinson M. R., John W. Facendola, Clifford P. Kubiak, Stephen E. Bradford, and Mark E. Thompson, "Symmetry Breaking Charge Transfer in Boron Dipyridylmethene (DIPYR) Dimers." *ACS Applied Energy Materials*, **2018**, *1*, 1083–1095.

Tyler M. Porter, Gavin P. Heim, and Clifford P. Kubiak "Effects of Electron Transfer on Hydrogen Bonds." *Chemical Science*, **2017**, *8*, 7324–7329.

Tyler M. Porter, Gabriele C. Canzi, Steven A. Chabolla, and Clifford P. Kubiak, "Tuning Electron Delocalization and Transfer Rates in Mixed-Valent Ru_3O Complexes through 'Push–Pull' Effects." *Journal of Physical Chemistry A*, **2016**, *120*, 6309–6316.

ABSTRACT OF THE DISSERTATION

From Electron Transfer to Isomerization:

Chemical Dynamics on the Ultrafast Timescale

By

Tyler Matthew Porter

Doctor of Philosophy in Chemistry

University of California San Diego, 2019

Professor Clifford P. Kubiak, Chair

Chemical exchange dynamics are often studied using a Bloch equation analysis of coalescing line shapes in nuclear magnetic resonance spectroscopy (NMR). A similar treatment has been applied to systems exchanging on the infrared (IR) vibrational timescale, where line shape analysis of coalesced FTIR and Raman spectra allow the study of reactions occurring in picoseconds (ps). In practice however, there are comparatively few examples of line shape analysis by vibrational spectra as inhomogeneous broadening, solvent environment fluctuations or other dynamic processes in addition to chemical exchange can contribute to the overall vibrational line shape. This work examines two model systems displaying exchange

dynamics on the vibrational timescale and the use of vibrational spectroscopy to describe their ultrafast dynamics. The first system details electron transfer dynamics in dimers of oxo-centered triruthenium clusters that are linked by non-covalent interactions, where we have shown how electron transfer *across* hydrogen bonds occurs on (or approaches) the vibrational time scale. While these studies have important implications in understanding long range ET in biological systems, the importance of non-covalent interactions also extends throughout the chemical sciences and as they readily affect the stability of artificial supramolecular structures, and selectivity of catalysts. In this dissertation the fundamental relationship between non-covalent molecular interactions and ET is examined to gain new understanding of ET processes occurring across hydrogen bonds. We were also able to show that electron delocalization across hydrogen bonds imparts substantial stability (~5 kcal mol^{-1}) to the hydrogen bonding interaction.

The second system, a penta-coordinate ruthenium dithitene complex seeks to examine vibrational lineshape coalescence and the application of an optical Bloch analysis in systems exhibiting *ultrafast dynamics*. The ruthenium complex undergoes structural rearrangement between three distinct structural isomers that differed only in the orientation of a carbonyl ligand about the metal center. In methylene chloride, the three isomers 1) square pyramidal equatorial, 2) trigonal bipyramidal, and 3) square pyramidal axial were found to exchange through the meta-stable trigonal bipyriamidal intermediate within picoseconds. This study was a direct validation of the mechanism and timescale of Berry pseudorotation – the pairwise exchange of ligands in a pentacoordinate complex – a process that was described nearly fifty years ago, and to our knowledge, was the first observation of an ultrafast dynamic equilibrium involving two distinct structural isomers and the intermediate connecting them.

Chapter 1

The Kinetics and Thermodynamics of Ultrafast Electron Transfer.

1.1 Introduction

Electron transfer is ubiquitous in the chemical, physical, and biological sciences. The movement of electrons lies at the core of any chemical reaction and without electron transfer (ET) chemistry does not occur. This is exemplified in photosynthesis and respiration, two processes essential to life, which fundamentally depend on efficient electron flow through the vast supramolecular structures of proteins. While all chemical reactions involve some form of electron transfer, most remain unfit for study, as the relatively simple transfer of an electron is obfuscated by more complicated chemical phenomena. The earliest study of electron transfer between two oxidation states of a single element was in 1920 by von Hevsey and Zechmeister. Through use of the naturally occurring radio isotope Pb^{212} as a tracer, they were able to show

electron transfer between Pb(II) and Pb(IV) in glacial acetic acid solutions occurred within minutes.[1] The first assignment of an electron transfer rate however, did not occur until nearly thirty years later, where Lewis, Coryell, and Irvine reported exchange between $Co^{II}(en)_3$ and $Co^{III}(en)_3$ (where en = ethylenediamine) occurred in microseconds (k_{et} = 5.2 x 10^{-5} M^{-1} s^{-1}).[2-3] It was here, post-World War II where the surplus of readily available radioisotopes allowed extensive investigations of electron self-exchange between solvated transition metal ions in aqueous solutions.

$$Ce(III) + {}^*Ce(IV) \rightarrow Ce(IV) + {}^*Ce(III) \qquad (1.01)$$

Early on, the majority of research focused on the study of bimolecular electron transfer reactions as shown above, where it was readily established that ET occurred by two basic mechanisms. The first mechanism, termed outer-sphere, is a bimolecular process where the donor and acceptor act as freely diffusing hard spheres. The two species first contact each other, transfer an electron, and then diffuse away. The second mechanism, inner-sphere ET, follows the same basic principle but, involves the formation of an intermediate complex prior to ET (equation 1.02). Here, the donor and acceptor diffuse into each other, and form an intermediate complex in which both redox sites are linked by a chemical bridge. The electron is the transferred across this chemical bridge after which they separate and freely diffuse again.

$$D^- + A \rightarrow D^-\text{–}A \rightarrow D\text{–}A^- \rightarrow D + A^- \qquad (1.02)$$

While the mechanistic differences between inner-sphere and outer-sphere electron transfer was well understood by 1950, a definitive theory of electron transfer was not developed until Rudy A. Marcus' presented is seminal work on electron transfer at a 1952 meeting.[4]

1.2 Marcus-Hush Theory: Kinetics and Thermodynamics of Electron Transfer

In the context of Marcus Theory, electron transfer reactions are be described through reaction coordinate diagram where the product and reactant surfaces approximated as simple harmonic oscillators (Figure 1.1Figure 1.2):

$$G_d = \lambda\, x^2 \tag{1.03}$$

$$G_a = \lambda\, (x-1)^2 + \Delta G_0 \tag{1.04}$$

The reaction coordinate, x, is the collection of all atomic coordinates, bond angles, and outer-sphere coordinates (including solvent) that are involved in the reaction. The reactant curve (G_d) represents the donor-acceptor (DA) complex before electron transfer while the product curve (G_a) represents the DA complex after electron transfer. The minima are arbitrarily centered about 0 and 1 corresponding to the most stable coordinates for the reactants and products respectively. In symmetric systems (when the donor and acceptor are identical) the minima of the surfaces lie at the same free energy while asymmetric systems have their minima are displaced by ΔG_0, reflecting the driving force to ET. The crossing point of the two diabatic surfaces (x = 0.5, Figure 1.1) is the point at which thermal electron transfer occurs by, dynamic fluctuations in the system promoting thermal ET. For this to occur, the nuclear coordinates (including solvent) must distort from their equilibrium states such that there is no energy difference between the reactant and product curves (conservation of energy). In the transition state electron transfer then occurs between the donor and acceptor by “hopping” between the two surfaces. After ET, the nuclear coordinates relax to an equilibrium position reflecting the product state. While dynamic fluctuations constantly displace the system from their equilibrium positions, this “hopping” does not always occur and is defined by a transmission coefficient (κ) ranging from 0 to 1. If ET does not occur, the reaction will instead continue to progress along the reactant surface to higher energies. The rate of thermal electron transfer (k_{ET}) can then be

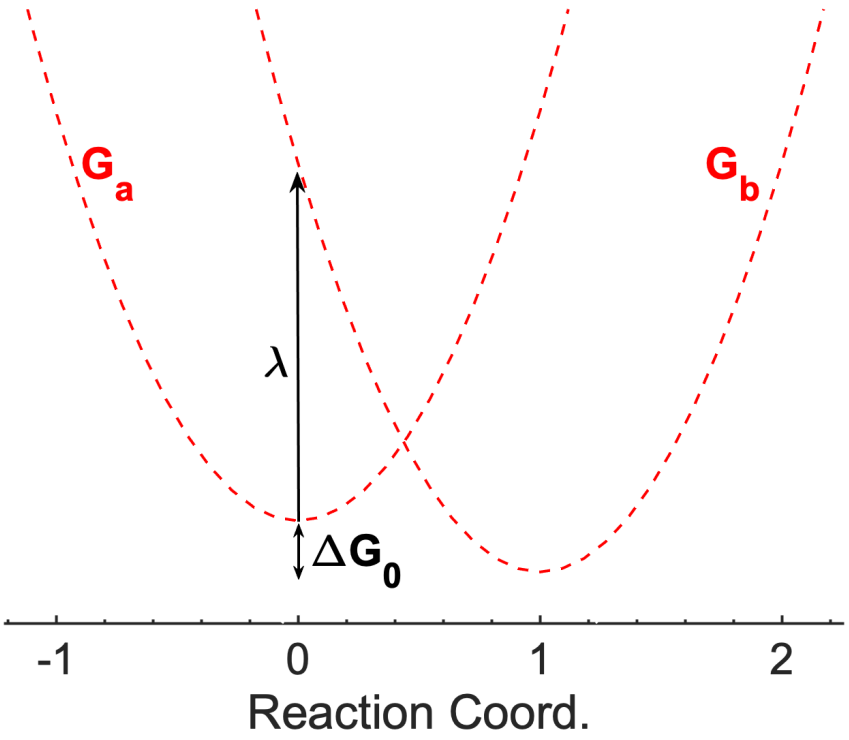

Figure 1.1. Diabatic potential energy surface of the electron donor (G_d) and electron acceptor (G_a) in the absence of electronic coupling.

expressed in the normal Arrhenius manner where ET is exponentially dependent on the energetic barrier (activation energy, ΔG^*) to ET (equation 1.05).[5]

$$k_{ET} = \kappa \nu_N e^{\frac{-\Delta G^*}{RT}} \tag{1.05}$$

Here, R and T have their normal meanings, κ is the transmission coefficient and ν_N is the collision frequency coefficient.

In addition to thermal ET, electron transfer can also occur by absorption of light of sufficient energy. As shown in Figure 1.1, the product curve extends some distance in energy above the reactant curve. When the system absorbs light matching this transition energy (λ), the electron can be promoted from the donor to the acceptor. Since the reaction does not progress along the reaction coordinate during this transition (Frank–Condon principle), the electron resides on the product curve, but the nuclear coordinates are significantly displaced from the products equilibrium geometry. This means, that while the electron resides on the

acceptor, the bond distances; bond angles; solvent dipole moments; and counter ions all exist in a configuration as if the electron were on the donor, not the acceptor. The energy required for this transition to occur is known as the reorganization energy (λ) and is the summation of all inner- and outer-sphere barriers to ET. Since the diabatic surfaces are constructed from simple harmonic oscillators, the reorganization energy can be related to the activation barrier through the following relationship:[5]

$$\Delta G^* = \frac{\lambda}{4}\left(1 + \frac{\Delta G_0}{\lambda}\right)^2 \tag{1.06}$$

This relationship is one of the greatest triumphs of Marcus theory and allows determination of the activation barrier as a function of the reorganization energy. This transition is typically observed as an absorption in the near infrared (nIR) region of the electronic spectrum in mixed-valence complexes. In the diabatic limit, the peak max (ν_{max}) of this transition is equal to the reorganization energy. Since this absorbance involves the movement of the electron from reactant to product (i.e. donor to acceptor), and hence involves an exchange of valencies, it is termed an intervalence charge transfer (IVCT) band.

While the discussion thus far has primarily focused on weakly interacting donor-acceptor complexes (outer-sphere ET), the assumptions made are not necessarily valid for systems linked by a chemical bridge (inner-sphere ET). Whether the bridge is transient (equation 1.02) or covalent (equation 1.07), the formation of a chemical bond linking the donor and acceptor has the ability to facilitate wavefunction overlap between the two sites.

$$D^-\text{–Bridge–A} \rightarrow \text{D–Bridge–}A^- \tag{1.07}$$

This mixing of the donor and acceptor wavefunctions means they can no longer be treated as a diabatic system, but instead must be treated adiabatically. The adiabatic surfaces (G_1 and G_2) are generated from the diabatic surfaces (G_d and G_a) by solving for E for the secular determinant of a 2 x 2 matrix (equation 1.08, Figure 1.2).

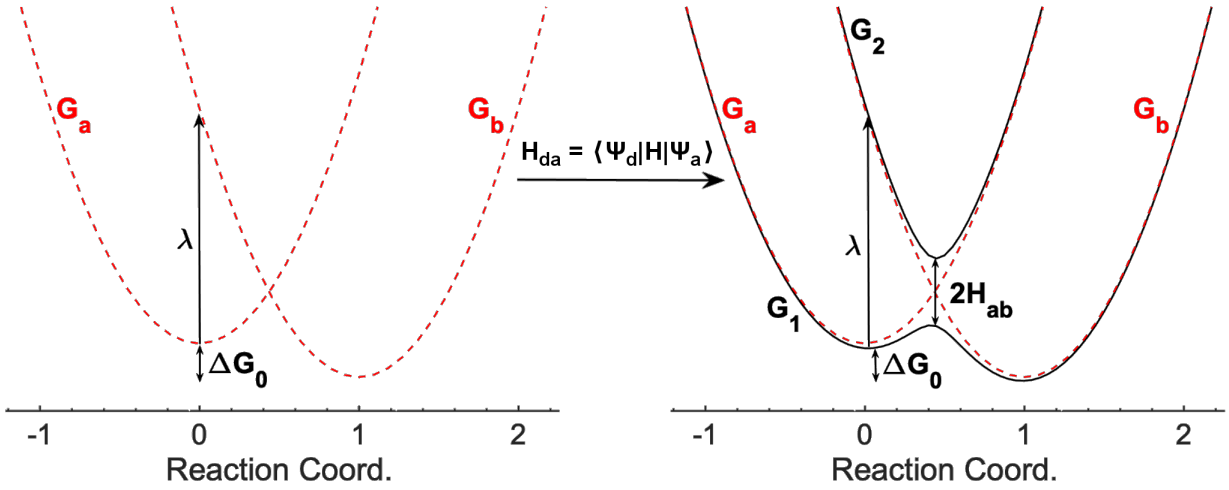

Figure 1.2. (left) Diabatic potential energy surface of the electron donor (G_d) and electron acceptor (G_a) in the absence of electronic coupling. (right) Adiabatic potential energy surfaces of the donor and acceptor in the moderately coupled regime. Coupling is governed by wavefunction overlap of the donor and acceptor producing two adiabatic surfaces. The ground state surface (G_1) and excited state surface (G_2) are separated by $2H_{ab}$ at the cross over region (x = 0.5) indicated by the double sided arrow. The driving force is additionally shown in both diagrams as ΔG_0.

$$\begin{vmatrix} G_d - E & H_{ad} \\ H_{da} & G_a - E \end{vmatrix} = 0 \qquad (1.08)$$

The eigenvalues obtained are the adiabatic surfaces consisting of a ground and excited state, G_1 and G_2 respectively (Figure 1.2).[6-7] The off-diagonal matrix elements H_{ad} and H_{da} physically describe the degree of wavefunction overlap between the donor and acceptor and serves to quantify the degree of electronic communication in the system. The effect of coupling is most clearly seen in Figure 1.2, where mixing of the two diabatic states (G_a and G_b) gives two new adiabatic surfaces: A stabilized ground state (G_1) and a destabilized excited state (G_2).

The magnitude of H_{da} has several important implications that are most clearly seen in Figure 1.3. Here, as H_{da} is increased, the ground state is continually stabilized while the excited state is destabilized. The increasing stabilization of G_1 leads to a convergence of the minima along the reaction coordinate to the point x = 0.5. The location of the minima as a function or

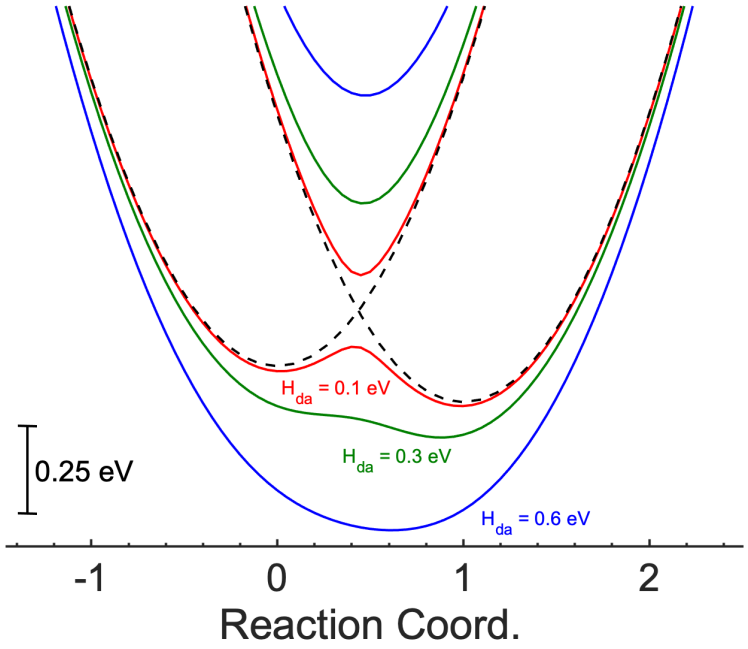

Figure 1.3. Adiabatic potential energy surfaces for an asymmetric donor–acceptor system with H_{da} = 0.1 eV (red), H_{da} = 0.3 eV (green), H_{da} = 0.6 eV (blue), and λ = 0.8 eV for all cases. The diabatic states (G_d and G_a) are also shown as the dashed traces.

$$x_{min} = \frac{H_{da}^2}{(\lambda + \Delta G_0)^2} \tag{1.09}$$

$$x_{min} = 1 - \frac{H_{da}^2}{(\lambda - \Delta G_0)^2} \tag{1.10}$$

H_{da} are expressed as equations 1.09 (reactant curve) and 1.10 (product curve). This is the direct result of wavefunction mixing, where the ground state (G_1) begins to incorporate properties of both reactant and product. That is, the most stable nuclear configuration for the ground state, more closely resembles the transition state. As the system beings to resemble the transition state, a net lowering of the activation barrier (ΔG^*) is also observed. This dependence is shown as equation 1.11 (or 1.12 in the absence of a driving force, $\Delta G_0 = 0$):

$$\Delta G^* = \frac{1}{4}(\lambda + 2\Delta G_0 - 4H_{da}) + \frac{\Delta G_0^2}{4(\lambda - 2H_{da})} + \frac{H_{da}^2}{(\lambda + \Delta G_0)} \tag{1.11}$$

$$\Delta G^* = \frac{(\lambda - 2H_{da})^2}{4\lambda} \tag{1.12}$$

An additional minor but important effect of this mixing is a leveling in the driving force (ΔG_0) to ET. That is, the difference in energy between the reactant and product minima (ΔG_0) decreases with increasing H_{da}.

The net lowering of ΔG^* with increasing coupling (H_{da}) has an extremely important consequence. Since the general expression for the rate of electron transfer depends on ΔG^* (equation 1.05) the rate of electron transfer in an adiabatic system also has a dependence on the electronic coupling. For simplicity consider a symmetric donor–acceptor system (ΔG_0 = 0 eV) whose activation barrier is governed by equation 1.12. Upon substitution of ΔG^* from equation 1.12 into 1.05, the rate of electron transfer now depends on both λ and H_{da} (equation 1.13).

$$k_{ET} = \kappa \nu_N e^{\frac{-(\lambda - 2H_{da})^2}{4\lambda RT}} \tag{1.13}$$

Here, analogous to equation 1.05, κ is the transmission coefficient, ν_N is the nuclear frequency factor, and λ is the reorganization energy. Unlike the weakly coupled diabatic systems where $\kappa < 1$, for an adiabatic system ($H_{da} > 0$) $\kappa = 1$. That is, at the intersection, the probability of ET from the reactants to products is unity. In this limit, the nuclear frequency factor ν_N also changes. In a weakly coupled, diabatic, system ν_N is proportional to the tunneling frequency $H_{da}^2/\sqrt{\lambda}$. In a strongly coupled, adiabatic, system however ν_N now depends on the nuclear coordinate frequencies – the nuclear motions that participate in reorganization of the system through the intersection at *x* = 0.5. These modes are the combination of intramolecular (inner-sphere) and solvent (outer-sphere) modes. In highly adiabatic systems as $H_{da} \rightarrow \lambda/2$, the activation barrier approaches zero and the exponential portion of k_{ET} approaches unity. In this limit, the rate of ET depends only on the nuclear frequency factor ν_N. This implies that when

substantial donor-acceptor mixing is present in the system, nuclear vibrations and solvent motion will begin to dominate the rate of ET.[8]

The last parameter of the rate expression that has largely been ignored up to this point is the reorganization energy, λ. The reorganization energy is the sum of all energetic requirements for the reconfiguration of the inner-sphere and outer-sphere nuclear coordinates (equation 1.14), where λ_i and λ_o describe the inner-sphere and outer-sphere reorganization

$$\lambda = \lambda_i + \lambda_o \tag{1.14}$$

energies respectively.[9] The inner-sphere term (λ_i) describes the energy required to reorganize the inner-sphere nuclear coordinates and is colloquially called the vibrational term. It is found by consideration of the force constants arising from the inner-sphere vibrational modes that connect the reactants and products (equation 1.15) through the crossing point.[5, 10-11]

$$\lambda_i = \sum_j \frac{k_j^d k_j^a}{k_j^d + k_j^a} (Q_j^d - Q_j^a)^2 \tag{1.14}$$

Here, k_j^d and k_j^a represent the force constants of the j^{th} vibrational mode for the donor and acceptor respectively, while the quantity $(Q_j^d - Q_j^a)^2$ accounts for the changes in bond lengths and angles. While several theories exist that describe λ_o, the most widely accepted and applied however, is based upon a dielectric continuum model as described by Marcus.[12]

$$\lambda_o = \Delta e^2 \left(\frac{1}{\varepsilon_{op}} - \frac{1}{\varepsilon_s}\right) \int (D_d - D_a)^2 \, d\tau \tag{1.14}$$

Here the solvent is treated electrostatically, where Δe^2 is the amount of charge transferred, ε_{op} and ε_s are the optical and static dielectric constants respectively, while D_d and D_a describe the radial separation of the donor and acceptor. The dielectric term $\left(\frac{1}{\varepsilon_{op}} - \frac{1}{\varepsilon_s}\right)$, is known as the Pekar factor and implies a dielectric continuum by treating multiple solvent dipoles as a whole.[9]

This provides a dipolar gradient about the system and greatly simplifies the treatment of the outer-sphere as individual solvent molecules no longer need to be considered.

In the same manner that ΔG^* was affected by the electronic coupling (H_{ab}), and since the reorganization energy is related to the thermal activation barrier (ΔG^*) it is natural to wonder how H_{ab} affects λ. Quantitatively, as coupling in a system increases the movement of the minima in the ground state (*vide supra*) actively decreases λ. This relationship is related to H_{ab} through equation 1.15:

$$\lambda' = \lambda - \frac{4H_{da}^2}{\lambda} \qquad (1.15)$$

It is important to note however, that this only applies to asymmetric systems, where a driving force to ET (ΔG_o) is present. For a symmetric system (i.e. when $\Delta G_o = 0$), the movement of the minima that decreases λ is exactly canceled out by the stabilization/destabilization of the ground and excited states (G_1 and G_2) along the y-axis. That is, in a symmetric system the value of λ is insensitive to H_{da} and remains constant.[6]

From the above discussion, it is clear that to understand any system exhibiting ET dynamics, it remains essential to know the magnitude of both λ and H_{da}. While λ is readily obtained from a near infrared (nIR) or UV-vis spectrum (the IVCT band), a methodology to determine H_{da} was not presented until 1967 when Noel Hush demonstrated that the location, shape, and intensity of the IVCT band could be used to determine H_{da}.[13] Owing to the energetics of electron transfer, the placement of the IVCT band is usually within the near Infrared (nIR) portion of the absorption spectrum whose peak max (ν_{max}) can be related to λ through equation 1.16:

$$\nu_{max} = \lambda + \Delta G_o \qquad (1.15)$$

The intensity of this band is governed by the extinction coefficient (ε) and is found to increase with H_{da} for transition metal complexes. This is an important point and is best explained through

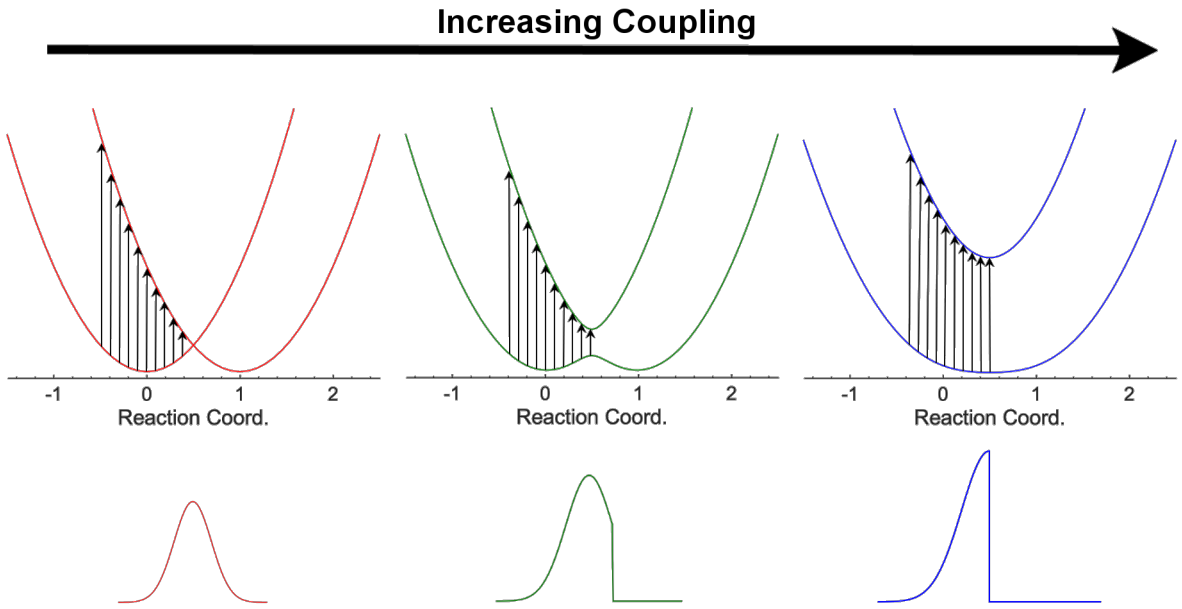

Figure 1.4. General effect of electronic coupling on the IVCT intensity and band shape when a Gaussian distribution of population is assumed for the ground state.

consideration of the Franck–Condon overlap integral.[14] As electronic coupling increases, the ground state (G_1) becomes more parabolic in shape and the ground state Boltzmann populations will in turn, have more favorable vibrational wavefunction overlap with the excited state (G_2). This in turn, leads to a greater probability of an electron populating the excited state surface, G_2, and results in greater IVCT intensity.[13, 15] The band shape as defined by the full-width half-max ($\Delta\nu_{1/2}$). $\Delta\nu_{1/2}$ is found to decrease with increasing H_{da},[6] and is best explained by consideration of the potential energy surfaces as presented in (Figure 1.4). In the uncoupled (diabatic) case, a Gaussian distribution of the energies is expected for the transition that is based upon a Boltzmann distribution of states in the ground state.[6] As H_{da} increases however, and the PES approaches a single-welled shape, the low energy side of the transition becomes increasingly cut-off, and ultimately truncated at ν_{max} in the most extreme cases.[6] Thus, while H_{da} aerves to sharpen the IVCT band, it can also be said that their shape is also indicative of the PES shape. That is, in the weakly coupled limit, the IVCT band will appear Gaussian but,

as coupling increases, the IVCT band will blue shift, sharpen, and become increasingly cut-off on the low energy side. While this is somewhat observed experimentally, its truncation at ν_{max} is never. The reason for this primarily lies within the uncertainty principle which, 1) does not allow for infinitely sharp energy cutoffs and 2) must noticeably contribute to the band shape. Additionally, since the transition is electronic in nature, it can further be accompanied by transitions of vibrational quanta as well, which also serves to broaden the IVCT band.

Nevertheless, Hush was able to derive an equation that relates the IVCT band shape, intensity, and placement to H_{da}.[6, 13]

$$H_{da} = \frac{2.06 * 10^{-2}(\nu_{max}\, \varepsilon\, \Delta\nu_{1/2})^{1/2}}{r_{da}} \qquad (1.15)$$

Here ν_{max}, ε, and $\Delta\nu_{1/2}$ have their usual meanings while r_{da} is the distance over which the electron is transferred. The Hush equation works reasonably well if H_{da} remains rather small ($H_{da} << \lambda/2$), but as $H_{da} \rightarrow \lambda/2$ however, the Hush equations give increasingly poor estimates due to deviation in r_{da} and $\Delta\nu_{1/2}$. The deviation in r_{da} arises from the increasingly delocalized electronic structure contracting the electron transfer distance, thus determination of r_{da} from X-ray crystallography becomes increasingly less accurate.[7, 16-18] Additionally, in the delocalized limit when nuclear frequencies begin to dominate ET, vibronic coupling to the electronic transition becomes so strong that it renders the $\Delta\nu_{1/2}$ value inaccurate.[19-20] Despite these drawbacks, the theories of electron transfer presented by Marcus and Hush have guided research for almost seven decades and continues to remain an integral part of the field. Their theories have inspired countless studies,[2, 5-9, 21-27] and still provide a common language spoken amongst the field.

1.3 Classification of Mixed-Valence Complexes

While numerous systems undergoing electron transfer can be termed mixed-valent, in reality there exists a spectrum of ET reactions that span the weakly interacting, diabatic limit to the strongly coupled, adiabatic limit. By definition a mixed-valence complex is one that contains two (or more) redox sites differing in their respective charge, where the two sites undergo electron exchange, and by way of this their oxidation states. The term mixed-valence reflects the fact that within the same molecule, their exists redox-sites in different valencies. The effects of H_{da} on these systems as discussed above draws specific attention to this parameter and their potential energy wells (PES, Figure 1.3 and Figure 1.4) as three possible shapes are observed. These shapes are entirely dependent on the value of H_{da} and represent three unique classes of coupling. First, when $H_{da} = 0$, two weakly interacting diabatic curves are present. The moment that H_{da} deviates from zero, the system becomes adiabatic and the ground state (G_1) is seen to contain two minima. This shape persists until $H_{da} = \lambda/2$ (i.e. $\Delta G^* = 0$), affording the final PES shape that is characterized by a single-minima and no activation barrier. Here, the electron neither resides exclusively on the donor or acceptor, but equally (and simultaneously) on both. While these effects were noticed relatively early in the field, shortly following Noel Hush's demonstration that location, intensity, and shape of the IVCT band could be used to determine the degree of electronic coupling, Melvin Robin and Peter Day in 1968 developed and published the currently accepted classification scheme for mixed-valence complexes.[28]

Their classification scheme is based upon discernable differences in the optical and electronic properties of mixed-valence complexes when the coupling (H_{da}) is some critical proportion of the reorganization energy (λ). As summarized in Figure 1.5, under this scheme, mixed-valence complexes are grouped into three primary classes: Class I, Class II, or

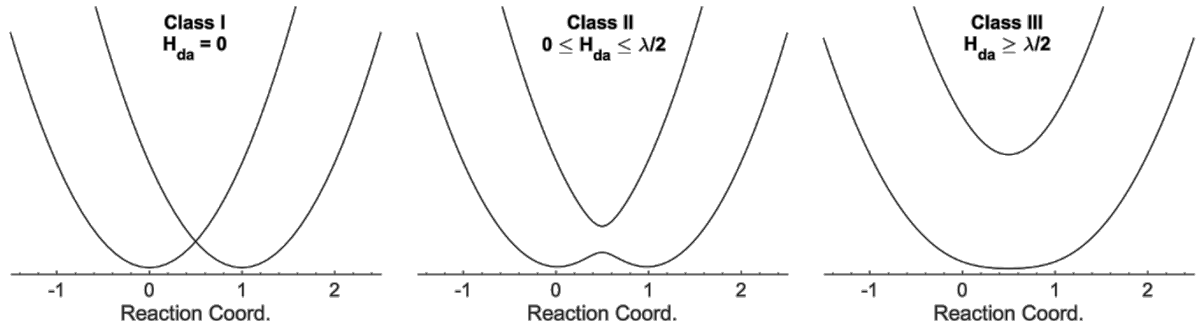

Figure 1.5. Potential energy surfaces for two-state mixed valences complexes highlighting the Robin-Day classification.

Class III.[6, 28] Class I complexes have no wavefunction overlap and therefore no electronic coupling ($H_{da} = 0$). They exist in the diabatic limit, are entirely charge localized, and exhibit no electronic communication between the donor and acceptor. Class II complexes are considered moderate to strongly coupled ($0 \leq H_{da} \leq \lambda/2$) and exist in the adiabatic limit. The small activation barrier towards thermal ET means these systems also exhibit charge localized behavior. Their localized behavior however, is associated with a timescale for thermal electron transfer. Class III complexes however, are highly coupled ($H_{da} \geq \lambda/2$) and exist in the strongly adiabatic limit. These complexes are characterized by a single-welled PESs with no activation barrier toward ET. The electron experiences unhindered movement between the donor and acceptor and is considered fully delocalized.

The mixed-valence complexes presented within this dissertation are Class II to Class II/III borderline and have with donor-acceptor units composed of oxocentered triruthenium acetate clusters of the type, $Ru_3(\mu^3\text{–}O)(OAc)_6(CO)(L_1)(BL)$ (L_1 = some pyridine based ligand and BL = some pyridine based bridging ligand). The rich redox chemistry of these clusters has proven them to be invaluable in studies of electron transfer dynamics across several decades.[29-51] While numerous studies within the Kubiak lab have focused on the use of 1,4-pyrazine as the bridging ligand between the Ru_3O cores, the studies presented in chapters 2–4 focus on the use of non-covalent interactions (π–π stacking and hydrogen bonding) as the

basis of the bridge. A brief history of the covalently bridged pyrazine clusters is presented in the following section to familiarize the reader with their optical, vibronic, and electronic properties.

1.4 Oxocentered Triruthenium Cluster: A Brief History

The dimers of ruthenium trimers presented in Figure 1.6 are neutral complexes, however upon a one electron reduction form thermodynamically stable mixed-valent complexes with an overall charge of –1,[30, 47] where, electron transfer between the two Ru_3O cores is mediated by the pyrazine π-system. Since the studies presented in this dissertation are based upon the formation of the mixed-valent state, it is beneficial to present and understand the redox chemistry of these systems in general. Electrochemical investigations present the clearest picture of the clusters redox chemistry and provide, in part, some insight of their electronic structure. At resting potentials, the clusters are found in their neutral (0) state with formal oxidation states of $Ru_3^{III,III,II}$–BL–$Ru_3^{III,III,III}$ (Figure 1.6). Upon sweeping to oxidative

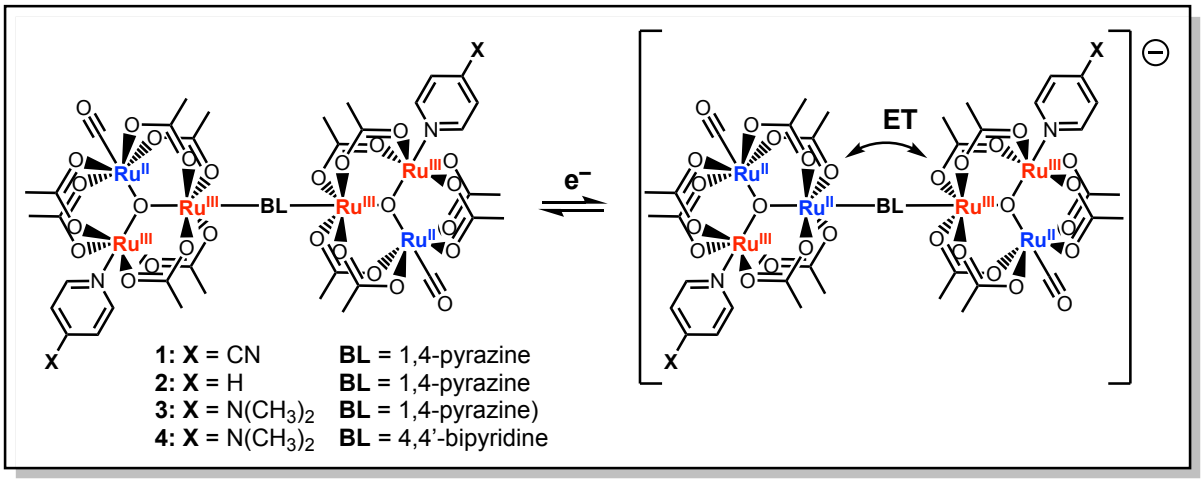

Figure 1.6. Pyrazine bridged oxo-centered triruthenium clusters before (left) and after (right) a one electron reduction. The respective oxidation state of each ruthenium atom have been highlighted for clairity.

potentials, the first feature observed is a two-electron (double current) oxidation at modest potentials ($E_{1/2}$ ≈ 0.5 V vs SCE) corresponding to the simultaneous oxidation of both Ru_3O

cores to the dicationic $Ru_3^{III,III,III}$–BL–$Ru_3^{III,III,III}$ state (0/+2 couple).[30, 47, 52] A second two-electron oxidation is additionally observed at even more positive potentials ($E_{1/2} \approx 1.2$ V vs SCE), corresponding to the formation of the $Ru_3^{III,III,IV}$– BL–$Ru_3^{III,III,IV}$ state (+2/+4 couple) that is stabilized by the μ-oxo bridge.[30, 47, 52] The reductive electrochemical behavior however is much more informative of the *intercluster* mixed-valent interactions between the two Ru_3O cores, where unlike the oxidative side, two one-electron reductions are observed near $E_{1/2} \approx -0.7$ V and –1.1 V vs SCE.[30, 47, 52] The first reduction corresponds to formation of the mixed-valent, $Ru_3^{III,II,II}$–BL–$Ru_3^{III,III,II}$ state (0/– couple), while the second reduction corresponds to the dianionic, $Ru_3^{III,II,II}$–BL–$Ru_3^{III,II,II}$ state (–/–2 couple).

Comparison of the electrochemical splitting between these two redox couples gives a qualitative estimation of the electronic communication in the system through the comproportionation constant (K_C) as follows:

$$K_C = e^{\frac{nF\Delta E}{RT}} \quad (1.16)$$

Here, the magnitude of K_C describes the thermodynamic stability of the mixed-valent, state with respect to disproportionation into the two isovalent states (0 and –2). That is, as ΔE increases so does K_C reflecting an increased stability of the mixed-valent state which is primarily facilitated by electronic coupling. For the clusters presented in Figure 1.6, the values for ΔE and K_C are observed to have a significant dependence on the ancillary pyridine ligands (ΔE, (K_C): **1**: 250 mV (1.7×10^4), **2**: 380 mV (2.7×10^6), **3**: 440 mV (2.8×10^7)), such that, the incorporation of stronger σ-donating ligands affords more highly coupled mixed-valent complexes.[30, 47, 52] This behavior is best explained through consideration of the orbital structure for the Ru_3O cores. The use of stronger σ-donors brings the ruthenium d-π manifold into closer energetic alignment with the pyrazine π* orbitals, which in turn facilitates greater electronic

communication across the bridged. This ultimately leads to more resonant electron delocalization across the bridging ligand between the two Ru_3O cores.

The incorporation of the carbonyl ligand on each of the Ru_3O cores is one of the most appealing modifications as it offers a convenient spectroscopic handle. Since frequency of the carbonyl stretching mode is highly sensitive to the nature of the π–backbonding interaction, the ν(CO) bands serve as a direct reporter of the electronic environment on each Ru_3O core. That is, when the clusters experience increased electron density the ν(CO) band will red-shift while decreased electron density will result in a blue-shift. The FTIR spectra of clusters **1**–**3** in each redox state are shown in Figure 1.7. The observation of a single, sharp, Gaussian shaped ν(CO) mode for the two isovalent oxidation states (0 and –2) supports that both ν(CO) modes experience an identical electronic environment.[30, 47, 52-53] The 40 cm^{-1} shift of the ν(CO) band in the dianionic state reflects the increased electron density residing on both Ru_3O cores. In the mixed valent state however, two nearly coalesced ν(CO) bands with half intensity are observed.[30, 47, 52-53]

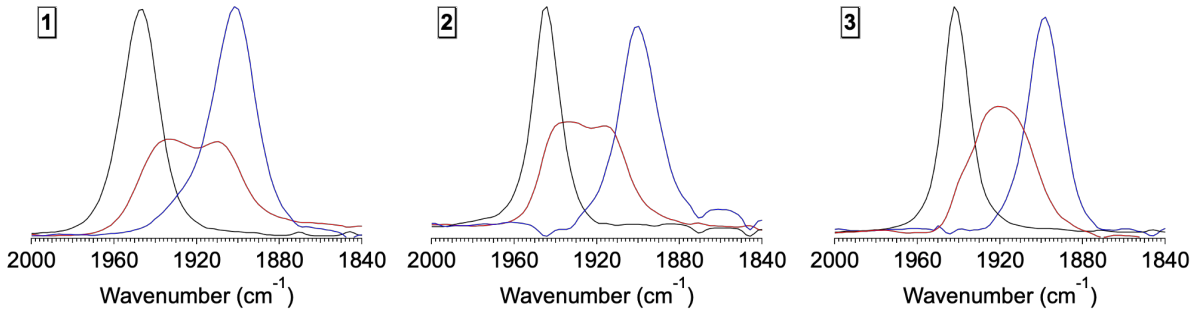

Figure 1.7. FTIR spectra of the ν(CO) bands for complexes **1**–**3** in the 0 (black), –1 (red), and –2 (blue) oxidation states. Spectra were recorded in acetonitrile and prepared by reduction with decamethylcobaltocene.

This behavior is indicative of a dynamic process occurring on the vibrational timescale.[52-56] Analogous to coalescence observed with dynamic NMR a typical dynamic NMR experiment,[57] the coalescence of the ν(CO) bands in $\mathbf{1}^{-}$–$\mathbf{3}^{-}$ indicate that electron is shared

between the two clusters with a rate near the vibrational timescale ($k_{ET} \approx 10^{-12}$ s^{-1}). Similar behavior has been observed previously in iron tricarbonyl systems, where coalescence of the ν(CO) bands was explained by a turn-style exchange mechanism of the carbonyl ligands.[55-56, 58-59] The rate of CO exchange was estimated on the picosecond timescale by use of an optical Bloch lineshape analysis.[60] This methodology is entirely analogous to the Bloch equations used in dynamic NMR,[61] however on a timescale that is a billion times faster. When a similar analysis is performed for **1**$^{-}$–**3**$^{-}$, picosecond exchange rates are predicted (k_{ET} (τ_{ET}) = **1**: 1 x 10^{11} s^{-1} (10 ps), **2**: 5 x 10^{11} s^{-1} (2 ps), **3**: 9 x 10^{11} s^{-1} (1.11 ps)),[30, 52] This analysis has specific importance and will be discussed in greater detail in chapters 4–6.

Up until this point the discussion has primarily focused on the application of a two-state model to mixed valency where only one IVCT band is predicted in the nIR. In the Ru_3O dimers presented thus far however, two IVCT bands in the nIR spectra (Figure 1.8) near 7000 and 10 000 cm^{-1} are observed. The appearance of these two charge transfer bands implies the existence of a second, additional state to which the ground state electron may transfer to.[6, 45] This behavior is best accounted for by a three-state model to mixed valency (right, Figure 1.8) where a third, bridging-ligand, state (G_c) is added to the two-state model.[6] The inclusion of this third state adds an additional electronic coupling term which describes the degree of wavefunction overlap between the donor and bridge (H_{ac}) or the acceptor and bridge (H_{bc}). The adiabatic surfaces are then generated analogous to the two-sate model, however, a 3 x 3 secular determinant (equation 1.17) is now solved for E.

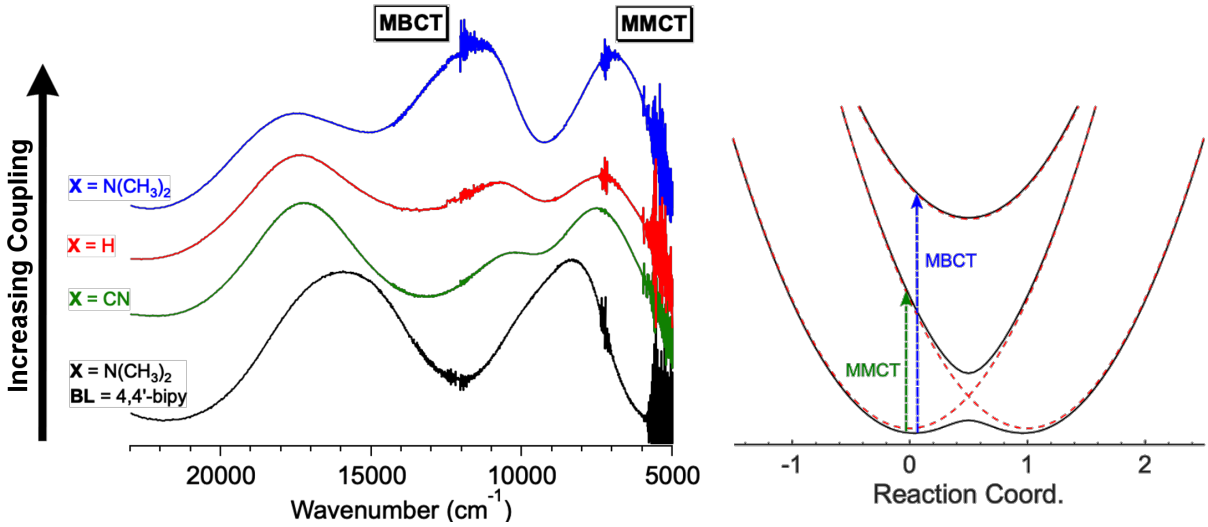

Figure 1.8. (left) Near infrared spectra for complexes **1**$^{-}$–**3**$^{-}$ (green, red, blue) and **4** (black, 4,4'-bipyridine as the bridging ligand) in acetonitrile highlighting the appearance of two IVCT bands. (right) Potential energy surface for the BCS three-state model.[6] The diabatic surfaces are shown as the dashed-red traces while adiabatic surfaces are shown in black.

$$\begin{vmatrix} G_a - E & H_{ca} & H_{ba} \\ H_{ac} & G_c - E & H_{bc} \\ H_{ab} & H_{cb} & G_b - E \end{vmatrix} = 0 \qquad (1.17)$$

The eigenvalues obtained here are the adiabatic surfaces consisting of a ground state (G_1), an excited acceptor state (G_2) and a third excited bridging state (G_3). States G_1 and G_2 are entirely analogous to the two-state model, while G_3 now represents the PES for charge transfer onto the bridging ligand. In the three-state model optical electron transfer can now occur from G_1, to either G_2 or G_3 resulting in the appearance of two IVCT bands in the nIR. The low energy IVCT band represents excitation from G_1 to G_2 and is termed metal-to-metal-charge-transfer (MMCT), while the high energy band represents excitation from G_1 to G_3 and is termed metal-to-bridge-charge-transfer (MBCT).

The appearance of two IVCT bands in **1**$^{-}$–**4**$^{-}$ is significant as it indicates substantial involvement of the bridging ligand in the mixed-valent state, observations additionally supported by resonance Raman experiments.[33, 62-64] Most importantly however, is the observation of a blue-shift in the MBCT band and a red-shift in the MMCT band across the

series presented in Figure 1.8.[45, 65] These observations are perhaps one of the most remarkable aspects of these systems as this behavior is directly predicted by the three-state model.[6, 45, 65] Analogous to the two-state model, this behavior is a direct result of wavefunction mixing as mediated by H_{ab} and H_{ac}. Here increased coupling stabilizes the G_1, destabilizes G_3, while G_2 remains essentially isoenergetic. This ultimately leads to a greater separation between G_1 and G_3, and a smaller separation between G_1 and G_2; thus, blue-shifting the MBCT band and red-shifting the MMCT band. Furthermore, both bands are observed to sharpen, and display an increasing cut-off on the low energy side; a direct result of G_1 becoming increasingly single-welled. These observations are unprecedented and represent the clearest picture of the localized (**4**$^-$) to nearly-delocalized (**3**$^-$) transition in mixed valency. These observations will have important implications in the next section and throughout chapters 1–4.

Recently, we extended our studies of mixed valency into complexes containing bridging ligands capable of forming hydrogen bonds. The complexes **5**–**7**, are based upon the same dimers of trimers motif, however, isonicotinic acid is now used in place of pyrazine. While these complexes exist predominantly as monomers in neutral solutions, upon a one-electron reduction the complexes rapidly dimerize to form hydrogen-bonded, mixed-valent anions

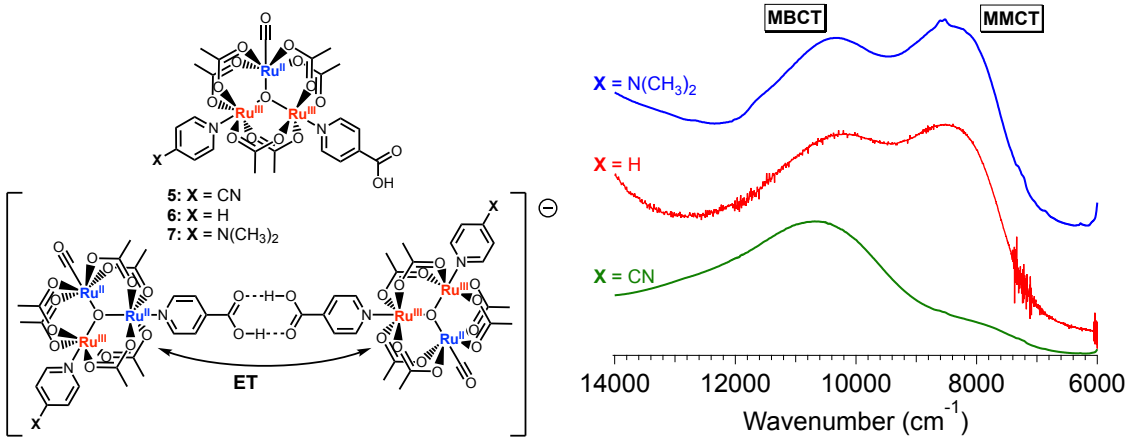

Figure 1.9. Structure of the free monomers (top) and the hydrogen-bonded dimers (bottom) upon a one-electron reduction, when **X** = CN (**5**), H (**6**), or $N(CH_3)_2$ (**7**). (right) nIR spectra of $(\mathbf{1}_2)^-$–$(\mathbf{3}_2)^-$ in DCM highlighting the appearance of two IVCT bands.

(Figure 1.9). This behavior was observable both electrochemically and spectroscopically.[44, 48] Through our studies we were able to show the observation of two, IVCT bands in the nIR spectrum (right, Figure 1.9) for complexes $(\mathbf{5}_2)^{-}$–$(\mathbf{7}_2)^{-}$.[44, 48] While a rate for electron transfer was never assigned, these findings mirror the previous observations in pyrazine bridged systems,[65] and signify that hydrogen bonds can support both ET and a sufficient degree of electronic coupling. These implications have specific importance in the presented in chapters 2–4 where the origin of this interaction is addressed in greater detail.

1.5Conclusions

To date, their remains limited study of complexes exhibiting mixed-valency across hydrogen bonds.[44, 50, 66-71] The study of ET across weak, non-covalent interactions has important implications not only in the understanding long range ET in biological systems,[72-75] but its importance also extends throughout the chemical sciences where weak, inter-molecular interactions readily affect the stability of artificial supramolecular structures,[76-77] and the selectivity of catalysts.[78-86] The purpose of this body of work is to examine the fundamental relationship between electron transfer and noncovalent interactions and the subsequent use of ν(CO) band coalescence in vibrational spectra to study the kinetics of ultrafast chemical dynamics. The results presented in the following chapters underscore the importance of the role that bridging ligands play in mediating wavefunction overlap between donor-acceptor units that are weakly associated.

1.6 References

1. von Hevesy, G.; Zechmeister, L., Über den intermolekularen Platzwechsel gleichartiger Atome. *Berichte der deutschen chemischen Gesellschaft (A and B Series)* **1920,** *53* (3), 410-415.
2. Sutin, N., Electron transfer reactions in solution: A historical perspective. *Advances in Chemical Physics* **1999,** *106*, 7-33.
3. Lewis, W. B.; Coryell, C. D.; Irvine, J. W., S 81. The electron transfer (exchange) between cobaltous and cobaltic amine complexes. *Journal of the Chemical Society (Resumed)* **1949,** (0), S386-S392.
4. *The proceedings of the 1952 meeting on electron trasfer was published in the 1952 October issue of The Journal of Chemical Physics (vol. 56)*.
5. Brunschwig, B.; Sutin, N., Energy surfaces, reorganization energies, and coupling elements in electron transfer. *Coord. Chem. Rev.* **1999,** *187*, 233-254.
6. Brunschwig, B. S.; Creutz, C.; Sutin, N., Optical transitions of symmetrical mixed-valence systems in the Class II-III transition regime. *Chem. Soc. Rev.* **2002,** *31* (3), 168-184.
7. D'Alessandro, D. M.; Keene, F. R., Current trends and future challenges in the experimental, theoretical and computational analysis of intervalence charge transfer (IVCT) transitions. *Chem. Soc. Rev.* **2006,** *35* (5), 424-440.
8. Weaver, M. J., Dynamical solvent effects on activated electron-transfer reactions: principles, pitfalls, and progress. *Chem. Rev.* **1992,** *92* (3), 463-480.
9. Sutin, N., Theory of electron transfer reactions: insights and hindsights. *Prog. Inorg.Chem.* **1983,** *30*, 441-498.
10. Nielson, R. M.; Golovin, M. N.; McManis, G. E.; Weaver, M. J., Orbital-overlap factor in electron transfer: sensitivity of homogeneous self-exchange kinetics for some metallocenes to electronic structure. *J. Am. Chem. Soc.* **1988,** *110* (6), 1745-1749.
11. Barbara, P. F.; Meyer, T. J.; Ratner, M. A., Contemporary issues in electron transfer research. *Journal of Physical Chemistry* **1996,** *100* (31), 13148-13168.
12. Marcus, R. A., On the Theory of Electrochemical and Chemical Electron Transfer Processes. *Can J Chem* **1959,** *37* (1), 155-163.
13. Hush, N. S., Intervalence-transfer absorption. II. Theoretical considerations and spectroscopic data. *Prog. Inorg.Chem.* **1967,** *8*, 391-444.
14. Turro, N. J., *Modern molecular photochemistry*. Benjamin/Cummings Pub. Co.: Menlo Park, Calif., 1978; p 628 p.
15. Hush, N. S., Homogeneous and heterogeneous optical and thermal electron transfer. *Electrochim. Acta* **1968,** *13* (5), 1005-1023.
16. Oh, D. H.; Boxer, S. G., Electrochromism in the near-infrared absorption spectra of bridged ruthenium mixed-valence complexes. *J. Am. Chem. Soc.* **1990,** *112* (22), 8161-2.
17. Karki, L.; Hupp, J. T., Orbital Specific Charge Transfer Distances, Solvent Reorganization Energies, and Electronic Coupling Energies: Electronic Stark Effect Studies of Parallel and Orthogonal Intervalence Transfer in (NC)5OsII-CN-RuIII(NH3)5. *J. Am. Chem. Soc.* **1997,** *119* (17), 4070-4073.
18. Bublitz, G. U.; Laidlaw, W. M.; Denning, R. G.; Boxer, S. G., Effective Charge Transfer Distances in Cyanide-Bridged Mixed-Valence Transition Metal Complexes. *J. Am. Chem. Soc.* **1998,** *120* (24), 6068-6075.

19. Piepho, S. B.; Krausz, E. R.; Schatz, P. N., Vibronic coupling model for calculation of mixed valence absorption profiles. *J. Am. Chem. Soc.* **1978,** *100* (10), 2996-3005.

20. Piepho, S. B., Vibronic coupling model for the calculation of mixed-valence line shapes: a new look at the Creutz-Taube ion. *J. Am. Chem. Soc.* **1990,** *112* (11), 4197-4206.

21. Newton, M. D.; Sutin, N., Electron transfer reactions in condensed phases. *Ann. Rev. Phys. Chem.* **1984,** *35*, 437-480.

22. Marcus, R. A.; Sutin, N., Electron transfers in chemistry and biology. *Biochimica et Biophysica Acta, Reviews on Bioenergetics* **1985,** *811* (3), 265-322.

23. Zhang, L. T.; Ko, J.; Ondrechen, M. J., Electronic structure of the Creutz-Taube ion. *J. Am. Chem. Soc.* **1987,** *109* (6), 1666-1671.

24. Zhang, L. T.; Ko, J.; Ondrechen, M. J., Nonadiabatic quantum mechanical treatment of the absorption lineshape of bridged mixed-valence dimers. *J. Phys. Chem.* **1989,** *93* (8), 3030-3034.

25. Marcus, R. A., Theory of charge-transfer spectra in frozen media. *Journal of Physical Chemistry* **1990,** *94* (12), 4963-4966.

26. Ito, T.; Hamaguchi, T.; Nagino, H.; Yamaguchi, T.; Kido, H.; Zavarine, I. S.; Richmond, T.; Washington, J.; Kubiak, C. P., Electron transfer on the infrared vibrational time scale in-the mixed valence state of 1,4-pyrazine- and 4,4 '-bipyridine-bridged ruthenium cluster complexes. *J. Am. Chem. Soc.* **1999,** *121* (19), 4625-4632.

27. Demadis, K. D.; Hartshorn, C. M.; Meyer, T. J., The Localized-to-Delocalized Transition in Mixed-Valence Chemistry. *Chem. Rev.* **2001,** *101*, 2655-2685.

28. Robin, M. B.; Day, P., Mixed Valence Chemistry-A Survey and Classification. In *Advances in Inorganic Chemistry and Radiochemistry*, Emeléus, H. J.; Sharpe, A. G., Eds. Academic Press: 1968; Vol. 10, pp 247-422.

29. Baumann, J. A.; Salmon, D. J.; Wilson, S. T.; Meyer, T. J.; Hatfield, W. E., Electronic structure and redox properties of the clusters [Ru3O(CH3CO2)6L3]n+. *Inorg Chem* **1978,** *17* (12), 3342-3350.

30. Ito, T.; Hamaguchi, T.; Nagino, H.; Yamaguchi, T.; Kido, H.; Zavarine, I. S.; Richmond, T.; Washington, J.; Kubiak, C. P., Electron transfer on the infrared vibrational time scale in-the mixed valence state of 1,4-pyrazine- and 4,4 '-bipyridine-bridged ruthenium cluster complexes. *J. Am. Chem. Soc.* **1999,** *121* (19), 4625-4632.

31. Londergan, C. H.; Salsman, J. C.; Ronco, S.; Dolkas, L. M.; Kubiak, C. P., Solvent dynamical control of electron-transfer rates in mixed-valence complexes observed by infrared spectral line shape coalescence. *J. Am. Chem. Soc.* **2002,** *124* (22), 6236-6237.

32. Londergan, C. H.; Kubiak, C. P., Vibronic participation of the bridging ligand in electron transfer and delocalization: New application of a three-state model in pyrazine-bridged mixed-valence complexes of trinuclear ruthenium clusters. *J. Phys. Chem. A* **2003,** *107* (44), 9301-9311.

33. Londergan, C. H.; Rocha, R. C.; Brown, M. G.; Shreve, A. P.; Kubiak, C. P., Intervalence involvement of bridging ligand vibrations in hexaruthenium mixed-valence clusters probed by resonance Raman spectroscopy. *J. Am. Chem. Soc.* **2003,** *125* (46), 13912-13913.

34. Londergan, C. H.; Salsman, J. C.; Ronco, S.; Kubiak, C. P., Infrared Activity of Symmetric Bridging Ligand Modes in Pyrazine-Bridged Hexaruthenium Mixed-Valence Clusters. *Inorg. Chem.,* **2003,** *42*, 926-928.

35. Ito, T.; Imai, N.; Yamaguchi, T.; Hamaguchi, T.; Londergan, C. H.; Kubiak, C. P., Observation and dynamics of "charge-transfer isomers". *Angew. Chem. Int. Ed.* **2004,** *43* (11), 1376-1381.

36. Salsman, J. C.; Kubiak, C. P., Mixed valence isomers. *J. Am. Chem. Soc.* **2005,** *127* (8), 2382-2383.

37. Londergan, C. H.; Salsman, J. C.; Lear, B. J.; Kubiak, C. P., Observation and dynamics of "mixed-valence isomers" and a thermodynamic estimate of electronic coupling parameters. *Chem. Phys.* **2006,** *324* (1), 57-62.

38. Salsman, J. C.; Ronco, S.; Londergan, C. H.; Kubiak, C. P., Tuning the Electronic Communication and Rates of Intramolecular Electron Transfer of Dimers of Trinuclear Ruthenium Clusters: Bridging Ligand and Ancillary Ligand Effects. *Inorg. Chem.* **2006,** *45*, 547-554.

39. Lear, B. J.; Glover, S. D.; Salsman, J. C.; Londergan, C. H.; Kubiak, C. P., Solvent dynamical control of ultrafast ground state electron transfer: implications for class II-III mixed valency. *J. Am. Chem. Soc.* **2007,** *129* (42), 12772-12779.

40. Lear, B. J.; Kubiak, C. P., Origins of Cooperative Noncovalent Host−Guest Chemistry in Mixed Valence Complexes. *J. Phys. Chem. B* **2007,** *111* (24), 6766–6771.

41. Glover, S. D.; Lear, B. J.; Salsman, C.; Londergan, C. H.; Kubiak, C. P., Electron transfer at the class II/III borderline of mixed valency: Dependence of rates on solvent dynamics and observation of a localized-to-delocalized transition in freezing solvents. *Philos. Trans. Roy. Soc. A* **2008,** *366* (1862), 177-185.

42. Goeltz, J. C.; Hanson, C. J.; Kubiak, C. P., Rates of Electron Self-Exchange Reactions between Oxo-Centered Ruthenium Clusters Are Determined by Orbital Overlap. *Inorg Chem* **2009,** *48* (11), 4763–4767.

43. Goeltz, J. C.; Benson, E. E.; Kubiak, C. P., Electronic Structural Effects in Self-Exchange Reactions. *The Journal of Physical Chemistry B* **2010,** *114* (45), 14729–14734.

44. Goeltz, J. C.; Kubiak, C. P., Mixed Valency across Hydrogen Bonds. *J. Am. Chem. Soc.* **2010,** *132* (49), 17390–17392.

45. Glover, S. D.; Kubiak, C. P., Persistence of the Three-State Description of Mixed Valency at the Localized-to-Delocalized Transition. *J. Am. Chem. Soc.* **2011,** *133* (22), 8721-8731.

46. Canzi, G.; Kubiak, C. P., Ultrafast Electron Transfer Across a Gold Nanoparticle: A Study of Ancillary Ligand and Solvent Influences. *Journal of Physical Chemistry C* **2012,** *116* (11), 6560-6566.

47. Kubiak, C. P., Inorganic Electron Transfer: Sharpening a Fuzzy Border in Mixed Valency and Extending Mixed Valency across Supramolecular Systems. *Inorg. Chem.* **2013,** *52* (10), 5663-5676.

48. Canzi, G.; Goeltz, J. C.; Henderson, J. S.; Park, R. E.; Maruggi, C.; Kubiak, C. P., On the Observation of Intervalence Charge Transfer Bands in Hydrogen-Bonded Mixed-Valence Complexes. *J. Am. Chem. Soc.* **2014,** *136* (5), 1710-1713.

49. Porter, T. M.; Canzi, G. C.; Chabolla, S. A.; Kubiak, C. P., Tuning Electron Delocalization and Transfer Rates in Mixed-Valent Ru3O Complexes through "Push-Pull" Effects. *J. Phys. Chem. A* **2016,** *120* (32), 6309-6316.

50. Porter, Tyler M.; Heim, G. P.; Kubiak, C. P., Effects of electron transfer on the stability of hydrogen bonds. *Chemical Science* **2017,** *8* (11), 7324-7329.

51. Porter, Tyler M.; Heim, G. P.; Kubiak, C. P., Stable mixed valence complexes formed by electron delocalization across hydrogen bonds of pyrimidinone linked metal clusters. *J. Am. Chem. Soc.* **2018,** *140*, submitted.

52. Ito, T.; Hamaguchi, T.; Nagino, H.; Yamaguchi, T.; Washington, J.; Kubiak, C. P., Effects of rapid intramolecular electron transfer on vibrational spectra. *Science* **1997,** *277* (5326), 660-663.

53. Londergan, C. H.; Kubiak, C. P., Electron transfer and dynamic infrared-band coalescence: It looks like dynamic NMR spectroscopy, but a billion times faster. *Chem. Eur. J.* **2003,** *9* (24), 5962-5969.

54. Turner, J. J.; Poliakoff, M., Infrared-Spectroscopy from Megaseconds to Picoseconds. *Polyhedron* **1989,** *8* (13-14), 1637-1640.

55. Turner, J. J.; Gordon, C. M.; Howdle, S. M., Infrared Spectral Features Due to Very Rapid Fluxional Motion - Changes in the Infrared Carbonyl Stretching Spectra of Tricarbonyl(Eta(4)-Norbornadiene)Iron with Temperature. *Journal of Physical Chemistry* **1995,** *99* (49), 17532-17538.

56. Grevels, F. W.; Kerpen, K.; Klotzbucher, W. E.; McClung, R. E. D.; Russell, G.; Viotte, M.; Schaffner, K., The very low barrier of CO site exchange in tricarbonyl(eta(4)-1,5-cyclooctadiene)iron: Picosecond kinetics in solution investigated by line shape simulation of the nu(CO) IR bands and complementary evidence from the course of (CO)-C-13 incorporation in a low-temperature matrix. *J. Am. Chem. Soc.* **1998,** *120* (40), 10423-10433.

57. Hore, P. J., *Nuclear magnetic resonance*. Oxford University Press: Oxford ; New York, 1995; p v, 90 p.

58. Grevels, F.-W.; Jacke, J.; Klotzbücher, W. E.; Krüger, C.; Seevogel, K.; Tsay, Y.-H., Dynamic Processes on the IR Time Scale: Coalescence of CO Stretching Vibrational Bands in [(η4-Diene)Fe(CO)3] Complexes. *Angewandte Chemie International Edition in English* **1987,** *26* (9), 885-887.

59. Turner, J. J.; Bühl, M., Infrared Dynamics of Iron Carbonyl Diene Complexes. *The Journal of Physical Chemistry A* **2018,** *122* (14), 3497-3505.

60. Grevels, F.-W.; Kerpen, K.; Klotzbücher, W. E.; McClung, R. E. D.; Russell, G.; Viotte, M.; Schaffner, K., The Very Low Barrier of CO Site Exchange in Tricarbonyl(η4-1,5-cyclooctadiene)iron: Picosecond Kinetics in Solution Investigated by Line Shape Simulation of the ν(CO) IR Bands and Complementary Evidence from the Course of 13CO Incorporation in a Low-Temperature Matrix. *J. Am. Chem. Soc.* **1998,** *120* (40), 10423-10433.

61. Hore, P. J., *Nuclear Magnetic Resonance*. Oxford University Press Inc.: New York, 1995.

62. Londergan, C. H.; Kubiak, C. P., Vibronic Participationof the Bridging Ligand in Electron Trasfer and Delocalization: New Application of a Three-Sate Model in Pyrazine-Bridged Mixed-Valence Complexes of Trinuclear Ruthenium Clusters. *Journal of Physical Chemistry, A* **2003,** *107*, 9301-9311.

63. Londergan, C. H.; Salsman, C. J.; Ronco, S.; Kubiak, C. P., Infrared Activity of Symmetric Bridging Ligand Modes in Pyrazine-Bridged Hexaruthenium Mixed-Valence Clusters. *Inorg Chem* **2003,** *42*, 926-928.

64. Rocha, R. C.; Brown, M. G.; Londergan, C. H.; Salsman, J. C.; Kubiak, C. P.; Shreve, A. P., Intervalence-resonant Raman spectroscopy of strongly coupled mixed-valence cluster dimers of ruthenium. *J. Phys. Chem. A.* **2005,** *109* (40), 9006-9012.

65. Kubiak, C. P., Inorganic Electron Transfer: Sharpening a Fuzzy Border in Mixed Valency and Extending Mixed Valency across Supramolecular Systems. *Inorg Chem* **2013,** *52* (10), 5663-5676.

66. Kaim, W.; Lahiri, G. K., Unconventional Mixed-Valent Complexes of Ruthenium and Osmium. *Angewandte Chemie International Edition* **2007,** *46* (11), 1778–1796.

67. Tadokoro, M.; Inoue, T.; Tamaki, S.; Fujii, K.; Isogai, K.; Nakazawa, H.; Takeda, S.; Isobe, K.; Koga, N.; Ichimura, A.; Nakasuji, K., Mixed-Valence States Stabilized by Proton Transfer in a Hydrogen-Bonded Biimidazolate Rhenium Dimer. *Angewandte Chemie International Edition* **2007,** *46* (31), 5938–5942.

68. Wilkinson, L. A.; McNeill, L.; Meijer, A. J. H. M.; Patmore, N. J., Mixed Valency in Hydrogen Bonded 'Dimers of Dimers'. *J. Am. Chem. Soc.* **2013,** *135* (5), 1723–1726.

69. Canzi, G.; Goeltz, J. C.; Henderson, J. S.; Park, R. E.; Maruggi, C.; Kubiak, C. P., On the Observation of Intervalence Charge Transfer Bands in Hydrogen-Bonded Mixed-Valence Complexes. *J. Am. Chem. Soc.* **2014,** *136* (5), 1710–1713.

70. Jin, L.; Matsuda, Y.; Uemura, K.; Ebihara, M., Mixed Valency in Quadruple Hydrogen-Bonded Dimers of Bis(biimidazolate)dirhodium Complexes. *Inorg Chem* **2015,** *54* (5), 2331–2338.

71. Porter, T. M.; Heim, G. P.; Kubiak, C. P., Stable Mixed-Valent Complexes Formed by Electron Delocalization Across Hydrogen Bonds of Pyrimidinone-Linked Metal Clusters. *J. Am. Chem. Soc.* **2018,** *140* (40), 12756-12759.

72. Gray, H. B.; Winkler, J. R., Electron tunneling through proteins. *Quarterly Reviews of Biophysics* **2003,** *36* (3), 341-372.

73. Gray, H. B.; Winkler, J. R., Long-range electron transfer. *Proceedings of the National Academy of Sciences of the United States of America* **2005,** *102* (10), 3534-3539.

74. Gray, H. B.; Winkler, J. R., Electron flow through proteins. *Chem Phys Lett* **2009,** *483* (1–3), 1-9.

75. Winkler, J. R.; Gray, H. B., Electron Flow through Metalloproteins. *Chem. Rev.* **2014,** *114* (7), 3369-3380.

76. Lodish, H.; Berk, A.; Kaiser, C. A.; Krieger, M.; Bretscher, B.; Ploegh, H.; Amon, A.; Martin, K. C., *Molecular Cell Biology*. 8 ed.; W. H. Freeman and Company: New York, NY, 2016.

77. Karshikoff, A., *Non-Covalent Interactions in Proteins*. PUBLISHED BY IMPERIAL COLLEGE PRESS AND DISTRIBUTED BY WORLD SCIENTIFIC PUBLISHING CO.: 2006; p 348.

78. Hashiguchi, S.; Fujii, A.; Takehara, J.; Ikariya, T.; Noyori, R., Asymmetric Transfer Hydrogenation of Aromatic Ketones Catalyzed by Chiral Ruthenium(II) Complexes. *J. Am. Chem. Soc.* **1995,** *117* (28), 7562-7563.

79. Noyori, R.; Hashiguchi, S., Asymmetric Transfer Hydrogenation Catalyzed by Chiral Ruthenium Complexes. *Acc. Chem. Res.* **1997,** *30* (2), 97-102.

80. Trost, B. M.; Machacek, M. R.; Aponick, A., Predicting the Stereochemistry of Diphenylphosphino Benzoic Acid (DPPBA)-Based Palladium-Catalyzed Asymmetric Allylic Alkylation Reactions: A Working Model. *Acc. Chem. Res.* **2006,** *39* (10), 747-760.

81. Casey, C. P.; Guan, H., Cyclopentadienone Iron Alcohol Complexes: Synthesis, Reactivity, and Implications for the Mechanism of Iron-Catalyzed Hydrogenation of Aldehydes. *J. Am. Chem. Soc.* **2009,** *131* (7), 2499-2507.

82. Rakowski DuBois, M.; DuBois, D. L., The roles of the first and second coordination spheres in the design of molecular catalysts for H2 production and oxidation. *Chem Soc Rev* **2009,** *38* (1), 62-72.

83. Knowles, R. R.; Jacobsen, E. N., Attractive noncovalent interactions in asymmetric catalysis: links between enzymes and small molecule catalysts. *Proc Natl Acad Sci U S A* **2010,** *107* (48), 20678-85.

84. Machan, C. W.; Chabolla, S. A.; Yin, J.; Gilson, M. K.; Tezcan, F. A.; Kubiak, C. P., Supramolecular Assembly Promotes the Electrocatalytic Reduction of Carbon Dioxide by Re(I) Bipyridine Catalysts at a Lower Overpotential. *J. Am. Chem. Soc.* **2014,** *136* (41), 14598–14607.

85. Zhang, X.; Jones, G. O.; Hedrick, J. L.; Waymouth, R. M., Fast and selective ring-opening polymerizations by alkoxides and thioureas. *Nat Chem* **2016,** *8* (11), 1047-1053.

86. Neel, A. J.; Hilton, M. J.; Sigman, M. S.; Toste, F. D., Exploiting Non-covalent pi Interactions for Catalyst Design. *Nature* **2017,** *543*, 637-646.

Chapter 2

Tuning Electron Delocalization and Transfer Rates Through Electronic 'Push–Pull' Effects.

2.1 Introduction

Non-covalent interactions such as hydrogen-bonding and π-π stacking are ubiquitous in supramolecular chemistry.[1-8] Over the last several decades there has been continued interest in the study of electron transfer (ET) across non-covalent interactions,[9-15] as these reactions are essential to the broader understanding of how long range ET occurs in both biological and artificial systems.[1-2, 8, 11, 16-17] While the study of ET across hydrogen bonds has received considerable interest,[9-15] other non-covalent interactions, such as π-π stacking, have remained relatively underexplored. The ease with which π interactions form in supramolecular systems makes them ideal candidates for self-assembling motifs in the development of molecular based electronic devices.[18-20]

Several theoretical and experimental studies on ET through π-interactions have shown that the electronic coupling parameter (H_{ab}), has a significant dependence on the overlap between exchanging units and minor structural variations readily perturb this interaction and can inhibit ET.[7, 20-21] The structural electronic effects that govern electron exchange in oxo-centered triruthenium clusters has been well reported in literature, where large electronic couplings have previously been observed in oxo-centered triruthenium clusters in the form of covalently linked dimers,[22-26] freely diffusing monomers,[27-28] and in hydrogen-bonded dimers.[13, 15] This rich history makes these clusters an excellent starting point to better understand the nature of electronic coupling across π-interactions. Herein, we report on the synthesis, characterization, and one-electron self-exchange behavior of mixed-valent oxocentered triruthenium clusters ($[Ru_3(\mu^3\text{-}O)(OAc)_6(CO)(L_1)(pep)]^-$, where L_1 = 4-cyanopyridine (cpy, **1**), pyridine (py, **2**), or 4-dimethylaminopyridine (dmap, **3**)) featuring an extended aromatic ancillary ligand, 4-(phenylethynyl)pyridine (pep), as the basis for the π-π bridging interaction (Figure 2.1).

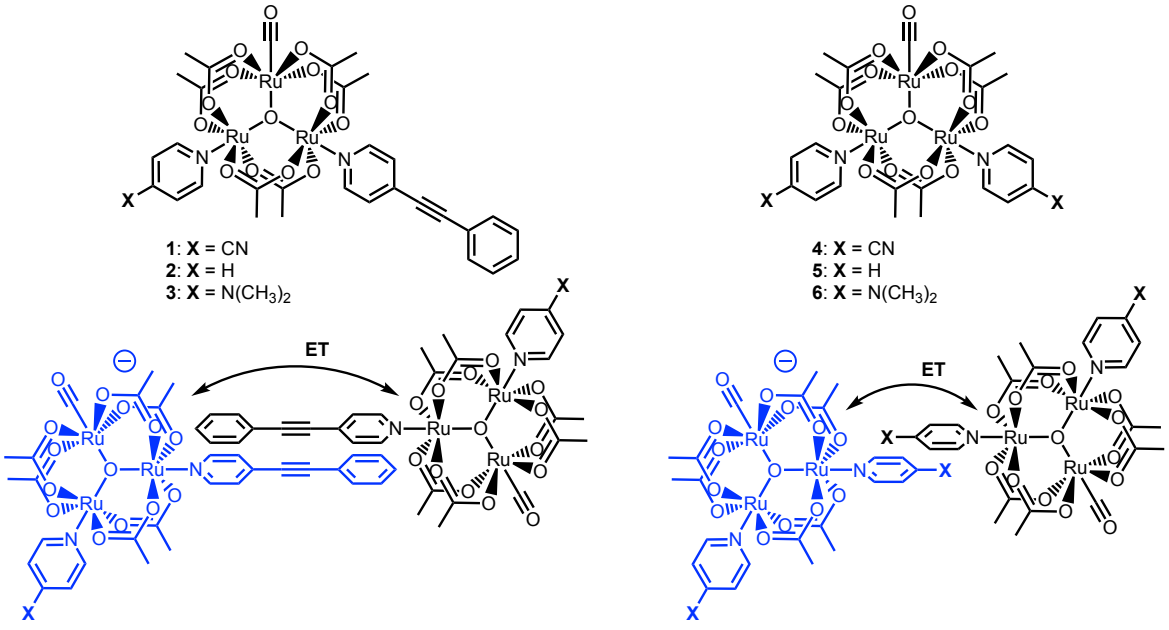

Figure 2.1. (top) Oxo-centered triruthenium clusters of the type $Ru_3(\mu^3\text{-}O)(OAc)_6(CO)(L_1)(pep)$ where L_1 = 4-cyanopyridine (cpy, **1**), pyridine (py, **2**), or 4-dimethylaminopyridine (dmap, **3**). (bottom) Proposed self-exchange interaction upon a one electron reduction forming the π-stacked self-exchanging pairs $(\mathbf{1}_2)^-$, $(\mathbf{2}_2)^-$, and $(\mathbf{3}_2)^-$.

2.2 Results and Discussion

While electron self-exchange reactions are some of simplest chemical transformations, they are also one of the most revealing. In the context of Marcus-Hush theory of electron transfer (ET), the rates of electron self-exchange (k_{et}) can be directly related to the total reorganization energy (λ_{tot}) for ET and to rates of *intermolecular* ET with other redox agents.[29] The kinetics of electron self-exchange for $[Ru_3(\mu^3\text{-}O)(OAc)_6(CO)(L_1)(pep)]^{0/-}$ pairs ($(\mathbf{1}_2)^-$–$(\mathbf{3}_2)^-$) were investigated by NMR line broadening experiments (Figure 2.2). In a typical self-exchange experiment, the mole fraction of the reduced species is varied with respect to the oxidized species and the NMR spectrum is recorded. The NMR lineshape is highly sensitive to the rate of chemical exchange between the oxidized and reduced pairs ($(\mathbf{1}_2)^-$–$(\mathbf{3}_2)^-$), when exchange is in the fast regime ($k_{et}C_{tot} >> 2\pi(\Delta\nu)$, $\Delta\nu$ is the frequency difference in Hz between the exchanging species) the chemical shifts of the exchanging species are the weighted average of the diamagnetic (oxidized) and paramagnetic (reduced) chemical shifts (Figure 2.2 and Figure 2.20–Figure 2.22).[30] After spectral deconvolution, the electron self-exchange rate constants are then determined by equation 2.1.

$$k_{et} = \frac{4\pi\chi_p\chi_d(\Delta\nu)^2}{(W_{dp}-\chi_p W_p-\chi_d W_d)C_{tot}} \qquad (2.1)$$

Here, $_p$ and χ_d are the mole fractions of paramagnetic and diamagnetic species, $\Delta\nu$ is the difference in chemical shift between paramagnetic and diamagnetic species in Hertz, W_{dp} is the peak width at half maximum of the mixture in question, W_p and W_d are the peak widths at half maximum of the pure paramagnetic and diamagnetic species, and C_{tot} is the total concentration in moles per liter.[30]

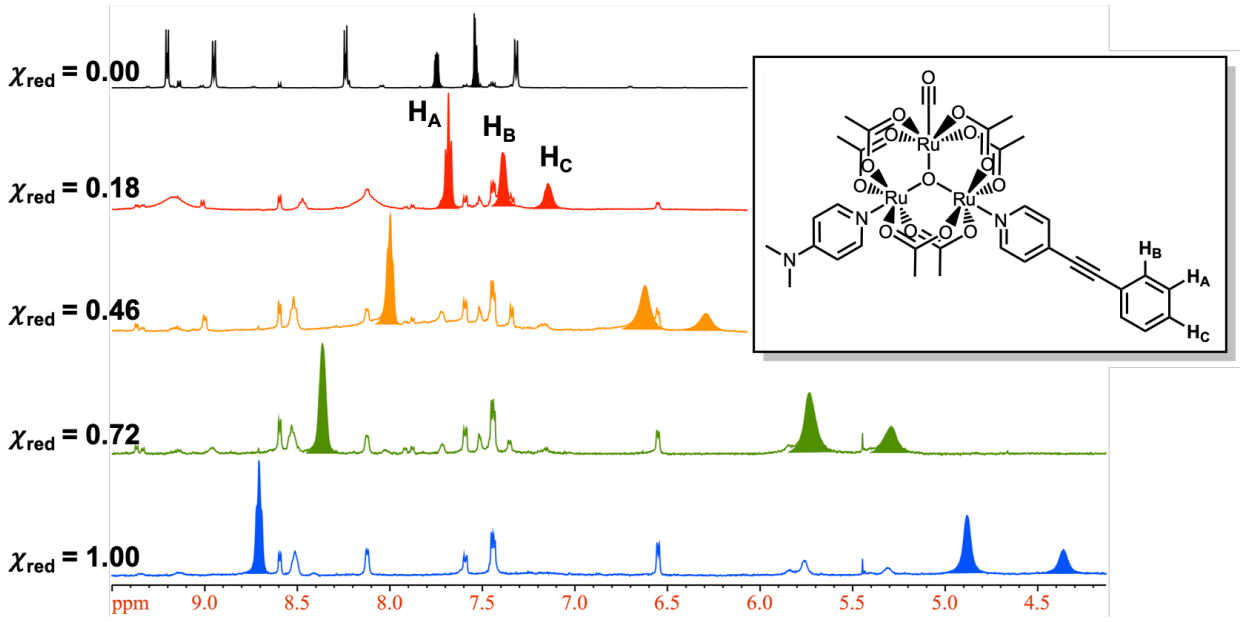

Figure 2.2. ^{1}H NMR of **3** in ACN-d_3 at 20 °C with increasing mole fraction of the reduced cluster (**3**)$^{-}$ from top to bottom. Protons H_A, H_B, and H_C have been highlighted to show increasing paramagnetic contact shift with increasing mole fraction of the reduced clusters.

Under an inert atmosphere in a nitrogen filled glove box, a 5-6 mM stock solution of complexes **1**–**3** was prepared in dry, degassed deuterated acetonitrile. Five aliquots of the *oxidized* stock solution (**1**–**3**) was added to six separate J-Young NMR tubes giving volumes of 100, 200, 250, 300, 400, and 500 μL respectively. The remaining stock solution was then cooled to –30 °C in a freezer and decamethylcobaltocene ($Co(cp^*)_2$) was added over a period of 30 minutes in small increments to fully reduce the sample by one electron (confirmed by FTIR spectroscopy). The reduced solution was then filtered over glass wool and added to the first five aforementioned J-Young tubes in five aliquots of 400, 300, 250, 200, 100 μL respectively bringing the total solution volume to 500 μL for each sample. An additional NMR tube was also prepared with 500 μL of the fully reduced sample giving seven NMR samples with mole fractions of the reduced species ranging from 0 to 1.00. After collecting ^{1}H NMR spectra, the samples were injected into a SPECAC sealed liquid IR cell with CaF_2 windows and a path length of 0.1 mm where the IR and UV-Visible spectra were subsequently collected, allowing determination of the

mole fractions of the exchanging species by IR spectroscopy. All samples were analyzed immediately and were stable for days unless subjected to atmosphere.

The ν(CO) region of the spectra was fit to two, well-resolved Voigt line shapes, and mole fraction ratios were found by integration of the ν(CO) bands of the neutral (1944 cm^{-1} (**1**), 1942 cm^{-1} (**2**), 1939 cm^{-1} (**3**)) and singly reduced (1905 cm^{-1} (**1**$^{-}$), 1902 cm^{-1} (**2**$^{-}$), 1899 cm^{-1} (**3**$^{-}$) species. Representative spectra for ν(CO) shifts upon reduction in acetonitrile are shown as Figure 2.3 for complex **3** (see appendix 2.5, Figure 2.23 for **1** and **2**). The 40 cm^{-1} difference between the ν(CO) modes of the exchanging species and lack of observed spectral coalescence indicates exchange is occurring slower than the IR timescale and places an upper bound to k_{et} of 10^{11} M^{-1} s^{-1}. Exchange however, was found to be in the fast regime for NMR spectroscopy,[30] with $k(C_{tot}) \gg 2\pi(\Delta\nu)$, as the chemical shifts for the exchanging species were observed as the averages of the diamagnetic and paramagnetic chemical shifts weighted by their respective mole fractions (right, Figure 2.3). Through equation 2.1, the electron self-exchange rate constants for **1–3** were found to range from 4.3 to 9.2 x 10^7 M^{-1} s^{-1} in ACN-d_3 (Table 2.1) and are comparable in magnitude for redox couples of the homoleptic clusters **4–6**.[27-28, 31]

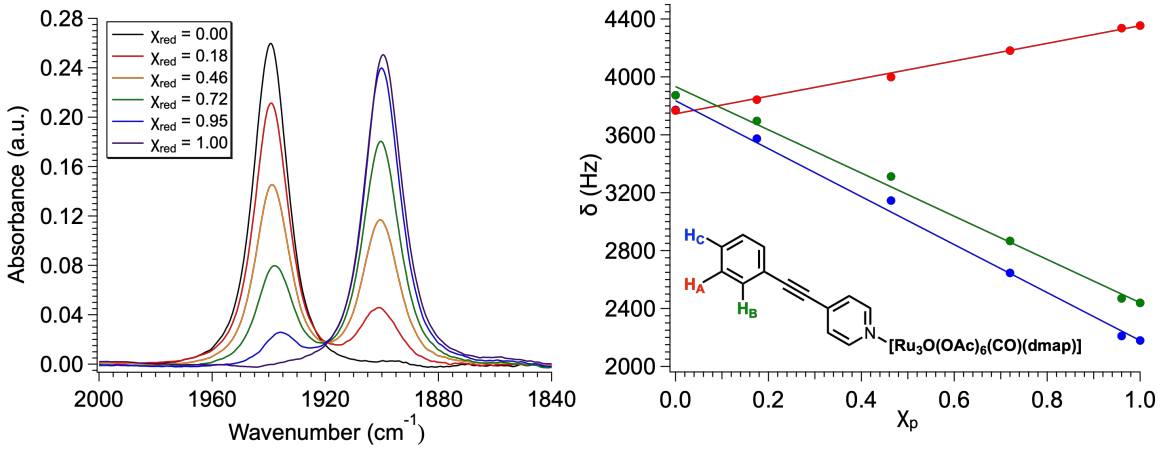

Figure 2.3. (left) IR spectra of the ν(CO) region for **3** in ACN with varying mole fractions of [red]/[ox], experimental mole fractions were determined from integration of ν(CO) bands. (right) Plot of χ_p determined from integration of ν(CO) bands versus chemical shift of the highlighted pep protons.

Table 2.1. Electron self-exchange rate constants (k_{et}) for complexes **1**–**3** and **4**–**6** in ACN-d_3 at 23 °C as determined through equation 2.1.

Complex	k_{ET} ACN (x 10^{-7} M^{-1} s^{-1})	Pyridine pK_a
1	4.3(2)	1.9
2	6.8(2)	5.1
3	9.9(6)	9.2
4	13(3)	1.9
5	1.8(5)	5.1
6	0.7(5)	9.2

In clusters **1**-**3**, the rate constants were found to scale linearly with pyridine ligand pK_a with the fastest self-exchange observed when the most electron-donating ligand was used. The near linearity in the logarithmic plot of rate constant versus pyridyl ligand pK_a (Figure 2.1) suggests that the electron-donating nature of the pyridyl ligands contribute to the activation energy, expressed below in the standard Marcus-Hush formalism (Equation 2.2).[32-33]

$$k_{et} = k\nu e^{\frac{\frac{\lambda}{4} - H_{ab} + \frac{H_{ab}^2}{\lambda}}{RT}} \qquad (2.2)$$

While equation 2.2 is only applicable in the adiabatic regime, it is important to note that H_{ab} needs only to be a few percent of λ to achieve adiabaticity.[23, 27-28] Consistent with previous studies,[27-28] the reorganization energies for the 0/– couple in **1**–**3** are estimated to be on the order of ~10 000 cm^{-1} while H_{ab} is estimated to be in the adiabatic regime at 10-15% of λ.[23, 27-28] When these conditions are used in conjunction with equation 2.2, rate constants on the order of 10^7 M^{-1} s^{-1} are predicted. It is unlikely that differences in the nuclear reorganization and inner-shell barriers contribute much to observed differences in rate between **1**–**3**, as the ~40 cm^{-1} shift in the ν(CO) mode upon reduction suggests that inner-sphere reorganization energies are comparable amongst the six clusters.[27-28] It is important to note however, that the ν(CO) modes are not as

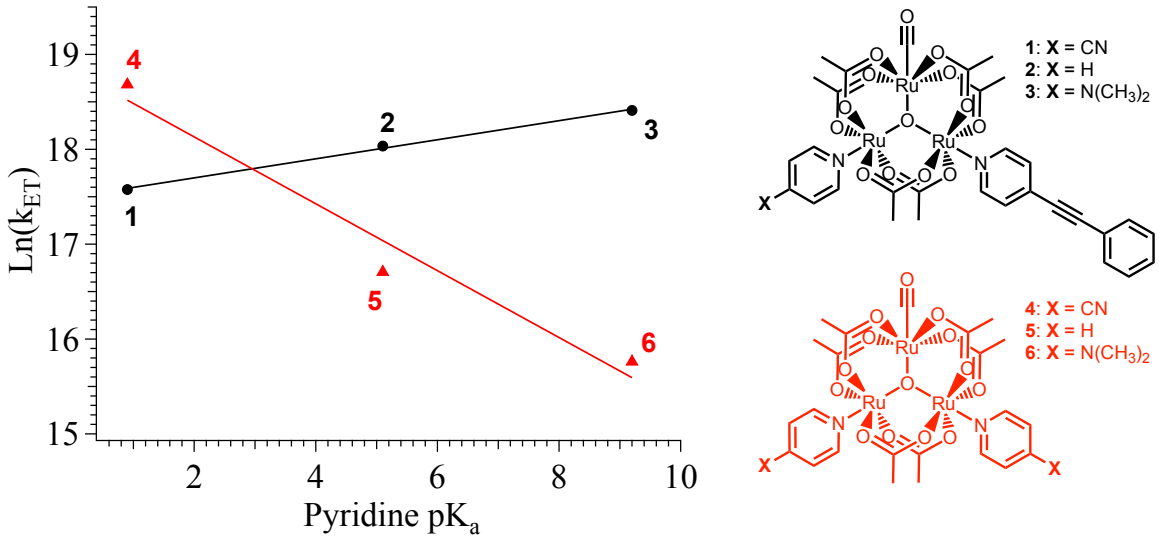

Figure 2.4. Plot of ln(k_{ET}) vs pyridyl pK_a, highlighting the linear correlation between rate constant and ligand pK_a.

important as the low frequency modes that dominate the contributions to the reorganization energy; they are however, used as probes of relative electronic redistribution within the clusters.

These findings are further supported by previous self-exchange studies conducted on the analogous homoleptic monomers $Ru_3(\mu^3\text{-}O)(OAc)_6(CO)(L_1)_2$ (**4**–**6**, Figure 2.1, L_1 = cpy, py, dmap), where self-exchange in these systems was found to proceed by electron delocalization onto the π^* system of the ancillary ligands which leads to large reorganization energies (λ) that are compensated by strong donor-acceptor couplings (H_{ab}).[28] This mechanism is consistent with an effective orbital overlap picture that is mediated by the effective contact area of the ancillary pyridyl ligand in self-exchanging pairs. As charge density is increasingly delocalized onto the ancillary pyridyl ligands, larger rate constants for self-exchange are observed. In complexes **4**–**6**, as the ancillary ligand becomes more electron-withdrawing, decreasing pyridine pKa, the self-exchange rate constants of the 0/– redox couple were found to increase by over an order of magnitude (Figure 2.4, red trace).[27-28]

While complexes **1**–**3** appear to follow the same mechanism of exchange as **4**–**6**, an inverted trend is observed in the variation of rate constants with pyridyl ligand pK_a (Figure 2.4,

Table 2.2. Hammett σ_p parameter for para substituents.[34]

Substituent	σ_p
–CN	0.66
–CC(C_6H_5)	0.16
–H	0.00
–N(CH_3)$_2$	-0.83

Table 2.1). These differences are best explained through consideration of the *relative* electron-withdrawing nature of the both 4-(phenylethynyl)pyridine and pyridyl ligands as summarized through the Hammett parameter (σ_p) in lieu of ligand pK_a. Here, the pyridine substituents (including the phenylethynyl group) can be assigned an empirical value describing the electron-withdrawing nature of the substituents (Table 2.2). Through consideration of the Hammett parameter the weak electron-withdrawing nature of the 4-(phenylethynyl)pyridine is clearly observed, effects that are most readily seen in the ^{1}H NMR where the paramagnetic contact shifts directly relate to the degree of electron-spin density delocalized onto each ligand. The paramagnetic contact shifts of both 4-(phenylethynyl)pyridine and pyridyl protons can be represented as the average change in ligand proton chemical shift ($\Delta\delta$) upon reduction. In the reduced clusters **1**$^-$–**3**$^-$, greater paramagnetic contact shifts correspond to increased (or decreased) electron-spin density delocalized onto each respective ligand. Through this definition, the substituent effects are most clearly seen in the plot of $\Delta\delta$ vs σ_p where the linear relationships observed conform to an electron spin-density "push-pull" effect (left, Figure 2.5).

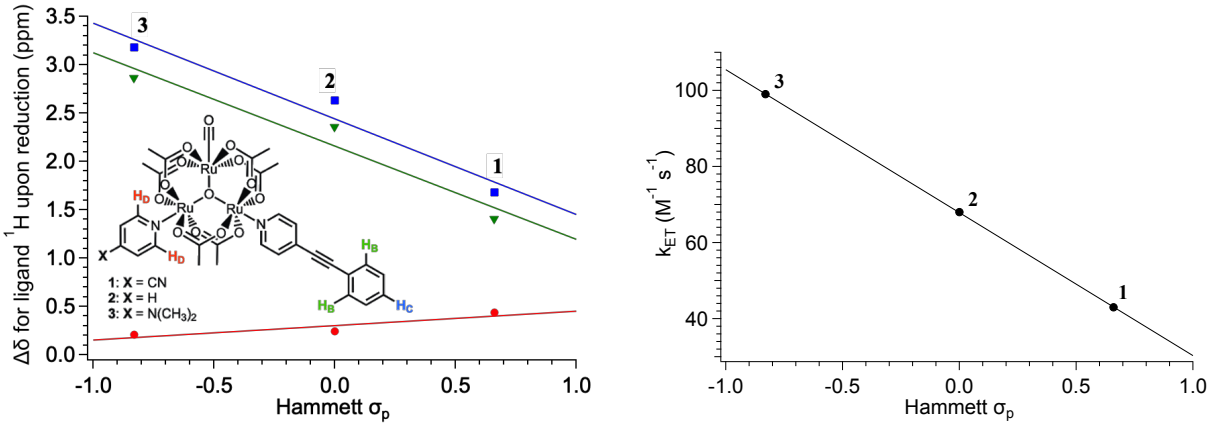

Figure 2.5. (left) Plot of the average chemical shift ($\Delta\delta$) of 4-(phenylethynyl)pyridine protons (H_B and H_C) and pyridyl protons (H_D) upon a one electron reduction versus σ_p. (right) Plot of k_{et} vs σ_p highlighting the increasing rates of ET with decreasing electron-donanting nature of the pyridyl substituent.

The positive linear trend observed for the *meta*-pyridyl protons (H_D) with increasing σ_p indicates that as more electron-withdrawing substituents are used (CN > H > $N(CH_3)_2$), increased electron density is drawn onto the pyridyl ligand. This effect is further illustrated as the negative linear trend for 4-(phenylethynyl)pyridine protons (H_B and H_C), where electron density is drawn *away* from the 4-(phenylethynyl)pyridine ligand when more electron-withdrawing substituents are used on the pyridyl ligand. These observations illustrate how the degree of electron distribution within Ru_3O acetate clusters can be readily tuned through ancillary ligand substitution. The use of more electron-donating ligands (dmap > py > cpy) pushes greater amounts of charge density onto the 4-(phenylethynyl)pyridine ligand which facilitates better donor-acceptor overlap through a greater effective contact area leading to larger cluster-to-cluster couplings (H_{ab}) and ultimately faster rates of ET (right, Figure 2.5).

The electrochemistry of **1**–**3** (Figure 2.6) further reflects the ability for the ancillary ligands to modulate the electronic structure of the clusters. As the pyridine substituent becomes more electron-withdrawing decreased electron density is found on the cluster, and the first (cluster-based) reduction shifts to more positive potentials (Figure 2.6). Furthermore, at more negative potentials, a second quasi-reversible (cluster-based) reduction is observed to follow the same

trend. This behavior is completely analogous to the homoleptic clusters **4**–**6** (Table 2.3), however, the second one-electron reduction is only observable in **4**, becoming irreversible in **5**, and unobservable in **6**. The observation of this second reduction in **1**–**3** highlights the ability of the 4-(phenylethynyl)pyridine to accept a significant degree of electron-density from Ru_3O core thereby stabilizing these highly reduced states that are otherwise unobservable. These observations are further confirmed by comparison of the large observed shifts between the first reduction potentials of the heteroleptic (**1**–**3**) vs homoleptic (**4**–**6**) clusters. In **3**, the first

Table 2.3. Reduction potentials of complexes **1**–**6** in acetonitrile at 20 °C referenced to $Fc^{+/0}$.

Complex	$E^1_{1/2}$ (V)	$E^2_{1/2}$ (V)
1	–1.11	–1.74
2	–1.22	–2.00
3	–1.31	–2.11[a]
4	–1.05	–1.60
5	–1.27	–2.36[a]
6	–1.47	---

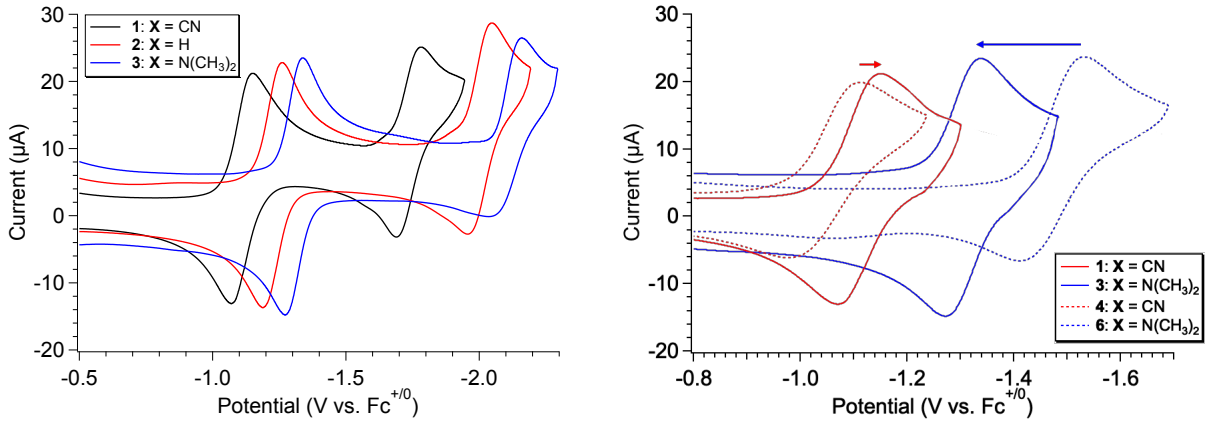

Figure 2.6. Cyclic voltammogram of **1**–**3** (~3 mM) in acetonitrile with 0.1 M tetrabutylammonium hexafluorophosphate ($TBAPF_6$) as the supporting electrolyte. All voltammograms are referenced to the ferrocene/ferricenium redox couple using an internal standard of ferrocene (Fc) and were recorded using a three electrode set-up consisting of a glassy carbon working electrode, a Pt wire auxillary electrode, and a Ag/AgCl reference electrode.

reduction is shifted 160 mV more positive in comparison to **6**, resulting in a net stabilization of the reduced state by nearly three orders of magnitude. This stabilization is thought to arises from the large differences in electron-withdrawing (or -donating) nature of the two ancillary ligands. By pairing a strong electron-donor with a weak electron-acceptor, electron density can be "pushed" onto the weak electron-acceptor (4-(phenylethynyl)pyridine) resulting in a highly-stabilized reduced state. The negative shift of 60 mV in complex **1** relative to **4** has similar origins, however, the 4-(phenylethynyl)pyridine is now considered weakly electron-donating relative to 4-cyanopyridine. This small difference reflects increased electron density on the Ru_3O core in comparison to **4** (which features two cyanopyridine ligands), producing a negative shift in the first reduction potential. The plot of the difference in reduction potentials for **1**–**3** and **4**–**6** vs σ_p () most clearly shows this effect. Here the shifts correlate well with the electron-withdrawing nature of the pyridine substituents and a slight positive shift can be observed for **2**, reflecting the electron-withdrawing nature of the 4-(phenylethynyl)pyridine ligand. The shifts in reduction potentials and their relationship to σ_p are consistent with the proposed mechanism suggested by NMR.

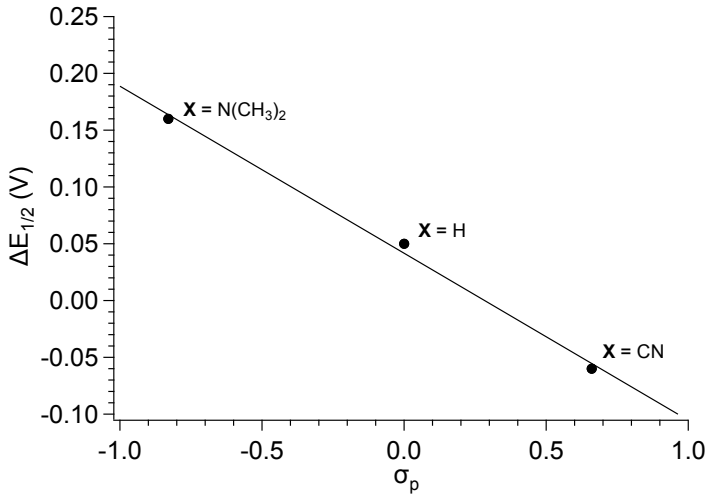

Figure 2.7. Plot in the difference of $E_{1/2}$ between clusters, **1**–**3** and **4**–**6** versus the Hammett parameter of the ancillary pyridine ligand highlighting the shift in redox properties observed upon coordination of 4-(phenylethynyl)pyridine.

The electronic and geometric effects of the ancillary ligands in electron self-exchange were investigated in greater detail through the use of density functional theory (DFT) calculations. The initial geometries for clusters **1**–**3** were adapted from the reported crystal structures of similar tri-substituted clusters ($Ru_3(\mu^3\text{-}O)(OAc)_6(CO)(iq)_2$ (iq = isoquinoline).[28] While several orientations of the ancillary ligands about the Ru_3O plane are possible, due to the computational expense associated with the calculations, only four orientations were considered: When the 4-(phenylethynyl)pyridine and pyridine ligands are considered parallel or perpendicular to the Ru_3O plane (Figure 2.8). Geometry optimizations for $(\mathbf{1})^-$–$(\mathbf{3})^-$ showed that the lowest optimized structure was when both ancillary ligands were parallel to the plane of the ruthenium atoms, while the highest was when both ligands are perpendicular ($\Delta E \approx 2.3$ kcal mol^{-1}). The two asymmetric conformers were found to be nearly isoenergetic with energy separations of $\Delta E \leq 0.5$ kcal mol^{-1} and with a $\Delta E \approx 1$ kcal/mol between the highest and lowest energy conformations. The four conformers showed nearly symmetric highest occupied molecular orbitals (HOMOs) and SOMOs, with the majority of the electron density localized on the Ru_3O core; however, as the ancillary

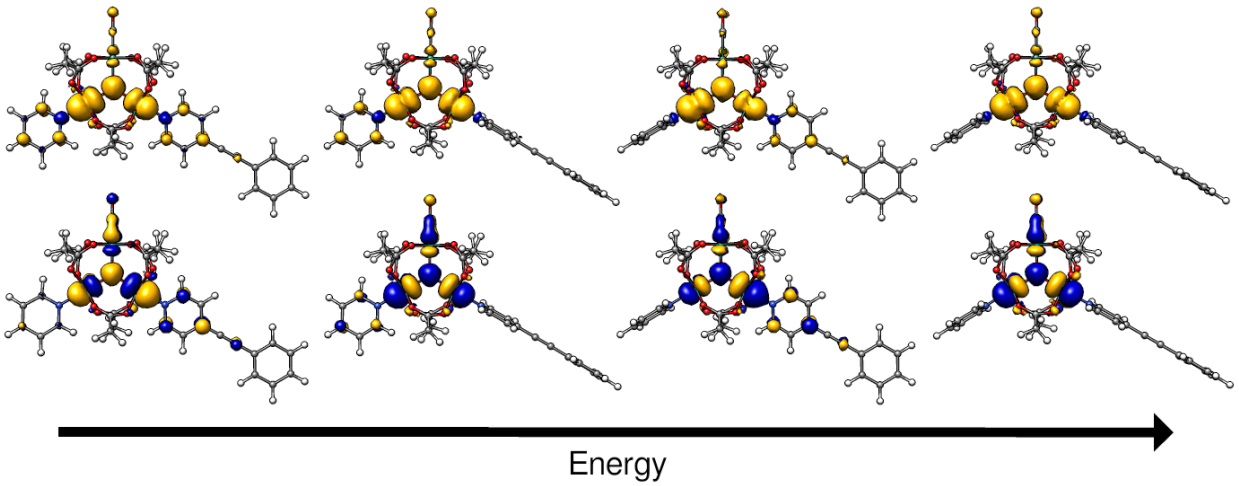

Figure 2.8. Electron spin-density (top) and SOMOs (bottom) of $(\mathbf{2})^-$ for each conformation of the ancillary ligands. While all four conformations are nearly isoenrgetic, the ancillary ligand torsional angles have a significant impact on the orbital structure of the three clusters. Note the electron spin-density and orbital density found on the ancillary ligands as they rotate into the Ru_3O atom plane.

ligands are rotated into their parallel conformers, increasing amounts of orbital density are found to reside on the ligands (Figure 2.8).

In addition to a ligand torsional angle dependence, the donor character of the ancillary ligand was found to greatly influence the extent of orbital delocalization onto the 4-(phenylethynyl)pyridine ligand. While clusters **1**$^{-}$–**3**$^{-}$ displayed significant orbital density on their Ru_3O cores, in their parallel conformation the orbital density of the SOMO was readily modulated by the electron-donating (or withdrawing) ability of the ancillary pyridine ligand (top, Figure 2.9). In (**1**)$^{-}$, a significant amount of the SOMO is delocalized on the 4-cyanopyridine ligand with almost no orbital density found on the 4-(phenylethynyl)pyridine ligand. The converse is true in (**3**)$^{-}$ where almost no orbital density is found on the 4-dimethylaminopyridine ligand but a significant amount of orbital density is on the 4-(phenylethynyl)pyridine ligand. A similar effect is observed for clusters **4**$^{-}$–**6**$^{-}$ however due to their symmetric nature, the orbital density is modulated about the Ru_3O core: When an electron withdrawing cyanopyridine ligand is used, orbital-density is drawn off of the Ru_3O core and onto the cyanopyridine ligand while an electron donating ligand such as dimethylaminopyridine pushes orbital density onto the Ru_3O core.

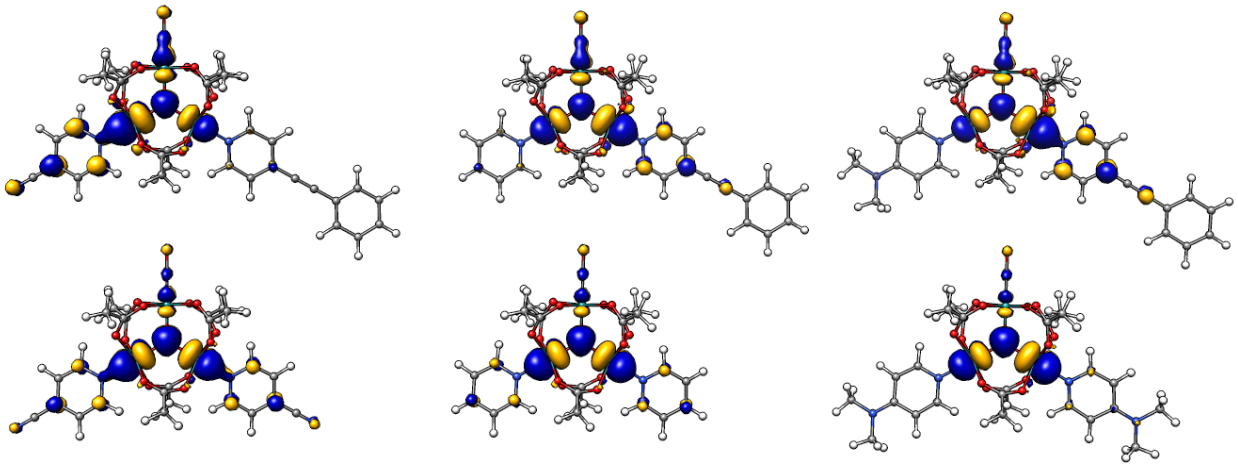

Figure 2.9. Singly occupied molecular orbitals (SOMOs) of **1**$^{-}$–**3**$^{-}$ (top) and **4**$^{-}$–**6**$^{-}$ (bottom) highlighting the dependence of orbital delocalization on the donor ability of the ancillary ligand.

These results present the clearest illustration of the observed rate dependence with ligand substitution in electron self-exchange for clusters **1**–**6**. These findings are consistent and support the observed experimental data, and highlights the ability of the pyridine substituent to tune the cluster electronic states, and ultimately the mechanism of self-exchange in these systems. While electron self-exchange in clusters **1**–**3** is consistent with the effective orbital overlap picture describing **4**–**6**, most importantly, these findings highlight that the ancillary ligand primarily involved in this interaction can readily be modulated through ligand substitution.
is a clear illustration of the push-pull effects observed with the dependence of electron self-exchange rates with ligand substitution.

2.3 Conclusion

These results build upon the previous studies of electron self-exchange interactions in tri-ruthenium mixed valent clusters and extend the concept of effective orbital overlap as a primary factor in determining electron transfer rates. By incorporating an extended aromatic ancillary ligand, a greater effective contact area was allowed leading to better donor-acceptor overlap, and ultimately, large electronic couplings. Through consideration of the Hammett parameter, the degree of coupling in these systems was shown to be influenced by both ancillary ligands and a 'push-pull' effect of the electron density. By incorporation of more electron-donating ancillary ligand substituents, electron self-exchange rate constants were shown to increase by an order of magnitude in comparison to similar systems.

2.4 Experimental

Preparation and Purification. All chemicals were used as received unless otherwise noted. The complexes **1**, **2**, and **3** were synthesized following previously reported procedures.[13, 24, 35] ACN-d_3 (D, 99.8%) was obtained from Cambridge Isotope Laboratories and was dried and stored over 3 Å molecular sieves for several days. Decamethylcobaltocene was received from Sigma-Aldrich,

stored in a glove box freezer at -20 ºC and used as received. All other solvents used in this study were obtained from Fisher Scientific and deoxygenated and dried on a custom drying system over alumina columns in an argon atmosphere.

$Ru_3(\mu^3\text{-}O)(OAc)_6(CO)(L)(pep)$ (**L** = cpy (**1**), py (**2**), dmap (**3**)): A 20 mL scintillation vial was charged with 200 mg (0.23 mmol) of $Ru_3(\mu^3\text{-}O)(OAc)_6(CO)(L)(MeOH)$ (Where L = cpy, py, or dmap), approximately 10 mL of dichloromethane, and set to stir. In a separate vial, 1 eq. of 4-(phenylethynyl)pyridine (pep) was dissolved in approximately 5 mL of dichloromethane and subsequently added to the original scintillation vial. After stirring 24 hours, the reaction mixture was reduced to dryness and purified using flash chromatography on silica gel with DCM:MeOH (95:5%) as an elutant. The second, blue-green band, identified as $Ru_3(\mu^3\text{-}O)(OAc)_6(CO)(L)(pep)$ was collected and isolated as dark blue, microcrystalline solid. The air-stable solid was stored under an inert atmosphere in a glove box until future use.

$Ru_3(\mu^3\text{-}O)(OAc)_6(CO)(cpy)(pep)$ (1): Yield: 179.6 mg; 76%. 1H NMR (ACN-d_3, 500 MHz): δ (ppm) = 9.13 (2H, m, *m*-pep(NC*H*)), 9.07 (2H, m, *m*-cpy(NC*H*)), 8.38 (2H, m, *o*-cpy(NCHC*H*)), 8.19 (2H, m, *o*-pep(NCHC*H*)), 7.71 (2H, m, *o*-pep(–CC–CC*H*)), 7.51 (2H, m, *m*-pep(–CC–CCHC*H*)), 7.50 (1H, s, *p*-pep(–CC–CCHCHC*H*)) 2.02 (6H, s, CH_3COO), 2.02 (6H, s, CH_3COO), 1.82 (6H, s, CH_3COO). ^{13}C {^1H} NMR (ACN-d_3, 500 MHz): δ (ppm) = 224.1 (*C*O), 193.6 (CH_3*C*OO), 193.1 (CH_3*C*OO), 193.0 (CH_3*C*OO), 153.4 (*o*-pep(N*C*H)), 153.3 (*o*-cpy(N*C*H)), 136.9 (*p*-pep(NCHCH*C*)), 133.2 (*o*-pep(–CC–C*C*H)), 131.1 (*m*-pep(–CC–CCH*C*H)), 129.9 (*p*-pep(–CC–CCHCH*C*H)), 127.5 (*m*-cpy(NCH*C*H)), 127.3 (*m*-pep(NCH*C*H)), 125.1 (*p*-cpy(NCHCH*C*–CN)), 122.4 (pep(–CC–*C*), 116.9 (NCHCHC–*C*N), 97.4 (–CC–(*C*$_6$H$_5$)), 86.8 ((NC5H4)–C*C*–), 23.8 (*C*H_3COO), 23.7 (*C*H_3COO), 22.0 (*C*H_3COO). Anal. Calcd for $C_{32}H_{31}N_3O_{14}Ru_3$: C, 39.03%; H, 3.17%; N, 4.27%; found: C, 39.29%; H, 3.70%; N, 4.34%; IR (cm^{-1}): 1944, 1611.0, 1571, 1504, 1427, 1354. UV-Vis (nm) 278 (28300 ± 200 M^{-1} cm^{-1}), 403 (10800 ± 100 M^{-1} cm^{-1}), 593 (7300 ±

200 M^{-1} cm^{-1}). ESI-MS (m/z) $[M + H^+]^+$ calcd: 988.90 (100.0%), 989.90 (92.5%). Found: 988.22, 989.91. Reduction potentials (V, vs. $Fc^{+/0}$, ACN): +2/+, 0.90; +/0, 0.25; 0/–, –1.11; –/–2, –1.74.

$Ru_3(\mu_3\text{-}O)(OAc)_6(CO)(py)(pep)$ (2): Yield: 199.2 mg; 83%. ^1H NMR (ACN-d_3, 500 MHz): δ (ppm) = 9.18 (m, 2H, *o*-py(NC*H*)), 9.15 (m, 2H, *o*-pep(NC*H*)), 8.36 (m, 1H, *p*-py(NCHCHC*H*)), 8.23 (m, 2H, *m*-pep(NCHC*H*)), 8.16 (m, 2H, *m*-py(NCHC*H*)), 7.75 (m, 2H, *o*-pep(–CC–CC*H*)), 7.54 (m, 2H, *m*-pep(–CC–CCHC*H*)), 7.53 (m, 1H, *p*-pep(–CC–CCHCHC*H*)), 2.00 (s, 6H, CH_3COO), 1.99 (s, 6H, CH_3COO), 1.78 (s, 6H, CH_3COO). ^{13}C {^1H} NMR (ACN-d_3, 500 MHz): δ (ppm) = 224.7 (*C*O), 193.1 (CH_3*C*OO), 192.8 (CH_3*C*OO), 192.7 (CH_3*C*OO), 153.6 (*o*-pep(N*C*H)), 153.4 (*o*-cpy(N*C*H)), 141.9 (*p*-py(NCHCH*C*H)), 136.8 (*p*-pep(NCHCH*C*)), 133.2 (*o*-pep(–CC–C*C*H)), 131.1 (*m*-pep(–CC–CCH*C*H)), 130.0 (*p*-pep(–CC–CCHCH*C*H)), 127.3 (*m*-pep(NCH*C*H)), 126.0 (*m*-py(NCH*C*H)), 122.3, (pep(–CC–*C*)), 97.3 (–C*C*–(C_6H_5)), 86.9 ((NC_5H_4)–*C*C–), 23.8 (*C*H_3COO), 23.7 (*C*H_3COO), 22.0 (*C*H_3COO). Anal. Calcd for $C_{31}H_{32}N_2O_{14}Ru_3$: C, 38.79%; H, 3.36%; N, 2.92%; found: C, 38.47%; H, 3.70%; N, 2.98%. IR (cm^{-1}): 1942, 1610, 1573, 1503, 1427, 1354. UV-Vis (nm): 284 (33357 ± 100 M^{-1} cm^{-1}), 400 (9100 ± 100 M^{-1} cm^{-1}), 584 (7760 ± 40 M^{-1} cm^{-1}). ESI-MS (*m/z*) $[M + H^+]^+$ calcd: 963.91 (100.0%), 964.91 (92.5%). Found: 963.32, 965.42. Reduction potentials (V, vs. $Fc^{+/0}$, ACN): +2/+, 0.86; +/0, 0.22; 0/–, –1.22; –/–2, –2.00.

$Ru_3(\mu_3\text{-}O)(OAc)_6(CO)(dmap)(pep)$ (3): Yield: 179.9 mg; 78%. ^1H NMR (ACN-d_3, 500 MHz): δ (ppm) = 9.20 (m, 2H, *o*-pep(NC*H*)), 8.95 (m, 2H, *o*-dmap(NC*H*)), 8.24 (m, 2H, *m*-pep(NCHC*H*)), 7.74 (m, 2H, *o*-pep(–CC–CC*H*)), 7.54 (m, 2H, *m*-pep(–CC–CCHC*H*)), 7.53 (m, 1H, *p*-pep(–CC–CCHCHC*H*)), 7.32 (m, 2H, dmap(NCHC*H*)), 3.30 (s, 6H, –N(CH_3)$_2$), 1.95 (s, 6H, CH_3COO), 1.94 (s, 6H, CH_3COO), 1.72 (s, 6H, CH_3COO). ^{13}C {^1H} NMR (ACN-d_3, 500 MHz): δ (ppm) = 224.5 (*C*O), 192.3 (CH_3*C*OO), 192.0 (CH_3*C*OO), 191.9 (CH_3*C*OO), 158.5 (*p*-dmap(NCHCH*C*), 154.4 (*o*-dmap(N*C*H)), 153.1 (*o*-pep(N*C*H)), 136.4 (*p*-pep(NCHCH*C*)), 133.2 (*o*-pep(–CC–C*C*H)), 131.1 (*m*-pep(–CC–CCH*C*H)), 129.9 (*p*-pep(–CC–CCHCH*C*H)), 127.3 (*m*-pep(NCH*C*H)), 122.4 (pep(–CC–*C*)), 108.9 (*m*-dmap(NCH*C*H)), 97.1 (–C*C*–(C_6H_5)), 87.0 ((NC_5H_4)–*C*C–), 39.9 (–N(*C*H_3)$_2$),

23.9 (*C*H_3COO), 23.9 (*C*H_3COO), 22.2 (*C*H_3COO). Anal. Calcd for $C_{33}H_{37}N_3O_{14}Ru_3$: C, 39.52%; H, 3.72%; N, 4.19%; found: C, 39.25%; H, 4.02%; N, 4.04%. IR (cm^{-1}): 1939, 1611, 1576, 1540, 1504, 1426, 1392, 1353. UV-Vis (nm): 286 (38000 ± 2000 M^{-1} cm^{-1}), 399 (11000 ± 1000 M^{-1} cm^{-1}), 589 (8000 ± 1000 M^{-1} cm^{-1}). ESI-MS (*m/z*) $[M + H^+]^+$ calcd: 1006.95 (100.0%), 1007.95 (92.5%). Found: 1007.19, 1008.28. Reduction potentials (V, vs. $Fc^{+/0}$, ACN): +2/+, 0.77; +/0, 0.18; 0/–, –1.31; –/–2, –2.11.

NMR Data Collection and Analysis. ^{1}H NMR spectra were collected on a JEOL or Varian 500 MHz NMR spectrometer and analyzed using iNMR software. A total of 64 scans of 16384 data points (0.46 Hz resolution) were collected from +20.0 to –10.0 ppm. Peak widths at half height were measured by fitting each absorbance to Lorentzian line shapes using iNMR software and each rate constant is an average of *at least* four values calculated from equation 1. All spectra were recorded at ambient temperatures of the instrument (20-23 ºC).

Infrared Data Collection and Analysis. Infrared spectra were collected on a Bruker Equinox 55 FTIR spectrometer, using a SPECAC sealed liquid IR cell with CaF_2 windows and a path length of 0.1 mm. After solvent subtraction, CO peaks were fit to Voigt functionals using Igor Pro software to obtain the ratios of neutral to reduced clusters in solution, which was subsequently used to determine the mol fraction of the samples.

UV-Visible Data Collection and Analysis. UV-visible spectra were collected on a Shimadzu UV-3600 UV/vis/NIR spectrometer. Samples were enclosed in a SPECAC sealed liquid IR cell with CaF_2 windows and a path length of 0.1 mm.

Electrochemical Measurements. Electrochemistry was performed on a BASi Epsilon potentiostat in dried, degassed acetonitrile with 0.1 M tetrabutylammonium hexaflurorophosphate ($TBAPF_6$, recrystallized from MeOH and vacuum dried at 80 ºC) and about 3 mM analyte at a scan rate of 100 mV/s under a nitrogen atmosphere. The electrode setup consisted of a glassy carbon disk (3 mm diameter) working electrode, a platinum wire counter electrode, and a Ag/AgCl

reference electrode separated from solution by a CoarlPor® tip. All experiments were referenced to an internal standard of ferrocene/ferrocenium.

DFT Calculations. Calculations were performed in the ORCA software suite (version 3.0.3) using the B3LYP/G functional with the RIJCOSX approximation.[36-40] Ruthenium atoms were treated with the ECP[DEF2-TZVP/J] basis set while the DEF2-SVP/J basis set was used for all other atoms.[41-44] Dispersion corrections were applied using the Becke-Johnson damping scheme (D3BJ) and solvation was accounted for using the COSMO solvation model in methylene chloride.[45-46] Analytical frequency calculations were run at the same level of theory, without the COSMO solvation model to confirm optimized geometries as minima on the potential energy surface. Molecular graphics and analyses were performed with the UCSF Chimera package. Chimera is developed by the Resource for Biocomputing, Visualization, and Informatics at the University of California, San Francisco (supported by NIGMS P41-GM103311).[47]

2.5. Appendix

Chapter 2: The majority of the material in this chapter comes directly from a manuscript entitled “Tuning electron delocalization and transfer rates in mixed-valent Ru_3O complexes through ‘push–pull’ effects,” by Tyler M. Porter, Gabriele C. Canzi, Steven A. Chabolla, and Clifford P. Kubiak, is published in *The Journal of Physical Chemistry A*, **2016**, *120 (32)*, 6309–6316. The dissertation author is the primary author.

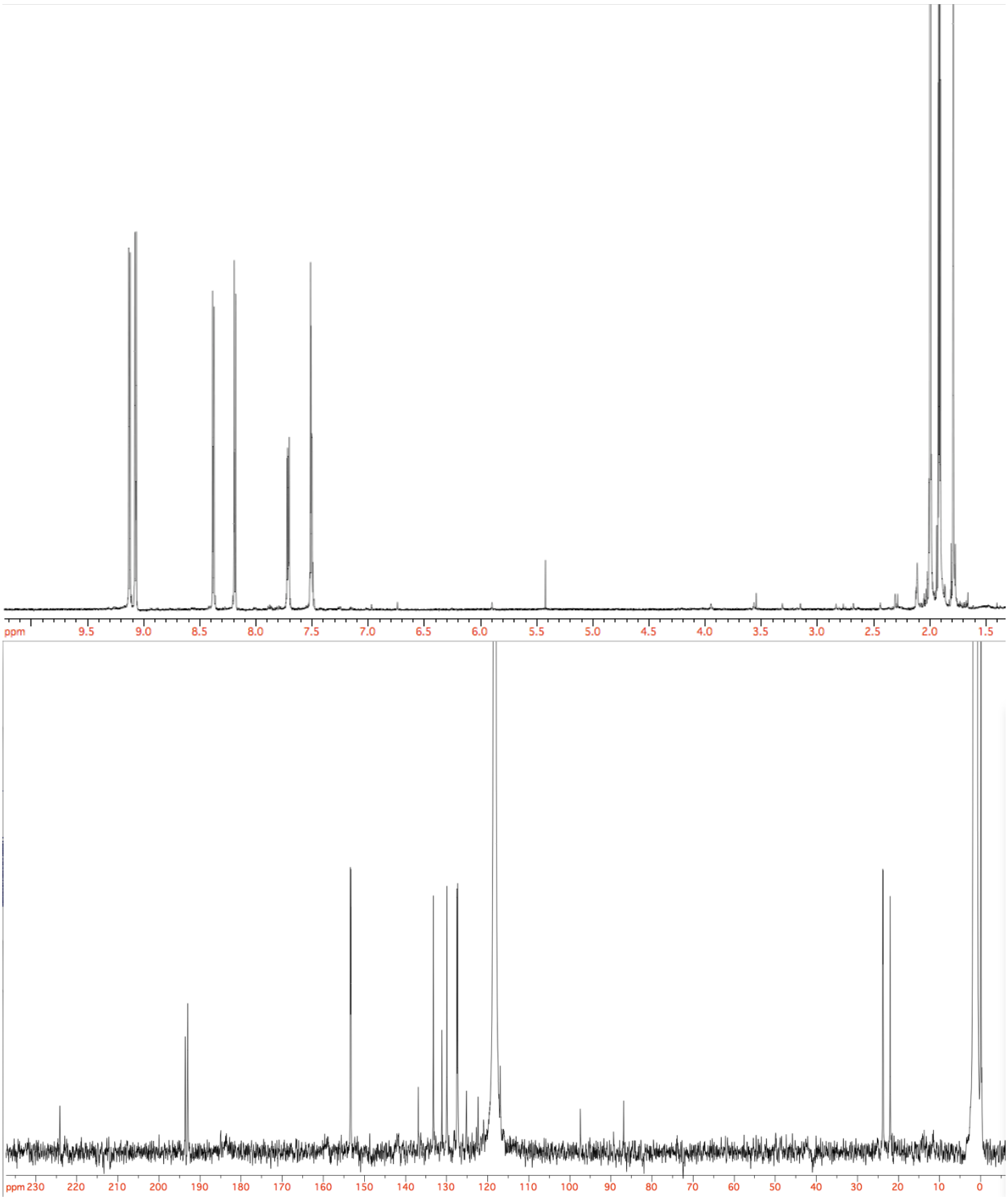

Figure 2.10. ^{1}H (top) and ^{13}C (bottom) NMR of **1** in deuterated acetonitrile (ACN-d_3).

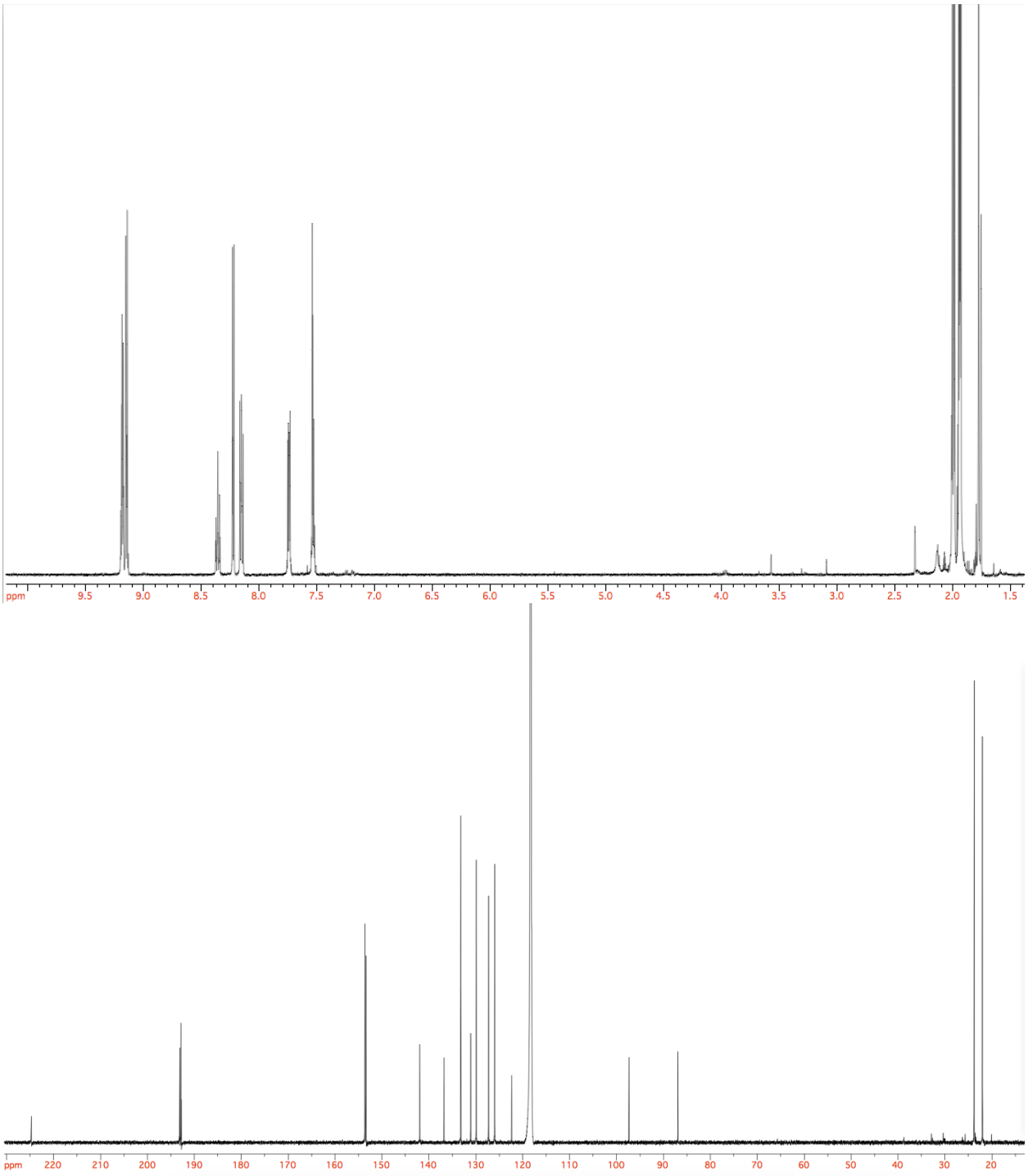

Figure 2.11. ^{1}H (top) and ^{13}C (bottom) NMR of **2** in ACN-d_3.

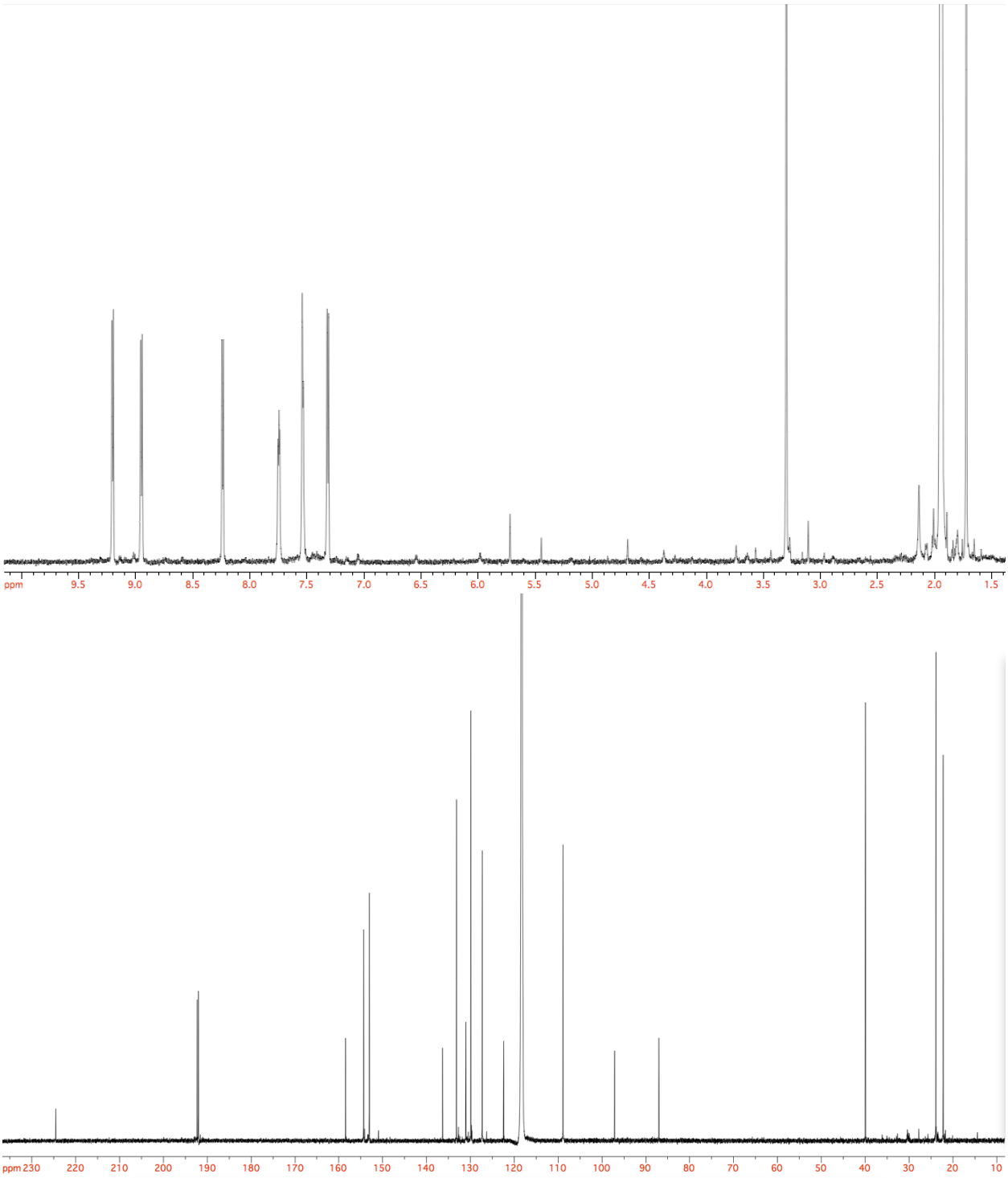

Figure 2.12. ^{1}H (top) and ^{13}C (bottom) NMR of **3** in ACN-d_3.

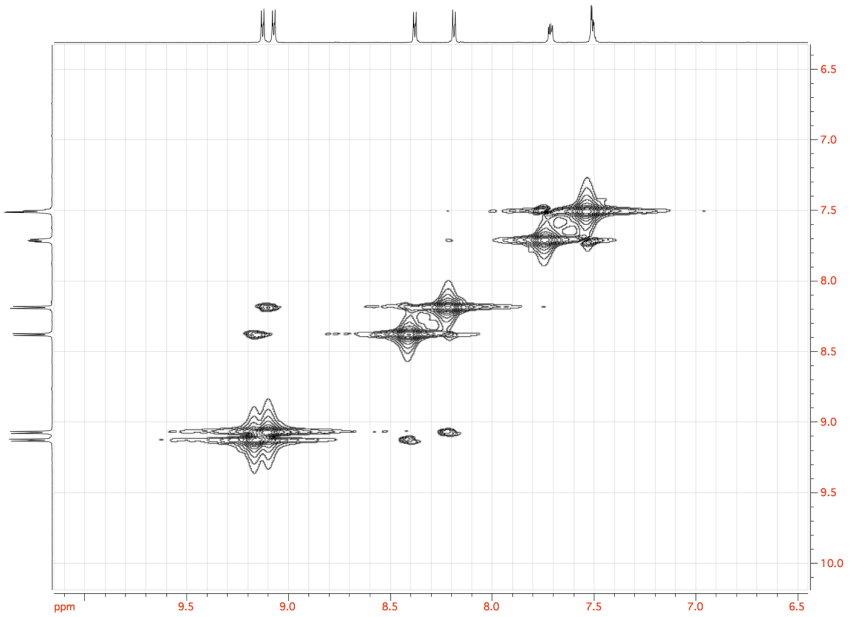

Figure 2.13. COSY of **1** in ACN-d_3.

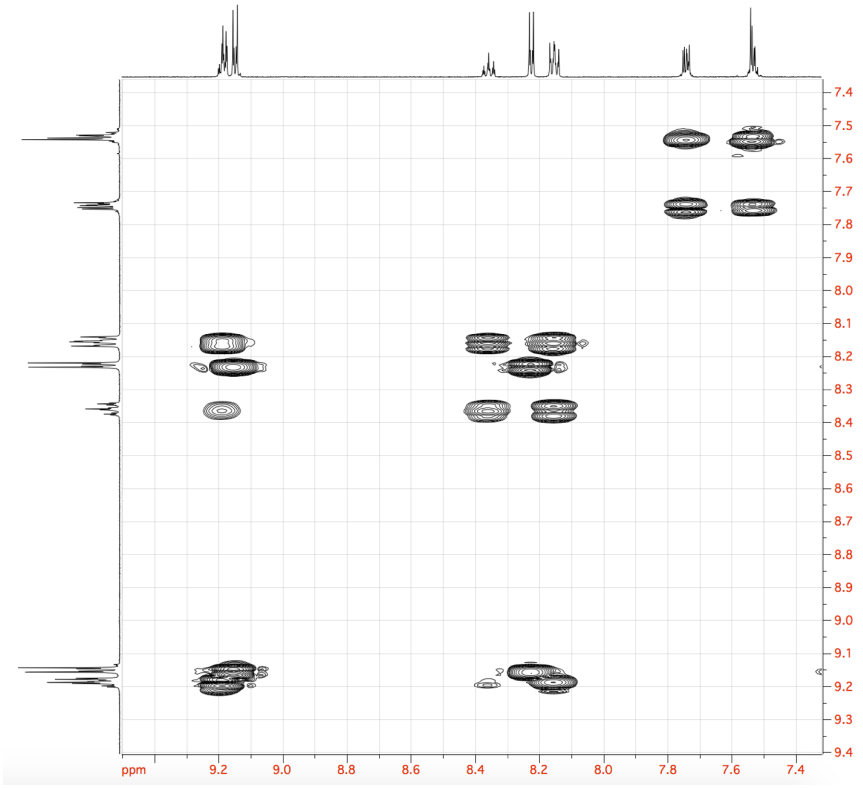

Figure 2.14. COSY of **2** in ACN-d_3.

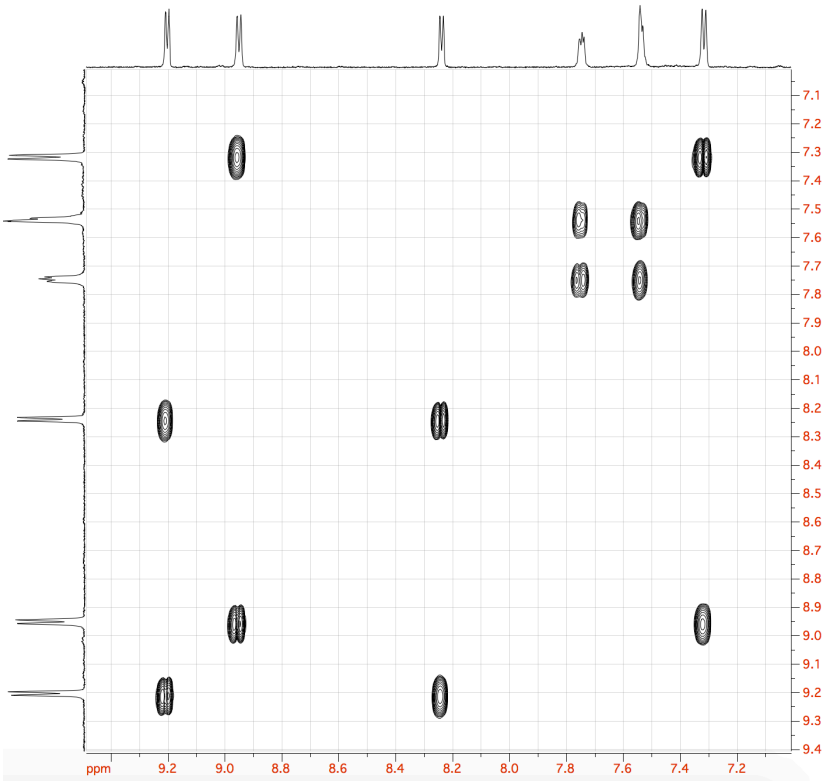

Figure 2.15. COSY of **3** in ACN-d_3.

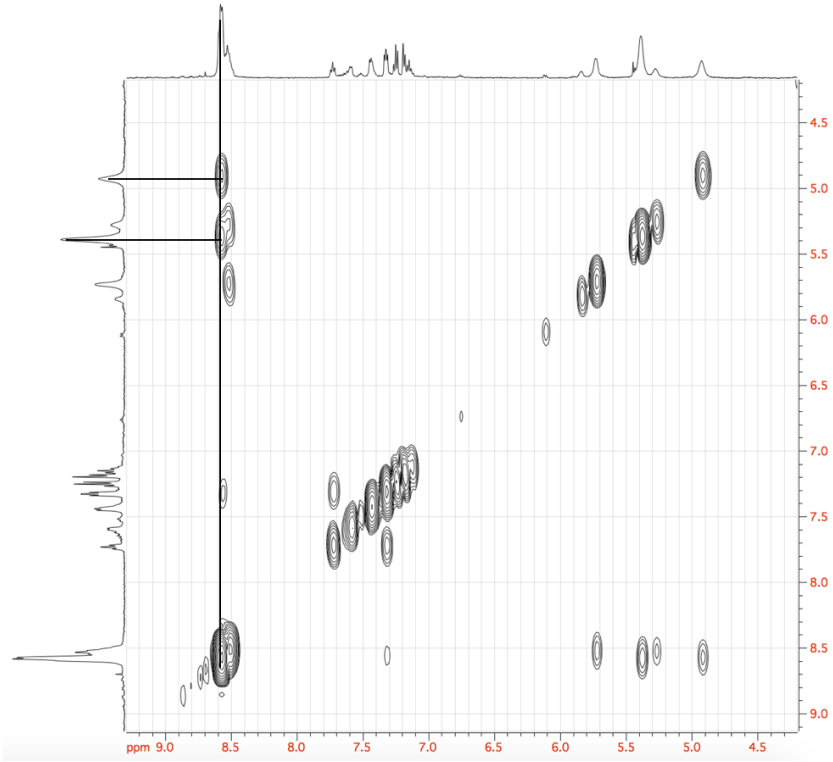

Figure 2.16. COSY of **2**$^-$ in ACN-d_3.

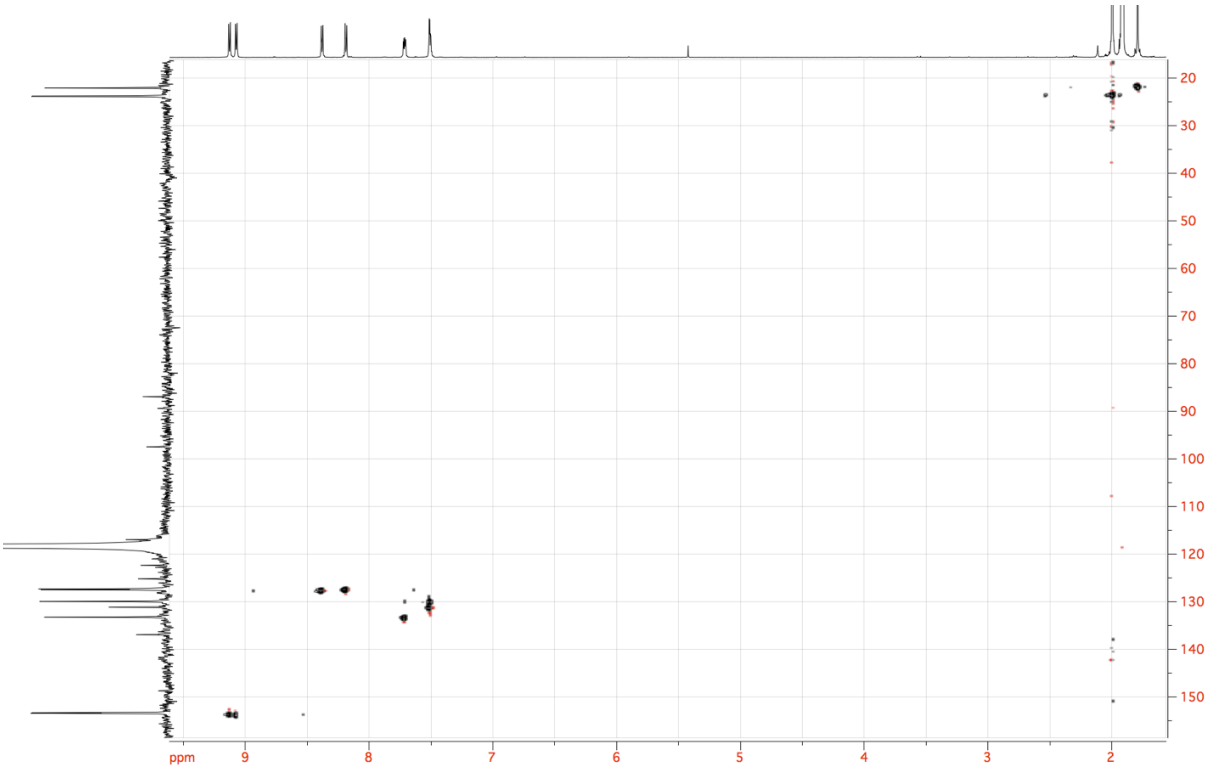

Figure 2.17. HSQC of **1** in ACN-d_3.

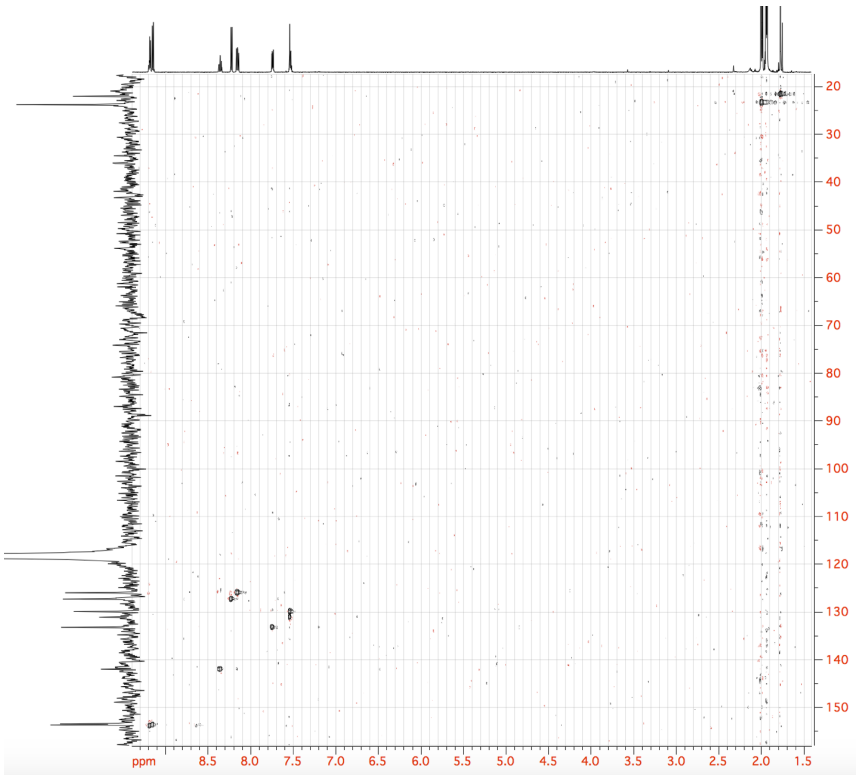

Figure 2.18. HSQC of **2** in ACN-d_3.

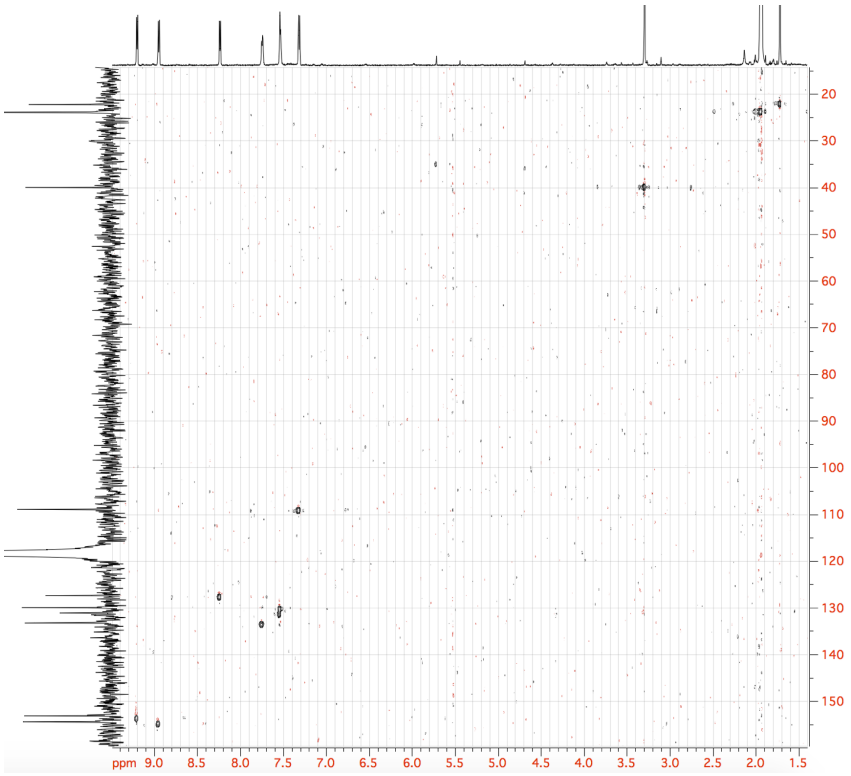

Figure 2.19. HSQC of **3** in ACN-d_3.

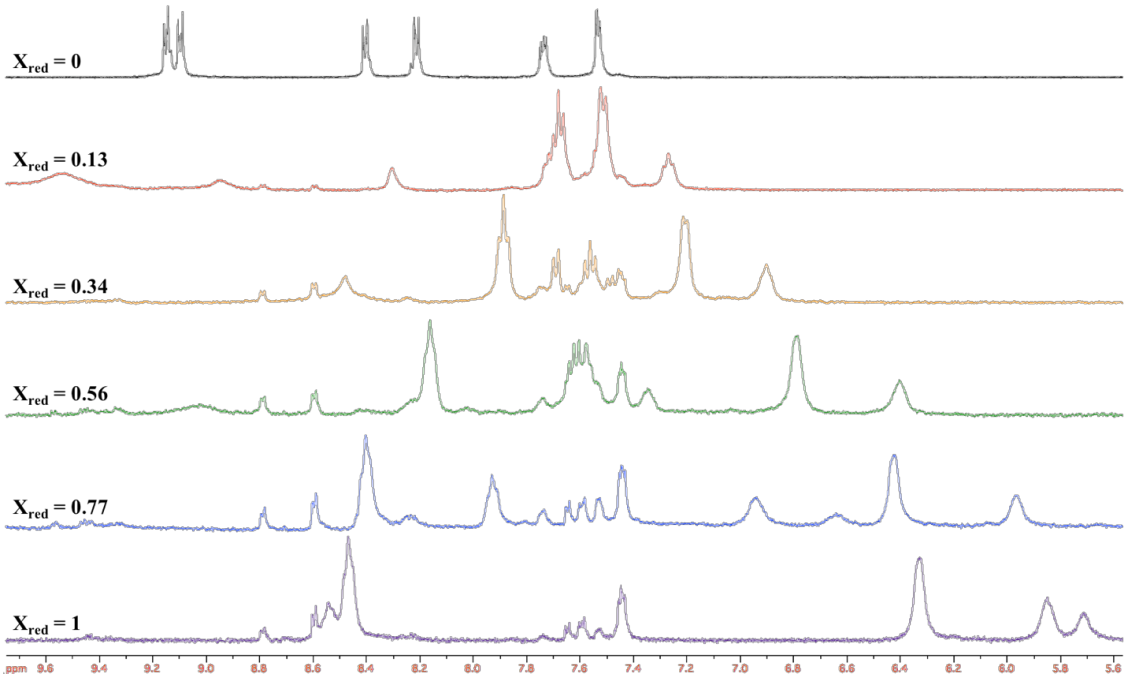

Figure 2.20. ^{1}H NMR self-exchange measurement of **1** at a total concentration of 3.9 mM in ACN-d_3 with increasing mole fraction of [red]/[ox] from top (only oxidized) to bottom (singly reduced). Experimental mole fractions were determined from integration of FTIR ν(CO) bands.

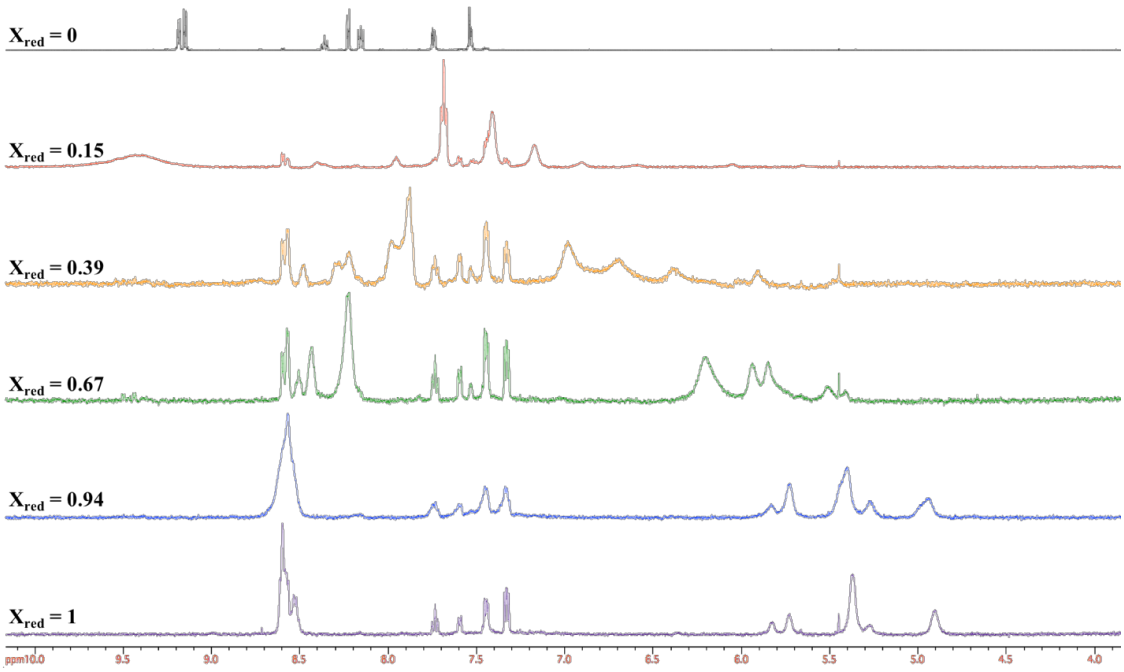

Figure 2.21. ^{1}H NMR self-exchange measurement of **2** at a total concentration of 3.5 mM in ACN-d_3 with increasing mole fraction of [red]/[ox] from top (only oxidized) to bottom (singly reduced). Experimental mole fractions were determined from integration of FTIR ν(CO) bands.

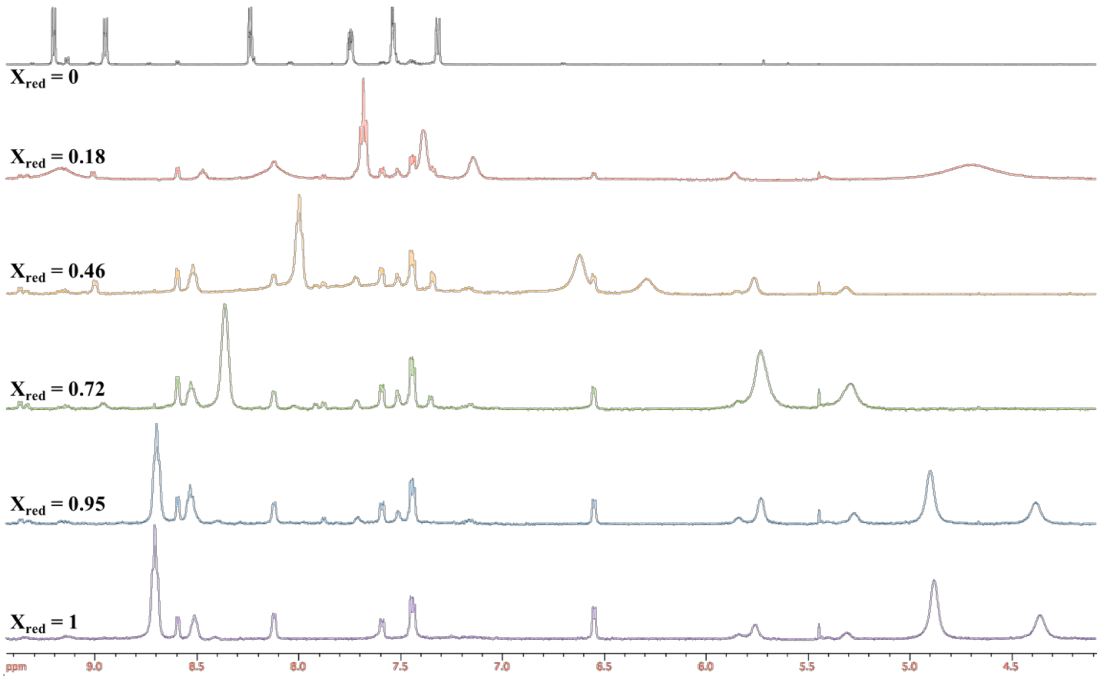

Figure 2.22. ^{1}H NMR self-exchange measurement of **3** at a total concentration of 6.0 mM in ACN-d_3 with increasing mole fraction of [red]/[ox] from top (only oxidized) to bottom (singly reduced). Experimental mole fractions were determined from integration of FTIR ν(CO) bands.

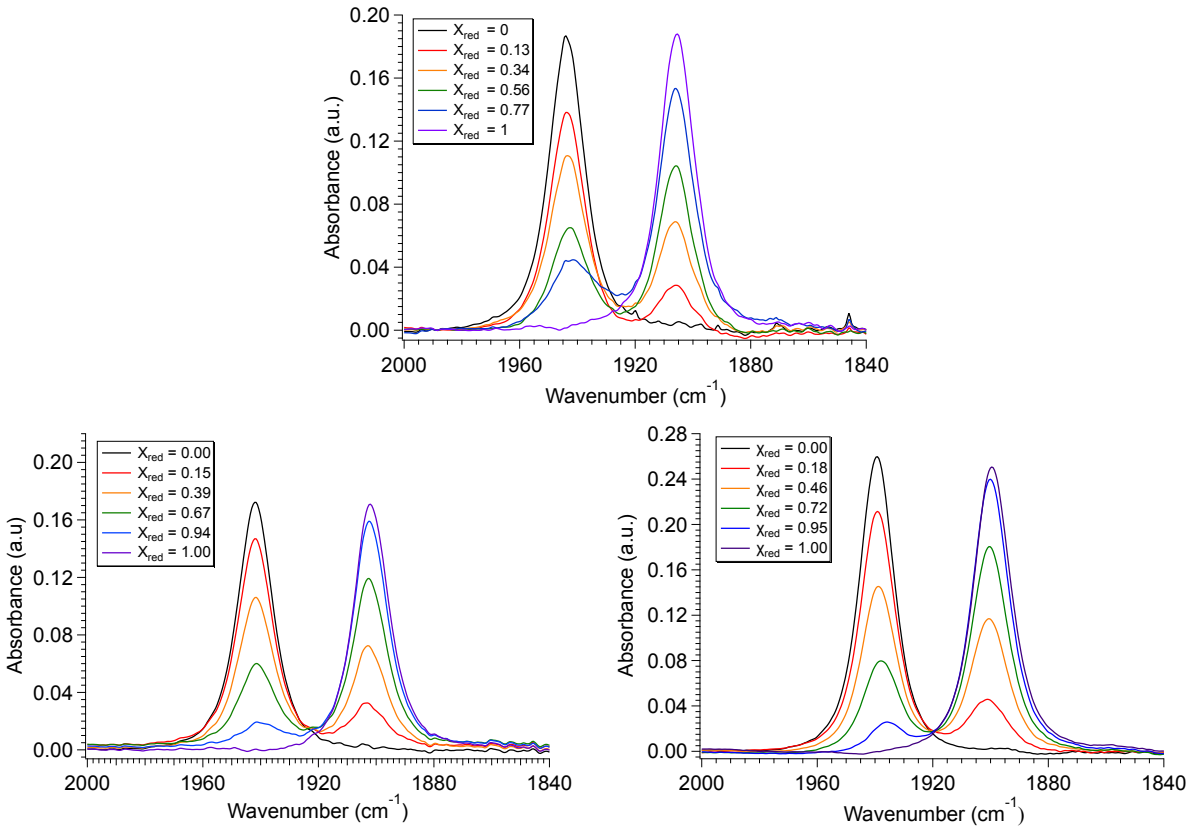

Figure 2.23. IR spectrum of the ν(CO) region of **1** (top, 3.9 mM in ACN-d_3), **2** (bottom left, 3.5 mM in ACN-d_3), and **3** (bottom right, 6.0 mM in ACN-d_3) with increasing mole fraction of reduced to oxidized species. Spectra were recorded directly from the samples used in ^{1}H NMR self-exchange studies.

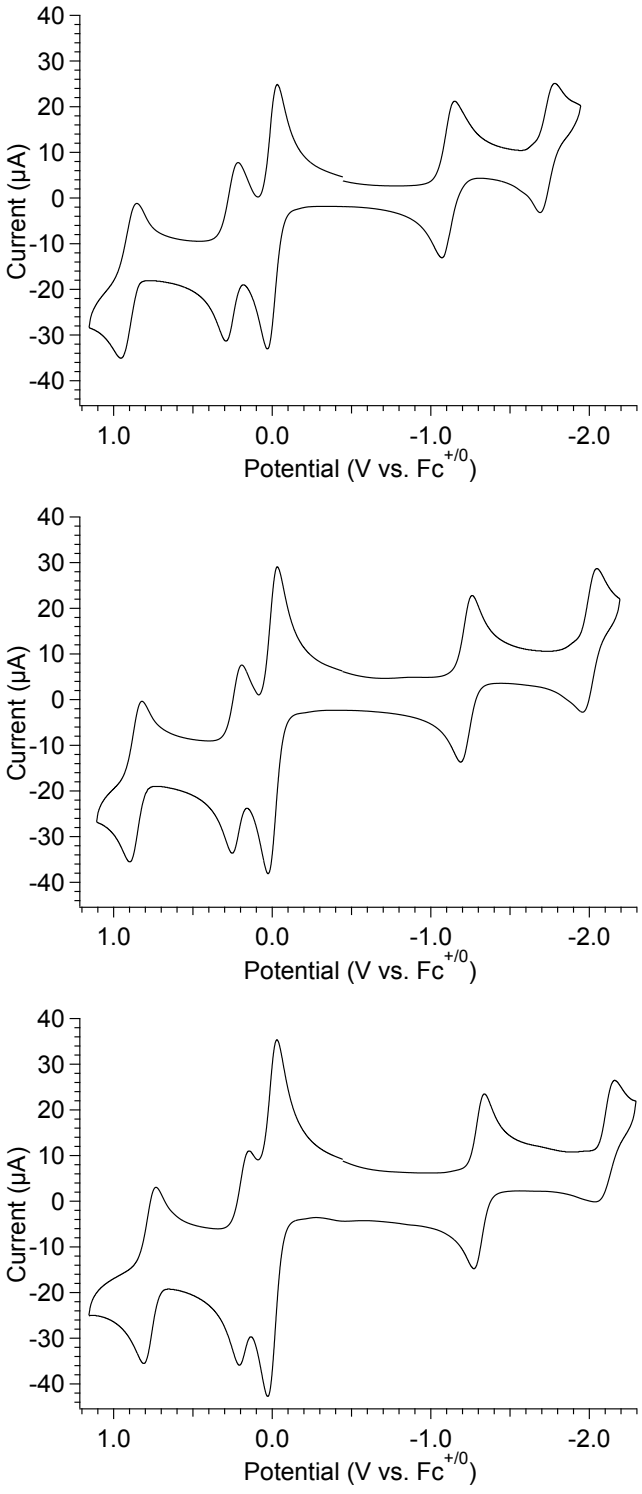

Figure 2.24. Cyclic votammograms of **1** (top), **2**, (middle), and **3** (botoom) in ACN with 0.1 M $TBAPF_6$ as a supporting electrolyte. Scans were recorded at 100 mV/s with a glassy carbon WE, Pt CE and Ag/AgCl reference. Ferrocene was used as an internal reference.

2.6. References

1. Iwata, S.; Ostermeier, C.; Ludwig, B.; Michel, H., Structure at 2.8 A resolution of cytochrome c oxidase from Paracoccus denitrificans. *Nature* **1995,** *376* (6542), 660–669.
2. Ward, M. D., Photo-induced electron and energy transfer in non-covalently bonded supramolecular assemblies. *Chem. Soc. Rev.* **1997,** *26* (5), 365–375.
3. McGaughey, G. B.; Gagné, M.; Rappé, A. K., π-Stacking Interactions: Alive and Well in Proteins. *J. Biol. Chem.* **1998,** *273* (25), 15458–15463.
4. Harmata, M., Chiral Molecular Tweezers. *Acc. Chem. Res.* **2004,** *37* (11), 862–873.
5. Meyer, T. J.; Huynh, M. H. V.; Thorp, H. H., The Possible Role of Proton-Coupled Electron Transfer (PCET) in Water Oxidation by Photosystem II. *Angew. Chem. Int. Ed.* **2007,** *46* (28), 5284–5304.
6. Sygula, A.; Fronczek, F. R.; Sygula, R.; Rabideau, P. W.; Olmstead, M. M., A Double Concave Hydrocarbon Buckycatcher. *J. Am. Chem. Soc.* **2007,** *129* (13), 3842–3843.
7. Delgado, M. C. R.; Kim, E.-G.; Filho, D. A. d. S.; Bredas, J.-L., Tuning the Charge-Transport Parameters of Perylene Diimide Single Crystals via End and/or Core Functionalization: A Density Functional Theory Investigation. *J. Am. Chem. Soc.* **2010,** *132* (10), 3375–3387.
8. Bonin, J.; Costentin, C.; Robert, M.; Savéant, J.-M.; Tard, C., Hydrogen-Bond Relays in Concerted Proton–Electron Transfers. *Acc. Chem. Res.* **2012,** *45* (3), 372–381.
9. Sun, H.; Steeb, J.; Kaifer, A. E., Efficient Electronic Communication between Two Identical Ferrocene Centers in a Hydrogen-Bonded Dimer. *J. Am. Chem. Soc.* **2006,** *128* (9), 2820–2821.
10. Lear, B. J.; Kubiak, C. P., Origins of Cooperative Noncovalent Host−Guest Chemistry in Mixed Valence Complexes. *J. Phys. Chem. B* **2007,** *111* (24), 6766–6771.
11. Tadokoro, M.; Inoue, T.; Tamaki, S.; Fujii, K.; Isogai, K.; Nakazawa, H.; Takeda, S.; Isobe, K.; Koga, N.; Ichimura, A.; Nakasuji, K., Mixed-Valence States Stabilized by Proton Transfer in a Hydrogen-Bonded Biimidazolate Rhenium Dimer. *Angew. Chem. Int. Ed.* **2007,** *46* (31), 5938–5942.
12. Pichlmaier, M.; Winter, R. F.; Zabel, M.; Záliš, S., Electron Transfer Across Multiple Hydrogen Bonds: The Case of Ureapyrimidinedione-Substituted Vinyl Ruthenium and Osmium Complexes. *J. Am. Chem. Soc.* **2009,** *131* (13), 4892–4903.
13. Goeltz, J. C.; Kubiak, C. P., Mixed Valency across Hydrogen Bonds. *J. Am. Chem. Soc.* **2010,** *132* (49), 17390–17392.
14. Wilkinson, L. A.; McNeill, L.; Meijer, A. J. H. M.; Patmore, N. J., Mixed Valency in Hydrogen Bonded 'Dimers of Dimers'. *J. Am. Chem. Soc.* **2013,** *135* (5), 1723–1726.
15. Canzi, G.; Goeltz, J. C.; Henderson, J. S.; Park, R. E.; Maruggi, C.; Kubiak, C. P., On the Observation of Intervalence Charge Transfer Bands in Hydrogen-Bonded Mixed-Valence Complexes. *J. Am. Chem. Soc.* **2014,** *136* (5), 1710–1713.
16. Meyer, T. J., Chemical approaches to artificial photosynthesis. *Acc. Chem. Res.* **1989,** *22* (5), 163-170.
17. Turro, C.; Chang, C. K.; Leroi, G. E.; Cukier, R. I.; Nocera, D. G., Photoinduced electron transfer mediated by a hydrogen-bonded interface. *J. Am. Chem. Soc.* **1992,** *114* (10), 4013–4015.
18. Brédas, J.-L.; Beljonne, D.; Coropceanu, V.; Cornil, J., Charge-Transfer and Energy-Transfer Processes in π-Conjugated Oligomers and Polymers: A Molecular Picture. *Chem. Rev.* **2004,** *104* (11), 4971–5004.
19. Coropceanu, V.; Cornil, J.; da Silva Filho, D. A.; Olivier, Y.; Silbey, R.; Brédas, J.-L., Charge Transport in Organic Semiconductors. *Chem. Rev.* **2007,** *107* (4), 926–952.

20. Solomon, G. C.; Vura-Weis, J.; Herrmann, C.; Wasielewski, M. R.; Ratner, M. A., Understanding Coherent Transport through π-Stacked Systems upon Spatial Dislocation. *J. Phys. Chem. B* **2010,** *114* (45), 14735–14744.

21. Coropceanu, V.; Nakano, T.; Gruhn, N. E.; Kwon, O.; Yade, T.; Katsukawa, K.-i.; Brédas, J.-L., Probing Charge Transport in π-Stacked Fluorene-Based Systems. *J. Phys. Chem. B* **2006,** *110* (19), 9482–9487.

22. Ito, T.; Hamaguchi, T.; Nagino, H.; Yamaguchi, T.; Washington, J.; Kubiak, C. P., Effects of Rapid Intramolecular Electron Transfer on Vibrational Spectra. *Science* **1997,** *277* (5326), 660–663.

23. Londergan, C. H.; Salsman, J. C.; Lear, B. J.; Kubiak, C. P., Observation and dynamics of "mixed-valence isomers" and a thermodynamic estimate of electronic coupling parameters. *Chem. Phys.* **2006,** *324* (1), 57–62.

24. Salsman, J. C.; Ronco, S.; Londergan, C. H.; Kubiak, C. P., Tuning the Electronic Communication and Rates of Intramolecular Electron Transfer of Dimers of Trinuclear Ruthenium Clusters: Bridging and Ancillary Ligand Effects. *Inorg. Chem.* **2006,** *45* (2), 547–554.

25. Lear, B. J.; Glover, S. D.; Salsman, J. C.; Londergan, C. H.; Kubiak, C. P., Solvent Dynamical Control of Ultrafast Ground State Electron Transfer: Implications for Class II−III Mixed Valency. *J. Am. Chem. Soc.* **2007,** *129* (42), 12772–12779.

26. Kubiak, C. P., Inorganic Electron Transfer: Sharpening a Fuzzy Border in Mixed Valency and Extending Mixed Valency across Supramolecular Systems. *Inorg. Chem.* **2013,** *52* (10), 5663–5676.

27. Goeltz, J. C.; Hanson, C. J.; Kubiak, C. P., Rates of Electron Self-Exchange Reactions between Oxo-Centered Ruthenium Clusters Are Determined by Orbital Overlap. *Inorg. Chem.* **2009,** *48* (11), 4763–4767.

28. Goeltz, J. C.; Benson, E. E.; Kubiak, C. P., Electronic Structural Effects in Self-Exchange Reactions. *J. Phys. Chem. B* **2010,** *114* (45), 14729–14734.

29. Nelsen, S. F.; Ismagilov, R. F.; Gentile, K. E.; Nagy, M. A.; Tran, H. Q.; Qu, Q.; Halfen, D. T.; Odegard, A. L.; Pladziewicz, J. R., Indirect Determination of Self-Exchange Electron Transfer Rate Constants. *J. Am. Chem. Soc.* **1998,** *120* (32), 8230-8240.

30. Chan, M.-S.; DeRoos, J. B.; Wahl, A. C., Rate of electron transfer between tris(3,4,7,8-tetramethyl-1,10-phenanthroline)iron(II) and -(III) ions from nuclear magnetic resonance studies. *J. Phys. Chem.* **1973,** *77* (18), 2163–2165.

31. Walsh, J. L.; Baumann, J. A.; Meyer, T. J., Rate of electron self-exchange between the delocalized clusters [RU3O(CH3CO2)6(PY)3]+/0. *Inorg. Chem.* **1980,** *19* (7), 2145–2151.

32. Marcus, R. A., Chemical and Electrochemical Electron-Transfer Theory. *Annu. Rev. Phys. Chem.* **1964,** *15* (1), 155–196.

33. Brunschwig, B. S.; Creutz, C.; Sutin, N., Optical transitions of symmetrical mixed-valence systems in the Class II-III transition regime. *Chem. Soc. Rev.* **2002,** *31* (3), 168–184.

34. Hansch, C.; Leo, A.; Taft, R. W., A survey of Hammett substituent constants and resonance and field parameters. *Chem. Rev.* **1991,** *91* (2), 165–195.

35. Ito, T.; Hamaguchi, T.; Nagino, H.; Yamaguchi, T.; Kido, H.; Zavarine, I. S.; Richmond, T.; Washington, J.; Kubiak, C. P., Electron Transfer on the Infrared Vibrational Time Scale in the Mixed Valence State of 1,4-Pyrazine- and 4,4'-Bipyridine-Bridged Ruthenium Cluster Complexes. *J. Am. Chem. Soc.* **1999,** *121* (19), 4625–4632.

36. Neese, F., An improvement of the resolution of the identity approximation for the formation of the Coulomb matrix. *J. Comput. Chem.* **2003,** *24* (14), 1740–1747.

37. Kossmann, S.; Neese, F., Comparison of two efficient approximate Hartee–Fock approaches. *Chem. Phys. Lett.* **2009,** *481* (4–6), 240–243.

38. Neese, F.; Wennmohs, F.; Hansen, A.; Becker, U., Efficient, approximate and parallel Hartree–Fock and hybrid DFT calculations. A 'chain-of-spheres' algorithm for the Hartree–Fock exchange. *Chem. Phys.* **2009,** *356* (1–3), 98–109.

39. Izsák, R.; Neese, F., An overlap fitted chain of spheres exchange method. *J. Chem. Phys.* **2011,** *135* (14), 144105.

40. Neese, F., The ORCA program system. *WIREs Comput. Mol. Sci.* **2012,** *2* (1), 73–78.

41. Andrae, D.; Häußermann, U.; Dolg, M.; Stoll, H.; Preuß, H., Energy-adjustedab initio pseudopotentials for the second and third row transition elements. *Theor. Chem. Acc.* **1990,** *77* (2), 123–141.

42. Schäfer, A.; Horn, H.; Ahlrichs, R., Fully optimized contracted Gaussian basis sets for atoms Li to Kr. *J. Chem. Phys.* **1992,** *97* (4), 2571–2577.

43. Schäfer, A.; Huber, C.; Ahlrichs, R., Fully optimized contracted Gaussian basis sets of triple zeta valence quality for atoms Li to Kr. *J. Chem. Phys.* **1994,** *100* (8), 5829–5835.

44. Weigend, F., Accurate Coulomb-fitting basis sets for H to Rn. *Phys. Chem. Chem. Phys.* **2006,** *8* (9), 1057–1065.

45. Sinnecker, S.; Rajendran, A.; Klamt, A.; Diedenhofen, M.; Neese, F., Calculation of Solvent Shifts on Electronic g-Tensors with the Conductor-Like Screening Model (COSMO) and Its Self-Consistent Generalization to Real Solvents (Direct COSMO-RS). *J. Phys. Chem. A* **2006,** *110* (6), 2235–2245.

46. Grimme, S.; Ehrlich, S.; Goerigk, L., Effect of the damping function in dispersion corrected density functional theory. *J. Comput. Chem.* **2011,** *32* (7), 1456–1465.

47. Pettersen, E. F.; Goddard, T. D.; Huang, C. C.; Couch, G. S.; Greenblatt, D. M.; Meng, E. C.; Ferrin, T. E., UCSF Chimera–a visualization system for exploratory research and analysis. *J. Comput. Chem.* **2004,** *25* (13), 1605–1612.

Chapter 3

Effects of Electron Transfer Across Hydrogen Bonds.

3.1 Introduction

Electron transfer reactions are among the simplest yet most important reactions in chemistry and biology. The transfer of electrons lies at the heart of any chemical reaction; and all biological energy transformations fundamentally depend on electron transfer through proteins and protein assemblies. In the last several decades, extensive experimental and theoretical investigations have been performed to elucidate the nature of electron transfer (ET) in biological energy transfer processes.[1-14] Electron flow through proteins typically occurs in a site-to-site manner between redox centers that are separated by distances of 10 to 20 Å.[13-14] Larger distances require coupling several of these site-to-site reactions such that distances upwards of 25 Å can be traversed.[6, 9-10, 12-14] Such ET multistep mechanisms are often mediated by intervening amino acid side chains where donor-acceptor ET is favored over tunneling across

bridges.[12-13] As demonstrated by Gray *et al.* in work on mutant azurin proteins, ET across such groups typically proceeds across weak, non-covalent interactions.[7-8, 13-14]

While it's easy to see that the study of ET across weak, non-covalent interactions has important implications in understanding the nature of long-range ET in biological systems, the importance of non-covalent interactions also extends throughout the chemical sciences. From small molecular catalysts to artificial supramolecular systems, non-covalent interactions have been shown to readily affect both catalyst selectivity[15-25] and the stabilization of large supramolecular structures. Herein, we examine the fundamental relationship between non-covalent molecular interactions and ET to gain new understanding of electron transfer processes ubiquitous in biological and artificial systems.[5, 7-9, 12, 14, 17, 23, 26-33]

While several examples of hydrogen-bonded mixed valency (HBMV) have emerged over the last decade,[29, 34-37] our laboratory has focused on oxo-centered

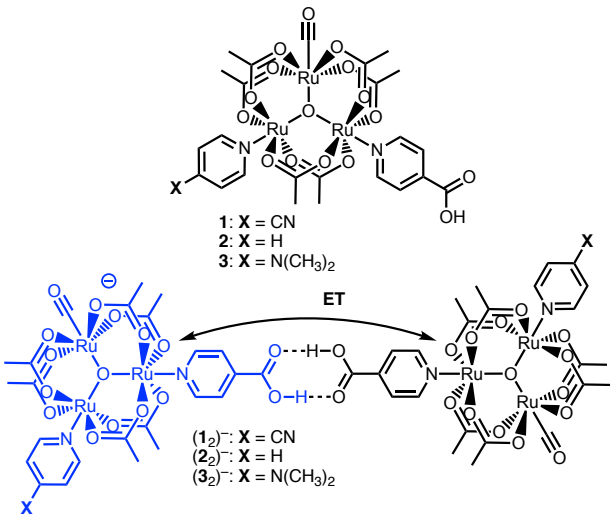

Figure 3.1. (top) Oxo-centered triruthenium cluster of the type $Ru_3(\mu_3\text{-}O)(OAc)_6(CO)(L_1)(ina)$ where L_1 = 4-cyanopyridine (cpy, **1**), pyridine (py, **2**), or 4-dimethylaminopyridine (dmap, **3**) and ina = isonicotinic acid. (bottom) Dimerization interaction upon a one electron reduction to generate the hydrogen-bonded, mixed-valent ions, $(\mathbf{1}_2)^-$, $(\mathbf{2}_2)^-$, $(\mathbf{3}_2)^-$.

triruthenium clusters featuring isonicotinic acid as the hydrogen-bonding bridging ligand ($Ru_3(\mu^3\text{-}O)(OAc)_6(CO)(L)(ina)$, L = 4-cyanopyridine (cpy, **1**), pyridine (py, **2**), or 4-dimethylaminopyridine (dmap, **3**) and ina = isonicotinic acid, Figure 3.1). Previous studies have shown that upon a one

electron reduction, **1**–**3** rapidly dimerize to form thermodynamically stable mixed-valence anions in solution (Figure 3.1).[38-39] Near-IR (nIR) spectroscopic analysis showed the appearance of intervalence charge transfer (IVCT) bands in the singly reduced, hydrogen-bonded dimers behavior indicative of moderately coupled mixed-valent anions.[38-39] In an effort to better understand the nature of ET across a weak, non-covalent interaction we determined the strength of the hydrogen bonds in dimers ($\mathbf{1}_2$)–($\mathbf{3}_2$) in the presence and absence of electron exchange.

3.2 Results and Discussion

In general, non-covalent, mixed-valent complexes such as $(\mathbf{1}_2)^-$, $(\mathbf{2}_2)^-$, and $(\mathbf{3}_2)^-$ can be described by the four dimerization equilibria below:

$$\begin{aligned}
M + M &\rightleftharpoons M_2 & K_D \\
M + (M)^- &\rightleftharpoons (M_2)^- & K_{MV} \\
(M)^- + (M)^- &\rightleftharpoons (M_2)^{2-} & K_{2-} \\
M_2 + (M_2)^{2-} &\rightleftharpoons 2\,(M_2)^- & K_C
\end{aligned}$$

Here, K_D and K_{2-} are the two isovalent equilibrium constants, which describe the self-dimerization of the neutral and one-electron reduced clusters respectively, K_C is the comproportionation constant, and K_{MV} is the equilibrium dimerization constant of the mixed-valent state. These terms offer thermodynamic information on the formation and stability of the hydrogen-bonded species in the three possible redox states. The direct comparison of K_{MV} to K_D or K_{2-} allows determination of the relative degree of stability gained from charge transfer *across* a hydrogen bond. While several spectroscopic methods for the determination of association constants have been established,[17, 40-44] it is clear that determination of any three of the constants, K_{MV}, K_C, K_{2-}, or K_D provides the fourth through equation 3.1.

$$K_{MV} = (K_D\, K_{2-}\, K_C)^{1/2} \qquad (3.1)$$

K_D, K_{2-}, and K_C can be readily obtained from established spectroscopic and electrochemical methods. The neutral dimerization constant (K_D) was measured by FTIR spectroscopy as the acidic proton of complexes **1**–**3** was not resolvable in the ^{1}H NMR but the ν(CO) band of the carboxylic acid for the monomer (1748 cm^{-1}) and dimer (1711 cm^{-1}) species were well resolved in the FTIR spectrum in methylene chloride (DCM) at 25 °C (Figure 3.2). Using a variable path length CaF_2 windowed call set to 2.0 mm, the FTIR spectra of complexes **1**–**3**, and their hydrogen bonded dimers were recorded in DCM across a range of concentrations from 2.3 mM to 0.26 mM. After solvent subtraction, the ν(CO) bands of the carboxylic acid were fit as two, well-resolved Gaussian functions (see appendix 3.5, Figure 3.10–Figure 3.12) to obtain the integrated spectral areas of each band (see appendix 3.5, Table 3.5). After obtaining the integrated spectral area for the monomer and dimer bands, K_D was determined by equation 3.2, using a 1:1 self-dimerization model (Figure 3.3).[42]

$$\frac{[M]_0}{A_m} = \frac{1}{\varepsilon_m \ell} + \left(\frac{2K_D}{(\varepsilon_m \ell)^2}\right) A_m \qquad (3.2)$$

Here, $[M]_0$ is the stoichiometric concentration of the solute, A_m is the integrated spectral area of the monomer band, ε_m is the molar absorptivity and ℓ is the cell path length. While previous studies have shown that the electronic couplings in complexes $(\mathbf{1}_2)^-$–$(\mathbf{3}_2)^-$, and Ru_3O clusters in general, have a large dependence on the electron–donating nature of the ancillary pyridine ligand.[38-39, 45-50] While similar trends between the donor-strength of the ancillary ligand and the equilibrium dimerization constant would be expected, no general trend in K_D is observed and the dimerization constants remain largely independent of the ancillary ligand (Table 3.1, K_D (M^{-1}): **1** = 119 (6), **2** = 75 (5), **3** = 130 (8)). In addition to treatment of the monomer band, K_D can also be determined by consideration of the dimer band through equation 3.3.

$$\frac{2A_d}{[M]_0} = \varepsilon_d \ell - \left(\frac{\varepsilon_d \ell}{K_D}\right)^{1/2} \frac{(A_d)^{1/2}}{[M]_0} \qquad (3.3)$$

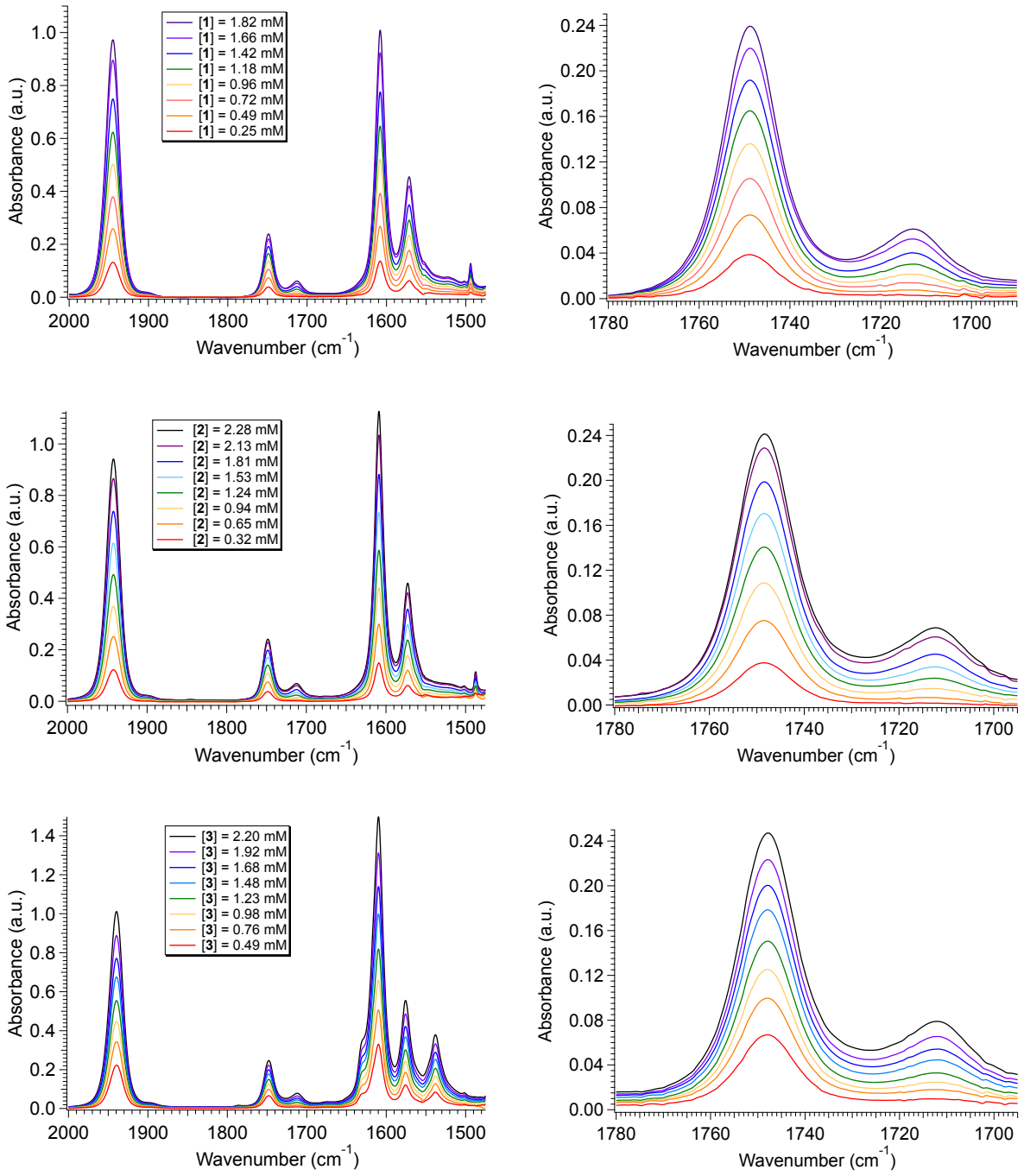

Figure 3.2. (left) FTIR spectra of **1**–**3** (top to bottom) in DCM at 25 °C. (right) ν(CO) region highlighting the monomer and dimer ν(CO) bands

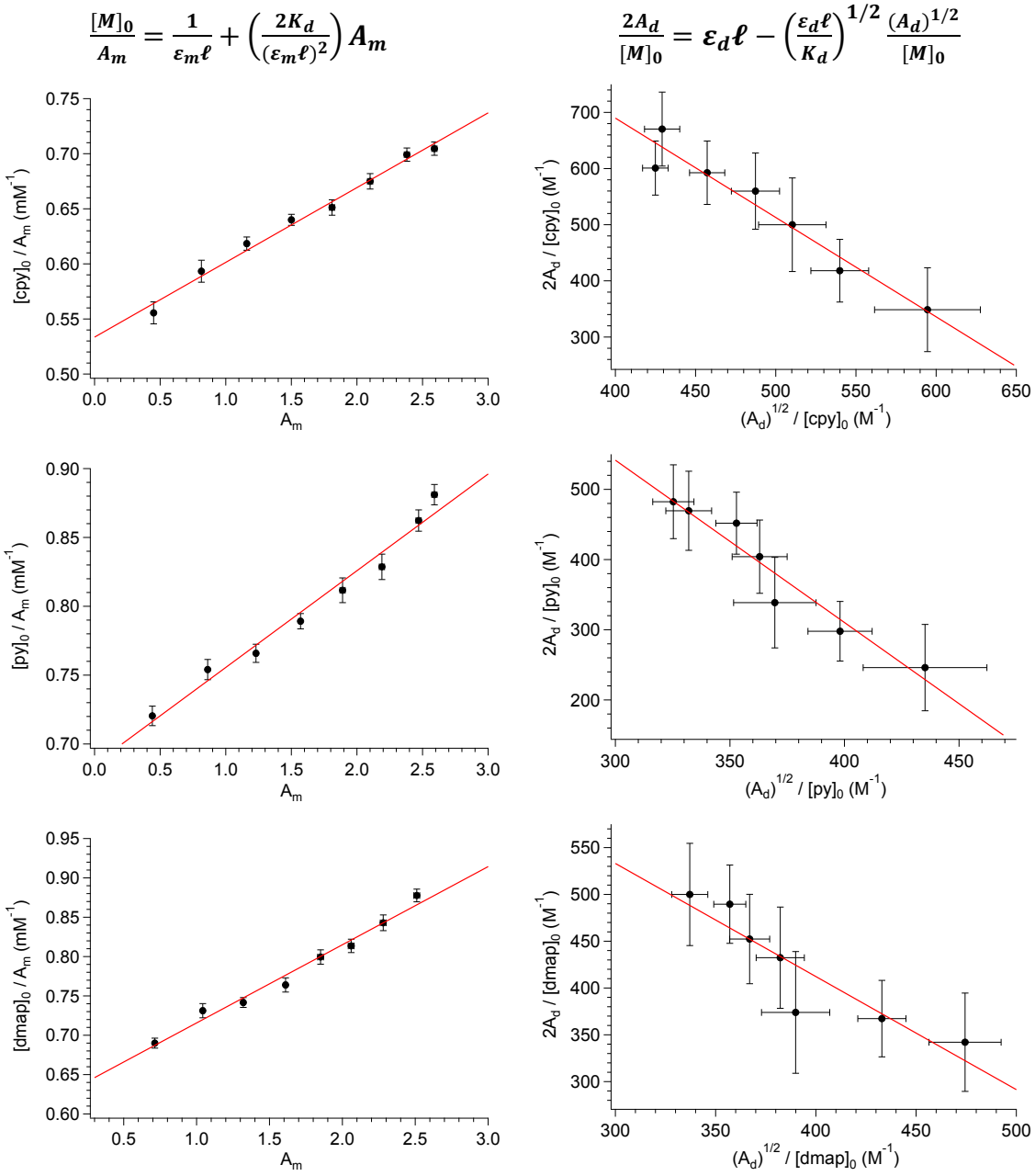

Figure 3.3. (left) Linear regression of the integrated spectral areas for **1**–**3** (top to bottom). Left side plots represent the monomeric band while the right side represents the dimer band. $[M]_0$ is the stoichiometric concentration of the solute, A_m and A_d are the integrated spectral areas of the monomeric and dimeric bands respectively, ε_m and ε_d are the molar absorptivity of the monomeric and dimeric species respectively, and ℓ is the cell pathlength.

Table 3.1. Equilibrium dimerization constants (K_D) of the neutral complexes **1**–**3** in DCM at 25 °C determined from equations 3.2 and 3.3.

Complex	K_D (monomer band, M^{-1})	K_D (dimer band, M^{-1})	K_D (average, M^{-1})
1	119 (6)	450 (70)	290 (40)
2	75 (5)	240 (90)	160 (50)
3	130 (8)	600 (200)	400 (100)

Table 3.2. Measured neutral dimerization constants (K_D) for **1**–**3** in DCM at 25 °C using equation 3.4 derived from the infinite dilution model.

Complex	K_D (Eq. 3.4, M^{-1})	K_D (Eq. 3.2, M^{-1})
1	120 (7)	119 (6)
2	73 (5)	75 (5)
3	126 (9)	130 (8)

It is important to note that determination of K_D should remain independent of ν(CO) band choice, when the dimer carboxylic acid ν(CO) band is used (Figure 3.3), a larger degree of uncertainty is found between the values (Table 3.1, K_D (M^{-1}): **1** = 450 (70), **2** = 240 (90), **3** = 600 (200)). This discrepancy is attributed to errors in the integration of the dimer ν(CO) band arising from errors in the Gaussian fits compounded by solvent background subtraction. This is effect is most clearly observed in the overlaid FTIR spectrum of DCM with complexes **1**–**3** (Figure 3.13), where a weak absorbance for DCM in the vicinity of 1730–1700 cm^{-1} coincides with the dimer ν(CO) band. Regardless, further support for these results can be found upon extrapolation of the dimerization model to infinite dilution through equation 3.4 as detailed by Luck (Figure 3.4).[51] Here, all values have their usual meanings, and excellent agreement is found upon comparison to those values as determined by equation 3.2 (**Error! Reference source not found.**). All results support the n otion that **1**–**3** form weak hydrogen bonds in solution at 25 °C (ΔG_D (kcal mol^{-1}): **1**: –2.83 (0.02), **2:** –2.56 (0.04), **3**: –2.88 (0.04)).

$$\frac{A_m}{[M]_0} = \varepsilon_m - \frac{K_d}{\varepsilon_m}\left(\frac{2(A_m)^2}{[M]_0}\right) \tag{3.4}$$

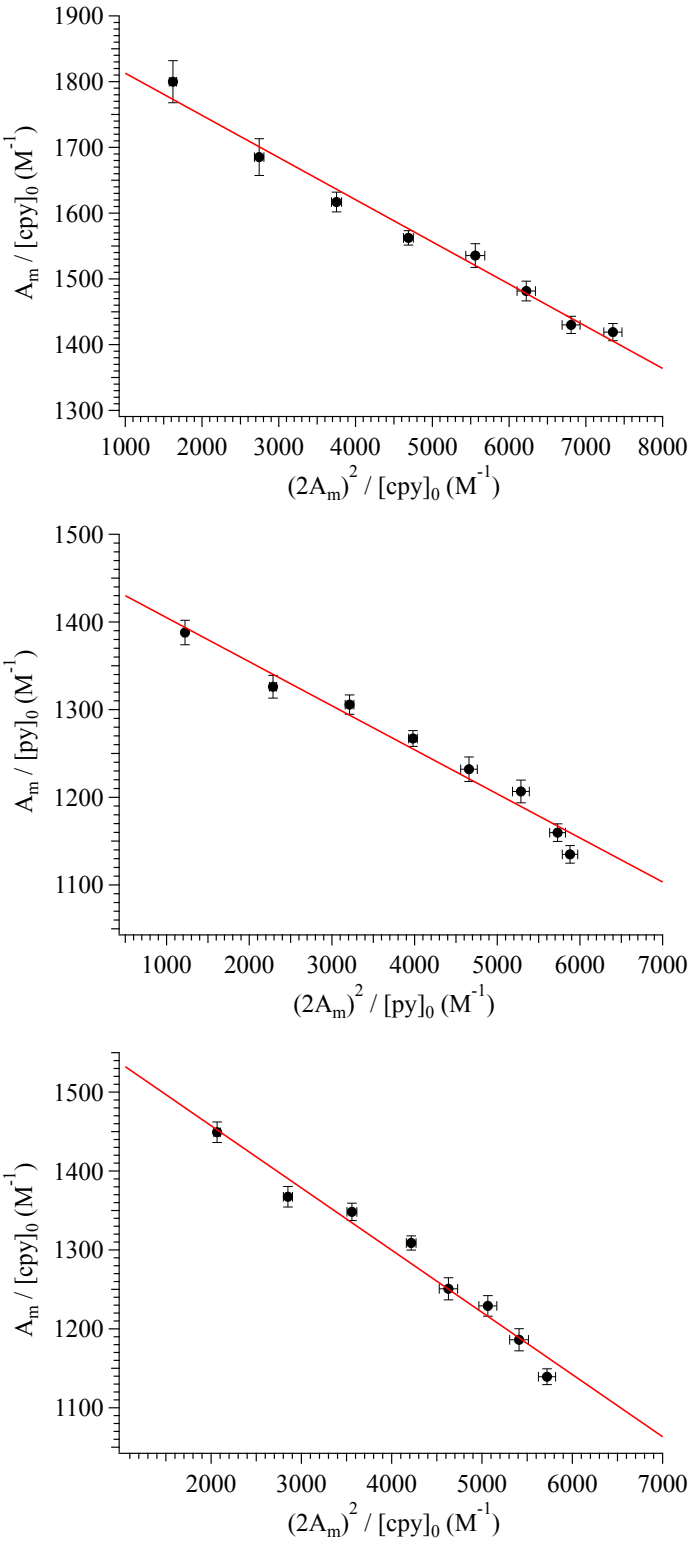

Figure 3.4. Linear regression of the integrated spectral areas for **1**–**3** (top to bottom) using equation 3.4 derived from the infinite dilution model.

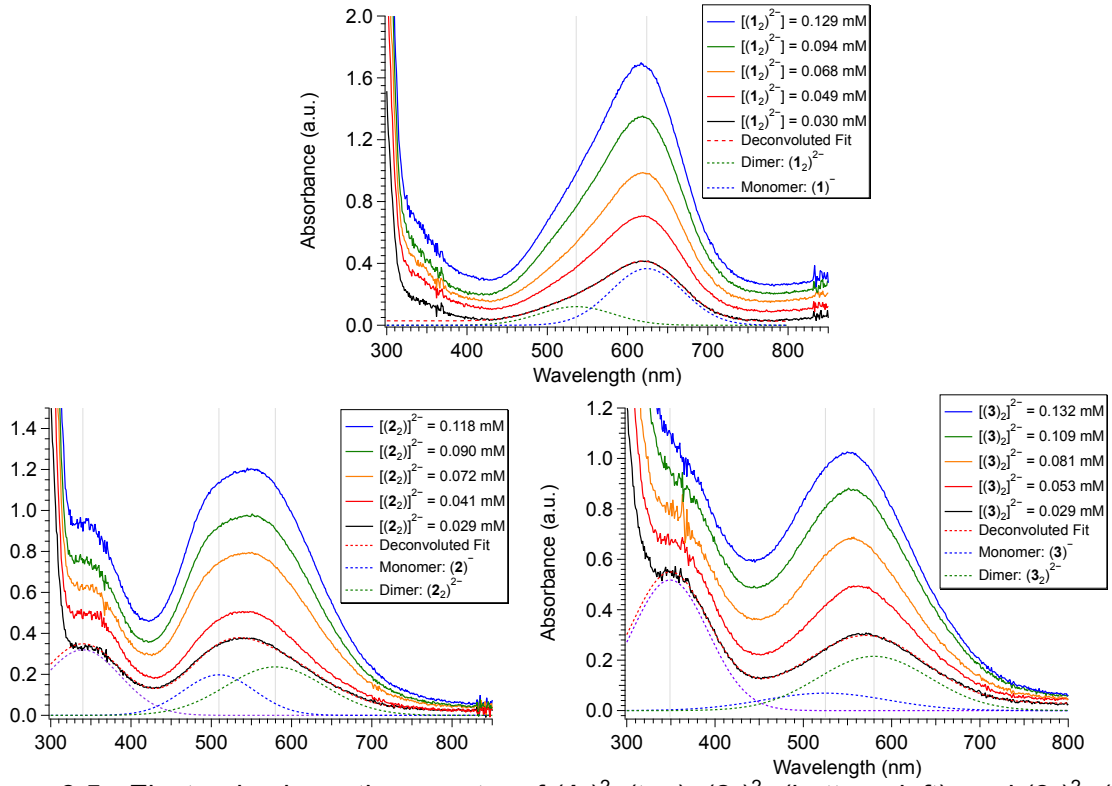

Figure 3.5. Electronic absorption spectra of $(\mathbf{1}_2)^{2-}$ (top), $(\mathbf{2}_2)^{2-}$ (bottom, left), and $(\mathbf{3}_2)^{2-}$ (bottom, right) in THF at 25 °C. Gaussian fits of the lowest concentration have been included highlighting the appearance of monomer (blue, dashed) and dimer (green, dashed) bands composing the broadened ICCT band.

Previous 1H DOSY NMR experiments have shown that in their singly reduced state, **1**–**3** exist as hydrogen bonded dimers, supporting a dimerization constant (K_{2-}) ≥ 103 M–1.[39] These findings are further confirmed through determination of K_{2-} by UV/vis/nIR absorption spectroscopy. Applying the same methodology for the determination of K_D, the absorption spectra of $(\mathbf{1}_2)^{2-}$, $(\mathbf{2}_2)^{2-}$, and $(\mathbf{3}_2)^{2-}$ in THF displays a broadened, intra-cluster charge transfer (ICCT) band in the visible region for both the anionic monomers, $(\mathbf{1})^{-}$, $(\mathbf{2})^{2-}$, $(\mathbf{3})^{-}$, and the dianionic, hydrogen-bonded dimers $(\mathbf{1}_2)^{2-}$, $(\mathbf{2}_2)^{2-}$, $(\mathbf{3}_2)^{2-}$ (Figure 3.5). Upon comparison of the electronic spectra of similar homoleptic clusters ($[Ru_3(\mu^3\text{-}O)(OAc)_6(CO)(L_1)_2]^{-}$ where L_1 = cpy, py, or dmap), which are incapable of dimerizing, it is clear to see that the broadened ICCT band consists of both monomeric and dimeric contributions (Figure 3.5 and Figure 3.6).[38-39, 45, 48-49] In lieu of determining spectral areas,

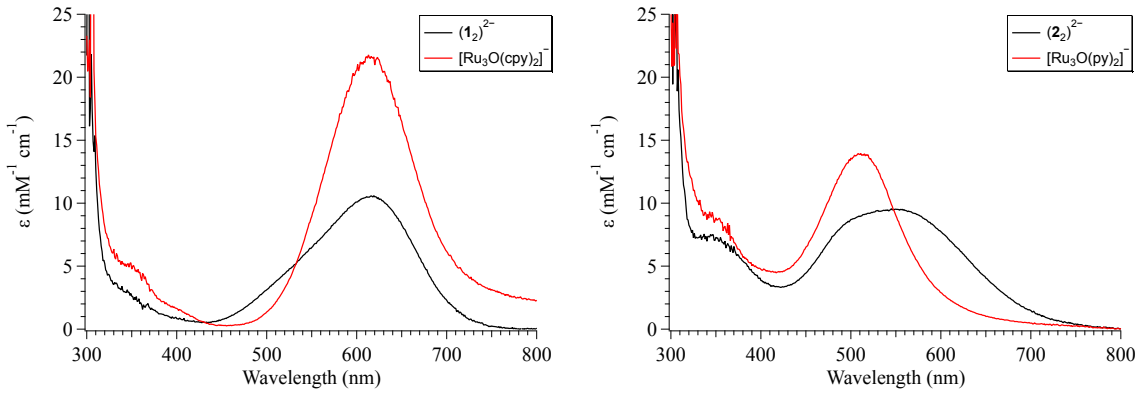

Figure 3.6. Electronic absorption spectra of $(\mathbf{1}_2)^{2-}$ and $[Ru_3(\mu_3\text{-}O)(OAc)_6(CO)(cpy)_2]^-$ (left) and of $(\mathbf{2}_2)^{2-}$ and $[Ru_3(\mu_3\text{-}O)(OAc)_6(CO)(py)_2]^-$ (right) in THF at –25 °C with $Co(cp^*)_2$ used as the chemical reductant.

Table 3.3. Measured dianionic dimerization constants (K_{2-}) for $(\mathbf{1})^-$–$(\mathbf{3})^-$ in THF at 25 °C using equation 3.2 and equation 3.4.

Complex	$\mathbf{K_{2-}}$ (Eq. 3.2, M^{-1})	$\mathbf{K_{2-}}$ (Eq. 3.4, M^{-1})
$(\mathbf{1})^-$	2000 (400)	2000 (400)
$(\mathbf{2})^-$	2200 (300)	2200 (300)
$(\mathbf{3})^-$	2500 (300)	2700 (300)

the peak heights of the monomeric band ($(\mathbf{1})^-$: 612 nm, $(\mathbf{2})^-$: 487 nm, $(\mathbf{3})^-$: 550 nm) were used in conjunction with equation 3.2 and K_{2-} was found to range from 2000 to 2500 M^{-1} (Figure 3.7; Table 3.3; K_{2-} (M^{-1}): $(\mathbf{1})^-$: 2000 (400), $(\mathbf{2})^-$: 2200 (300), $(\mathbf{3})^-$: 2500 (300)). These values are further supported by use of equation 3.4 (infinite dilution model), where the values are found to be nearly identical within experimental error (Figure 3.7; Table 3.3; K_{2-} (M^{-1}): $(\mathbf{1})^-$: 2000 (400), $(\mathbf{2})^-$: 2200 (300), $(\mathbf{3})^-$: 2700 (300)), and indicate the formation of moderately strong hydrogen bonds in solution ($\Delta G°_{2-}$ (kcal mol^{-1}), $(\mathbf{1})^-$: –4.5 (0.1), $(\mathbf{2})^-$: –4.56 (0.08), $(\mathbf{3})^-$: –4.63 (0.07)).

(3.5)

$$\frac{[M]_0}{H_m} = \frac{1}{\varepsilon_m \ell} + \left(\frac{2K_d}{(\varepsilon_m \ell)^2}\right) H_m \qquad \frac{A_m}{[M]_0} = \varepsilon_m - \frac{K_d}{\varepsilon_m}\left(\frac{(2A_m)^2}{[M]_0}\right)$$

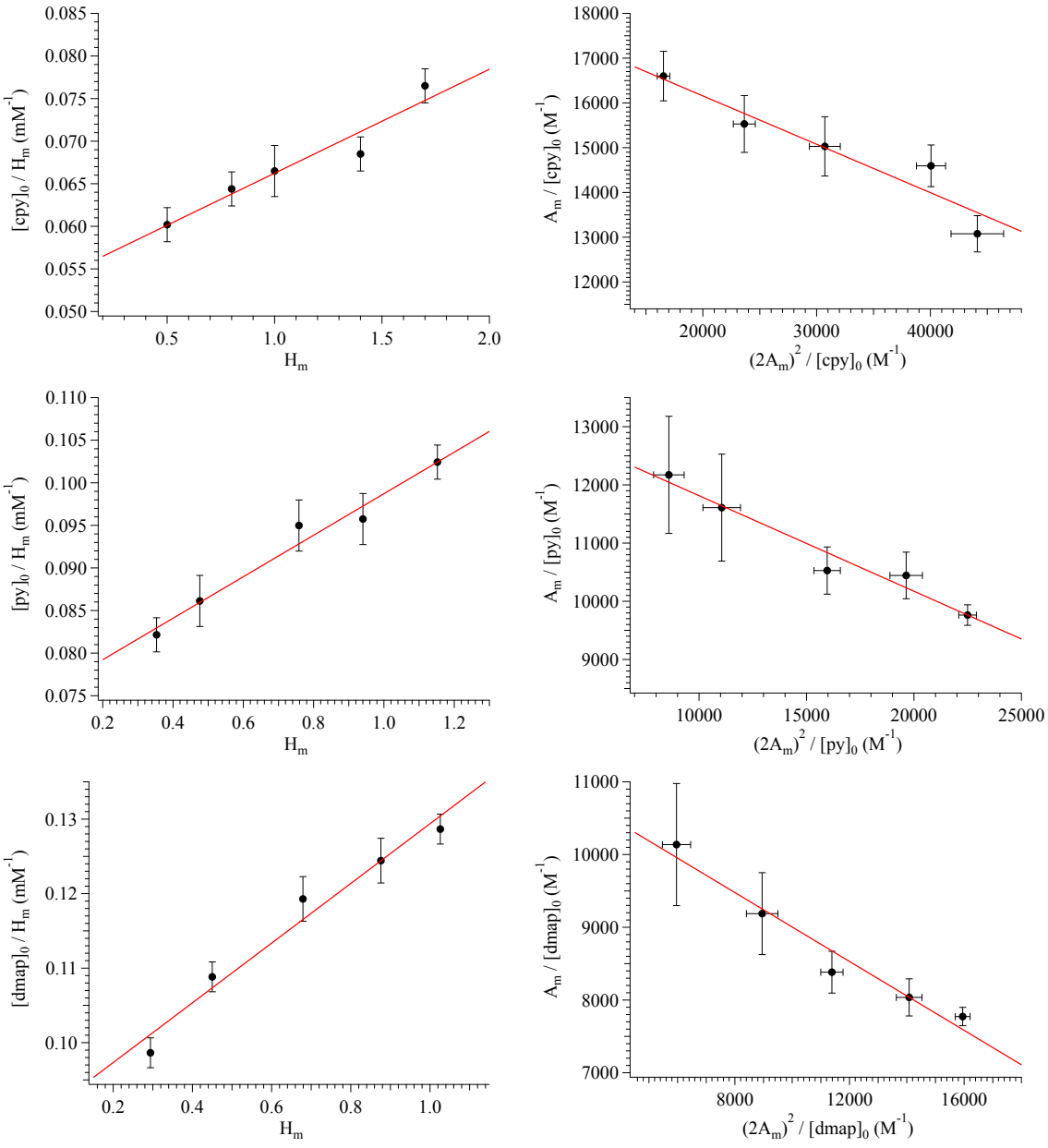

Figure 3.7. (left) Linear regression of the spectral heights for $(\mathbf{1}_2)^{2-}$ (top), $(\mathbf{2}_2)^{2-}$ (middle), and $(\mathbf{3}_2)^{2-}$ (bottom) following equation 3.2. (right) Linear regression of the spectral heights for $(\mathbf{1}_2)^{2-}$ (top), $(\mathbf{2}_2)^{2-}$ (middle), and $(\mathbf{3}_2)^{2-}$ (bottom) following equation 3.4. Here, $[M]_0$ is the stoichiometric concentration of the solute, H_m is the peak height of the monomer band, ε_m is the molar absorbtivity of the monomer bands, and $\boldsymbol{\ell}$ is the cell path length.

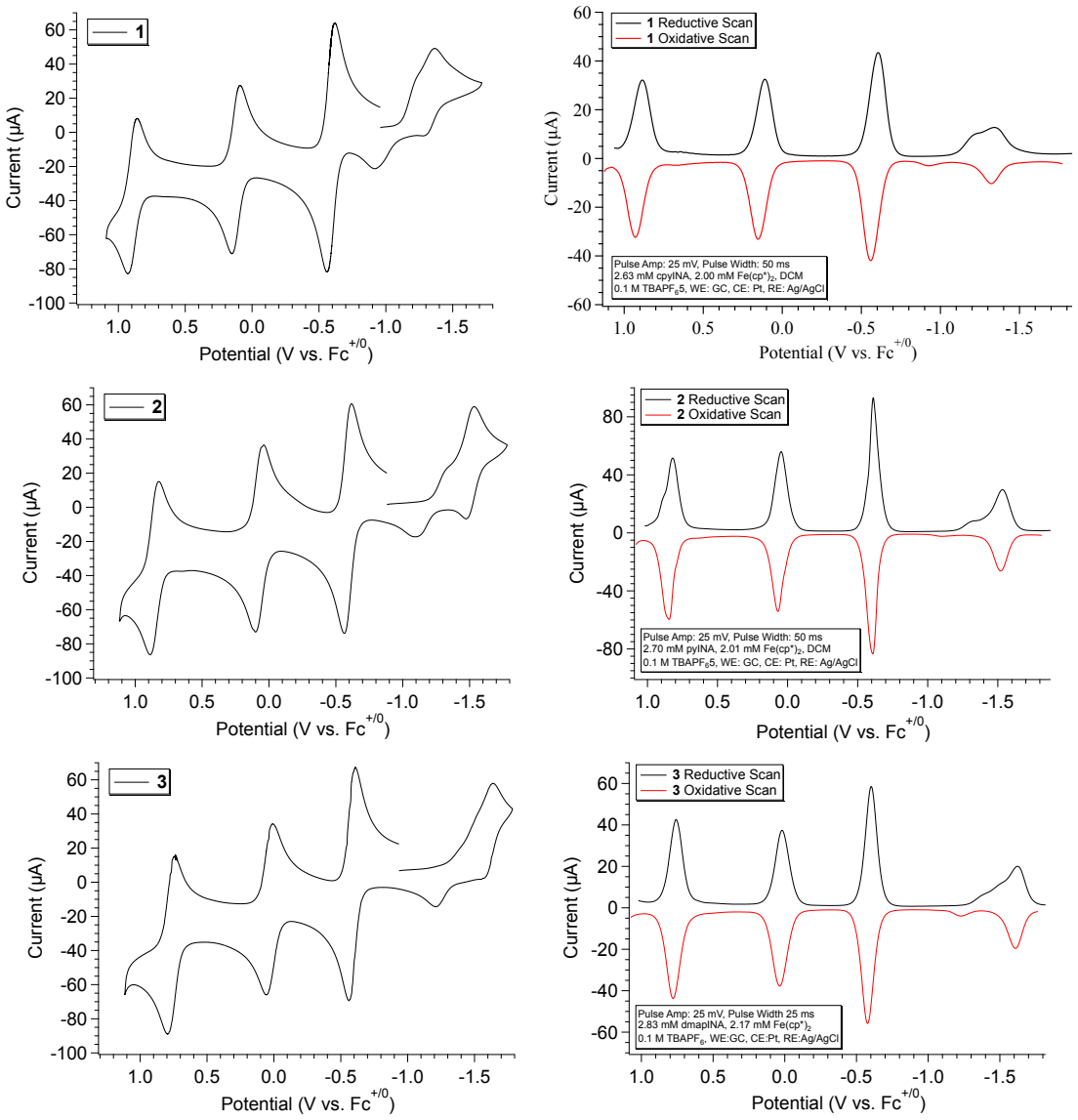

Figure 3.8. Cyclic (right) and differential pulse (left) voltammograms of **1**–**3** at analyte concentrations of ~2.7 mM, in DCM with 0.1 M $TBAPF_6$ as the supporting electrolyte and $Fe(cp^*)_2$ as an internal standard. CVs were recorded at 100 mVs and referenced to the $Fc^{+/0}$ redox couple.

The comproportionation constant (K_C), is largely a measure of the thermodynamic stability of the mixed-valent (1–) state with respect to the isovalent states (0 and 2–) and can be determined from the electrochemical splitting (ΔE) of the 0/– and –/2– redox couples as measured by cyclic voltammetry through equation 3.5.[52]

$$K_C = e^{\frac{nF\Delta E}{RT}}$$

For complexes **1**–**3**, the values for K_C were determined from the electrochemical splitting's of the oxidative features observed on the return sweep of the cyclic voltammograms (CVs, Figure 3.8).[38-39] At 23 °C in DCM, K_C is found to be on the order of 10^6 for all clusters (**1**: K_C = 1.09 (0.04) x 10^6, **2**: K_C = 32. (0.1) x 10^6, **3**: K_C = 4.8 (0.2) x 10^6). Unlike K_D, K_C is observed to increase with increasing pK_a of the ancillary ligand, suggesting the formation of more thermodynamically stable mixed-valence ions as more donating pyridine ligands are used.

Utilizing equation 3.1, K_{MV} was found to be on average four orders of magnitude larger than K_D, three orders of magnitude larger than K_{2-}, and range from 0.5 to 1.2 x 10^6 M^{-1} in DCM (Table 3.5). Much like K_C, K_{MV} was also observed to increase linearly with as more electron-donating pyridine ligands (See appendix 3.5, Figure 3.14, pK_a: **1**, cpy = 1.9; **2**, py = 5.1; **3**, dmap = 9.2) were used. This behavior indicates the formation of more highly coupled, hydrogen-bonded mixed valence anions when electron-rich pyridine ligands are used. This effect is be best explained through a ligand-field description, where the use of stronger field pyridine ligands raises the Ru_3O dπ manifold into closer energetic alignment with the isonicotinic acid π^* orbitals.[46] This ultimately gives rise to more resonant delocalization across the hydrogen-bond, where the direct mixing of metal center and bridging ligand wave-functions provides an indirect method for donor-acceptor overlap to occur.[38] The difference in free energies obtained between K_{MV}, K_D, and K_{2-} ($\Delta\Delta G°$, Table 3.4) reveal the relative stabilities of the mixed-valent states relative to the two

Table 3.4. Equilibrium dimerization constants for complexes **1**–**3** in DCM at 25 °C.

Complex	K_D (M^{-1})	K_{2-} (10^3 M^{-1})[a]	K_C (10^6)	K_{MV} (10^6 M^{-1})	$\Delta\Delta G°_D$ (kcal/mol)[b]	$\Delta\Delta G°_{2-}$ (kcal/mol)[b]
1	119 (6)	2.0 (0.4)	1.09 (0.04)	0.5 (0.1)	–4.95 (0.07)	–3.3 (0.1)
2	75 (5)	2.2 (0.3)	3.2 (0.1)	0.7 (0.1)	–5.4 (0.1)	–3.4 (0.1)
3	130 (8)	2.5 (0.3)	4.8 (0.2)	1.2 (0.1)	–5.43 (0.06)	–3.68 (0.08)

[a]Value for K_{2-} was determined in THF with $Co(cp^*)_2$ used as a chemical reductant.
[b]$\Delta\Delta G°_D = \Delta G°_{MV} - \Delta G°_D$ and $\Delta\Delta G°_{2-} = \Delta G°_{MV} - \Delta G°_{2-}$

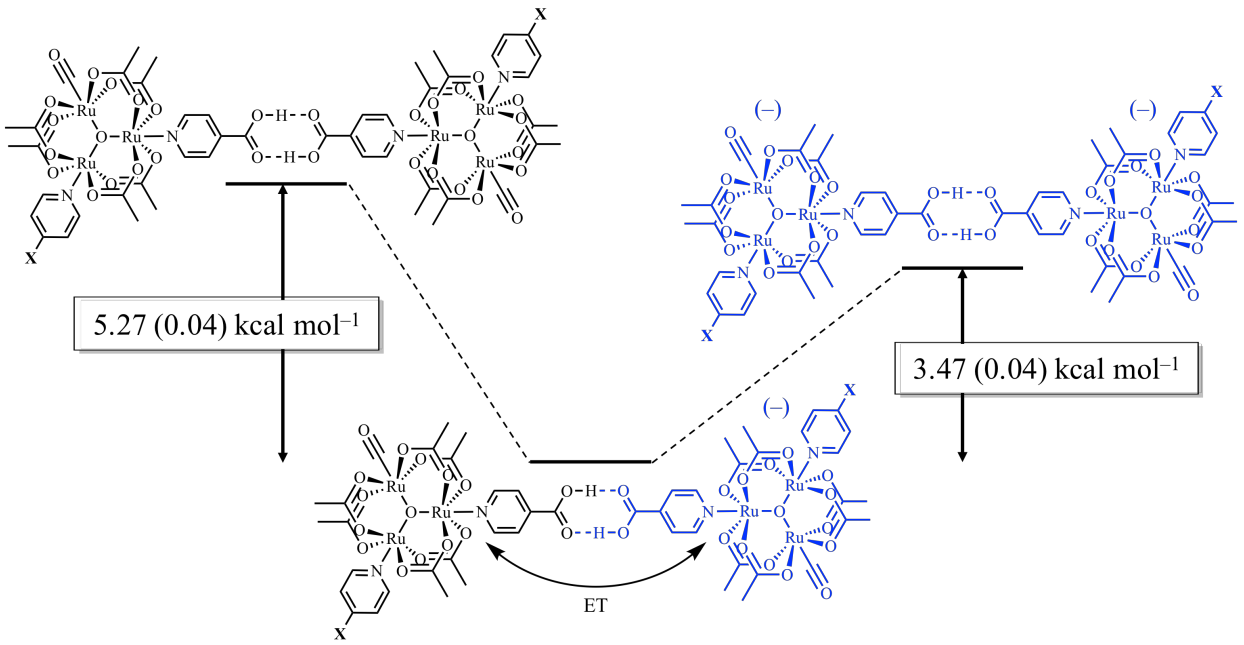

Figure 3.9. Relative free energy diagram of hydrogen-bond formation showing the additional stabilization of hydrogen bonds participating in electron delocalization.

isovalent, hydrogen-bonded states. On average, a stabilization –5.27 (0.04) kcal mol^{-1} (1850 (10) cm^{-1}) and –3.47 (0.06) kcal mol^{-1} (1210 (20) cm^{-1}) is gained upon the formation of the mixed-valent, hydrogen-bonded dimers ((**1**$_2$)$^-$, (**2**$_2$)$^-$, and (**3**$_2$)$^-$), relative to the neutral (**1**$_2$, **2**$_2$, and **3**$_2$) and dianionic ((**1**$_2$)$^{2-}$, (**2**$_2$)$^{2-}$, and (**3**$_2$)$^{2-}$), isovalent states respectively (Figure 3.9).

3.3 Conclusion

While hydrogen bonding likely plays a small role in the stabilization of the mixed-valent states, the large observed stabilization appears to be derived primarily from electron exchange. It is believed that significant mixing of the metal and bridging ligand wave functions in the mixed-valent states provides larger than expected electronic couplings between metal centers traditionally considered too far apart or too weakly interacting to support significant electronic interaction. To our knowledge, this is the first determination of a significant increase in the strength of hydrogen-bonding when those bonds participate in the delocalization of an electron.

3.4 Experimental

Preparation and Purification.

Complexes **1**–**3** were synthesized following previously reported procedures.[38-39] The isonicotinic acid was used as received from MP Biomedical Inc. while decamethyl ferrocene and decamethyl cobaltocene were received from Sigma-Aldrich, and used after sublimation at 2 x 10^{-4} torr. The dichloromethane (DCM) and tetrahydrofuran (THF) were purchased from VWR International LLC, deoxygenated and dried over alumina columns on a custom built solvent system under and argon atmosphere and stored over activated 4 Å molecular sieves in a nitrogen filled glove box.

Chemical Reductions.

Stock solutions of 0.60 mM of **1**–**3** and 3.60 mM of $Co(cp^*)_2$ were prepared in dry THF under an inert atmosphere. From the stock solution of **1**–**3**, five aliquots were prepared for each sample directly into an air tight 10 mm path length quartz cuvette ranging in concentrations from 0.13 mM to 0.03 mM. The absorption spectrum of each aliquot was recorded prior to reduction to determine the exact molarity of each aliquot. A stoichiometric amount of $Co(cp^*)_2$ was then injected into each aliquot, using a Hamilton gas-tight micro-syringe, to fully reduce the samples by one electron. After injection the cell was sealed and the absorption spectrum was promptly collected.

FTIR Data Collection and Analysis.

Infrared spectra were collected on a Bruker Equinox 55 FTIR spectrometer using a SPECAC variable path length IR cell with CaF_2 windows set to a path length of 2.0 mm. Solutions were prepared in a glove box under a nitrogen atmosphere using pre-dried DCM and subsequently analyzed. After solvent subtraction, the carboxylic acid ν(CO) bands were fit to two, well resolved Gaussian functions using the Igor Pro software to obtain integrated spectral areas used in the equilibrium analysis.

UV/visible Data Collection and Analysis.

UV-visible spectra were collected on a Shimadzu UV–3600 UV/vis/NIR spectrometer. Samples from the determination of K_D were taken directly from FTIR solutions and enclosed in a 1.0 mm path length, while samples for determination of K_{2-} were diluted directly into air tight 10 mm path length quartz cuvettes from stock solutions of **1**–**3** and subsequently reduced with $Co(cp^*)_2$.

Electrochemical Measurements.

Electrochemistry was performed on a BASi Epsilon potentiostat, in dried degassed DCM with 0.1 M tetrabutylammonium hexafluorophosphate ($TBAPF_6$, recrystallized from MeOH vacuum dried at 80 °C) used as a supporting electrolyte. Cyclic voltammograms (CVs) and differential pulse voltammograms (DPVs) were recorded at 298 K with ~ 2.7 mM analyte concentrations using a three-electrode setup consisting of a glassy carbon working electrode (3 mm diameter), a Pt auxiliary electrode, and an Ag/AgCl wire reference electrode. All samples were referenced to the ferrocene +/0 redox couple using an internal standard of decamethyl ferrocene ($E_{1/2}$ = –0.59 vs $Fc^{+/0}$).

3.5. Appendix.

Chapter 3: The majority of the material in this chapter comes directly from a manuscript entitled “Effects of electron on hydrogen bonds,” by Tyler M. Porter, Gavin P. Heim, and Clifford P. Kubiak, is published in *Chemical Science*, **2017**, *8*, 7324–7329. The dissertation author is the primary author.

Derivation of K_{MV} Cross Relation:

$$
\begin{aligned}
M + M &\rightleftharpoons M_2 && K_D \\
M + (M)^- &\rightleftharpoons (M)_2^- && K_{MV} \\
(M)^- + (M)^- &\rightleftharpoons (M)_2^{-2} && K_{-2} \\
M_2 + (M)_2^{-2} &\rightleftharpoons 2\,(M)_2^- && K_C
\end{aligned}
$$

$$[\mathbf{1}]^2 = \frac{[(\mathbf{1})_2]}{K_D} \qquad [(\mathbf{1})_2^-] = K_C[(\mathbf{1})_2^{2-}][(\mathbf{1})_2] \qquad [(\mathbf{1})^-] = \frac{[(\mathbf{1})_2^{2-}]}{K_{2-}}$$

$$(K_{mv})^2 = \frac{K_C[(\mathbf{1})_2^{2-}][(\mathbf{1})_2]}{\left(\frac{[(\mathbf{1})_2]}{K_D}\right)\left(\frac{[(\mathbf{1})_2^{2-}]}{K_{2-}}\right)}$$

$$(K_{mv})^2 = K_C K_{2-} K_D$$

$$K_{mv} = (K_C K_{2-} K_D)^{1/2}$$

Derivation of Dimerization Model:

Consider a 1:1 self-dimerization:

$$\mathrm{M} + \mathrm{M} \rightleftharpoons \mathrm{M}_2$$

$$\mathrm{K_D} = \frac{[\mathrm{M_2}]}{[\mathrm{M}]^2} \qquad [\mathrm{M}]_0 = [\mathrm{M}] + 2[\mathrm{M_2}]$$

Solving the mass balance for $[M_2]$ and substituting into K_D

$$\mathrm{K_D} = \frac{[\mathrm{M}]_0 - [M]}{2[\mathrm{M}]^2}$$

Using the quadratic equation to solve for [M] and keeping the positive solution yields:

$$[\mathrm{M}] = \frac{-1 + (1 + 8K_D[M]_0)^{1/2}}{4K_D}$$

Multiplying top and bottom by the conjugate of $(-1 - (1 + 8K_D[M]_0)^{\frac{1}{2}})$ yields:

$$[\mathrm{M}] = \frac{2[M]_0}{1 + (1 + 8K_D[M]_0)^{1/2}}$$

Substitution of [M] into mass balance equation and solving for $[M_2]$ yields:

$$[\mathrm{M_2}] = \frac{[M]_0}{2} - \frac{2[M]_0}{1 + (1 + 8K_D[M]_0)^{1/2}}$$

Combine using a common denominator of $2(1+(1+8K_D[M]_0)^{\frac{1}{2}})$

$$[\mathrm{M_2}] = \frac{[M]_0\left(1+(1+8K_D[M]_0)^{\frac{1}{2}}\right)-2[M]_0}{2\left(1+(1+8K_D[M]_0)^{\frac{1}{2}}\right)}$$

$$[\mathrm{M_2}] = \left(\frac{[M]_0}{2}\right)\left(\frac{(1+8K_D[M]_0)^{\frac{1}{2}}-1}{(1+8K_D[M]_0)^{\frac{1}{2}}+1}\right)$$

From the above we end at two expressions for the monomer and dimer concentrations in solution.

$$[\mathrm{M}] = \frac{2[M]_0}{1+(1+8K_D[M]_0)^{1/2}} \qquad [\mathrm{M_2}] = \left(\frac{[M]_0}{2}\right)\left(\frac{(1+8K_D[M]_0)^{\frac{1}{2}}-1}{(1+8K_D[M]_0)^{\frac{1}{2}}+1}\right)$$

Using the Beer-Lambert law we can then describe the absorbance of monomer and dimer bands as follows:

$$\mathrm{A_m}(\tilde{\nu}) = \varepsilon_{\mathrm{m}}(\tilde{\nu})\ell[\mathrm{M}] \qquad \mathrm{A_d}(\tilde{\nu}) = \varepsilon_{\mathrm{d}}(\tilde{\nu})\ell[\mathrm{M_2}]$$

Where $\mathrm{A_m}(\tilde{\nu})$ and $\mathrm{A_d}(\tilde{\nu})$ are the absorbance of the monomer and dimer at a specific wavelength, $\varepsilon_{\mathrm{m}}(\tilde{\nu})$ and $\varepsilon_{\mathrm{m}}(\tilde{\nu})$ are the molar absorptivity at $\tilde{\nu}$, and ℓ the optical path length. The integrated absorbance of the whole band is then given by:

$$\mathrm{A_m} = (\ell[\mathrm{M}])\int \varepsilon_{\mathrm{m}}(\tilde{\nu})\mathrm{d}\tilde{\nu} \qquad \mathrm{A_d} = (\ell[\mathrm{M_2}])\int \varepsilon_{\mathrm{d}}(\tilde{\nu})\mathrm{d}\tilde{\nu}$$

Where A_m and A_d are now the integrated absorbance's of the monomer and dimer bands respectively and $\int \varepsilon_{\mathrm{m}}(\tilde{\nu})\mathrm{d}\tilde{\nu}$ and $\int \varepsilon_{\mathrm{d}}(\tilde{\nu})\mathrm{d}\tilde{\nu}$ are the molar absorptivity's of the monomer and dimer bands respectively. Substituting in for the concentrations of [M] and [M_2] then yields:

$$\mathrm{A_m} = \frac{2[\mathrm{M}]_0\varepsilon_{\mathrm{m}}\ell}{1+(1+8\mathrm{K_D}[\mathrm{M}]_0)^{1/2}} \qquad \mathrm{A_d} = \left(\frac{\varepsilon_{\mathrm{d}}\ell[\mathrm{M}]_0}{2}\right)\left(\frac{(1+8\mathrm{K_D}[\mathrm{M}]_0)^{\frac{1}{2}}-1}{(1+8\mathrm{K_D}[\mathrm{M}]_0)^{\frac{1}{2}}+1}\right)$$

Focusing on the monomer equation, we can divide the first and last terms by $2[M]_0\varepsilon_m\ell$ and inverting the resulting fraction yields:

$$\frac{2[\mathrm{M}]_0\varepsilon_m\ell}{\mathrm{A_m}} = 1 + (1 + 8\mathrm{K_D}[\mathrm{M}]_0)^{1/2}$$

If we set $a = \frac{2[\mathrm{M}]_0\varepsilon_m\ell}{\mathrm{A_m}}$, subtract by unity, take the squares of both sides, and simplify we arrive at:

$$(\mathrm{a} - 1)^2 = 1 + 8\mathrm{K_D}[\mathrm{M}]_0$$

$$\mathrm{a}^2 - 2\mathrm{a} + 1 = 1 + 8\mathrm{K_D}[\mathrm{M}]_0$$

$$\mathrm{a}^2 = 2\mathrm{a} + 8\mathrm{K_D}[\mathrm{M}]_0$$

$$\left(\frac{2[\mathrm{M}]_0\varepsilon_m\ell}{\mathrm{A_m}}\right)^2 = \frac{4[\mathrm{M}]_0\varepsilon_m\ell}{\mathrm{A_m}} + 8\mathrm{K_D}[\mathrm{M}]_0$$

We can then linearize by dividing both sides by $\left(\frac{4\varepsilon_m{}^2\ell^2[M]_0}{A_m}\right)$

$$\left(\frac{\mathrm{A_m}}{4\varepsilon_m{}^2\ell^2[\mathrm{M}]_0}\right)\left(\frac{2[\mathrm{M}]_0\varepsilon_m\ell}{\mathrm{A_m}}\right)^2 = \left(\frac{4[\mathrm{M}]_0\varepsilon_m\ell}{\mathrm{A_m}} + 8\mathrm{K_D}[\mathrm{M}]_0\right)\left(\frac{\mathrm{A_m}}{4\varepsilon_m{}^2\ell^2[\mathrm{M}]_0}\right)$$

$$\frac{[\mathrm{M}]_0}{\mathrm{A_m}} = \left(\frac{2\mathrm{K_D}}{\varepsilon_m{}^2\ell^2}\right)\mathrm{A_m} + \frac{1}{\varepsilon_m\ell}$$

We can treat the dimer band in the same manner, remembering that:

$$\mathrm{A_d} = \left(\frac{\varepsilon_d\ell[\mathrm{M}]_0}{2}\right)\left(\frac{(1 + 8\mathrm{K_D}[\mathrm{M}]_0)^{\frac{1}{2}} - 1}{(1 + 8\mathrm{K_D}[\mathrm{M}]_0)^{\frac{1}{2}} + 1}\right)$$

Divide both sides of the equation by $\left(\frac{\varepsilon_d\ell[\mathrm{M}]_0}{2}\right)$:

$$\frac{2\mathrm{A_d}}{\varepsilon_d\ell[\mathrm{M}]_0} = \frac{(1 + 8\mathrm{K_D}[\mathrm{M}]_0)^{\frac{1}{2}} - 1}{(1 + 8\mathrm{K_D}[\mathrm{M}]_0)^{\frac{1}{2}} + 1}$$

Using the relationship if $\frac{a}{b} = \frac{c}{d}$ then $\frac{a+b}{a-b} = \frac{c+d}{c-d}$ is we can reduce to the following:

$$\frac{\varepsilon_d \ell [M]_0 + 2A_d}{\varepsilon_d \ell [M]_0 - 2A_d} = (1 + 8K_D[M]_0)^{\frac{1}{2}}$$

$$a = \varepsilon_d \ell [M]_0 \qquad b = 2A_d$$

$$c = (1 + 8K_D[M]_0)^{\frac{1}{2}} \qquad d = 1$$

Again using the relationship that if $\frac{a}{b} = \frac{c}{d}$ then $\frac{a-b}{b} = \frac{c-d}{d}$ we arrive at:

$$\frac{\varepsilon_d \ell A_d}{K_D} = (\varepsilon_d \ell [M]_0 - 2A_d)^2$$

We can then linearize the expression by taking the square roots of both sides and dividing by $[M]_0$ we get:

$$\frac{{\varepsilon_d}^{1/2} \ell^{1/2} {A_d}^{1/2}}{[M]_0 {K_D}^{1/2}} = \varepsilon_d \ell - \frac{2A_d}{[M]_0}$$

$$\frac{2A_d}{[M]_0} = \varepsilon_d \ell - \left(\frac{\varepsilon_d \ell}{K_D}\right)^{1/2} \left(\frac{A_d^{\frac{1}{2}}}{[M]_0}\right)$$

We now have two linear expressions for the determination of K_D from both the monomer band and the dimer band.

$$\frac{[M]_0}{A_m} = \left(\frac{2K_D}{{\varepsilon_m}^2 \ell^2}\right) A_m + \frac{1}{\varepsilon_m \ell}$$

$$\frac{2A_d}{[M]_0} = \varepsilon_d \ell - \left(\frac{\varepsilon_d \ell}{K_D}\right)^{1/2} \left(\frac{A_d^{\frac{1}{2}}}{[M]_0}\right)$$

Where now a plot of $\frac{[M]_0}{A_m}$ vs. A_m would yield a line with a slope $p = \left(\frac{2K_D}{{\varepsilon_m}^2 \ell^2}\right)$ and an intercept of $q = \frac{1}{\varepsilon_m \ell}$ where K_D can then be found by:

$$p = \frac{2K_D}{{\varepsilon_m}^2 \ell^2} \qquad q = \frac{1}{\varepsilon_m \ell}$$

$$K_D = \frac{p}{2q^2}$$

$$\varepsilon_m = \left(\frac{1}{q}\right)\left(\frac{1}{\ell}\right)$$

While a plot of $\frac{2A_d}{[M]_0}$ vs. $\frac{A_d{}^{\frac{1}{2}}}{[M]_0}$ would yield a line with a slope $p = -\left(\frac{\varepsilon_d \ell}{K_D}\right)^{1/2}$ and intercept $q = \varepsilon_m \ell$ where K_D could then be found by:

$$p = -\left(\frac{\varepsilon_d \ell}{K_D}\right)^{\frac{1}{2}} \qquad\qquad q = \varepsilon_m \ell$$

$$K_D = \frac{q}{p^2}$$

$$\varepsilon_m = \frac{q}{\ell}$$

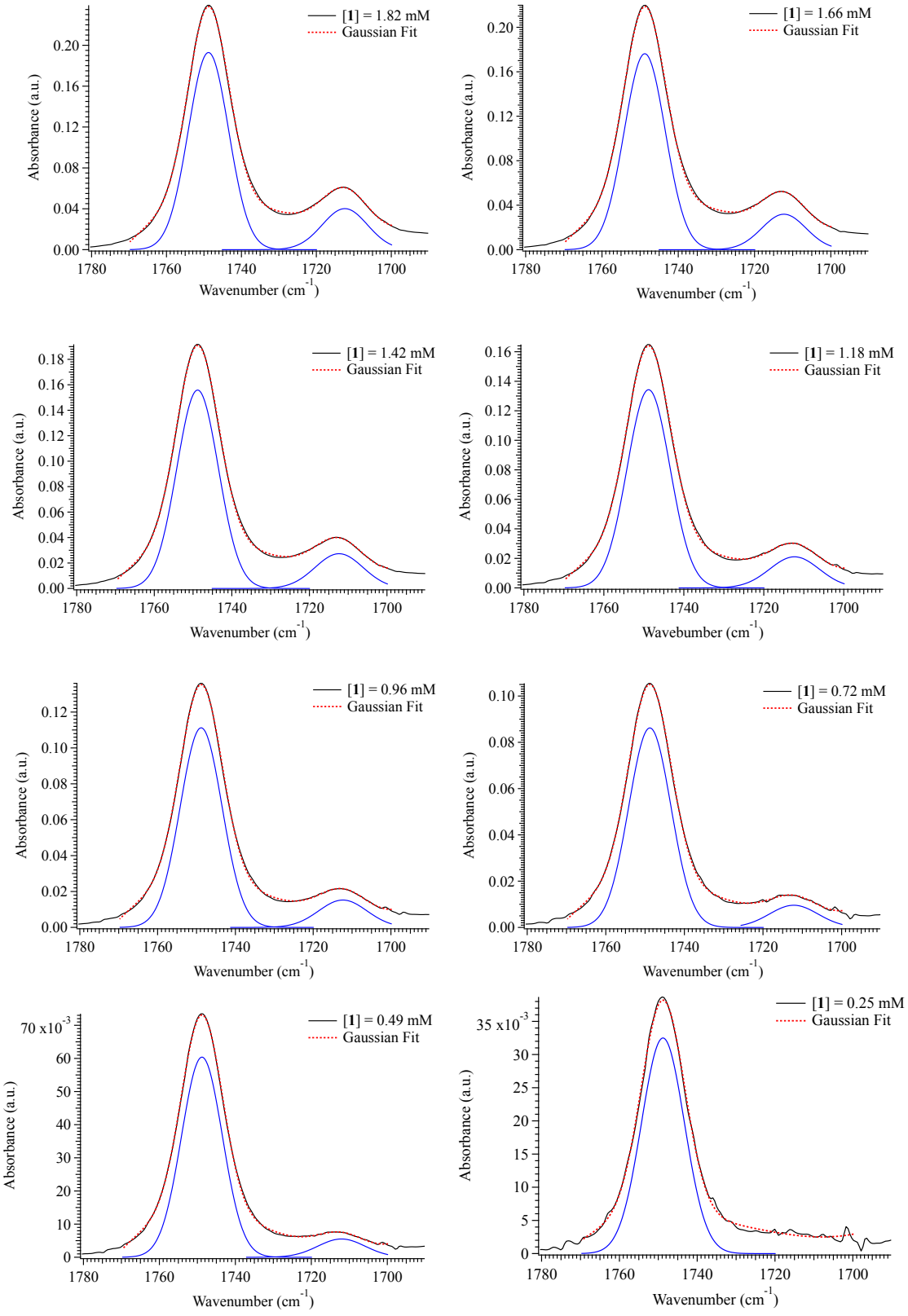

Figure 3.10. FTIR Gaussian fits of ν(*C*OOH) stretching region of **1** in DCM.

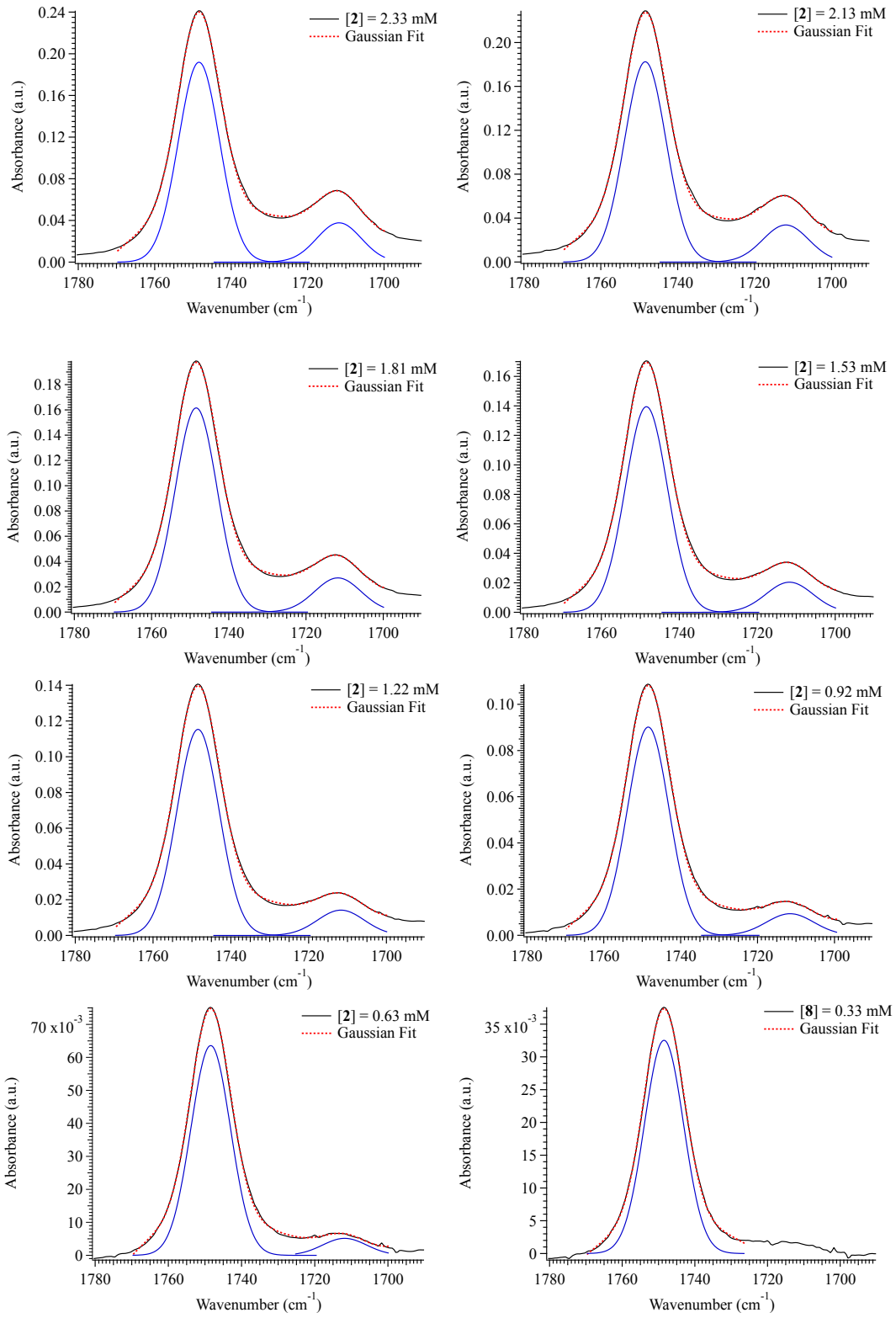

Figure 3.11. FTIR Gaussian fits of ν(*C*OOH) stretching region of **2** in DCM.

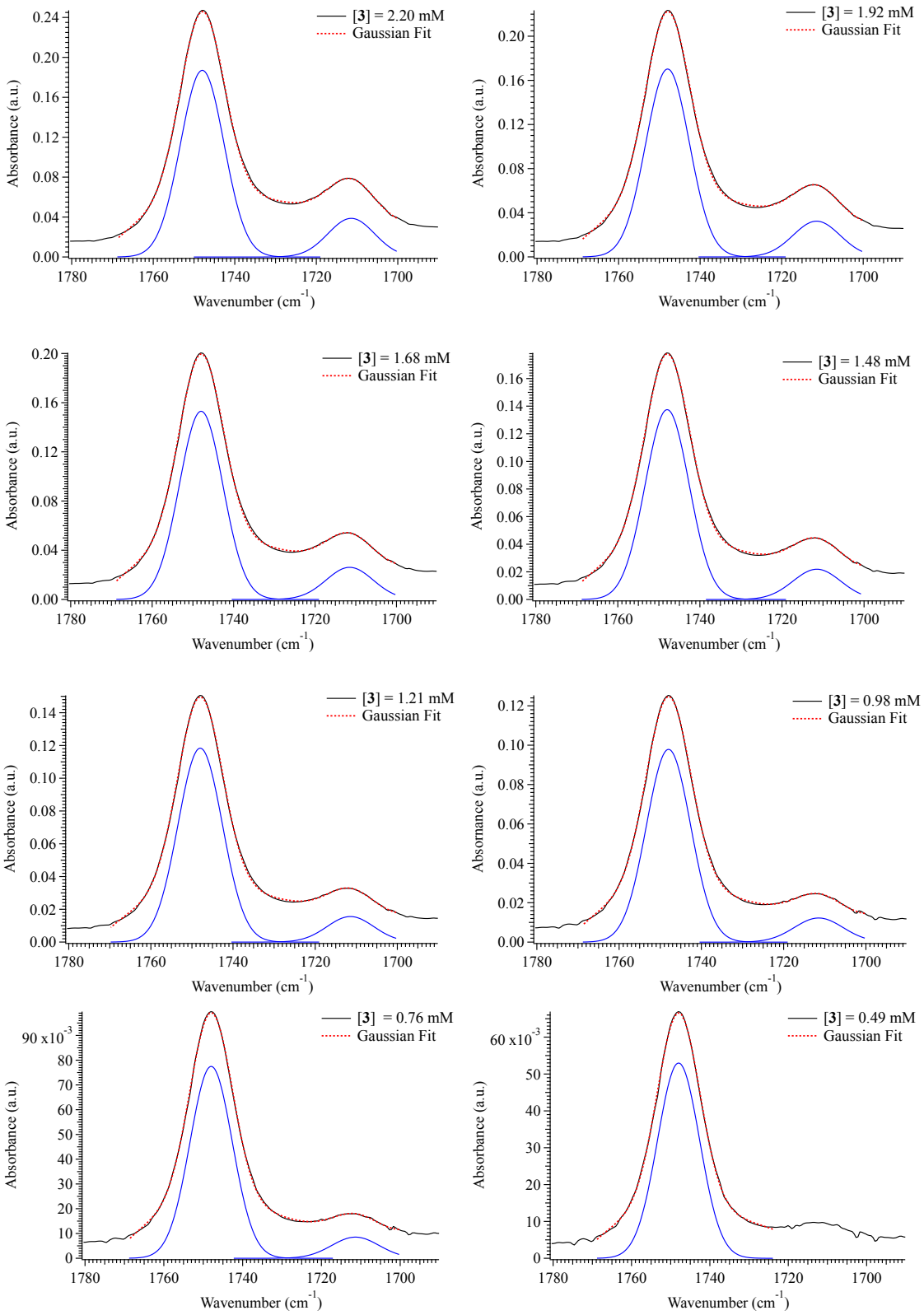

Figure 3.12. FTIR Gaussian fits of ν(*C*OOH) stretching region of **3** in DCM.

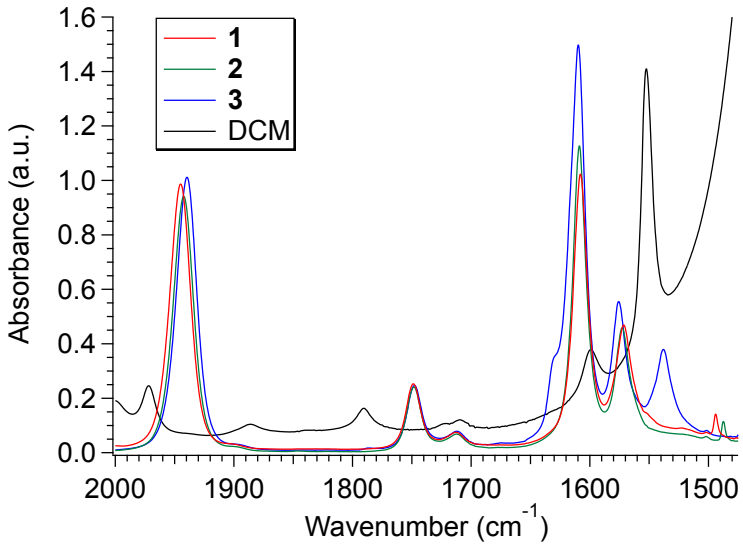

Figure 3.13. (top) FTIR spectrum of DCM at a path length of 2.0 mm. (bottom) Overlaid FTIR spectra of DCM and solvent subtracted 1–3, noting the overlapping absorbances in the vicinity of 1730–1700 cm^{-1}.

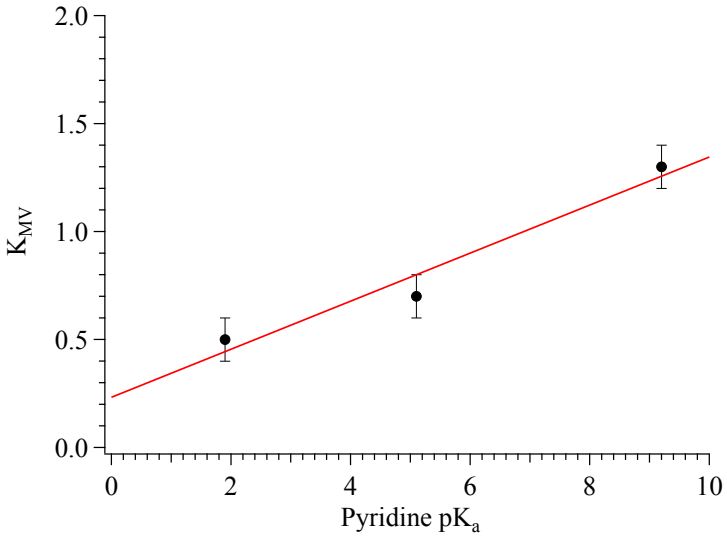

Figure 3.14. Plot of K_{MV} vs. pyridine pK_a.

Table 3.5. Integrated spectral areas and concentrations of the carboxylic acid ν(CO) band for **1**–**3** in DCM obtained from the Gaussian fits presented in Figure 3.10–Figure **3.12**. Note that the absorbance for the dimer band at 0.25 mM was not great enough to obtain an accurate fit and area.

Complex	**Concentration** (mM)	A_m	A_d
1	1.825 (0.009)	2.59 (0.02)	0.61 (0.03)
	1.664 (0.006)	2.38 (0.02)	0.53 (0.02)
	1.417 (0.004)	2.10 (0.02)	0.42 (0.02)
	1.179 (0.003)	1.81 (0.02)	0.33 (0.02)
	0.960 (0.003)	1.50 (0.01)	0.24 (0.02)
	0.717 (0.002)	1.16 (0.01)	0.15 (0.01)
	0.483 (0.007)	0.814 (0.007)	0.086 (0.009)
	0.250 (0.003)	0.450 (0.006)	----
2	2.28 (0.01)	2.59 (0.02)	0.55 (0.03)
	2.130 (0.008)	2.47 (0.02)	0.49 (0.03)
	1.82 (0.01)	2.19 (0.02)	0.41 (0.02)
	1.534 (0.005)	1.89 (0.02)	0.31 (0.02)
	1.239 (0.004)	1.57 (0.01)	0.21 (0.02)
	0.942 (0.002)	1.24 (0.01)	0.14 (0.01)
	0.650 (0.003)	0.862 (0.008)	0.08 (0.01)
	0.317 (0.001)	0.440 (0.004)	---
3	2.20 (0.01)	2.51 (0.02)	0.55 (0.03)
	1.92 (0.02)	2.28 (0.02)	0.47 (0.02)
	1.676 (0.007)	2.06 (0.02)	0.38 (0.02)
	1.479 (0.005)	1.85 (0.02)	0.32 (0.02)
	1.230 (0.004)	1.61 (0.01)	0.23 (0.02)
	0.979 (0.004)	1.32 (0.01)	0.18 (0.01)
	0.762 (0.003)	1.042 (0.009)	0.13 (0.01)
	0.492 (0.002)	0.713 (0.006)	---

3.6 References

1. Abrahams, J. P.; Leslie, A. G. W.; Lutter, R.; Walker, J. E., Structure at 2.8 A resolution of F1-ATPase from bovine heart mitochondria. *Nature* **1994,** *370* (6491), 621-628.
2. Iwata, S.; Ostermeier, C.; Ludwig, B.; Michel, H., Structure at 2.8 A resolution of cytochrome c oxidase from Paracoccus denitrificans. *Nature* **1995,** *376* (6542), 660-669.
3. Xia, D.; Yu, C.-A.; Kim, H.; Xia, J.-Z.; Kachurin, A. M.; Zhang, L.; Yu, L.; Deisenhofer, J., Crystal Structure of the Cytochrome bc1 Complex from Bovine Heart Mitochondria. *Science* **1997,** *277* (5322), 60.
4. Iwata, S.; Lee, J. W.; Okada, K.; Lee, J. K.; Iwata, M.; Rasmussen, B.; Link, T. A.; Ramaswamy, S.; Jap, B. K., Complete Structure of the 11-Subunit Bovine Mitochondrial Cytochrome bc1 Complex. *Science* **1998,** *281* (5373), 64.
5. Zhang, Z.; Huang, L.; Shulmeister, V. M.; Chi, Y.-I.; Kim, K. K.; Hung, L.-W.; Crofts, A. R.; Berry, E. A.; Kim, S.-H., Electron transfer by domain movement in cytochrome bc1. *Nature* **1998,** *392* (6677), 677-684.
6. Saraste, M., Oxidative Phosphorylation at the fin de siecle. *Science* **1999,** *283* (5407), 1488.
7. Gray, H. B.; Winkler, J. R., Electron tunneling through proteins. *Quarterly Reviews of Biophysics* **2003,** *36* (3), 341-372.
8. Gray, H. B.; Winkler, J. R., Long-range electron transfer. *Proceedings of the National Academy of Sciences of the United States of America* **2005,** *102* (10), 3534-3539.
9. Hinchliffe, P.; Sazanov, L. A., Organization of Iron-Sulfur Clusters in Respiratory Complex I. *Science* **2005,** *309* (5735), 771.
10. Sun, F.; Huo, X.; Zhai, Y.; Wang, A.; Xu, J.; Su, D.; Bartlam, M.; Rao, Z., Crystal Structure of Mitochondrial Respiratory Membrane Protein Complex II. *Cell* **2005,** *121* (7), 1043-1057.
11. Sazanov, L. A.; Hinchliffe, P., Structure of the Hydrophilic Domain of Respiratory Complex I from Thermus Thermophilus. *Science* **2006,** *311* (5766), 1430.
12. Shih, C.; Museth, A. K.; Abrahamsson, M.; Blanco-Rodriguez, A. M.; Di Bilio, A. J.; Sudhamsu, J.; Crane, B. R.; Ronayne, K. L.; Towrie, M.; Vlček, A.; Richards, J. H.; Winkler, J. R.; Gray, H. B., Tryptophan-Accelerated Electron Flow Through Proteins. *Science* **2008,** *320* (5884), 1760.
13. Gray, H. B.; Winkler, J. R., Electron flow through proteins. *Chemical Physics Letters* **2009,** *483* (1–3), 1-9.
14. Winkler, J. R.; Gray, H. B., Electron Flow through Metalloproteins. *Chemical Reviews* **2014,** *114* (7), 3369-3380.
15. Neel, A. J.; Hilton, M. J.; Sigman, M. S.; Toste, F. D., Exploiting Non-covalent pi Interactions for Catalyst Design. *Nature* **2017,** *543*, 637-646.
16. Zhang, X.; Jones, G. O.; Hedrick, J. L.; Waymouth, R. M., Fast and selective ring-opening polymerizations by alkoxides and thioureas. *Nat Chem* **2016,** *8* (11), 1047-1053.
17. Machan, C. W.; Chabolla, S. A.; Yin, J.; Gilson, M. K.; Tezcan, F. A.; Kubiak, C. P., Supramolecular Assembly Promotes the Electrocatalytic Reduction of Carbon Dioxide by Re(I) Bipyridine Catalysts at a Lower Overpotential. *Journal of the American Chemical Society* **2014,** *136* (41), 14598–14607.
18. Knowles, R. R.; Jacobsen, E. N., Attractive noncovalent interactions in asymmetric catalysis: links between enzymes and small molecule catalysts. *Proc Natl Acad Sci U S A* **2010,** *107* (48), 20678-85.

19. Rakowski DuBois, M.; DuBois, D. L., The roles of the first and second coordination spheres in the design of molecular catalysts for H2 production and oxidation. *Chem Soc Rev* **2009,** *38* (1), 62-72.

20. Casey, C. P.; Guan, H., Cyclopentadienone Iron Alcohol Complexes: Synthesis, Reactivity, and Implications for the Mechanism of Iron-Catalyzed Hydrogenation of Aldehydes. *Journal of the American Chemical Society* **2009,** *131* (7), 2499-2507.

21. Noyori, R.; Hashiguchi, S., Asymmetric Transfer Hydrogenation Catalyzed by Chiral Ruthenium Complexes. *Accounts of Chemical Research* **1997,** *30* (2), 97-102.

22. Hashiguchi, S.; Fujii, A.; Takehara, J.; Ikariya, T.; Noyori, R., Asymmetric Transfer Hydrogenation of Aromatic Ketones Catalyzed by Chiral Ruthenium(II) Complexes. *Journal of the American Chemical Society* **1995,** *117* (28), 7562-7563.

23. Weinberg, D. R.; Gagliardi, C. J.; Hull, J. F.; Murphy, C. F.; Kent, C. A.; Westlake, B. C.; Paul, A.; Ess, D. H.; McCafferty, D. G.; Meyer, T. J., Proton-Coupled Electron Transfer. *Chemical Reviews* **2012,** *112* (7), 4016–4093.

24. Trost, B. M.; Machacek, M. R.; Aponick, A., Predicting the Stereochemistry of Diphenylphosphino Benzoic Acid (DPPBA)-Based Palladium-Catalyzed Asymmetric Allylic Alkylation Reactions: A Working Model. *Accounts of Chemical Research* **2006,** *39* (10), 747-760.

25. Noyori, R.; Tokunaga, M.; Kitamura, M., Stereoselective Organic Synthesis via Dynamic Kinetic Resolution. *Bulletin of the Chemical Society of Japan* **1995,** *68* (1), 36-55.

26. Gentry, E. C.; Knowles, R. R., Synthetic Applications of Proton-Coupled Electron Transfer. *Accounts of Chemical Research* **2016,** *49* (8), 1546–1556.

27. Hammes-Schiffer, S., Proton-Coupled Electron Transfer: Moving Together and Charging Forward. *Journal of the American Chemical Society* **2015,** *137* (28), 8860–8871.

28. Bonin, J.; Costentin, C.; Robert, M.; Savéant, J.-M.; Tard, C., Hydrogen-Bond Relays in Concerted Proton–Electron Transfers. *Accounts of Chemical Research* **2012,** *45* (3), 372–381.

29. Tadokoro, M.; Inoue, T.; Tamaki, S.; Fujii, K.; Isogai, K.; Nakazawa, H.; Takeda, S.; Isobe, K.; Koga, N.; Ichimura, A.; Nakasuji, K., Mixed-Valence States Stabilized by Proton Transfer in a Hydrogen-Bonded Biimidazolate Rhenium Dimer. *Angewandte Chemie International Edition* **2007,** *46* (31), 5938–5942.

30. Meyer, T. J.; Huynh, M. H. V.; Thorp, H. H., The Possible Role of Proton-Coupled Electron Transfer (PCET) in Water Oxidation by Photosystem II. *Angewandte Chemie International Edition* **2007,** *46* (28), 5284–5304.

31. Huynh, M. H. V.; Meyer, T. J., Proton-Coupled Electron Transfer. *Chemical Reviews* **2007,** *107* (11), 5004–5064.

32. Ward, M. D., Photo-Induced Electron and Energy Transfer in Non-Covalently Bonded Supramolecular Assemblies. *Chemical Society Reviews* **1997,** *26* (5), 365–375.

33. Meyer, T. J., Chemical Approaches to Artificial Photosynthesis. *Accounts of Chemical Research* **1989,** *22* (5), 163–170.

34. Jin, L.; Matsuda, Y.; Uemura, K.; Ebihara, M., Mixed Valency in Quadruple Hydrogen-Bonded Dimers of Bis(biimidazolate)dirhodium Complexes. *Inorganic Chemistry* **2015,** *54* (5), 2331–2338.

35. Wilkinson, L. A.; McNeill, L.; Meijer, A. J. H. M.; Patmore, N. J., Mixed Valency in Hydrogen Bonded 'Dimers of Dimers'. *Journal of the American Chemical Society* **2013,** *135* (5), 1723–1726.

36. Pichlmaier, M.; Winter, R. F.; Zabel, M.; Záliš, S., Electron Transfer Across Multiple Hydrogen Bonds: The Case of Ureapyrimidinedione-Substituted Vinyl Ruthenium and Osmium Complexes. *Journal of the American Chemical Society* **2009,** *131* (13), 4892–4903.

37. Sun, H.; Steeb, J.; Kaifer, A. E., Efficient Electronic Communication between Two Identical Ferrocene Centers in a Hydrogen-Bonded Dimer. *Journal of the American Chemical Society* **2006,** *128* (9), 2820–2821.

38. Canzi, G.; Goeltz, J. C.; Henderson, J. S.; Park, R. E.; Maruggi, C.; Kubiak, C. P., On the Observation of Intervalence Charge Transfer Bands in Hydrogen-Bonded Mixed-Valence Complexes. *Journal of the American Chemical Society* **2014,** *136* (5), 1710–1713.

39. Goeltz, J. C.; Kubiak, C. P., Mixed Valency across Hydrogen Bonds. *Journal of the American Chemical Society* **2010,** *132* (49), 17390–17392.

40. Andujar-Sanchez, M.; Cámara-Artigas, A.; Jara-Perez, V., Thermodynamic Study of the Dimerization of 8-Anilino-1-Naphthalenesulfonic Acid by Isothermal Titration Calorimetry. *The Journal of Chemical Thermodynamics* **2010,** *42* (3), 337-341.

41. Lafitte, V. G. H.; Aliev, A. E.; Horton, P. N.; Hursthouse, M. B.; Bala, K.; Golding, P.; Hailes, H. C., Quadruply Hydrogen Bonded Cytosine Modules for Supramolecular Applications. *Journal of the American Chemical Society* **2006,** *128* (20), 6544–6545.

42. Kao, D.-Y.; Shu, W.-T.; Chen, J.-S., A Consistent Determination of the Dimerization Constants of the Self-Association of 2,2-Dimethyl-3-ethyl-3-pentanol in Carbon Tetrachloride from its Infrared Spectral Data. *Journal of the Chinese Chemical Society* **2005,** *52* (6), 1171–1178.

43. Satchell, D. P. N.; Wardell, J. L., Dimerization of Carboxylic Acids in o-Dichlorobenzene. *Transactions of the Faraday Society* **1965,** *61* (0), 1199–1201.

44. Harris, J. T.; Hobbs, M. E., A Study of the Association of Some Organic Acids by Infrared Absorption Measurements. *Journal of the American Chemical Society* **1954,** *76* (5), 1419–1422.

45. Porter, T. M.; Canzi, G. C.; Chabolla, S. A.; Kubiak, C. P., Tuning Electron Delocalization and Transfer Rates in Mixed-Valent Ru3O Complexes through “Push–Pull” Effects. *The Journal of Physical Chemistry A* **2016,** *120* (32), 6309–6316.

46. Kubiak, C. P., Inorganic Electron Transfer: Sharpening a Fuzzy Border in Mixed Valency and Extending Mixed Valency across Supramolecular Systems. *Inorganic Chemistry* **2013,** *52* (10), 5663–5676.

47. Glover, S. D.; Kubiak, C. P., Persistence of the three-state description of mixed valency at the localized-to-delocalized transition. *J Am Chem Soc* **2011,** *133* (22), 8721-8731.

48. Goeltz, J. C.; Benson, E. E.; Kubiak, C. P., Electronic Structural Effects in Self-Exchange Reactions. *The Journal of Physical Chemistry B* **2010,** *114* (45), 14729–14734.

49. Goeltz, J. C.; Hanson, C. J.; Kubiak, C. P., Rates of Electron Self-Exchange Reactions between Oxo-Centered Ruthenium Clusters Are Determined by Orbital Overlap. *Inorganic Chemistry* **2009,** *48* (11), 4763-4767.

50. Salsman, J. C.; Ronco, S.; Londergan, C. H.; Kubiak, C. P., Tuning the Electronic Communication and Rates of Intramolecular Electron Transfer of Dimers of Trinuclear Ruthenium Clusters: Bridging and Ancillary Ligand Effects. *Inorganic Chemistry* **2006,** *45* (2), 547–554.

51. Huyskens, P. L.; Luck, W. A. P.; Zeegers-Huyskens, T., *Intermolecular Forces An Introduction to Modern Methods and Results*. Springer-Verlag Berlin: Heidelberg, 1991.

52. Richardson, D. E.; Taube, H., Mixed-Valence Molecules: Electronic Delocalization and Stabilization. *Coordination Chemistry Reviews* **1984,** *60*, 107–129.

Chapter 4

Stable Mixed-Valent Complexes Formed by Electron Delocalization Across Hydrogen Bonds of Pyrimidinone-Linked Metal Clusters.

4.1 Introduction

We recently reported a methodology to compare the strengths of hydrogen bonds in mixed-valent, hydrogen-bonded complexes both in the presence and absence of electron exchange.[1] By employing hydrogen bonds of isonicotinic acid to link the two Ru_3O redox centers, we found that stabilities of the mixed-valent state were significantly greater than those of the two isovalent states.[1] Determination of the formation constants for the hydrogen bonds in all of the redox states directly showed that electron exchange *across* the hydrogen bond imparts about

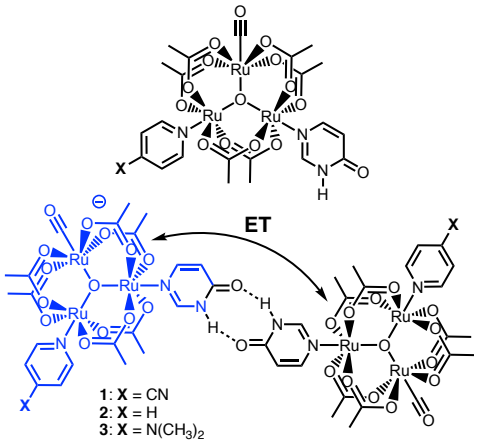

Figure 4.1. Structure of the free monomers (top) and the hydrogen bonded dimers (bottom) when **X** = CN (4-cyanopyridine, cpy, **1**), H (pyridine, py, **2**) or $N(CH_3)_2$ (4-dimethylaminopyridine, dmap, **3**).

3–5 kcal mol^{-1} of stability to hydrogen bonding relative to the hydrogen bonds formed in the isovalent states. Applying a similar methodology herein, we report on the observation of a hydrogen-bonded, mixed-valent dimer of oxocentered triruthenium clusters, bridged by hydrogen bonds of the pyrimidinone, 4(3H)-pyrimidinone (Figure 4.1).

4.2Results and Discussion

Complexes **1**–**3** were synthesized by treatment of $Ru_3O(OAc)_6(CO)(L_1)(MeOH)$ (where L_1 = 4-cyanopyridine (cpy), pyridine (py), or 4-dimethylaminopyridine (dmap)) with a stoichiometric amount of 4(3H)-pyrimidinone in a 2:1 solution of DCM:MeOH. For all three complexes, investigation of the mechanism of ground state electron transfer (ET) proceeded by measurement of the cyclic voltammogram (CV). Using a single compartment electrochemical cell consisting of a glassy carbon working electrode, a platinum auxiliary electrode, and an Ag/AgCl reference electrode, the CV of **1**–**3** was recorded in a solution of DCM with 0.1 M of tetrabutylammonium hexafluorophosphate ($TBAPF_6$) as the supporting electrolyte (Figure 4.2). At oxidative potentials, the usual two, reversible, single-electron oxidations are observed that correspond to the monomeric $Ru_3O^{III,III,III/II,III,III}$ ($E_{1/2}$ (V): **1**: 0.13, **2**: 0.09, **3**: 0.05 vs $Fc^{+/0}$) and $Ru_3O^{IV,III,III/III,III,III}$ ($E_{1/2}$ (V): **1**: 0.91, **2**: 0.88, **3**: 0.79 vs $Fc^{+/0}$) redox couples.[2] Upon sweeping to reducing potentials however,

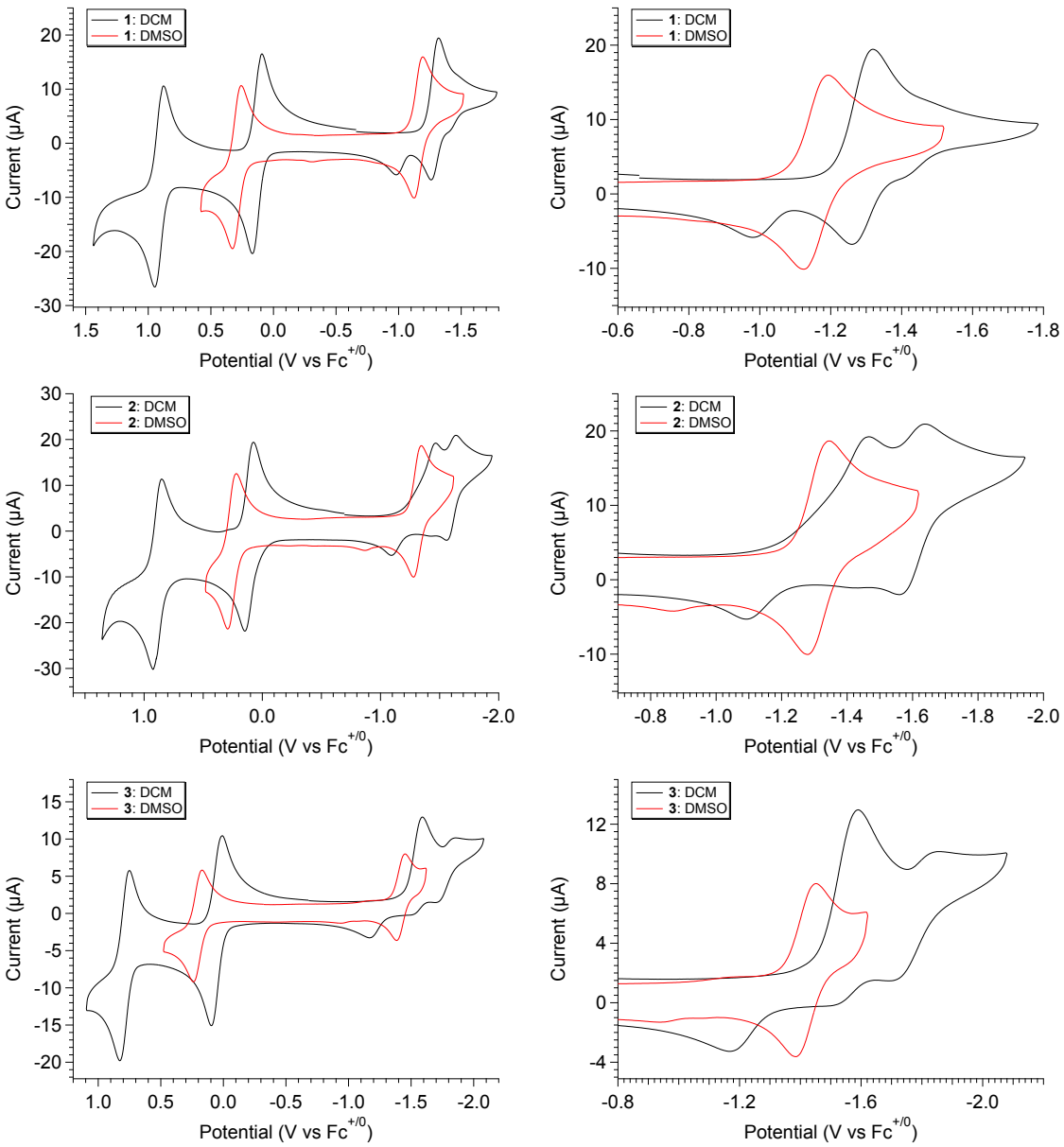

Figure 4.2. Cyclic voltammograms of **1**–**3** in DCM (black) and DMSO (red) at 23 °C. CVs were recorded at 100 mV/s with analyte concentrations of *ca.* 2.0 mM and referenced to the $Fc^{+/0}$ redox couple using an internal standard of ferrocene.

all three clusters display one, quasi-reversible response ($E_{1/2}$ (V): **1**: –1.29, **2**: –1.45, **3**: –1.56 vs $Fc^{+/0}$) one reversible response ($E_{1/2}$ (V): **1**: –1.44, **2**: –1.65, **3**: –1.79 vs $Fc^{+/0}$) respectively, and one irreversible, oxidative response (E_a (V): **1**: –0.98, **2**: –1.08, **3**: –1.17 vs $Fc^{+/0}$) on the return sweep. Furthermore, differential pulse voltammetry (DPV) confirms that all redox features are single-electron processes, and the electrochemical behavior was additionally observed to be both

scan rate and solvent dependent. As the scan rate is increased, the second reduction ($E_{1/2}$ (V): **1**: –1.44, **2**: –1.65, **3**: –1.79 vs $Fc^{+/0}$) and irreversible re-oxidation (E_a (V): **1**: –0.98, **2**: –1.08, **3**: –1.17 vs $Fc^{+/0}$) are both observed to nearly vanish, while the first reduction ($E_{1/2}$ (V): **1**: –1.29, **2**: –1.45, **3**: –1.56 vs $Fc^{+/0}$) gains considerable reversibility (See appendix 4.5, Figure 4.9). Upon dissolution of **1**–**3** into dimethyl sulfoxide (DMSO), a solvent known to interrupt hydrogen bonds, only a single reversible response is observed (Figure 4.2, $E_{1/2}$ (V): **1**: –1.16, **2**: –1.31, **3**: –1.42 vs $Fc^{+/0}$). These results are consistent with the formation of hydrogen-bonded mixed valent dimers in DCM but not DMSO.

The electrochemical behavior for complexes **1**–**3** is be best described as following an ECE mechanism, where after a one electron reduction (E), a chemical step occurs (C, self-dimerization) which is then followed by a second reduction (E, see appendix 4.5, Figure 4.10). In the CVs of **1**–**3**, the first quasi-reversible reduction ($E_{1/2}$ (V): **1**: –1.29, **2**: –1.45, **3**: –1.56 vs $Fc^{+/0}$) corresponds to reduction of neutral monomers (**1**, **2**, **3**) to form anionic monomers ($(\mathbf{1})^-$, $(\mathbf{2})^-$, $(\mathbf{3})^-$). The anionic monomers then rapidly dimerize with neutral monomers in the diffusion layer forming mixed-valent, hydrogen bonded dimers ($(\mathbf{1}_2)^-$, $(\mathbf{2}_2)^-$, $(\mathbf{3}_2)^-$). At the second, reversible reduction ($E_{1/2}$ (V): **1**: –1.44, **2**: –1.65, **3**: –1.79 vs $Fc^{+/0}$) the mixed-valent, hydrogen bonded dimers are reduced by a second electron forming the isovalent, dianionic, hydrogen-bonded state ($(\mathbf{1}_2)^{2-}$, $(\mathbf{2}_2)^{2-}$, $(\mathbf{3}_2)^{2-}$). Upon reversal of the scan direction, the first oxidative feature ($E_{1/2}$ (V): **1**: –1.44, **2**: –1.65, **3**: –1.79 vs $Fc^{+/0}$) corresponds to *re-oxidation* of the isovalent, dianionic, hydrogen-bonded state to form the mixed-valent, hydrogen bonded dimers ($(\mathbf{1}_2)^-$, $(\mathbf{2}_2)^-$, $(\mathbf{3}_2)^-$). Due to electron exchange occurring *across* the hydrogen bonds, this state is sufficiently stable to persist until is subsequent re-oxidation (E_a (V): **1**: –0.98, **2**: –1.08, **3**: –1.17 vs $Fc^{+/0}$) whereby neutral dimers ($\mathbf{1}_2$, $\mathbf{2}_2$, $\mathbf{3}_2$) are formed, which then rapidly dissociate into neutral monomers.

The stability of the mixed valent state is expressed by the comproportionation constant (equation 4.1):

$$K_C = e^{\frac{nF\Delta E}{RT}} \quad (4.1)$$

Here, one needs only to know the difference between the potentials relating the two isovalent states to the mixed-valent state. For complexes **1**–**3**, this is taken as the difference between the two oxidative features observed on the return sweep ($\Delta E_{1/2}$ (V): **1**: 410 mV, **2**: 470 mV, **3**: 530 mV vs. $Fc^{+/0}$), where splittings correspond to comporportionation constants on the order of 10^7 (K_C (10^7): **1**: 0.86, **2**: 8.9, **3**: 92 vs. $Fc^{+/0}$). These splittings are on average 90 mV larger than those observed for their isonicotinic counterparts (Figure 4.1, **4**–**6**), described in previous studies ($\Delta\Delta E = \Delta E_{pyrim} - \Delta E_{ina}$: **1**: 53 mV, **2**: 85 mV, **3**: 135 mV),[1, 3-4] and indicate the formation of highly stable mixed valence anions with respect to the two isovalent states.

These observations are further supported by determination of the formation constants for the relevant redox states. In general, any mixed-valent hydrogen-bonded system can be described by a series of four dimerization equilibria (Figure 4.3). K_D and K_{2-} are the equilibrium constants for the two isovalent states, which describe the self-dimerization of the neutral and one-electron reduced clusters respectively. K_C is the comproportionation constant and K_{MV} is the equilibrium dimerization constant of the mixed-valent state.[1] In the presented systems, these terms describe the thermodynamics of formation and the relative degree of stability gained from charge transfer *across* a hydrogen bond.

Applying these ideas with complex **2** and using the 1:1 dimerization model described previously in Chapter 3, we find that **2** exists primarily as monomers in solution with a dimerization constant of $K_D = 360\ M^{-1}$ in the isovalent neutral state (Figure 4.4). While studies for complexes **1** and **3** are underway, owing to their similar chemical nature, complexes **1** and **3** are expected to have dimerization constants of similar magnitudes. The equilibrium constant of the doubly

$$M + M \rightleftharpoons M_2 \quad K_D$$
$$M + (M)^- \rightleftharpoons (M_2)^- \quad K_{MV}$$
$$(M)^- + (M)^- \rightleftharpoons (M_2)^{2-} \quad K_{2-}$$
$$M_2 + (M_2)^{2-} \rightleftharpoons 2\,(M_2)^- \quad K_C$$

Figure 4.3. Dimerization equilibria of a mixed-valent hydrogen-bonded system in solution.

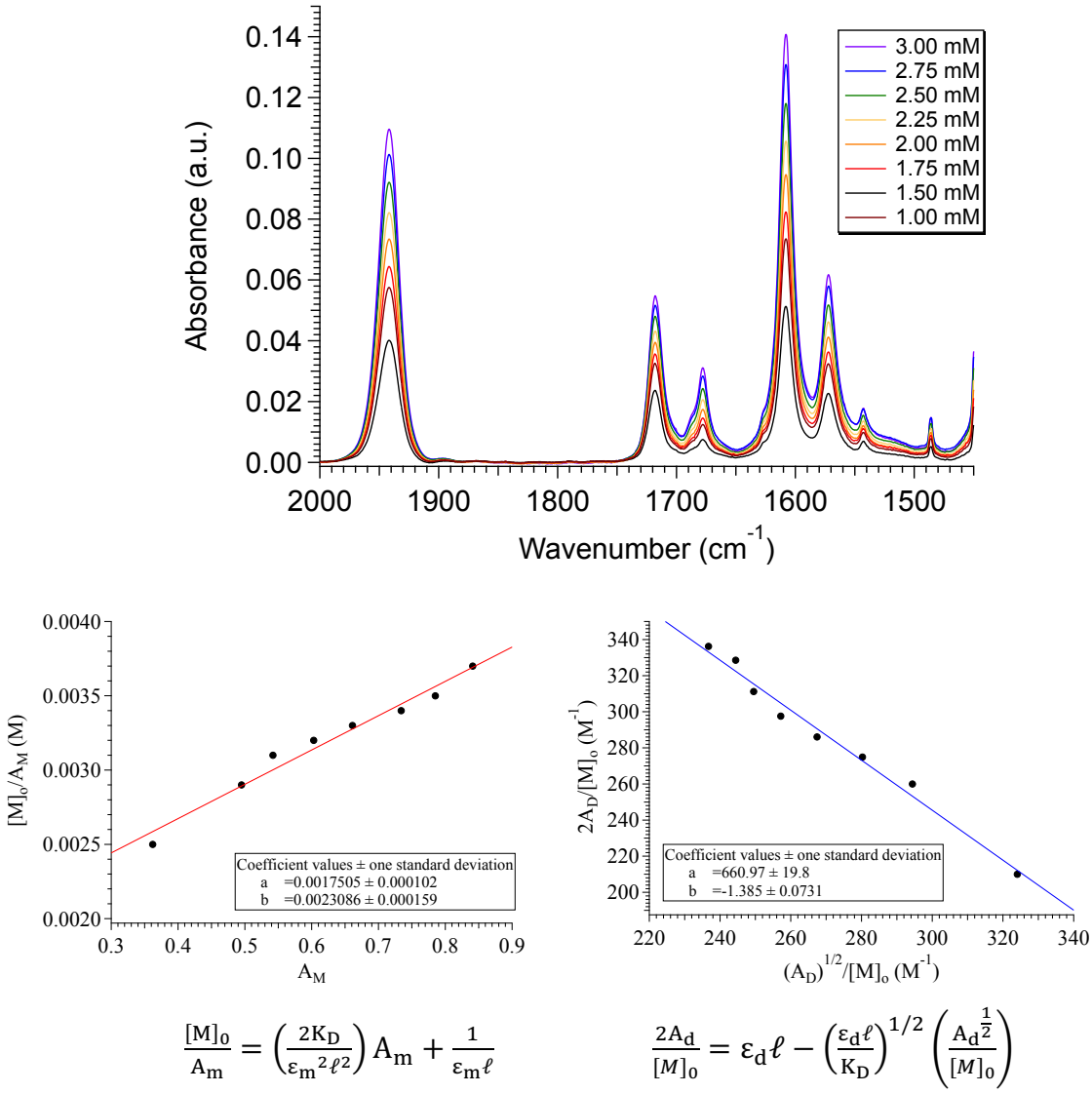

$$\frac{[M]_0}{A_m} = \left(\frac{2K_D}{\varepsilon_m{}^2\ell^2}\right) A_m + \frac{1}{\varepsilon_m \ell} \qquad \frac{2A_d}{[M]_0} = \varepsilon_d \ell - \left(\frac{\varepsilon_d \ell}{K_D}\right)^{1/2} \left(\frac{A_d{}^{\frac{1}{2}}}{[M]_0}\right)$$

Figure 4.4. (top) FTIR dilution spectra of **2** in DCM at 23 °C used in determination of the neutral dimerization constant K_D. (bottom) Linear regressions of the integrated spectral areas of the monomer (left) and dimer (right) bands using the aforementioned 1:1dimerization model. Spectral deconvolutions and areas are shown in appendix 4.5 as Figure 4.11 and Table 4.3.

Table 4.1. Equilibrium dimerization constants for complexes **1**–**6** in DCM at 25 °C.

Complex	K_D (M^{-1})	K_{2-} (M^{-1})	K_C (10^6)	K_{MV} (10^6 M^{-1})	$\Delta\Delta G°_D$ (kcal/mol)[a]	$\Delta\Delta G°_{2-}$(kcal/mol)[b]
1	360[c]	1000[c]	8.59	1.8	–5.03	–4.4
2	360	1000[c]	88.8	5.7	–5.7	–5.1
3	360[c]	1000[c]	919	18.2	–6.41	–5.81
4	119	2000	1.09	0.5	–4.95	–3.3
5	75	2200	3.2	0.7	–5.4	–3.4
6	130	2500	4.8	1.2	–5.43	–3.68

[a]$\Delta\Delta G°_D = \Delta G°_{MV} - \Delta G°_D$
[b]$\Delta\Delta G°_{2-} = \Delta G°_{MV} - \Delta G°_{2-}$
[c]Estimated values were used.

reduced states (K_{2-}) for **1**–**3** however is much more difficult to determine but it can be estimated from the electrochemical experiments. The observation of a small return oxidation in both the CVs and DPVs (Figure 4.2, $E_{1/2}$ (V): **1**: –1.29, **2**: –1.45, **3**: –1.56 vs $Fc^{+/0}$) corresponding to the re-oxidation of anionic monomers, $(\mathbf{1})^-$, $(\mathbf{2})^-$, and $(\mathbf{3})^-$, suggests that the doubly reduced state is weakly hydrogen-bonded and a small amount dissociates into reduced monomers upon formation. However, the fact that an appreciable amount of dimer is observed in the DPV (Figure 4.9) suggests that a majority of the complex is still dimerized. By comparison with the isonicotinic acid systems,[1] where monomer reoxidation was not observed and K_{2-} was calculated to be near 2200 M^{-1} we estimate K_{2-} to be on the order of 1000 M^{-1} for $(\mathbf{1}_2)^{2-}$–$(\mathbf{3}_2)^{2-}$.

With the relevant formation constants known, K_{MV} can then be determined through equation 4.2:

$$K_{MV} = (K_D\, K_{2-}\, K_C) \qquad (4.2)$$

For complex **2**, where K_D is explicitly known, K_{MV} is found to be four orders of magnitude larger than K_D and three orders of magnitude larger than K_{2-} with a value near 6 x 10^6 M^{-1}. Assuming complexes **1** and **3** have a similar magnitude for K_D as complex **2**, estimations place K_{MV} to be on a similar order of magnitude near 2 x 10^6 M^{-1} and 18 x 10^6 M^{-1} for **1** and **3** respectively (Table 4.1). Here, these results suggest that on average the hydrogen-bonded mixed-valent state is 5.7

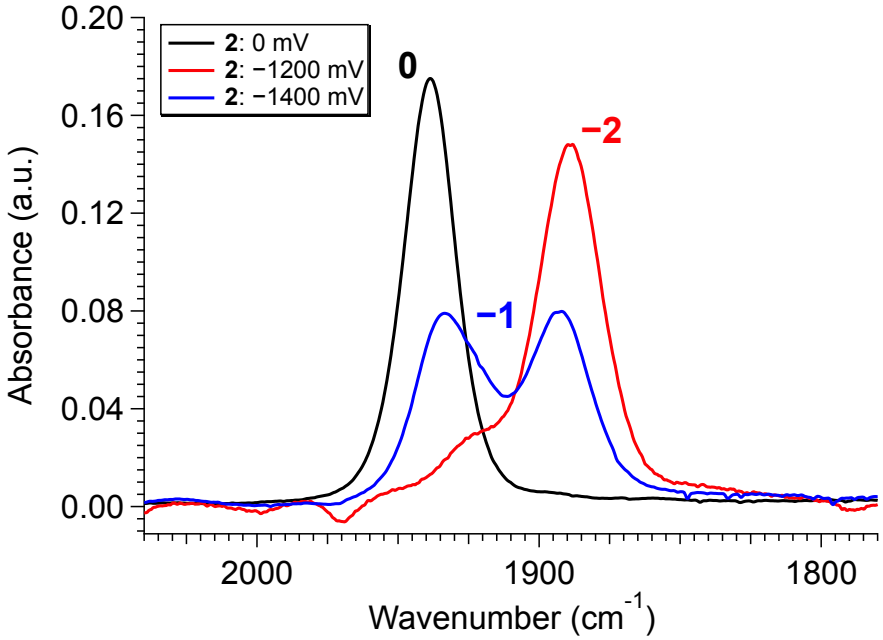

Figure 4.5. Infrared spectroelectrochemical (IRSEC) spectra of the ν(CO) region for **2** in DCM at each oxidation state. The neutral isovalent state, (**2**) is shown in black, the hydrogen-bonded mixed-valent state, $(\mathbf{2}_2)^-$ is shown in red, and the doubly-reduced isovalent state, $(\mathbf{2}_2)^{2-}$ is shown in red. Note the, significantly broadened, partially coalesced ν(CO) bands in the hydrogen-bonded mixed-valent state (blue).

kcal mol^{-1} (1994 cm^{-1}) and 5.1 kcal mol^{-1} (1784 cm^{-1}) more stable than the isovalent neutral and doubly reduced dimers respectively. These findings suggest that complexes **1**–**3** have a strongly delocalized electronic structure in their mixed-valent state that extends from the Ru_3O redox centers, through the π system of the pyrimidinone ligand, and ultimately, *across* their hydrogen bonds.

Perhaps the most remarkable aspect of the pyrimidinone systems however, is that complex **2** exhibits significantly broadened, partially coalesced ν(CO) bands in its hydrogen-bonded mixed-valent state (Figure 4.5). This behavior has not been previously observed in a hydrogen-bonded mixed-valent complex before and allows estimation of the rate of ET by application of an optical Bloch equation line shape analysis, a well-documented procedure for the covalently bridged pyrazine clusters extensively studied by our lab.[2, 5-6] Simulation of the FTIR line shape proceeded through the use of the MATLAB program Zoerbex developed by the Harris

Table 4.2. Summary of values used for the Zoerbex input.

Peak Center (cm^{-1})	1885	1930
Lorentzian Width (cm^{-1})	13	7
Gaussian Width (cm^{-1})	15	18
Population	1.29	1

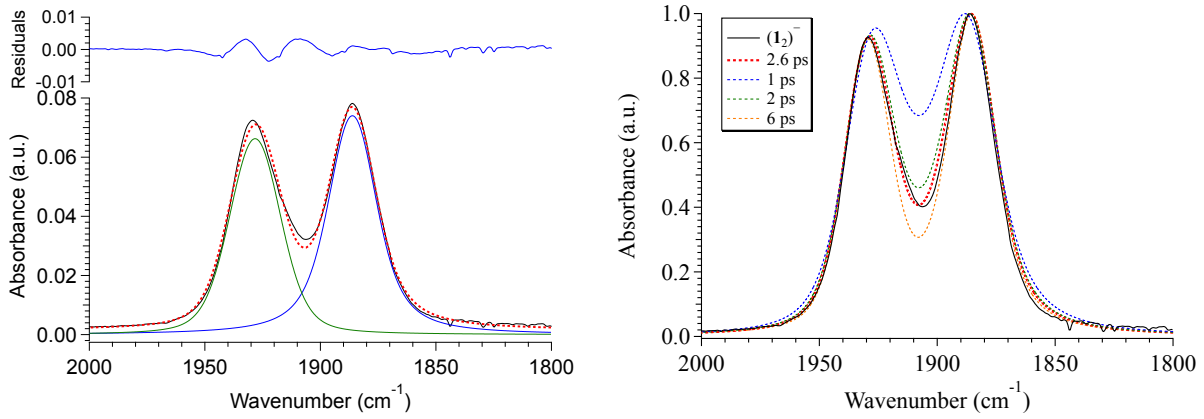

Figure 4.6. (left) Spectral deconvolution of **2** using two Voigt functions centered about 1985 and 1930 cm^{-1}. (right) Comparison of the experimental FTIR (black trace) to the simulated FTIR at different exchange time constants (τ, dashed traces). The best agreement is found when the time constant is equal to 2.6 ps.

t lab.[7] The dynamic FTIR line shapes in the program are simulated using the optical Bloch formalism where two species exchange 100% of their intensity with a rate of k_{ex}. The program simulates vibrational spectra by Fourier transformation of the vibrational time correlation function into the frequency domain. Simulated FTIR spectra are represented as Voigt line shapes where the center peak frequencies, the Gaussian and Lorentzian FWHM, populations of each exchanging species, and their exchange time constant are taken as inputs.

To best determine the input parameters, the IRSEC spectra was fit to two well resolved Voigt functions (Figure 4.6) whose parameters were then taken as the input for the Zoerbex program (Table 4.2). The exchange time constant, τ, was manipulated until simulated spectra were in good agreement with experiment (Figure 4.6). The best agreement between experiment and theory was found when the exchange time constant was set to 2.6 ps, giving a rate of electron transfer (k_{et}) near 3.8×10^{11} s^{-1}. These estimates are in excellent agreement with those of similar

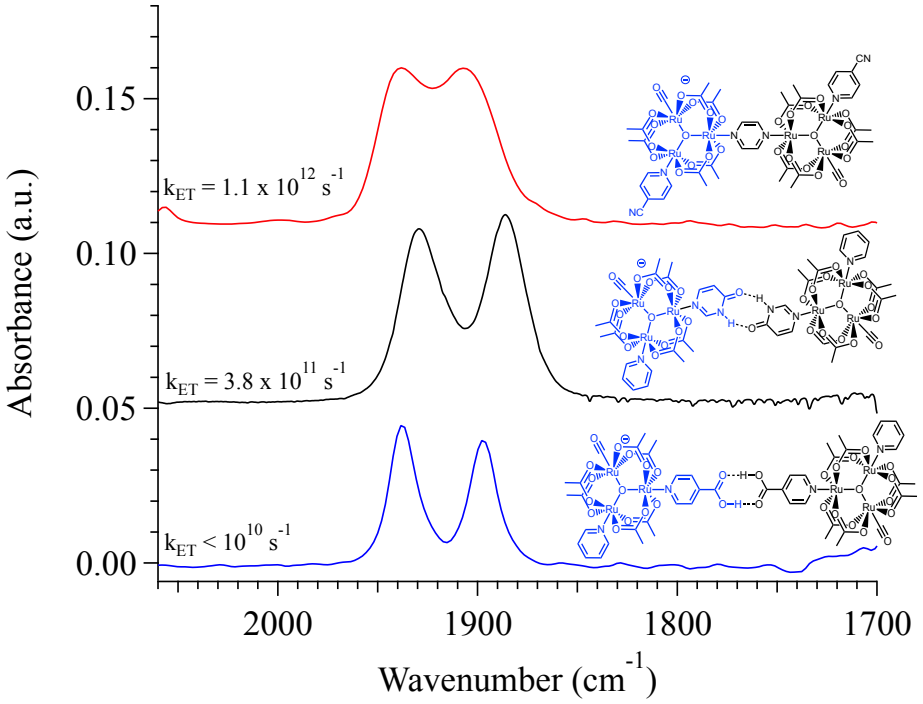

Figure 4.7. Infrared spectroelectrochemical (IRSEC) spectra of **1** (black, 4.85 mM) when the potential is fixed at –1200 mV. Also shown for comparison is the IRSEC of the corresponding isonicotinic acid bridged clusters (blue) and the covalently linked pyrazine bridged clusters (red).

Ru_3O systems where the predicted rate of ET in **1** lies between the moreweakly coupled isonicotinic acid systems and the more highly coupled pyrazine bridged systems (Figure 4.7). It is important to note, that the application of such an analysis has been heavily debated in the literature,[8-11] as many processes in addition to chemical exchange such as inhomogeneous broadening, solvent environment fluctuation and other dynamic processes can contribute to the overall FTIR lineshape. Until these systems can be the subjects of higher order spectroscopic analysis, and in view of the well documented nature of ultrafast ET in similar mixed-valent Ru_3O systems,[2, 5-6] the methods here provide a reasonable first estimate of k_{ET}.

The highly delocalized electronic structure of these hydrogen-bonded mixed valent complexes is also partly revealed by the observation of an enormous intensity enhancement of the pyrimidinone amide ν(NH) band (3350 cm^{-1}) in the IR spectrum of the mixed-valent, hydrogen bonded state, which is absent in the neutral and doubly reduced states (Figure 4.8). Based on

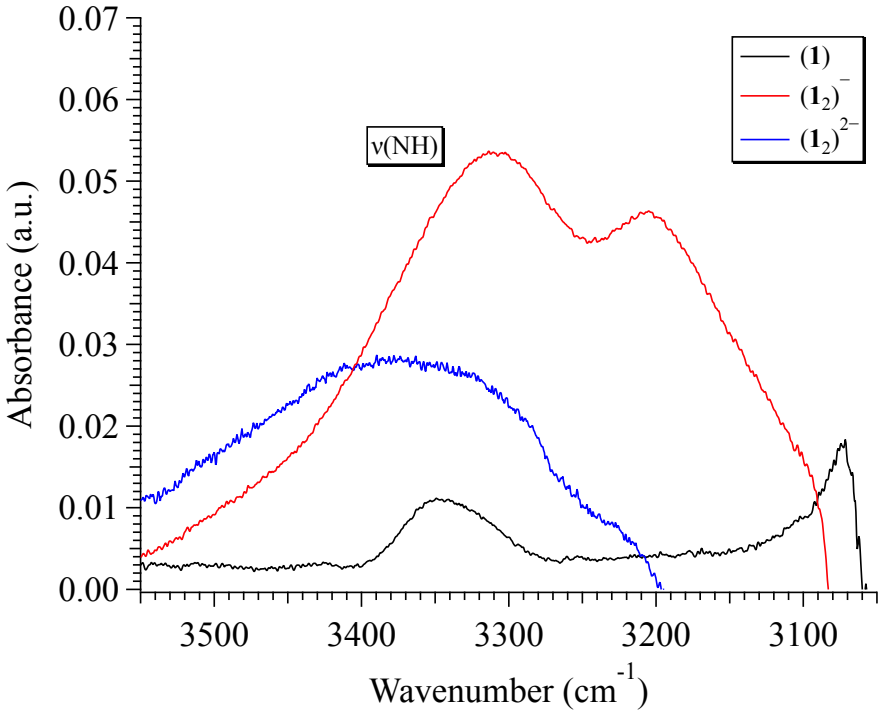

Figure 4.8. IRSEC spectra of **1** (4.85 mM), highlighting the enormous intensity enhancement of the ν(NH) band in the hydrogen-bonded, mixed valent state (red) in comparison to the isovalent neutral (black) and doubly-reduced (blue) states.

previous studies of the pyrazine (pz) bridged dimers of trimers (Ru_3O-pz-Ru_3O)[2, 12-14], this is a signature of strong vibronic coupling of the pyrimidinone amide ν(NH) mode with the Ru_3O electronic wavefunctions in the mixed-valent state. These results suggest that the ν(NH) mode may be an important promoter mode for ET.[15-17]

4.3 Conclusion

Together these findings demonstrate the presence of strong donor-bridge-acceptor coupling across hydrogen bonds, and that highly delocalized electronic structures can be attained in non-covalent assemblies that are often considered to be too weak to support strong electronic communication. A study is forthcoming detailing the nature of electronic and vibronic coupling in these systems through variation of the cluster electronics by ancillary ligand substitution and consideration of kinetic isotope effects.

4.4 Experimental

Preparation and Purification:

The 4-(3H)pyrimidinone (pyrim), ferrocene, and anhydrous dimethyl sulfoxide (DMSO) was purchased from Sigma-Aldrich. The 4-(3H)pyrimidinone was used as received, ferrocene was sublimed prior to use, and DMSO was sparged with argon for 10 minutes and stored over 4 Å molecular seives. The HPLC grade dichloromethane (DCM) and tetrahydrofuran (THF) were purchased from VWR International LLC, deoxygenated and dried over alumina columns on a Grubbs style solvent system under an argon atmosphere and stored over activated 3 Å molecular seives in a nitrogen filled glove box. DCM-d_2 was purchased from Cambridge Isotope Laboratories, dexoygenated by sparging with argon for 5 minutes, and stored over 3 Å molecular seives in a nitrogen filled glove box.

$Ru_3(\mu^3\text{-}O)(OAc)_6(CO)(cpy)(pyrim)$ (**1**): A 20 mL scintillation vial was charged with 100 mgs (0.119 mmol) of $Ru_3O(OAc)_6(CO)(cpy)(MeOH)$,[1-2] 13.8 mgs (0.143 mmol) of 4-(3H)pyrimidinone, and 15 mL of a 4:1 DCM/MeOH mixture. The resulting blue reaction mixture was stirred at room temperature for 24 hours and then transferred to a 50 mL round bottom flask followed by the addition of 10 cm^3 of celite. The volatiles were removed under vacuum and flash chromatography with a 9:1 DCM:MeOH mixture as the elutant was used to purify the blue powder. The product, **1**, was isolated as the second green-blue band and removal of volatiles under vacuum afforded a blue microcrystalline solid. Yield: 66.7 mg (0.074 mmol, 62%). ^{1}H NMR (DCM-d_2, 500 MHz): δ (ppm) = 11.81 (s, 1H, N*H*), 8.96 (s, 1H, NC*H*N), 8.91 (m, 2H, C*H*), 8.57 (d, 1H, NC*H*, J = 7.4 Hz), 8.24 (m, 2H, C*H*), 7.09 (m, 1H, COC*H*), 2.08 (s, 12H, OOCH_3), 1.87 (s, 6H, OOCH_3). Anal. Calcd for $C_{23}H_{26}N_4O_{15}Ru_3$: C, 30.64%; H, 2.91%; N, 6.21%; found: C, 30.46%; H, 2.82%; N, 6.32%; FTIR (CH_2Cl_2) ν_{max} (cm^{-1}) = 1942, 1715, 1676, 1606, 1570, 1482, 1429. UV-Vis λ_{max} (nm) = 589, 437.

$Ru_3(\mu^3\text{-}O)(OAc)_6(CO)(py)(pyrim)$ (**2**): A 20 mL scintillation vial was charged with 143.0 mgs (0.1760 mmol) of $Ru_3O(OAc)_6(CO)(py)(MeOH)$,[1-2] 20.3 mgs (0.211 mmol) of 4-(3H)pyrimidinone, and 15 mL of a 4:1 DCM/MeOH mixture. The resulting blue reaction mixture was stirred at room temperature for 24 hours and then transferred to a 50 mL round bottom flask followed by the addition of 10 cm^3 of celite. The volatiles were removed under vacuum and flash chromatography with a 9:1 DCM:MeOH mixture as the elutant was used to purify the blue powder. The product, **1**, was isolated as the second blue band and removal of volatiles under vacuum afforded a blue microcrystalline solid. Yield: 100 mg (0.1141 mmol, 65%). ^{1}H NMR (DCM-d_2, 500 MHz): δ (ppm) = 13.03 (1H, s, 4(3H)-pyrimidinone: N*H*), 9.13 (1H, s, 4(3H)-pyrimidinone: NC*H*N), 9.09 (2H, d, pyridine: *o*-CH), 8.67 (1H, d, 4(3H)-pyrimidinone: NC*H*), 8.24 (1H, t, pyridine: *p*-C*H*), 8.07 (2H, t, pyridine: *m*-CH), 7.15 (1H, d, COC*H*), 2.09 (6H, s, CH_3), 2.07 (6H, s, CH_3), 1.86 (6H, s, CH_3). ^{13}C {^{1}H} NMR (DCM-d_2, 500 MHz): 222.30 (Ru-*C*O), 192.06 (O*C*O), 191.94 (OCO), 191.80 (O*C*O), 163.31 (4(3H)-pyrimidinone: *C*O), 157.14 (4(3H)-pyrimidinone: N*C*H), 155.94 (4(3H)-pyrimidinone: N*C*HN), 152.56 (pyridine: *o*-*C*H), 140.55 (pyridine: *p*-*C*H), 125.11 (pyridine: *m*-*C*H), 117.39 (4(3H)-pyrimidinone: CO*C*H), 23.96 (*C*H_3), 23.89 (*C*H_3), 22.18 (*C*H_3). Anal. Calcd for $C_{22}H_{27}N_3O_{15}Ru_3$: C, 30.14%; H, 3.10%; N, 4.79%; found: C, 30.12%; H, 3.11%; N, 4.66%; FTIR (CH_2Cl_2) ν_{max} (cm^{-1}) = 1942, 1718, 1687, 1678, 1608, 1572, 1543, 1486, 1450, 1426, 1417. UV-Vis λ_{max} (nm) = 587 (ε = 5530(70) M^{-1} cm^{-1}), 350 (ε = 6300(200) M^{-1} cm^{-1}).

$Ru_3(\mu^3\text{-}O)(OAc)_6(CO)(dmap)(pyrim)$ (**3**): A 20 mL scintillation vial was charged with 100 mgs (0.117 mmol) of $Ru_3O(OAc)_6(CO)(dmap)(MeOH)$,[1-2] 13.5 mgs (0.140 mmol) of 4-(3H)pyrimidinone, and 15 mL of a 4:1 DCM/MeOH mixture. The resulting blue reaction mixture was stirred at room temperature for 24 hours and then transferred to a 50 mL round bottom flask followed by the addition of 10 cm^3 of celite. The volatiles were removed under vacuum and flash chromatography with a 9:1 DCM:MeOH mixture as the elutant was used to purify the blue powder. The product, **3**, was isolated as the second blue band and removal of volatiles under vacuum

afforded a blue microcrystalline solid. Yield: 79.5 mg (0.086 mmol, 74%). ^{1}H NMR (DCM-d_2, 500 MHz): δ (ppm) = 12.13 (s, 1H, N*H*), 9.13 (s, 1H, NC*H*N), 8.93 (d, 2H, CH, J = 7 Hz), 8.72 (d, 1H, NC*H*, J = 7.8 Hz), 7.24 (d, 2H, C*H*, J = 7 Hz), 7.13 (d, 1H, COC*H*, J = 7.3 Hz), 3.30 (s, 6H, N(CH_3)$_2$), 2.04 (s, 6H, OOCCH_3), 2.02 (s, 6H, OOCCH_3), 1.81 (s, 6H, OOCCH_3). Anal. Calcd for $C_{24}H_{32}N_4O_{15}Ru_3$: C, 31.34%; H, 3.51%; N, 6.09%; found: C, 31.01%; H, 3.77%; N, 6.04%; FTIR (CH_2Cl_2) ν_{max} (cm^{-1}) = 1938, 1715, 1676, 1610, 1575, 1536, 1443, 1428. UV-Vis λ_{max} (nm) = 585, 387.

NMR Data Collection and Analysis. NMR spectra were recorded on a JEOL 500 MHz NMR spectrometer and analyzed using iNMR software. Samples were prepared in dichloromethane-d_2 and referenced to solvent residuals for ^{1}H and ^{13}C. A total of 16 scans of 18556 data points from –2 to 14 ppm were collected for ^{1}H NMR while 256 scans of 41682 data points from –5 to 250 ppm were collected for ^{13}C NMR.

Electrochemical Data Collection and Analysis: Electrochemistry was performed on a BASi Epsilon potentiostat in dried, degassed DCM at analyte concentrations of 2.00 mM with 0.1 M tetrabutylammonium hexaflurorophosphate ($TBAPF_6$, recrystallized from MeOH and vacuum dried at 80 ºC) as the supporting electrolyte. The electrode setup consisted of a glassy carbon disk (3 mm diameter) working electrode, a platinum wire counter electrode, and a Ag/AgCl reference electrode. All experiments were referenced to the ferrocene/ferrocenium using an internal standard of ferrocene.

Spectroelectrochemistry Data Collection and Analysis: Spectroelectrochemistry (SEC) was performed using a custom built SEC cell consisting of a 1 cm diameter Pt working electrode, a Pt counter electrode, and Ag pseudo-reference electrode that have been polished to a mirror finish.[3] Under an inert atmosphere, the cell was loaded with a DCM solution consisting of **1** (4.85 mM) and tetrabutylammonium hexaflourophosphate (0.1 M). The SEC spectra were then collected

across a potential range of 0 mV to –1400 mV. The potential of the SEC cell was controlled using a Pine Instrument Co. Model AFCBP1 bipotentiostat. As the potential was scanned, thin-layer bulk electrolysis was monitored by reflectance spectroscopy off of the polished platinum electrode. Scans were recorded every 50 mV, until a change in the spectra was observed, where the potential was then held constant while multiple spectra were acquired until the observable species has equilibrated at the new potential. This process was continued over the 1500 mV potential range allowing observation of the relevant redox sequences by slow electrolysis of the bulk solution. The infrared spectra were collected on a Bruker Equinox 55.

Infrared Data Collection and Analysis for K_D Determination. Infrared spectra were collected on a Bruker Equinox 55 FTIR spectrometer using a SPECAC variable path length IR cell with CaF_2 windows set to a path length of 0.1 mm. Solutions were prepared in a glove box under a nitrogen atmosphere using pre-dried DCM and subsequently analyzed. After solvent subtraction, the amide ν(CO) bands were fit to two, well resolved Gaussian functions using the Igor Pro software to obtain integrated spectral areas used in the equilibrium analysis. Derivation of the fit equations are described below as follows:

4.5 Appendix

Chapter 4: Some of the material in this chapter is unpublished. The majority of the material comes directly from a manuscript entitled “Stable mixed-valent complexes formed by electron delocalization across hydrogen bonds of pyrimidinone-linked metal clusters,” by Tyler M. Porter, Gavin P. Heim, and Clifford P. Kubiak, is published in *The Journal of the American Chemical Society*, **2018**, *140*, 12756–12759. The dissertation author is the primary author.

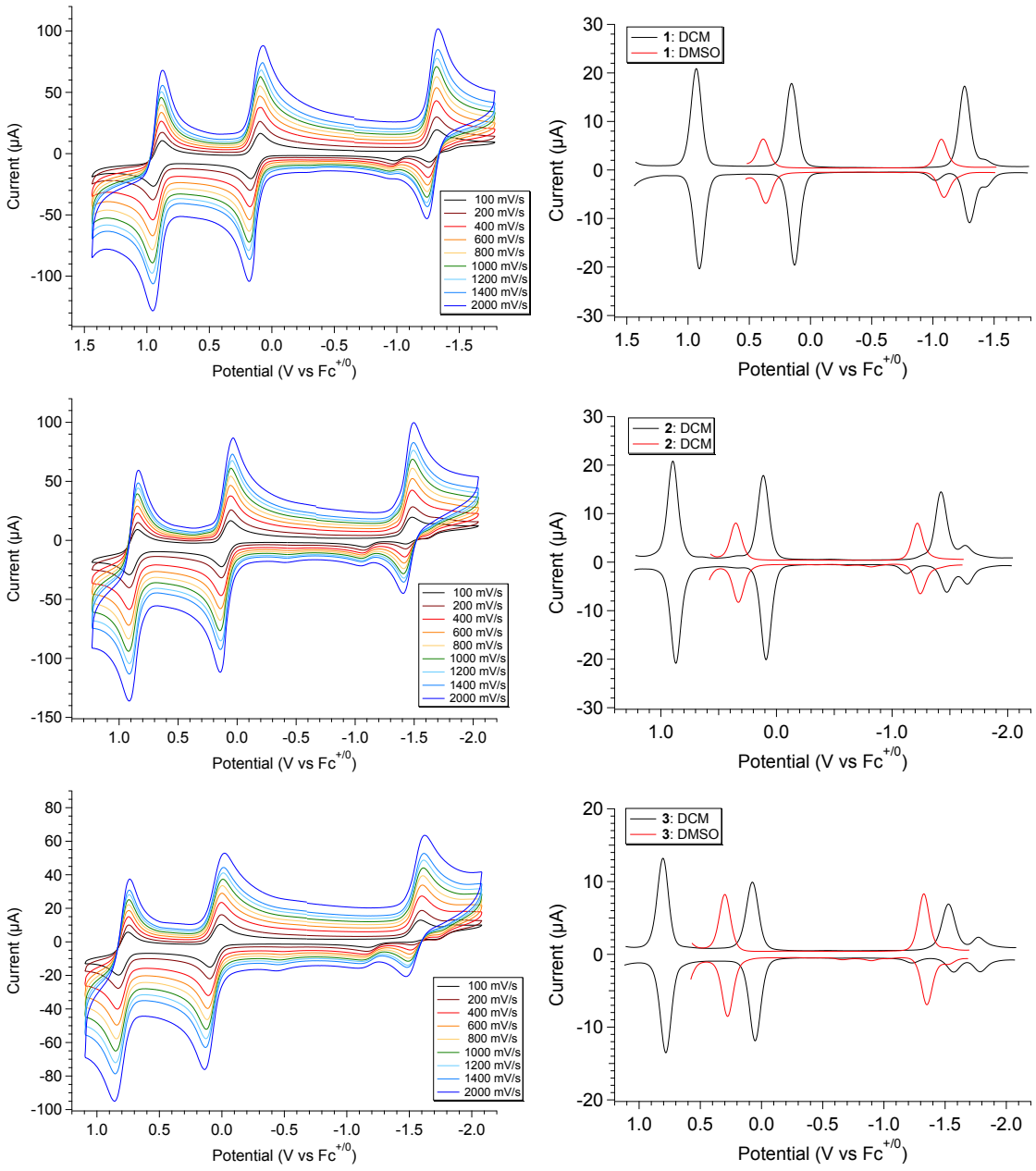

Figure 4.9. (left) Scan rate dependent CVs of **1**–**3** in DCM at 23 °C across a scan rate range of 100 mV/s to 2000 mV/s. Note the increasing reversibility of the first reduction as scan rate is increased for complexes **1**–**3**. (right) Differential pulse voltammetry of **1**–**3** in DCM (black) and DMSO (red).

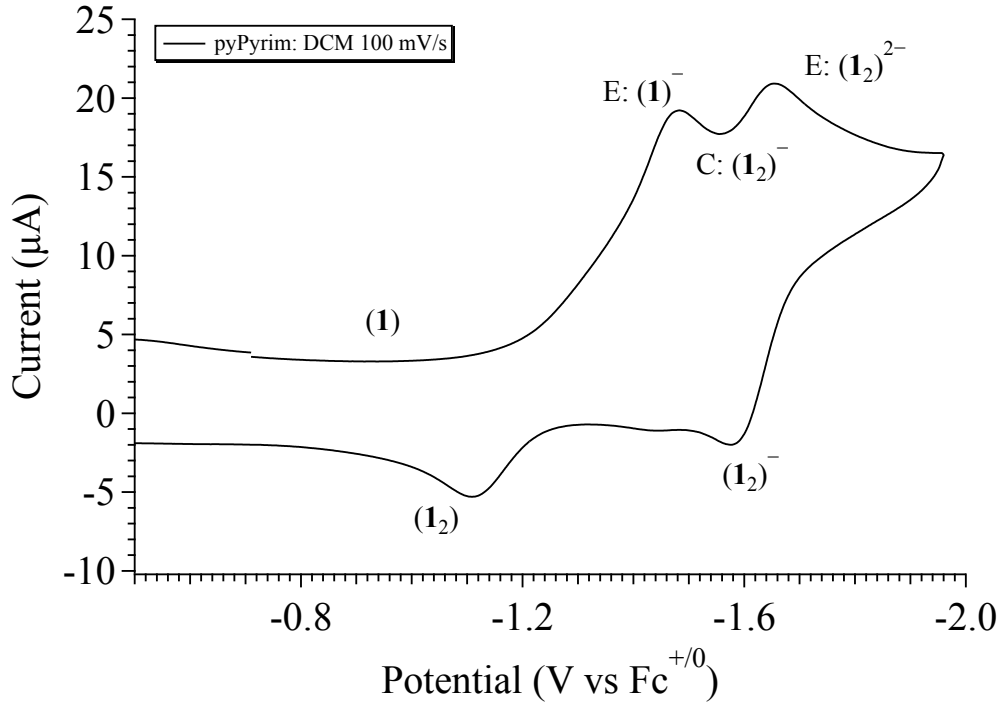

Figure 4.10. Cyclic voltammogram of **1** highlighting the ECE mechanism and the species present upon passing each redox wave.

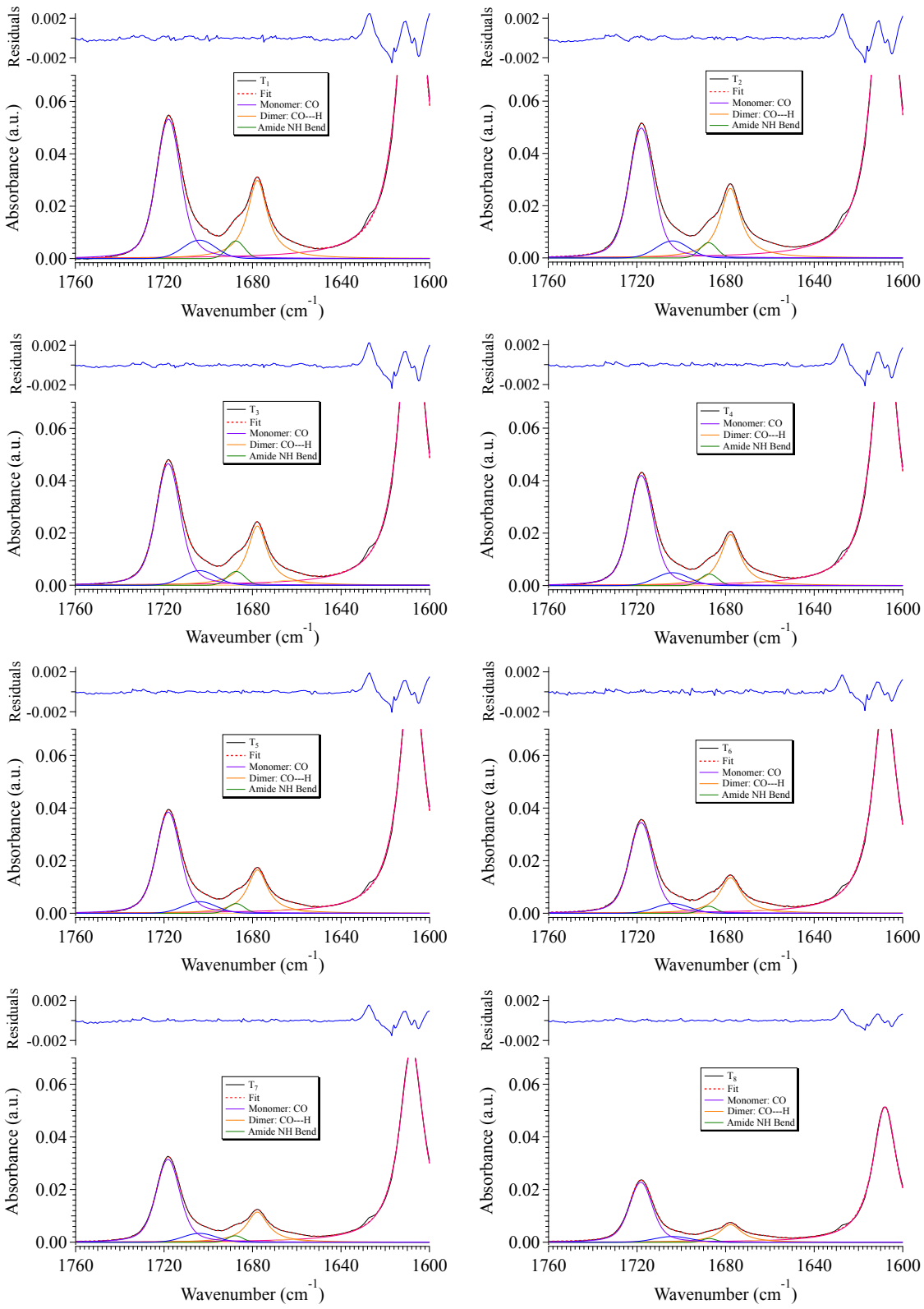

Figure 4.11. Spectral deconvolution of the ν(CO) region for the amide ν(CO) band across the concentration range of 3.00 to 1.00 mM.

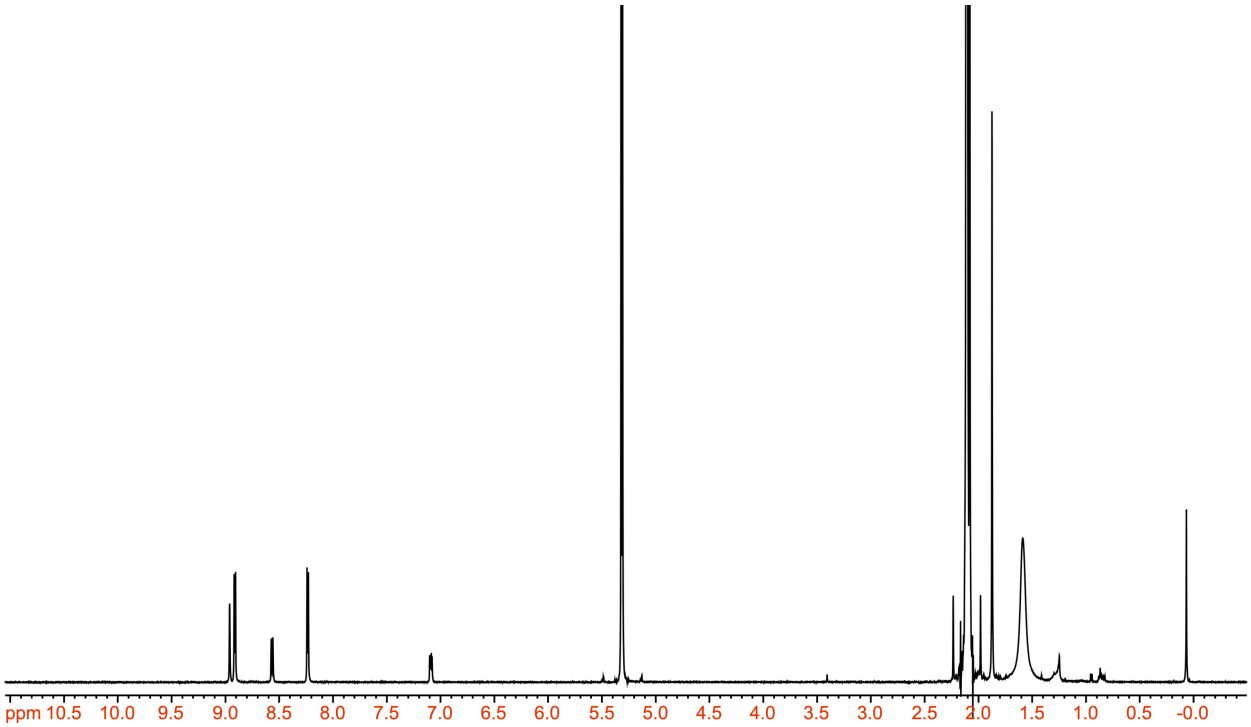

Figure 4.12. ^{1}H NMR of **1** in DCM-d_2.

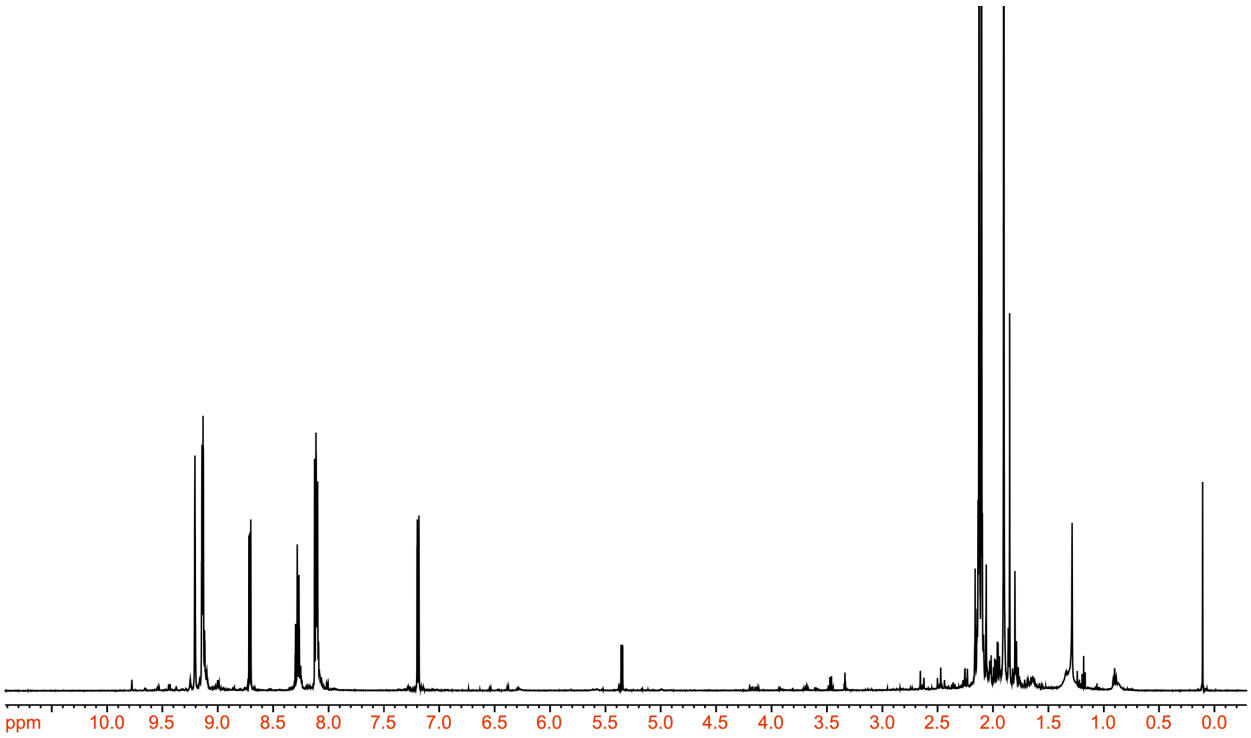

Figure 4.13. ^{1}H NMR of **2** in DCM-d_2.

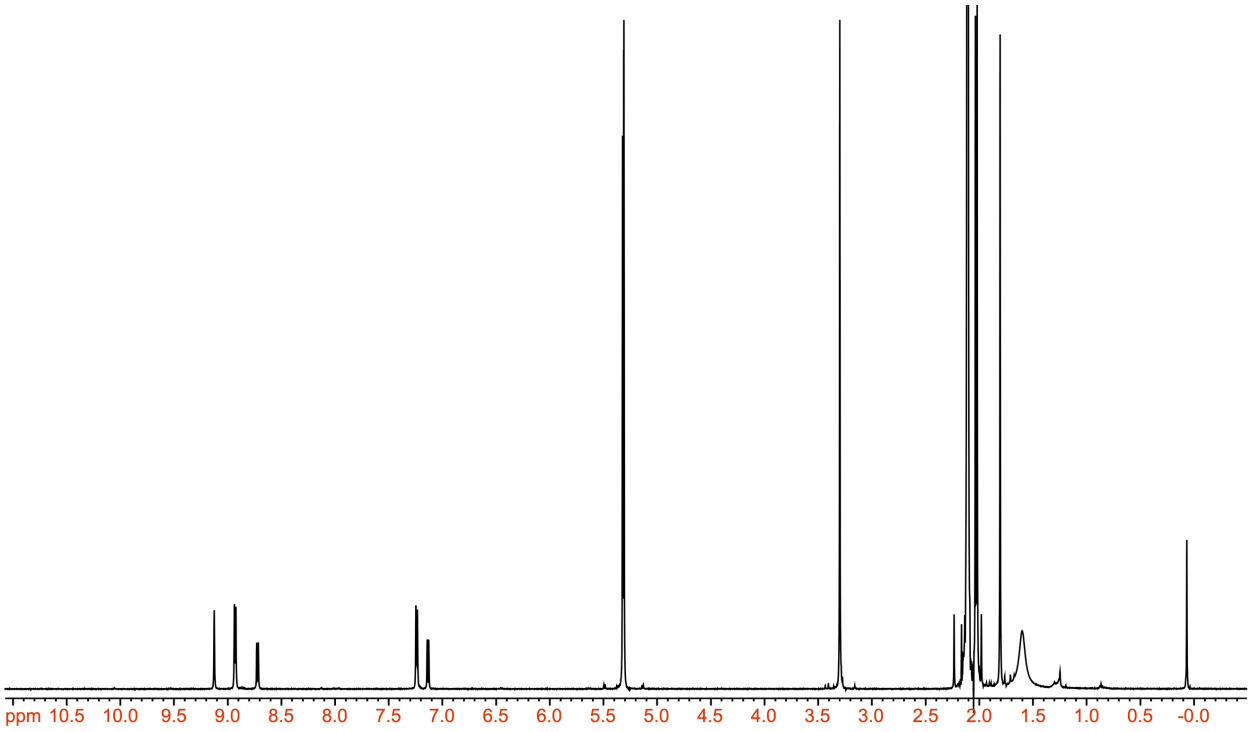

Figure 4.14. ^{1}H NMR of **3** in DCM-d_2.

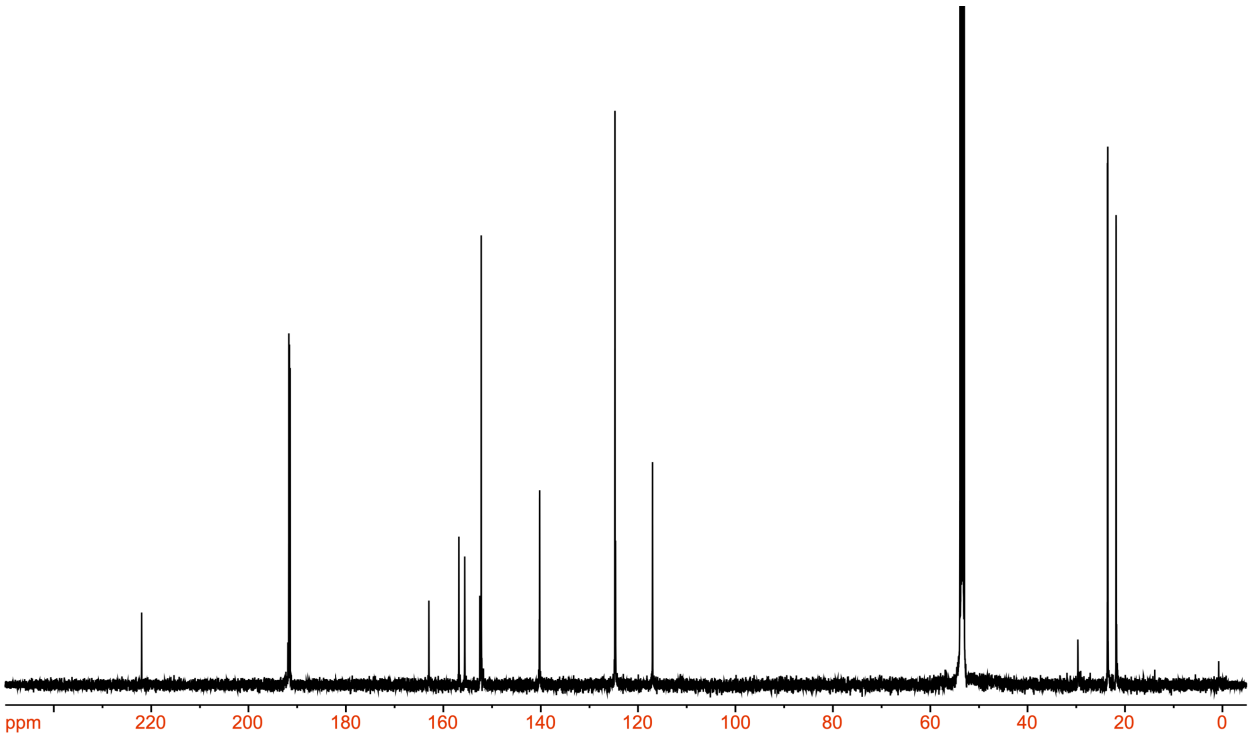

Figure 4.15. ^{13}C NMR of **2** in DCM-d_2.

Table 4.3. Table of values for 1:1 dimerization model used for the determination of K_D from the monomer and dimer amide ν(CO) bands.

Monomer Band		**Dimer Band**	
A_m	$[M]_0/A_m$	$(A_d)^{1/2}/[M]_0$	$2A_d/[M]_0$
0.820	0.0037	236.7	336.2
0.785	0.0035	244.4	328.5
0.734	0.0034	249.5	311.2
0.661	0.0034	257.2	297.6
0.620	0.0032	267.4	286.1
0.558	0.0031	280.3	274.9
0.510	0.0029	294.4	260.0
0.395	0.0025	324.0	210.0

4.6 References

1. Porter, Tyler M.; Heim, G. P.; Kubiak, C. P., Effects of electron transfer on the stability of hydrogen bonds. *Chem. Sci.* **2017,** *8* (11), 7324-7329.
2. Kubiak, C. P., Inorganic Electron Transfer: Sharpening a Fuzzy Border in Mixed Valency and Extending Mixed Valency across Supramolecular Systems. *Inorg. Chem.* **2013,** *52* (10), 5663-5676.
3. Goeltz, J. C.; Kubiak, C. P., Mixed Valency across Hydrogen Bonds. *J. Am. Chem. Soc.* **2010,** *132* (49), 17390–17392.
4. Canzi, G.; Goeltz, J. C.; Henderson, J. S.; Park, R. E.; Maruggi, C.; Kubiak, C. P., On the Observation of Intervalence Charge Transfer Bands in Hydrogen-Bonded Mixed-Valence Complexes. *J. Am. Chem. Soc.* **2014,** *136* (5), 1710–1713.
5. Ito, T.; Hamaguchi, T.; Nagino, H.; Yamaguchi, T.; Kido, H.; Zavarine, I. S.; Richmond, T.; Washington, J.; Kubiak, C. P., Electron Transfer on the Infrared Vibrational Time Scale in the Mixed Valence State of 1,4-Pyrazine- and 4,4'-Bipyridine-Bridged Ruthenium Cluster Complexes. *J. Am. Chem. Soc.* **1999,** *121* (19), 4625-4632.
6. Londergan, C. H.; Kubiak, C. P., Electron transfer and dynamic infrared-band coalescence: It looks like dynamic NMR spectroscopy, but a billion times faster. *Chem. Eur. J.* **2003,** *9* (24), 5962-5969.
7. Zoerb, M. C.; Harris, C. B., A Simulation Program for Dynamic Infrared (IR) Spectra. *J. Chem. Ed.* **2013,** *90* (4), 506-507.
8. Lu, R.; Gan, W.; Wu, B.-h.; Zhang, Z.; Guo, Y.; Wang, H.-f., C−H Stretching Vibrations of Methyl, Methylene and Methine Groups at the Vapor/Alcohol (n = 1−8) Interfaces. *J. Phys. Chem. B* **2005,** *109* (29), 14118-14129.
9. MacPhail, R. A.; Strauss, H. L., Can the Bloch equations describe the vibrational spectra of a reacting molecule? *J. Chem. Phys.* **1985,** *82* (3), 1156-1166.
10. Strauss, H. L., Changes of the carbonyl stretching spectra with temperature. *J. Am. Chem. Soc.* **1992,** *114* (3), 905-907.
11. Wood, K. A.; Strauss, H. L., The integrated intensities of chemically-exchanging vibrational bands as given by the Bloch equations. *Ber. Bungsenges. Phys. Chem.* **1989,** *93* (5), 615-616.
12. Londergan, C. H.; Kubiak, C. P., Vibronic participation of the bridging ligand in electron transfer and delocalization: New application of a three-state model in pyrazine-bridged mixed-valence complexes of trinuclear ruthenium clusters. *J. Phys. Chem. A* **2003,** *107* (44), 9301-9311.
13. Londergan, C. H.; Rocha, R. C.; Brown, M. G.; Shreve, A. P.; Kubiak, C. P., Intervalence involvement of bridging ligand vibrations in hexaruthenium mixed-valence clusters probed by resonance Raman spectroscopy. *J. Am. Chem. Soc.* **2003,** *125* (46), 13912-13913.
14. Londergan, C. H.; Salsman, J. C.; Ronco, S.; Kubiak, C. P., Infrared Activity of Symmetric Bridging Ligand Modes in Pyrazine-Bridged Hexaruthenium Mixed-Valence Clusters. *Inorg. Chem.,* **2003,** *42*, 926-928.
15. Williams, R. D.; Petrov, V. I.; Lu, H. P.; Hupp, J. T., Intramolecular Electron Transfer in Biferrocene Monocation: Evaluation of Franck−Condon Effects via a Time-Dependent Analysis of Resonance Raman Scattering in the Extended Near-Infrared. *J. Phys. Chem. A* **1997,** *101* (43), 8070-8076.
16. Marin, T. W.; Homoelle, B. J.; Spears, K. G.; Hupp, J. T.; Spreer, L. O., Vibrational Coherence Due to Promoting Mode Activity in the Relaxation Dynamics of the Class III Mixed-Valence Molecule $[Ru_2TIEDCl_4]^+$. *J. Phys. Chem. A* **2002,** *106* (7), 1131-1143.
17. Spears, K. G., Models for Electron Transfer with Vibrational State Resolution. *J. Phys. Chem.* **1995,** *99* (9), 2469-2476.

Chapter 5

Direct Observation of the Intermediate in an Ultrafast Isomerization.

5.1 Introduction

Chemical exchange dynamics are often studied by using Bloch equation analysis of coalescing line shapes in nuclear magnetic resonance spectroscopy (NMR).[1] The typical frequencies (radio) used in NMR experiments determine that dynamical timescales in the range of milliseconds to microseconds can be studied. A similar treatment has been applied to systems exchanging on the infrared (IR) vibrational timescale,[2-10] where line shape analysis of FTIR and Raman vibrational spectra can be applied to study reactions occurring in picoseconds (ps). In practice however, there are comparatively few examples of chemical exchange measurable by linear IR or Raman vibrational spectroscopy, as inhomogeneous broadening, solvent environment fluctuation, and multiple dynamic processes in addition to chemical exchange can contribute to the overall line shape. Here, we present the study of the rapid structural isomerization of a five-coordinate ruthenium complex on the ultrafast (vibrational) timescale (Figure 5.1).

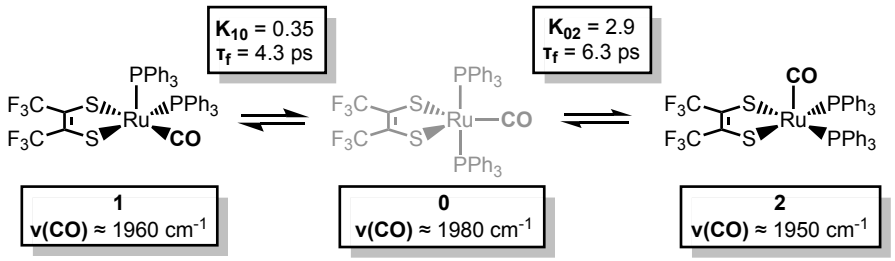

Figure 5.1. Isomerization of $Ru(S_2C_2(CF_3)_2)(CO)(PPh_3)_2$ as observed by 2D IR.

The ruthenium complex, $Ru(S_2C_2(CF_3)_2)(CO)(PPh_3)_2$, was first reported by Miller and Balch in 1971,[11] where the solvent from which the complex is recrystallized determines whether orange crystals or a mixture of orange and violet crystals are obtained.[12-14] X-ray crystal structure analysis revealed that both the orange and violet isomers were square pyramidal, differing only in the position of the carbonyl ligand. The more stable orange isomer was found to have the CO in the apical position, and is referred to as **2**, while the violet isomer has the CO in the equatorial position and is referred to as **1**. The solid state FTIR stretching frequencies for the CO in each of these isomers are separated by *ca.* 30 cm^{-1} (**1**: $\nu(CO_{ap})$ = 1944 cm^{-1}, **2**: $\nu(CO_{eq})$ = 1973 cm^{-1}),[11] while in methylene chloride (DCM) solutions at 20 °C, only one broad absorption (FWHM ≈ 50 cm^{-1}) appears near the average frequency of isomers **1** and **2** (*ca*. 1958 cm^{-1}).

Complete fittings of the solution 1D IR line shape consisting of contributions from only these two isomers are less than satisfactory; owing an extra absorbance in the vicinity of 1980 cm^{-1} from a possible third isomer (*vide infra*, Figure 5.2). The solution state ^{31}P NMR in DCM-d_2 shows only one resonance at 47.6 ppm indicating that the ruthenium bound triphenylphosphine ligands experience an identical *average* environment and that the fluctional behavior of the ligands is faster than the NMR timescale (Appendix 5.5, Figure 5.11, $k_{ex} > 10^6$ s^{-1}).[15] Together, these spectroscopic observations suggest dynamic averaging on the ultrafast timescale of molecular vibrational modes.

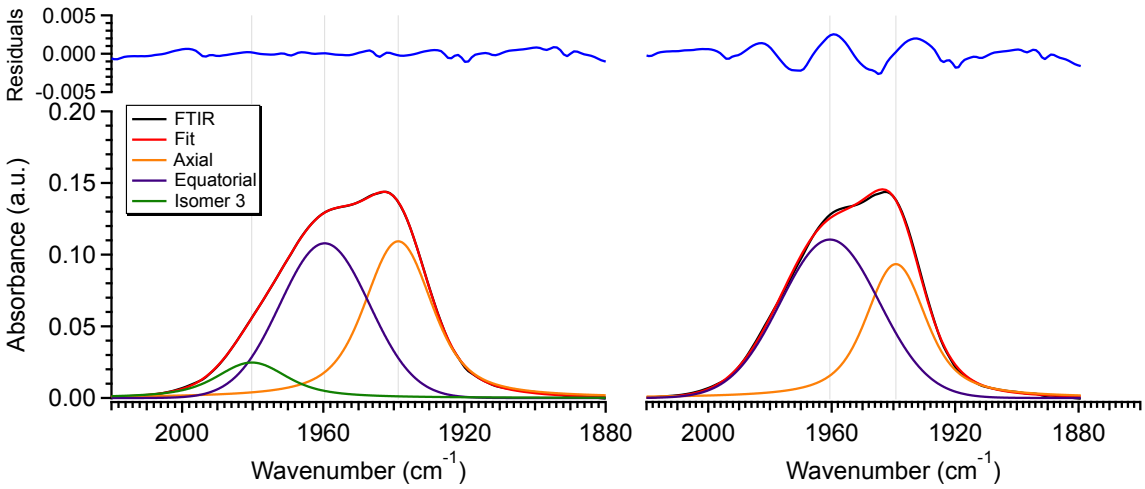

Figure 5.2. (left) and two-component Voigt functional fits of the 1D IR line shape for $Ru(S_2C_2(CF_3)_2)(CO)(PPh_3)_2$ in DCM solutions at 20 °C.

Ultrafast two-dimensional infrared (2D IR) spectroscopy is a powerful method that can obtain molecular structural information and provide details of dynamic processes with sub-picosecond time resolution.[16-22] 2D IR spectroscopy has been applied to measure chemical exchange between two conformations in solution phased under thermal equilibrium.[23-30] In 2D IR spectroscopy, three ultrafast mid-IR pulses interact with the sample sequentially: The first two pulses initialize and interrogate vibrational coherences, which generate a transient vibrational tag, while the third pulse probes the evolution of the tagged vibrational modes (Figure 5.12). Because vibrational modes of molecules are sensitive to molecular conformations, local solvent enviroments, and excess internal energy, scanning the waiting time (τ_2) between the second and third pulses can track the dynamics of chemical exchange,[20, 23-24] solvent fluctuation,[31-34] and vibrational energy relaxation.[28, 35-37] In the present study, 2D IR is employed to understand chemical exchange in the pentacoordinate ruthenium complex $Ru(S_2C_2(CF_3)_2)(CO)(PPh_3)_2$.

5.2 Results and Discussion

The 2D IR spectra of $Ru(S_2C_2(CF_3)_2)(CO)(PPh_3)_2$ in DCM at 20 °C are shown in Figure 5.3. The spectra are essentially 2D frequency correlation maps of vibrational coherences, which

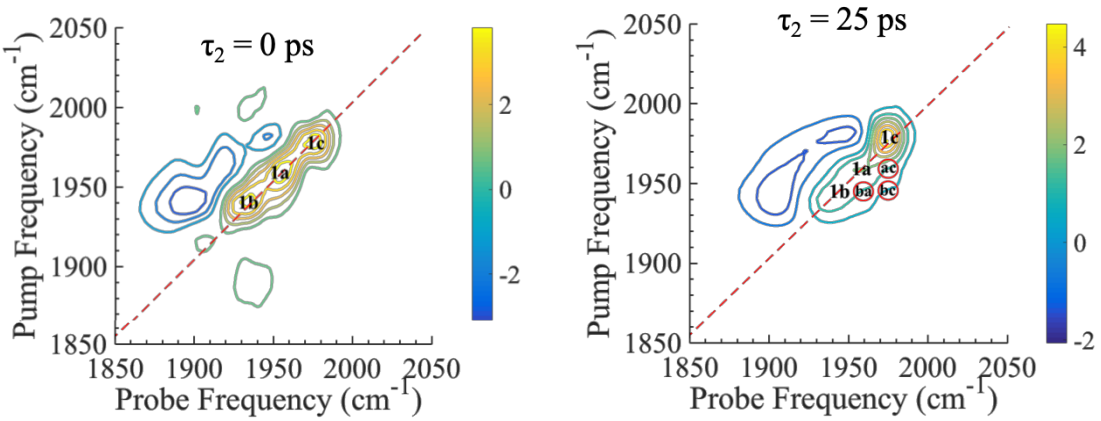

Figure 5.3. (left) 2D IR spectrum of $Ru(S_2C_2(CF_3)_2)(CO)(PPh_3)_2$ in DCM at τ_2 = 0 ps. Peaks 0, 1, and 2 are diagonal peaks that lie along the dashed diagonal line. (right) 2D IR spectrum of $Ru(S_2C_2(CF_3)_2)(CO)(PPh_3)_2$ in DCM at τ_2 = 25 ps. Red boxes indicate locations of the cross peaks corresponding to peaks 0, 1, and 2. For instance, peak 10 is the cross peak that corresponds to population transfer from **1** to **0**.

are plotted against the initially tagged pump frequency (y-axis) and the probe frequency (x-axis). On the diagonal line, we observe three individual peaks for $Ru(S_2C_2(CF_3)_2)(CO)(PPh_3)_2$ at τ_2 = 0 ps, labeled as peak 0 (1980 cm^{-1}), peak 1 (1960 cm^{-1}) and peak 2 (1940 cm^{-1}). The three diagonal peaks indicate three different ν(CO) modes in the system with the peaks at 1960 and 1940 cm^{-1} corresponding to isomers **1** (CO_{eq}) and **2** (CO_{ap}) respectively, as previously observed in the solid-state FTIR spectra. The third ν(CO) band in the vicinity of 1980 cm^{-1} corresponds to a third isomer of the ruthenium complex (**0**), that was not isolable in the solid-state, and appears only as a small shoulder in the solution phased FTIR spectra (Figure 5.2). The third isomer has been determined to be a metastable, trigonal bipyramidal structure of $Ru(S_2C_2(CF_3)_2)(CO)(PPh_3)_2$ (*vide infra*).

The dynamics between the three isomers are revealed by 2D IR spectra collected at a series of τ_2 time delays. As τ_2 increases, the three diagonal peaks decay due to population relaxation of the vibrational modes, while cross peaks increase in intensity relative to the diagonal peaks. The appearance of cross peaks in the 2D IR spectrum are important and represent the occurrence of chemical exchange between the species appearing along the diagonal trace. For

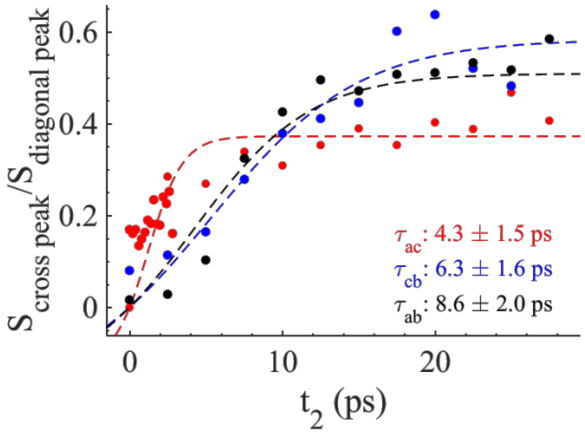

$$\frac{S_{BA}}{S_{AA}} = \frac{1 - e^{-(k_{AB}+k_{BA})\cdot t_2}}{1 + \frac{k_{AB}}{k_{BA}} \cdot e^{-(k_{AB}+k_{BA})\cdot t_2}}$$

Figure 5.4. Cross peak ratios as a function of the delay time τ_2. Chemical exchange constants (k_{AB} and k_{BA}) are obtained through fits (dashed lines) using the expression of cross peak ratios as a function of τ_2.

instance, a cross peak located at the pump frequency of **1**, and the probe frequency of **0** indicates exchange between isomers **1** and **0**. Chemical exchange time constants between each isomer are then extracted by fitting cross peak intensity ratios as a function of the τ_2 time delay (Figure 5.4). The extracted time constants indicate that the transition from **1** to **0** occurs with a 4.3 (1.5) ps time constant, while the transition from **0** to **2** requires 6.3 (1.6) ps. A cross peak for the conversion of **1** to **2** was also observed with a time constant of 8.6 (2.0) ps; however, the dynamics of a direct conversion between **1** and **2** are not expected to compete with the faster interconversions *via* **0** as an intermediate (see kinetic analysis section). We note that spectral diffusion could be another source of line shape change that manifests as off-diagonal intensity growth; however, spectral diffusion for $Ru(S_2C_2(CF_3)_2)(CO)(PPh_3)_2$ in DCM was observed separately with a time constant of 83.3 (15.3) ps, which is much longer than the cross peak intensity growth, indicating that the cross peak dynamics reflect chemical exchange.[38] It is important to note that the power of the mid-IR pulses interacting with the system are of insufficient energy to perturb the system from thermal equilibrium, and does not drive the system away from a persistent, steady-state population. The mid IR pulse sequence serve only to tag and probe

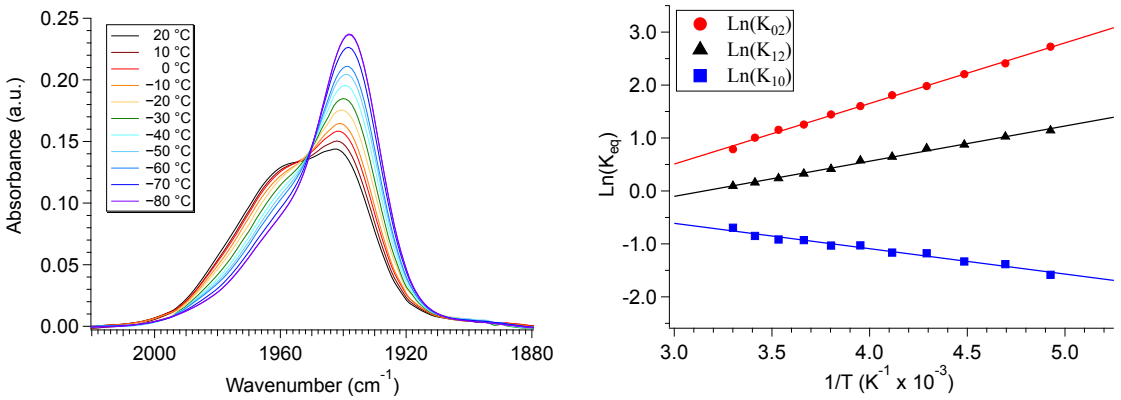

Figure 5.5. (left) VT-FTIR of $Ru(S_2C_2(CF_3)_2)(CO)(PPh_3)_2$ in DCM across a temperature range from 20 °C to –80 °C. (right) Van 't Hoff plot of the isomerization reaction. K_{02} represents the isomerization equilibrium constant for exchange between **0** and **2**, K_{12} represents exchange between **1** and **2**, and K_{10} represents exchange between **1** and **0**.

the vibrational modes at different time delays. This allows the observation of the intramolecular rearrangement of interest under thermal equilibrium.

To investigate the thermodynamics of the chemical exchange process observed here, the variable temperature 1D FTIR (VT-FTIR) spectra of the complex were collected using a SPECAC flow-through optical cryostat. The sample was enclosed in a CaF_2 windowed cell contained in a vacuum jacketed housing and cooled from 20 °C to –80 °C using a methanol liquid nitrogen slurry. Upon cooling, the broad, ν(CO) band centered about 1958 cm^{-1} red-shifts to lower frequencies (*ca.* 1938 cm^{-1}), sharpens and gains considerable intensity while the shoulders near 1960 cm^{-1} and 1980 cm^{-1} significantly lose intensity (Figure 5.5). The temperature dependence is completely reversible and suggests that at low temperature, DCM solutions contain predominantly the more favored CO_{apical} isomer, **2**. After solvent subtraction, the VT-FTIR line shapes were fit to three Gaussian functions centered about the equilibrium positions for each isomer (**Figure 5.13**, ν(CO) ≈ **0**: 1980 cm^{-1}, **1**: 1960 cm^{-1}, and **2**: 1940 cm^{-1}). Using the determined spectral areas, the population ratios of the isomers at all temperatures were then determined and a Van 't Hoff analysis was performed (Figure 5.5). Exchange between **1** and **0** was found to be endergonic in nature with ΔH = 0.84 (0.08) kcal mol^{-1}, ΔS = 0.6 (0.4) eu, and ΔG^{298} = 0.7 (0.1) kcal mol^{-1}, while

Table 5.1. Summary of thermochemical and kinetic data at 20 °C (293 K) in DCM.

	K_{eq}		ΔH (kcal mol^{-1})	ΔS (eu)	τ_f (ps)	E_a (kcal mol^{-1})
	K_{10}	0.35 (0.03)	0.84 (0.08)	0.6 (0.4)	4.3 (1.5)	2.2 (0.2)
IR	K_{02}	2.9 (0.2)	–2.18 (0.06)	–5.3 (0.3)	6.3 (1.6)	2.4 (0.1)
	K_{12}	1.0 (0.1)	–1.3 (0.1)	–4.8 (0.5)	8.6 (2.0)	2.6 (0.1)
UV-vis	K_{12}	1.4 (0.3)	–1.3 (0.1)	–3.4 (0.2)	---	---

exchange between **0** and **2** was found to be exergonic with ΔH = –2.18 (0.06) kcal mol^{-1}, ΔS = –5.3 (0.3) eu, and ΔG^{298} = –0.6 (0.1) kcal mol^{-1}. The exchange process overall from **1** to **2** ($CO_{equatorial}$ to CO_{apical}) was found to be thermodynamically favored in DCM with ΔH = –1.3 (0.1) kcal mol^{-1} and ΔS = –4.8 (0.5) eu (Table 5.1). While the direct exchange between **1** and **2** is possible, given literature precedent, the kinetic analysis (see kinetic analysis in appendix 5.5), and DFT results (*vide infra*) all exchange is believed to involve the TBP intermediate (**0**).[39-40]

It is important to note that since both the equilibrium constant and the exchange rate constant will contribute to the overall FTIR line shape, it is useful to determine the equilibrium constants for the isomers independently. This was done by variable temperature UV-visible spectroscopy. Electronic spectra of the solid-state isomers in a KBr pellet present a single transition for the orange isomer (**2**) at 466 nm while the violet isomer (**1**) presents three transitions at 571 nm, 460 nm, and 396 nm (Figure 5.6). In DCM solutions at 20 °C, three transitions are present with band maxima at 385, 466, and 561 nm respectively. Upon cooling to –80 °C, the bands at 386 and 561 nm are seen to decrease in intensity while the band at 470 nm gains significant intensity and blue-shifts to 455 nm (Figure 5.6). The bands are assigned to the equatorial (**1**) and apical (**2**) isomers respectively and both are related by clear isosbestic points at 396 and 490 nm, indicative of absorbing species in equilibrium. After spectral deconvolution (Figure 5.15), the equilibrium constants were determined from the spectral areas and a Van 't Hoff analysis was performed giving a ΔH = –1.21 (0.06) kcal mol^{-1} and ΔS = –3.4 (0.2) eu (Figure 5.6). These values are in excellent agreement with those determined from the analysis of 1D IR

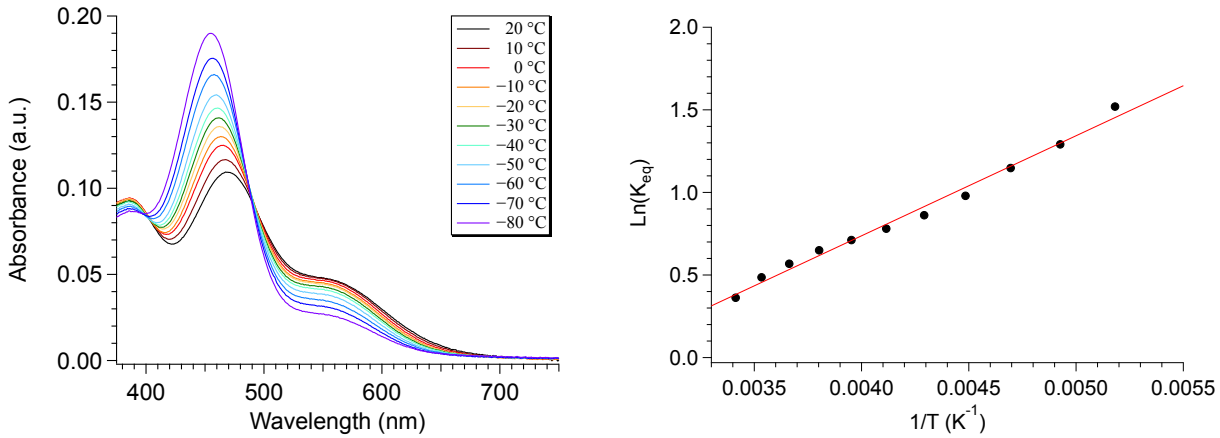

Figure 5.6. (left) VT-UV/vis spectra in DCM ranging from 20 °C to –80 °C. (right) Van 't Hoff plot obtained from UV-vis spectral analysis.

spectra described above.

The most closely related examples of transition metal complexes undergoing dynamic exchange on the IR timescale can be found in both (η^4-diene)$Fe(CO)_3$ complexes and $Co_2(CO)_8$.[4, 6, 10, 20, 41-42] In the former (η^4-diene)$Fe(CO)_3$ complexes, the three carbonyl ligands exchange through a very low barrier, turn-style type, Berry pseudorotation.[4, 6, 41-42] This corresponds to a degenerate self-exchange, quite different from the exchange between populations of two structurally different isomers sharing an observable intermediate as observed in both $Ru(S_2C_2(CF_3)_2)(CO)(PPh_3)_2$ and $Co_2(CO)_8$.[20] An Arrhenius analysis (eq. 5.1) provides the barrier heights of the observed exchange process:

$$k_{ex} = Ae^{\frac{-E_a}{RT}} \qquad (5.1)$$

Using the determined rate constants from 2D IR and an estimate of the exponential prefactor (A) to be on the order of 10^{13} s^{-1},[4, 6, 10, 30, 41-42] the barrier to exchange from **1** to **0** was found to be 2.2 (0.2) kcal mol^{-1}, while the barrier to exchange from **0** to **2** was found to be 2.4 (0.1) kcal mol^{-1} (Figure 5.7 and Table 5.1). These values are sufficiently low to be expected to produce coalesced line shapes, like those observed in the 1D IR spectra.[6, 8-10, 42] It is also important to note that careful examination of the structures and application of simple principles of

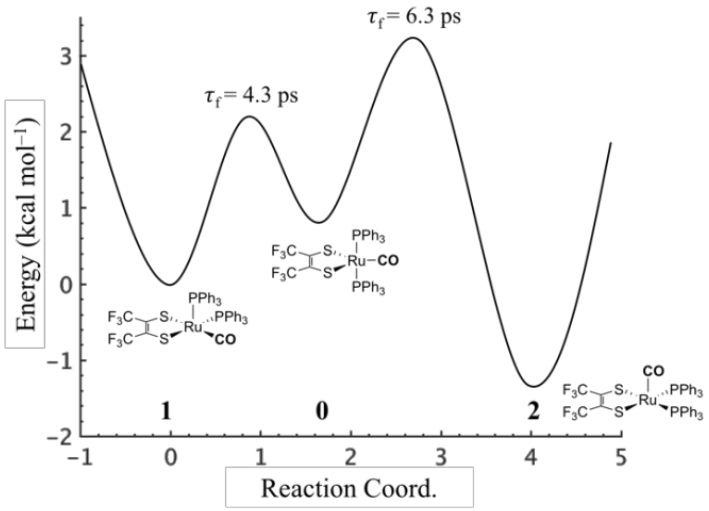

Figure 5.7. Qualitative potential energy surface for the presented isomerization reaction. The potential energy surface was constructed using the experimental kinetic and thermochemical data obtained from 2D IR and VT-FTIR.

least motion would predict that isomerization between **1** and **0** would require less rearrangement than that required to proceed between **0** and **2**, an observation consistent with the experimentally determined barriers.

The isomers are believed to exchange from **1** to **0** by movement of a phosphine ligand in **1** from an equatorial to an axial position. Isomerization between **0** and **2** then occurs following twisting of the dithietane ligand in **0** to place the dithietane ligand in the equatorial plane. Calculated structures and frequency calculations were obtained using density functional theory (DFT) at the BP86 level of theory with basis sets def2-TZVP (Ru, S, P, and O) and def2-SVP (H and C) for the isolated molecules. The reported crystal structure data for **1**and **2** were used for the initial geometries while the TBP (**0**) isomer was adapted from the reported crystal structure of **1**. After geometry optimization, frequency calculations were performed at the same level of theory to verify optimized geometries as minima. The predicted FTIR spectrum from the DFT frequency calculation was in excellent agreement with that observed experimentally (Figure 5.8, ν(CO) DFT: **0** = 1975 cm^{-1}; **1** = 1955 cm^{-1}; **2** = 1940 cm^{-1}) supporting the experimental observation of the TBP

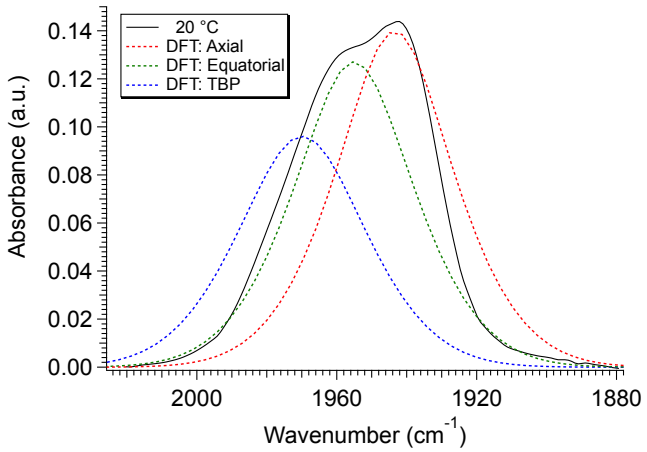

Figure 5.8. Predicted FTIR spectrum from DFT calculation. Experimental data at 20 °C is shown as the black trace, apical isomer shown as the red trace, equatorial isomer shown as green trace, and TBP isomer as blue trace.

isomer. These ideas of isomerization are further supported by consideration of the vibrational normal modes as calculated from the DFT frequency analysis. For all three isomers, several low frequency normal modes have been identified in which nuclear displacements align with the described rearrangement pathways.

5.3 Conclusion

The fact that a relatively large transition metal complex undergoes isomerization at rates comparable to the rotational isomerization reactions of small organic molecules is surprising.[2-3, 30, 43] To our knowledge, this is the first observation of an ultrafast dynamic equilibrium involving two distinct structural isomers and the intermediate connecting them. This work confirms that the ground states of five-coordinate transition metal complexes can have remarkably low kinetic barriers for axial-equatorial exchange. This study also validates the mechanism of Berry pseudorotation and clearly demonstrates its dynamical time scale.[44] This work presents new opportunities for potential molecular device applications based on switching between three distinct states of a system exhibiting electronic tri-stability on the ps time scale.

5.4 Experimental

Materials and Methods:

Preparation and Purification: The 2,3-hexafluorobutyne was used as received from Oakwood Chemicals while the triruthenium doedecacarbonyl and triphenyl phosphine was used as received from Acros Organics. The cyclohexane stabilized dichloromethane (DCM), was purchased from VWR International LLC, deoxygenated and dried over alumina columns on a custom built solvent system under an argon atmosphere and stored over activated 4 Å molecular seives in a nitrogen filled glove box. The 2,3-dithiolene and $Ru(S_2C_2(CF_3)_2)(CO)(PPh_3)_2$ were prepared following modified literature reported proceudures.[11] In brief:

Bis(perfluoromethyl)-1,2-dithietene. In accord with literature,[45] in a well ventilated fumehood, a 2 neck round bottom flask equipped with a short path distillation head was charged with 25 g (97.46 mmol) of sulfer and heated to 325 ºC under a nitrogen stream. Upon reaching 325 ºC, the 2,3-hexafluorobutyne was bubbled through the molten sulfer in short puffs and the dithietene was collected in a receiving Schlenk flask as a red-tinted oil.

$Ru(S_2C_2(CF_3)_2)(CO)(PPh_3)_2$. Under an inert atmosphere a 250 mL Schlenk flask was charged with 400 mg (0.63 mmol) of triruthenium dodecacarbonyl, 580 mg (2.57 mmol) of bis(perfluoromethyl)-1,2-dithietene, and approximately 100 mL of *n*-heptane that was heated under reflux. After 45 minutes, following carbon monoxide evolution an orange solid had precipitated. The flask was cooled and the orange solid was collected by vacuum filtration, washed with *n*-heptane, and dried under vacuum. The orange solid, tentatively identified as $Ru_2(S_2C_2(CF_3)_2)(CO)_6$ [359 mg (0.60 mmol)], was then added to a flask containing 1.1427 g (4.36 mmol) of triphenylphosphine suspended in 50 mL of *n*-heptane. After heating to reflux for 12 hours, the flask was cooled to 0 ºC and the crystalline complex was collected by filtration. Futher

purification was achieved by recrystalization for dichloromethane/hexanes solutions where a mixture of orange and violet crystals were obtained.

Infrared Data Collection and Analysis. Infrared spectra were collected on a Bruker Equinox 55 FTIR spectrometer using a SPECAC flow through optical cryostat (model, 21525) with a 1.12 mm path length (determined from infringing pattern), CaF_2 windowed cell enclosed in a vacuum jacketed housing. Solutions were prepared in a glove box under a nitrogen atmosphere using pre-dried DCM from a mixture of orange and violet crystals. Cell temperature (± 1 °C) was regulated by addition of liquid nitrogen/methanol to the cooling compartment and heating to the desired temperature with a computer controlled thermocouple/heating coil system. Both solutions of the complex and solvent blanks were recorded at temperature ranging from 20 °C to –80 °C to ensure accurate solvent subtraction. To obtain the integrated spectral areas for the exchanging species, spectral curve fitting was carried out in MATLAB (version 9.1.0.44655). The ν(CO) bands were fit by constraining three Gaussian functions ± 4 cm^{-1} centered around 1940, 1960, and 1980 cm^{-1} for all temperatures, while fixing a fourth Gaussian centered at 1920 cm^{-1}.

UV/visible Data Collection and Analysis. Cryostatic UV-visible spectra were collected on a Shimadzu UV–3600 UV/vis/NIR spectrometer, using the same cell setup described above for FTIR data collection. Samples were contained in SPECAC sealed liquid FTIR cells with CaF_2 crystal optic windows and a path length of 1.12 mm. Spectral curve fitting was carried out in MATLAB (version 9.1.0.44655).

Density Functional Theory Analysis. Calculations were performed in the ORCA software suite (version 3.0.3) at the BP86 level of theory with the RIJCOSX approximation.[46-50] Ruthenium, phosphorous, sulfur, and oxygen atoms were treated with the DEF2-TZVP/J basis sets while DEF2-SVP/J was used for all other atoms.[51-59] Dispersion corrections were applied using the atom-pairwise dispersion correction with a Becke-Johnson damping scheme (D3BJ) and solvation was

accounted for using the COSMO solvation model in methylene chloride.[60-62] Analytical frequency calculations were performed at the same level of theory and molecular graphics were performed with the UCSF Chimera package.[63]

NMR Data Collection and Analysis. ^{1}H NMR spectra were recorded on a JEOL 500 MHz NMR spectrometer and analyzed using iNMR software. A total of 64 scans of 32768 data points were collected from from –185 to 185 ppm. ^{31}P spectra were recorded in predried dichloromethane-d_2 solutions from 25 to – 80 °C.

2DIR Experimental Set up, Data Collection, and Analysis. 2D IR spectra were collected in pump-probe geometry.[64-65] The pulse sequence is described in Figure S2. In brief, three mid-IR pulses were sent to interact with the sample, where two vibrational coherences were created during t_1 and t_3 period. To generate the pulse sequence, 800nm laser pulses (~35 fs, ~6 W, 1 kHz) were generated by ultrafast Ti:Sapphire regenerative amplifier (Astrella, Coherent) . The 800nm was converted into mid-IR pulses by optical parametric amplifier (TOPAS, Coherent) followed by a different frequency generation process on a Type II $AgGaS_2$ crystal (Eksma). The mid-IR pulse (30 μJ) was split into two beams by a beam-splitter. The majority (95%) was sent into a Ge-AOM based pulse shaper (QuickShape Kit, PhaseTech) to prepare the two pump pulse in the pulse sequences, whereas 5% mid-IR served as the probe.[64-65] The pump pulse pair (2 μJ at the sample), the probe (<0.5 μJ) were all focused and spatially overlapped on the sample by a f = 10 cm parabolic mirror and collimated by another parabolic mirror in a symmetric geometry.

In the 2D IR experiments, two vibrational coherences were generated during t_1 and t_3 periods, respectively. The first coherence was measured by scanning t_1 time from 0 to 2000 fs in steps of 20 fs using the pulse shaper, where a rotating frame at f_0 = 1583 cm^{-1} was used to shift

the oscillation period to 80 fs, so that the scanning step can meet with the Nyquist frequency requirement. In order to detect the 2D IR signal (the second vibrational coherence) by the CCD camera (256 × 1,024, Andor), the collimated signal and the probe beam were then upconverted by a residue 800 nm beam on a 5%Mg: $LiNbO_3$ crystal.[66-67] Since the 800 nm served as a window function, the t_3 time delay were covered by the upconversion process and the 800 nm pulse duration determined how long t_3 was "scanned".[68-69] The up-converted 2D IR signals were experimentally Fourier transformed by a spectrograph and detected by a CCD camera. To get full absorptive 2D IR spectra, the first vibrational coherence was numerical Fourier transformed along t_1 axis. The pump and probe pulses had the same polarization in 2D IR measurements. For the time dependent 2D IR measurements, t_2 was scanned by a computerized delay stage.

Obtaining Chemical Exchange Rate Constants from Time Dependent 2D IR Spectra. The volume of each peak with respect to t_2 was obtained from the t_2-dependent 2D IR spectra.[24-25] As shown in Figure S3, multiple Gaussian functions were used to fit the 2D IR spectral cut along the probe axis at the peak 2 frequency (~1940 cm^{-1}) on the pump axis. All 2D IR spectra at different t_2 times were fit following the same method. Each Gaussian function represents one species in the 2D IR spectrum. For example, at t_2 = 0 ps, the single Gaussian was used to fit the positive peak of the spectral cut corresponding to the fundamental transition of diagonal peak 2. Similarly, at t_2 = 25 ps, three Gaussians were needed to account for the cross peaks resulting from chemical exchange. Peak volumes for each species were obtained from the Gaussian fitting parameters, assuming a circular 2D Gaussian distribution for each peak component. In the generalized transition of a species A to B, the lower corner cross peak of the diagonal peak ratios in the 2D IR spectrum can be expressed as functions of t_2. [70]

$$\frac{S_{BA}}{S_{AA}} = \frac{1 - e^{-(k_{AB}+k_{BA})\cdot t_2}}{1 + \frac{k_{AB}}{k_{BA}} \cdot e^{-(k_{AB}+k_{BA})\cdot t_2}}$$

The sum of the rate constants of a transition (k_f + k_r) was directly obtained from fitting $S_{cross\ peak}/S_{diagonal\ peak}$ with respect to t_2. Given the K_{eq} from VT-FTIR data in Table 1, k_f and k_r can be calculated separately.

5.5 Appendix

Chapter 5: The majority of the material in this chapter comes directly from a manuscript entitled “Direct observation of the intermediate in an ultrafast isomerization,” by Tyler M. Porter, Jiaxi Wang, Yingmin Li, Bo Xiang, Catherine Salsman, Joel S. Miller, Wei Xiong, and Clifford P. Kubiak, is published in *Chemical Science*, **2019**, *10*, 113–117. The dissertation author is a primary author.

Kinetic analysis:

Consider three isomers exchanging in a triangular fashion:

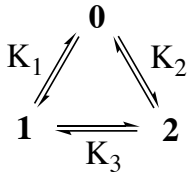

$$K_1 = \frac{k_1}{k_{-1}} \qquad K_2 = \frac{k_2}{k_{-2}} \qquad K_3 = \frac{k_3}{k_{-3}}$$

The kinetic equations governing three-site exchange are defined as:

$$\frac{d[\mathbf{1}]}{dt} = k_{-1}[\mathbf{0}] - k_1[\mathbf{1}] + k_{-3}[\mathbf{2}] - k_3[\mathbf{1}] \tag{5.2}$$

$$\frac{d[\mathbf{0}]}{dt} = k_1[\mathbf{1}] - k_{-1}[\mathbf{0}] - k_2[\mathbf{0}] + k_{-2}[\mathbf{2}] \tag{5.3}$$

$$\frac{d[\mathbf{2}]}{dt} = k_2[\mathbf{0}] - k_{-2}[\mathbf{2}] + k_3[\mathbf{1}] - k_{-3}[\mathbf{2}] \tag{5.4}$$

The mass balance for the system is:

$$[\mathbf{1}]_0 = [\mathbf{1}] - [\mathbf{0}] - [\mathbf{2}] \tag{5.5}$$

Applying a Laplace Transform to the kinetic equations we obtain:

$$P[\mathbf{1}] - P[\mathbf{1}]_0 = k_{-1}[\mathbf{0}] - k_1[\mathbf{1}] + k_{-3}[\mathbf{2}] - k_3[\mathbf{1}] \tag{5.6}$$

$$P[\mathbf{0}] = k_1[\mathbf{1}] - k_{-1}[\mathbf{0}] - k_2[\mathbf{0}] + k_{-2}[\mathbf{2}] \tag{5.7}$$

$$P[\mathbf{2}] = k_2[\mathbf{0}] - k_{-2}[\mathbf{2}] + k_3[\mathbf{1}] - k_{-3}[\mathbf{2}] \tag{5.8}$$

Which can be written as:

$$\begin{pmatrix} P + k_1 + k_3 & -k_{-1} & -k_{-3} \\ -k_1 & P + k_{-1} + k_2 & -k_{-2} \\ -k_3 & -k_2 & P + k_{-2} + -k_{-3} \end{pmatrix} \cdot \begin{pmatrix} [\mathbf{1}] \\ [\mathbf{0}] \\ [\mathbf{2}] \end{pmatrix} = \begin{pmatrix} [\mathbf{1}]_0 \\ 0 \\ 0 \end{pmatrix} \tag{5.9}$$

$$\begin{pmatrix} [\mathbf{1}] \\ [\mathbf{0}] \\ [\mathbf{2}] \end{pmatrix} = \begin{pmatrix} P + k_1 + k_3 & -k_{-1} & -k_{-3} \\ -k_1 & P + k_{-1} + k_2 & -k_{-2} \\ -k_3 & -k_2 & P + k_{-2} + -k_{-3} \end{pmatrix}^{-1} \cdot \begin{pmatrix} [\mathbf{1}]_0 \\ 0 \\ 0 \end{pmatrix} \tag{5.10}$$

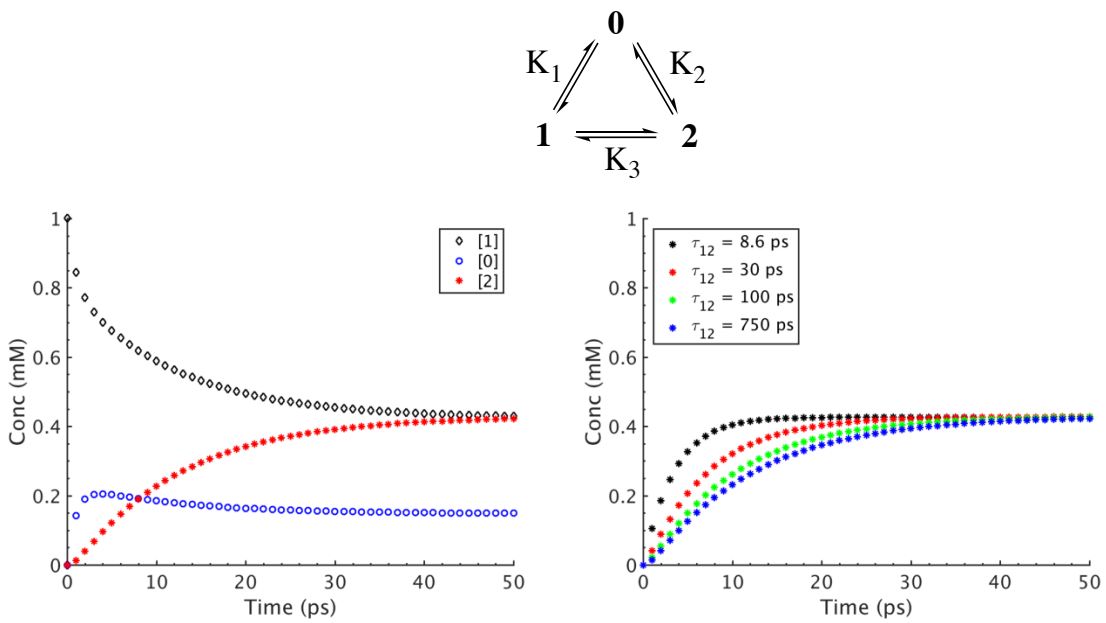

Figure 5.9. (left) Concentration profiles of **0** (black, diamonds), **1** (blue, circles), and **2** (red, stars), as a function of time as determined by analytically solving a triangular equilibrium. (right). Concentration profiles of **0** (circles), **1** (diamonds), and **2** (stars), as a function of time as with increasing τ_{12} (Black: τ_{12} = 8.6 ps; Red: τ_{12} = 30 ps; Green: τ_{12} = 100 ps; Blue: τ_{12} = 750 ps;).

Using MATLAB and the inverse Laplacian transform, expression 5.10 was solved analytically in conjunction with the 2D IR determined values for the exchange time constants allowing determination of the concentration profiles for complexes **1**, **0**, and **2** as a function of time. When only species **1** is present at t = 0 (initial conditions of $[\mathbf{1}]_0$ = 0.01 M and $[\mathbf{0}]_0 = [\mathbf{2}]_0$ = 0 M), and the 2D IR determined exchange time constants are used (Table 5.1) the concentration profiles shown on the left of Figure 5.9 are obtained. By fitting the concentration profile of **2** to a simple exponential model (eq. 5.11), a time constant of 3 ps is obtained indicating the conversion of **1** to **2** has occured several picoseconds faster than what is experimentally observed by 2D IR (8.6 (2.0) ps). While this does not directly refute the idea that direct isomerization of **1** to **2** is possible, it does indicate that a triangular pathway remains inconsistent with the experimentally observed data.

$$[\mathbf{2}] = b - ae^{\frac{-t}{\tau}} \qquad (5.11)$$

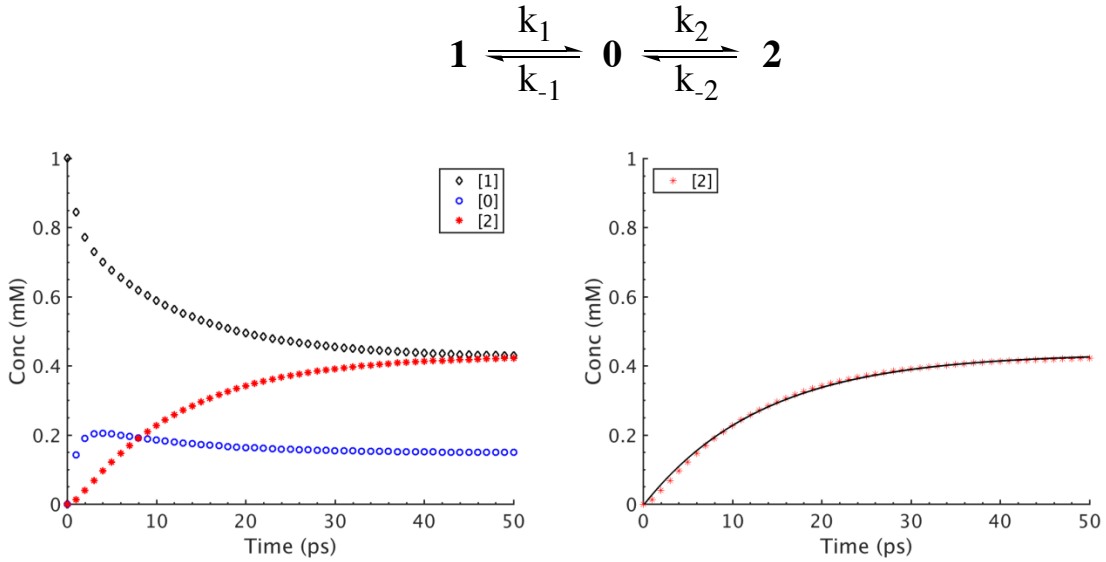

Figure 5.10. (left) Concentration profiles of **0** (black, diamonds), **1** (blue, circles), and **2** (red, stars), as a function of time as determined by analytically solving a triangular equilibrium. (right). Concentration profile of **2** (stars) as a function of time as with an exponential model supporting a time constant of 13.4 (4) ps.

Further evidence in support of a linear pathway however, is found when the exchange time constant used in the simulation (τ_{12}) is increased from 8.6 ps to 750 ps, effectively removing this pathway from the isomerization process (right, Figure 5.9). Here, when τ_{12} = 750 ps, the concentration profile of **2** is fit to equation 5.11 exchange time constant of 13.0 (4) ps are neded. This value is found to be within the experimental error of the 2D IR determined time-constant and indicates that the direct isomerization of **1** to **2** is an unlikely pathway. Furthermore, when the pathway defined as K_{12} is removed entirely and the expressions are solved for a traditional three-site exchange problem (Figure 5.10) an exponential fit of **2** using equation 5.11 require a time constant of 13.4 ps, a value in excellent agreement with the results from triangle exchange when τ_{12} = 750 ps and within the experimental error of the 2D IR observed time constant. These combined data suggest that while a definitive answer remains undetermined, it is unlikely that the dynamics of the direct **1** to **2** exchange process can compete with those involving the faster interconversions that pass through **0** as an intermediate.

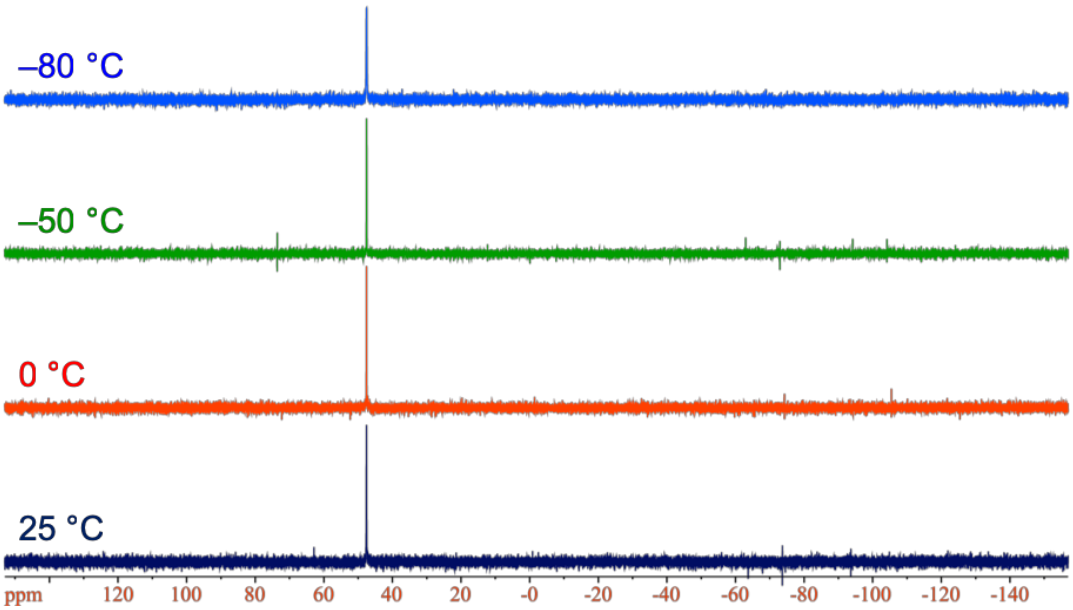

Figure 5.11. (top) Variable temperature ^{31}P NMR of $Ru(S_2C_2(CF_3)_2)(CO)(PPh_3)_2$ in DCM-d_2. (bottom) three-component.

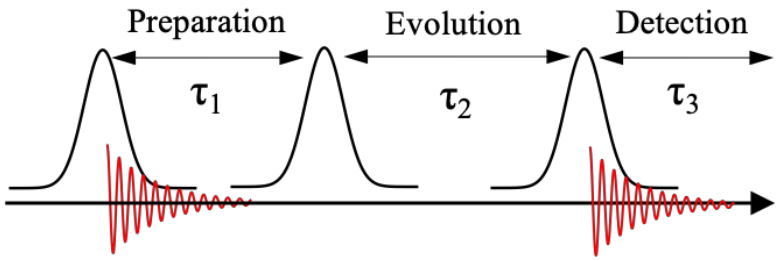

Figure 5.12. Pulse sequence used in a typical 2D IR experiment.

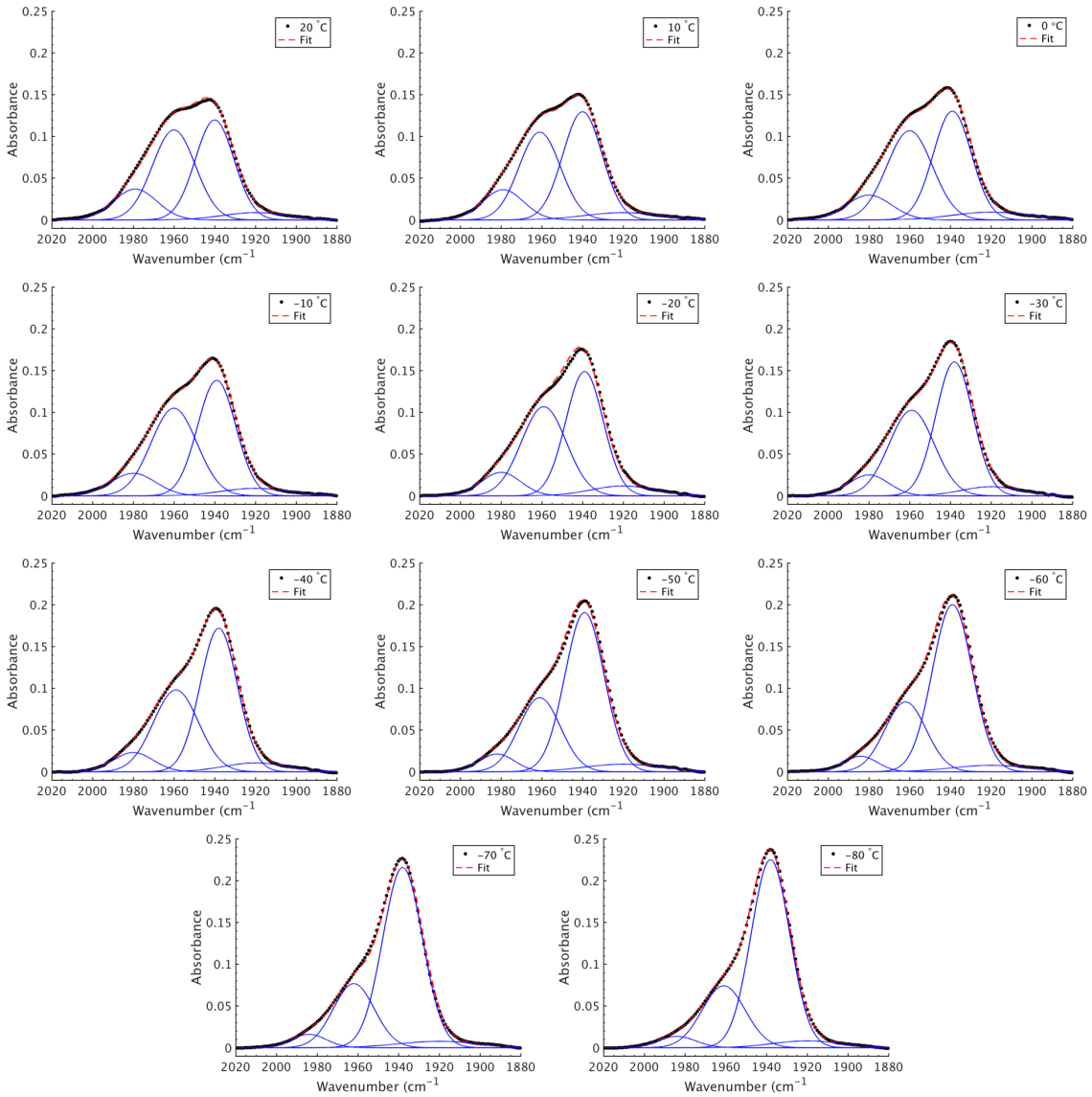

Figure 5.13. VT-FTIR fits of ν(CO) bands across the temperature range of 20 °C to –80 °C for 0 (1980 cm^{-1}), 1 (1960 cm^{-1}) and 2 (1940 cm^{-1}) in DCM.

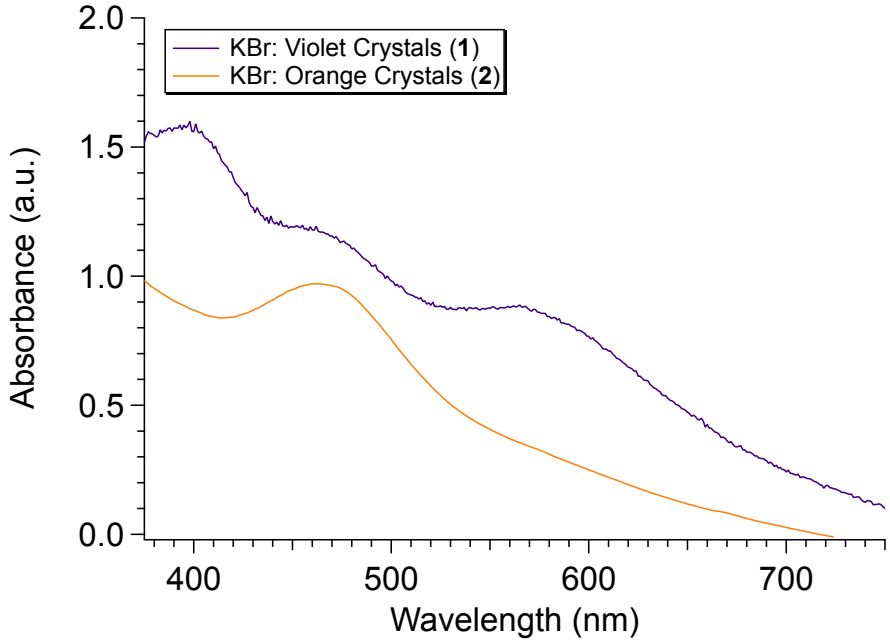

Figure 5.14. (middle). UV-vis spectra of **1** (violet trace) and **2** (orange trace) taken from independently prepared KBr pellets.

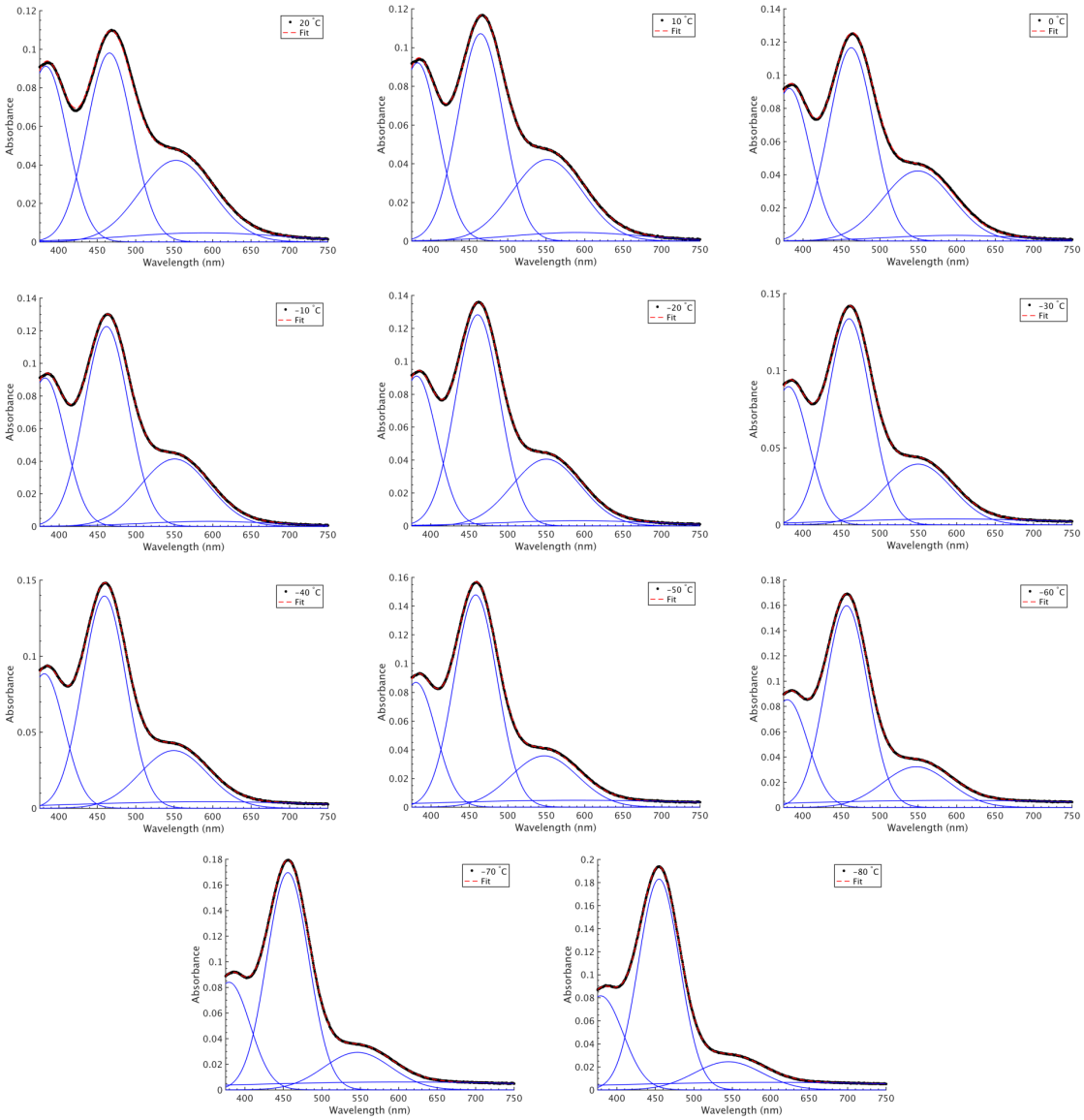

Figure 5.15. VTFT–UV/vis fits of 1 (385 and 561 nm), and 2 (470 nm) ranging from 20 to –80 °C in DCM.

5.6 References

1. Hore, P. J., *Nuclear Magnetic Resonance*. Oxford University Press Inc.: New York, 1995.
2. Cohen, B.; Weiss, S., IR lines broadened by chemical exchange. *J. Chem. Phys.* **1980,** *72* (12), 6804-6804.
3. Cohen, B.; Weiss, S., Picosecond kinetics by exchange broadening in the infrared and Raman. 1. 1,2-Dichloroethane. *J. Phys. Chem.* **1983,** *87* (19), 3606-3610.
4. Grevels, F.-W.; Jacke, J.; Klotzbücher, W. E.; Krüger, C.; Seevogel, K.; Tsay, Y.-H., Dynamic Processes on the IR Time Scale: Coalescence of CO Stretching Vibrational Bands in [(η^4-Diene)$Fe(CO)_3$] Complexes. *Angew. Chem. Int. Ed.* **1987,** *26* (9), 885-887.
5. Ito, T.; Hamaguchi, T.; Nagino, H.; Yamaguchi, T.; Washington, J.; Kubiak, C. P., Effects of Rapid Intramolecular Electron Transfer on Vibrational Spectra. *Science* **1997,** *277* (5326), 660-663.
6. Grevels, F.-W.; Kerpen, K.; Klotzbücher, W. E.; McClung, R. E. D.; Russell, G.; Viotte, M.; Schaffner, K., The Very Low Barrier of CO Site Exchange in Tricarbonyl(η^4-1,5-cyclooctadiene)iron: Picosecond Kinetics in Solution Investigated by Line Shape Simulation of the ν(CO) IR Bands and Complementary Evidence from the Course of 13CO Incorporation in a Low-Temperature Matrix. *J. Am. Chem. Soc.* **1998,** *120* (40), 10423-10433.
7. Londergan, C. H.; Kubiak, C. P., Electron transfer and dynamic infrared-band coalescence: It looks like dynamic NMR spectroscopy, but a billion times faster. *Chemistry-a European Journal* **2003,** *9* (24), 5962-5969.
8. Kubiak, C. P., Inorganic Electron Transfer: Sharpening a Fuzzy Border in Mixed Valency and Extending Mixed Valency across Supramolecular Systems. *Inorg. Chem.* **2013,** *52* (10), 5663-5676.
9. Porter, T. M.; Heim, G. P.; Kubiak, C. P., Stable Mixed-Valent Complexes Formed by Electron Delocalization Across Hydrogen Bonds of Pyrimidinone-Linked Metal Clusters. *J. Am. Chem. Soc.* **2018,** *140* (40), 12756-12759.
10. Turner, J. J.; Bühl, M., Infrared Dynamics of Iron Carbonyl Diene Complexes. *J. Phys. Chem. A* **2018,** *122* (14), 3497-3505.
11. Balch, A. L.; Miller, J., 1,2-Dithiolene complexes of ruthenium and iron. *Inorg. Chem.* **1971,** *10* (7), 1410-1415.
12. Bernal, I.; Clearfield, A.; Epstein, E. F.; Ricci, J. S.; Balch, A.; Miller, J. S., Isomeric conformations in a pentaco-ordinated ruthenium compound; crystal and molecular structures of the orange and violet isomers of $(Ph_3P)_2[(CF_3)_2C_2S_2]Ru(CO)$. *Chem. Commun.* **1973,** (2), 39-40.
13. Bernal, I.; Clearfield, A.; Ricci, J. S., Crystal structure of the orange isomer of $[(C_6H_5)_3P]_2[C_2S_2(CF_3)_2]RuCO$. *J. Cryst. Mol. Struct.* **1974,** *4* (1), 43-54.
14. Clearfield, A.; Epstein, E. F.; Bernal, I., The Crystal and Molecular Structure of the Violet Isomer of $Ru(S_2C_2(CF_3)_2)(CO)(PPh_3)_2$. *J. Coord. Chem.* **1977,** *6* (4), 227-240.
15. Hoffman, P. R.; Caulton, K. G., Solution structure and dynamics of five-coordinate d6 complexes. *J. Am. Chem. Soc.* **1975,** *97* (15), 4221-4228.
16. Hamm, P.; Lim, M.; Hochstrasser, R. M., Structure of the Amide I Band of Peptides Measured by Femtosecond Nonlinear-Infrared Spectroscopy. *J. Phys. Chem. B* **1998,** *102* (31), 6123-6138.
17. Asplund, M. C.; Zanni, M. T.; Hochstrasser, R. M., Two-dimensional infrared spectroscopy of peptides by phase-controlled femtosecond vibrational photon echoes. *Proc. Natl. Acad. Sci.* **2000,** *97* (15), 8219-8224.
18. Khalil, M.; Demirdöven, N.; Tokmakoff, A., Coherent 2D IR Spectroscopy: Molecular Structure and Dynamics in Solution. *J. Phys. Chem. A* **2003,** *107* (27), 5258-5279.

19. Zheng, J.; Kwak, K.; Fayer, M. D., Ultrafast 2D IR Vibrational Echo Spectroscopy. *Acc. Chem. Res.* **2007,** *40* (1), 75-83.

20. Anna, J. M.; Ross, M. R.; Kubarych, K. J., Dissecting Enthalpic and Entropic Barriers to Ultrafast Equilibrium Isomerization of a Flexible Molecule Using 2DIR Chemical Exchange Spectroscopy. *J. Phys. Chem. A* **2009,** *113* (24), 6544-6547.

21. Nilsen, I. A.; Osborne, D. G.; White, A. M.; Anna, J. M.; Kubarych, K. J., Monitoring equilibrium reaction dynamics of a nearly barrierless molecular rotor using ultrafast vibrational echoes. *J. Chem. Phys.* **2014,** *141* (13), 134313.

22. Eckert, P. A.; Kubarych, K. J., Dynamic Flexibility of Hydrogenase Active Site Models Studied with 2D-IR Spectroscopy. *J. Phys. Chem. A* **2017,** *121* (3), 608-615.

23. Kim, Y. S.; Hochstrasser, R. M., Chemical exchange 2D IR of hydrogen-bond making and breaking. *Proc. Natl. Acad. Sci.* **2005,** *102* (32), 11185-11190.

24. Zheng, J.; Kwak, K.; Asbury, J.; Chen, X.; Piletic, I. R.; Fayer, M. D., Ultrafast Dynamics of Solute-Solvent Complexation Observed at Thermal Equilibrium in Real Time. *Science* **2005,** *309* (5739), 1338.

25. Kwak, K.; Zheng, J.; Cang, H.; Fayer, M. D., Ultrafast Two-Dimensional Infrared Vibrational Echo Chemical Exchange Experiments and Theory. *J. Phys. Chem. B* **2006,** *110* (40), 19998-20013.

26. Cahoon, J. F.; Sawyer, K. R.; Schlegel, J. P.; Harris, C. B., Determining Transition-State Geometries in Liquids Using 2D-IR. *Science* **2008,** *319* (5871), 1820.

27. Roberts, S. T.; Ramasesha, K.; Tokmakoff, A., Structural Rearrangements in Water Viewed Through Two-Dimensional Infrared Spectroscopy. *Acc. Chem. Res.* **2009,** *42* (9), 1239-1249.

28. Rubtsov, I. V., Relaxation-Assisted Two-Dimensional Infrared (RA 2DIR) Method: Accessing Distances over 10 Å and Measuring Bond Connectivity Patterns. *Acc. Chem. Res.* **2009,** *42* (9), 1385-1394.

29. Anna, J. M.; Kubarych, K. J., Watching solvent friction impede ultrafast barrier crossings: A direct test of Kramers theory. *J. Chem. Phys.* **2010,** *133* (17), 174506.

30. Lee, K.-K.; Park, K.-H.; Joo, C.; Kwon, H.-J.; Han, H.; Ha, J.-H.; Park, S.; Cho, M., Ultrafast internal rotational dynamics of the azido group in (4S)-azidoproline: Chemical exchange 2DIR spectroscopic investigations. *Chem. Phys.* **2012,** *396*, 23-29.

31. Roberts, S. T.; Loparo, J. J.; Tokmakoff, A., Characterization of spectral diffusion from two-dimensional line shapes. *J. Chem. Phys.* **2006,** *125* (8), 084502.

32. Rosenfeld, D. E.; Gengeliczki, Z.; Smith, B. J.; Stack, T. D. P.; Fayer, M. D., Structural Dynamics of a Catalytic Monolayer Probed by Ultrafast 2D IR Vibrational Echoes. *Science* **2011,** *334* (6056), 634.

33. Rosenfeld, D. E.; Nishida, J.; Yan, C.; Kumar, S. K. K.; Tamimi, A.; Fayer, M. D., Structural Dynamics at Monolayer–Liquid Interfaces Probed by 2D IR Spectroscopy. *J. Phys. Chem. C* **2013,** *117* (3), 1409-1420.

34. Kiefer, L. M.; Kubarych, K. J., Solvent-Dependent Dynamics of a Series of Rhenium Photoactivated Catalysts Measured with Ultrafast 2DIR. *J. Phys. Chem. A* **2015,** *119* (6), 959-965.

35. King, J. T.; Anna, J. M.; Kubarych, K. J., Solvent-hindered intramolecular vibrational redistribution. *Phys. Chem. Chem. Phys.* **2011,** *13* (13), 5579-5583.

36. King, J. T.; Ross, M. R.; Kubarych, K. J., Water-Assisted Vibrational Relaxation of a Metal Carbonyl Complex Studied with Ultrafast 2D-IR. *J. Phys. Chem. B* **2012,** *116* (12), 3754-3759.

37. Fedoseeva, M.; Delor, M.; Parker, S. C.; Sazanovich, I. V.; Towrie, M.; Parker, A. W.; Weinstein, J. A., Vibrational energy transfer dynamics in ruthenium polypyridine transition metal complexes. *Phys. Chem. Chem. Phys.* **2015,** *17* (3), 1688-1696.

38. Urbanek, D. C.; Vorobyev, D. Y.; Serrano, A. L.; Gai, F.; Hochstrasser, R. M., The Two-Dimensional Vibrational Echo of a Nitrile Probe of the Villin HP35 Protein. *J. Phys. Chem. Lett.* **2010,** *1* (23), 3311-3315.

39. Mutterties, E. L.; Schunn, R. A., Pentaco-ordination. *Quarterly Reviews* **1966,** *20*, 245-299.

40. Couzijn, E. P. A.; Slootweg, J. C.; Ehlers, A. W.; Lammertsma, K., Stereomutation of Pentavalent Compounds: Validating the Berry Pseudorotation, Redressing Ugi's Turnstile Rotation, and Revealing the Two- and Three-Arm Turnstiles. *J. Am. Chem. Soc.* **2010,** *132* (51), 18127-18140.

41. Giordano, A. N.; Lear, B. J., Solvent versus Temperature Control over the Infrared Band Shape and Position in Fe(CO)3(η4-Ligand) Complexes. *J. Phys. Chem. A* **2013,** *117* (47), 12313-12319.

42. Giordano, A. N.; Lear, B. J., Comparing the Energetic and Dynamic Contributions of Solvent to Very Low Barrier Isomerization Using Dynamic Steady-State Vibrational Spectroscopy. *J. Phys. Chem. A* **2015,** *119* (15), 3545-3555.

43. Zheng, J.; Kwak, K.; Xie, J.; Fayer, M. D., Ultrafast Carbon-Carbon Single-Bond Rotational Isomerization in Room-Temperature Solution. *Science* **2006,** *313* (5795), 1951.

44. Berry, R. S., Correlation of Rates of Intramolecular Tunneling Processes, with Application to Some Group V Compounds. *J. Chem. Phys.* **1960,** *32* (3), 933-938.

45. Krespan, C. G., Bis-(polyfluoroalkyl)-acetylenes. IV. Fluorinated Dithietenes and Related Heterocyclic Compounds From Bis-(polyfluoroalkyl)-acetylenes and Sulfur1. *J. Am. Chem. Soc.* **1961,** *83* (16), 3434-3437.

46. Neese, F., An improvement of the resolution of the identity approximation for the formation of the Coulomb matrix. *J. Comput. Chem.* **2003,** *24* (14), 1740–1747.

47. Kossmann, S.; Neese, F., Comparison of two efficient approximate Hartee–Fock approaches. *Chem. Phys. Lett.* **2009,** *481* (4–6), 240–243.

48. Neese, F.; Wennmohs, F.; Hansen, A.; Becker, U., Efficient, approximate and parallel Hartree–Fock and hybrid DFT calculations. A 'chain-of-spheres' algorithm for the Hartree–Fock exchange. *Chem. Phys.* **2009,** *356* (1–3), 98–109.

49. Izsák, R.; Neese, F., An overlap fitted chain of spheres exchange method. *J. Chem. Phys.* **2011,** *135* (14), 144105.

50. Neese, F., The ORCA program system. *Wiley Interdisciplinary Reviews: Computational Molecular Science* **2012,** *2* (1), 73–78.

51. Huzinaga, S.; Andzelm, J.; Radzio-Andzelm, E.; Sakai, Y.; Tatewaki, H.; Klobukiwski, M., *Gaussian Basis Sets for Molecular Calculations*. Elsevier Science: 1983; Vol. 16, p 434.

52. Andrae, D.; Häußermann, U.; Dolg, M.; Stoll, H.; Preuß, H., Energy-adjustedab initio pseudopotentials for the second and third row transition elements. *Theor. Chem. Acc.* **1990,** *77* (2), 123–141.

53. Schäfer, A.; Horn, H.; Ahlrichs, R., Fully optimized contracted Gaussian basis sets for atoms Li to Kr. *J. Chem. Phys.* **1992,** *97* (4), 2571–2577.

54. Schäfer, A.; Huber, C.; Ahlrichs, R., Fully optimized contracted Gaussian basis sets of triple zeta valence quality for atoms Li to Kr. *J. Chem. Phys.* **1994,** *100* (8), 5829–5835.

55. Weigend, F., Accurate Coulomb-fitting basis sets for H to Rn. *Phys. Chem. Chem. Phys.* **2006,** *8* (9), 1057–1065.

56. Pantazis, D. A.; Neese, F., All-electron scalar relativistic basis sets for the 6p elements. *Theor. Chem. Acc.* **2012,** *131* (11), 1292.

57. Pantazis, D. A.; Neese, F., All-Electron Scalar Relativistic Basis Sets for the Actinides. *J. Chem. Theory Comput.* **2011,** *7* (3), 677-684.

58. Pantazis, D. A.; Neese, F., All-Electron Scalar Relativistic Basis Sets for the Lanthanides. *J. Chem. Theory Comput.* **2009,** *5* (9), 2229-2238.

59. Pantazis, D. A.; Chen, X.-Y.; Landis, C. R.; Neese, F., All-Electron Scalar Relativistic Basis Sets for Third-Row Transition Metal Atoms. *J. Chem. Theory Comput.* **2008,** *4* (6), 908-919.

60. Sinnecker, S.; Rajendran, A.; Klamt, A.; Diedenhofen, M.; Neese, F., Calculation of Solvent Shifts on Electronic g-Tensors with the Conductor-Like Screening Model (COSMO) and Its Self-Consistent Generalization to Real Solvents (Direct COSMO-RS). *J. Phys. Chem. A* **2006,** *110* (6), 2235–2245.

61. Grimme, S.; Ehrlich, S.; Goerigk, L., Effect of the damping function in dispersion corrected density functional theory. *J. Comput. Chem.* **2011,** *32* (7), 1456–1465.

62. Grimme, S.; Antony, J.; Ehrlich, S.; Krieg, H., A consistent and accurate ab initio parametrization of density functional dispersion correction (DFT-D) for the 94 elements H-Pu. *J. Chem. Phys.* **2010,** *132* (15), 154104.

63. Pettersen, E. F.; Goddard, T. D.; Huang, C. C.; Couch, G. S.; Greenblatt, D. M.; Meng, E. C.; Ferrin, T. E., UCSF Chimera–a visualization system for exploratory research and analysis. *J. Comput. Chem.* **2004,** *25* (13), 1605–1612.

64. Shim, S.-H.; Strasfeld, D. B.; Fulmer, E. C.; Zanni, M. T., Femtosecond pulse shaping directly in the mid-IR using acousto-optic modulation. *Opt. Lett.* **2006,** *31* (6), 838-840.

65. Shim, S.-H.; Zanni, M. T., How to turn your pump-probe instrument into a multidimensional spectrometer: 2D IR and Vis spectroscopiesvia pulse shaping. *Phys. Chem. Chem. Phys.* **2009,** *11* (5), 748-761.

66. Nee, M. J.; McCanne, R.; Kubarych, K. J.; Joffre, M., Two-dimensional infrared spectroscopy detected by chirped pulse upconversion. *Opt. Lett.* **2007,** *32* (6), 713-715.

67. Rock, W.; Li, Y.-L.; Pagano, P.; Cheatum, C. M., 2D IR Spectroscopy using Four-Wave Mixing, Pulse Shaping, and IR Upconversion: A Quantitative Comparison. *J. Phys. Chem. A* **2013,** *117* (29), 6073-6083.

68. Hommel, E. L.; Allen, H. C., Broadband Sum Frequency Generation with Two Regenerative Amplifiers: Temporal Overlap of Femtosecond and Picosecond Light Pulses. *Anal. Sci.* **2001,** *17* (1), 137-139.

69. Laaser, J. E.; Xiong, W.; Zanni, M. T., Time-Domain SFG Spectroscopy Using Mid-IR Pulse Shaping: Practical and Intrinsic Advantages. *J. Phys. Chem. B* **2011,** *115* (11), 2536-2546.

70. Hamm, P.; Zanni, M. T., *Concepts and methods of 2D Infrared Spectroscopy*. Cambridge University Press: New York, 2011.

Chapter 6

Phosphine Steric Electronic Effects of an Ultrafast Isomerization

6.1 Introduction

We have recently reported on the exchange dynamics of an ultrafast (picosecond) isomerization in a pentacoordinate ruthenium complex, $Ru((CF_3)_2C_2S_2)(CO)(P(Ph)_3)_2$,[1] whose fluctional nature was first reported by Miller and Balch in 1971 (Figure 6.1).[2] Early reports highlighted the isolation of two, crystals (violet (**1a**) and orange (**1c**)) whose solid state structure differed only in the orientation of the CO group about the metal.[2-5] While interconversion of the two forms was possible through judicious choice of recrystallization media,[2] the dynamics of interconversion were not resolved until nearly five decades later.[1]

Through the use of two dimensional infrared (2D IR) spectroscopy, the complex was observed to exchange in picoseconds ($k_{ex} \approx 10^{-12}$) through an observable, meta-stable intermediate.[1] A combined spectroscopic and DFT analysis suggested that the mechanism of

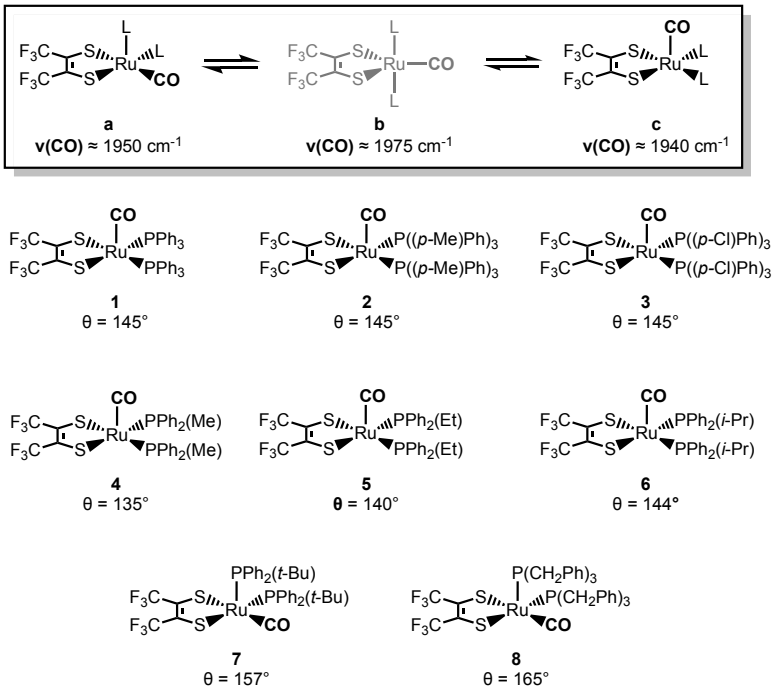

Figure 6.1. (top) Spectroscopically observed isomerization in $Ru((CF_3)_2C_2S_2)(CO)(L)_2$ as determined from **1**.[1] (bottom) The six isolated species and their respective phosphine cone angles.

isomerization followed a Berry pseudorotation (BPR) like pathway where exchange between the two square pyramidal geometries (**1a** and **1c**) involved the TBP intermediate (**1b**). To further probe what effects, steric or electronic, govern this low barrier isomerization, we report the synthesis and characterization of seven new ruthenium dithietene complexes by following a Tolman steric-electronic map.[6]

Since Tolman's original conceptualization of ligand cone angles in 1970 and despite its relative simplicity,[6] the concept of ligand cone-angles has enjoyed considerable success in describing the reactivities of numerous transition metal complexes through the consideration of ligand sterics alone. The parameter was originally developed for mono-dentate phosphine ligands and is defined as the average apex angle of the smallest cone encompassing the entire phosphine ligand. The apex of the cone originates at the metal center with the edges lying along the van der Waals' spheres of the phosphine substituents outermost atoms (Figure 6.2).[6] Following these guidelines, the phosphine ligands used in the present study were selected such that the cone

angle (θ) or the relative σ-donor strength is held constant for any given series. To account for the electronic effects of the phosphine ligands, they are ranked based upon the CO stretching frequency of monosubstituted transition metal carbonyls (such as $Ni(CO)_3L$).

Plotting the electronic parameter (ν) as a function of the ligand cone angle (θ) affords a 2D plot where both electronic and steric effects of several phosphine ligands can be readily benchmarked (Figure 6.2). Here, the steric and electronic effects of the monodentate phosphine ligands are readily accounted for by consideration of the phosphine cone angles and their relative σ–donor strengths. Complexes **1**–**3** address the of phosphine electronic effects, as *para*-substitution on the phenyl rings readily perturbs the σ–donor strength while the cone angle remains fixed. In complexes **4**–**8** however, the σ–donor strength of the phosphine ligand remains relatively constant, while the cone angle can be varied across a 29° span (135 < θ < 165°).

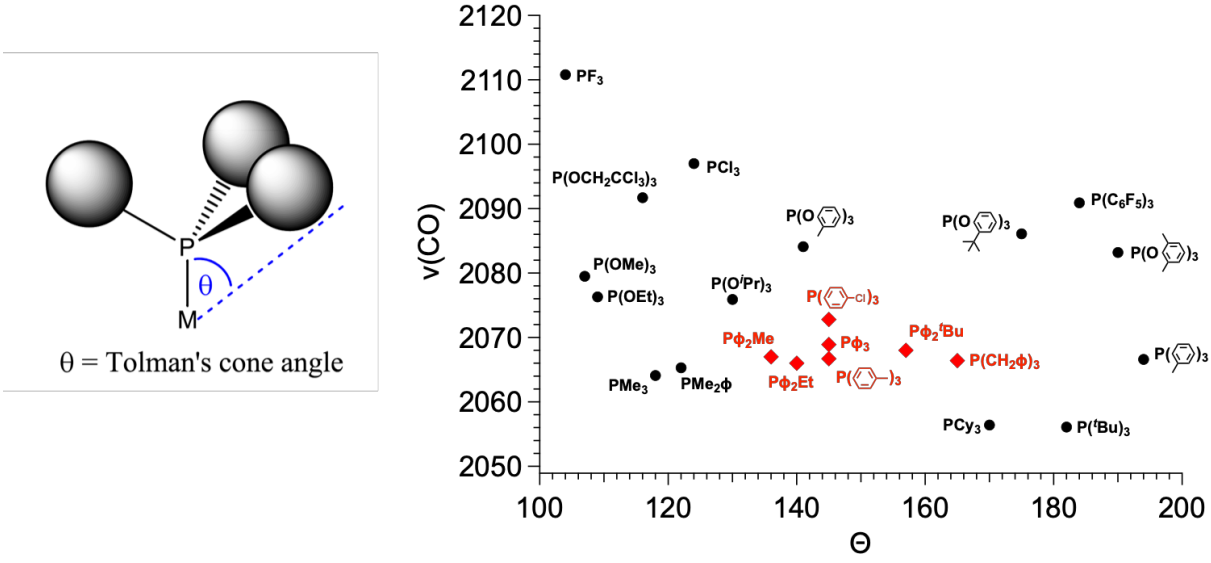

Figure 6.2. (left) Schematic representation of the Tolman cone angle for a monodentate phosphine ligand. (right) Plot of the ν(CO) frequency for $Ni(CO)_3L$ species (L = monodentate phosphine) as a function of the phosphine ligand cone angle. Phosphine ligands shown in red were of interest in the present study. Values for the electronic and steric parameters were taken from reference 6.

6.2 Results and Discussion

Complexes **2**–**8** were synthesized following a modified literature procedure, in brief: Under an inert atmosphere, ruthenium dodecacarbonyl was suspended in dry, degassed heptanes and refluxed for one hour in the presence of 1,2-hexafluorodithioketone ($(CF_3)_2C_2S_2$). After one hour, and the formation of an orange precipitate, six equivalents of the respective phosphine ligand were titrated into the heptanes solution under a stream of dry nitrogen. The resulting reaction mixture was then refluxed an additional twelve hours where complexes **2**–**8** were isolated as the second red (or green for **7**) band by column chromatography using an elutant of 7:3 DCM:Hexanes. Single crystals suitable for X-ray diffraction were then grown from DCM:Pentane mixtures (acetonitrile for **6**) at –30 °C (**2**–**6**: orange crystals, **7** and **8**: violet crystals).

Single crystal X-ray diffraction studies revealed that all complexes were square-pyramidal and differed only in the orientation of the carbonyl ligand about the metal center. The orange crystals (**2**–**6**) were found to have the CO ligand in the apical plane while the violet crystals (**7** and **8**) were found to have the CO ligand in the equatorial plane (Figure 6.3). While each complex is predicted to have additional stable isomers,[1-5] their crystallization is remarkably condition dependent and any additional isomers have yet to be crystallized. It is rather surprising however,

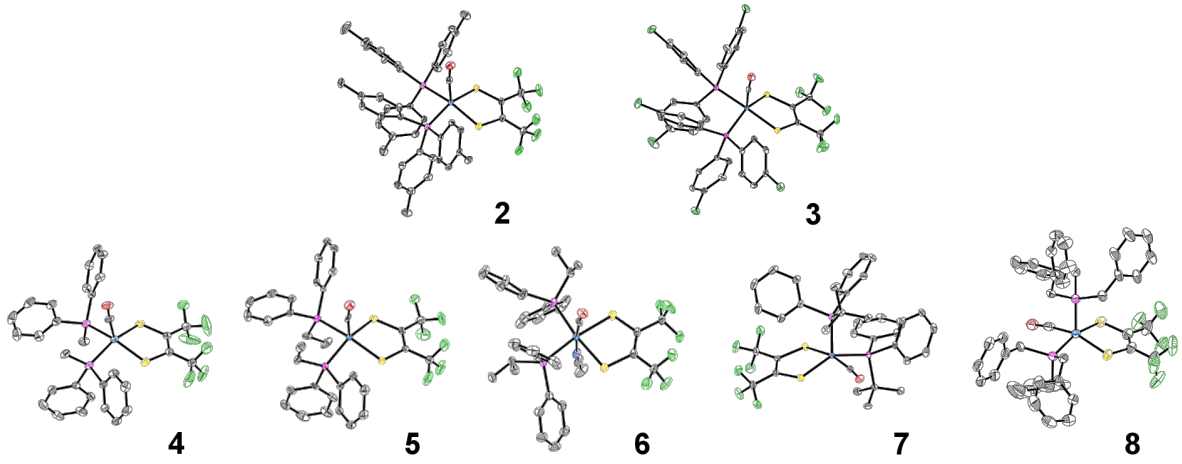

Figure 6.3. ORTEP structures of complexes **2**–**8** shown at 50% probability ellipsoids. Hydrogen atoms, co-crystallized solvent, and the rotational disorder in CF_3 groups have been omitted for clairity.

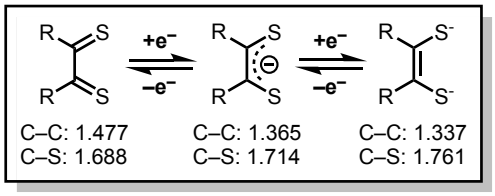

Figure 6.4. 1,2-Dithiolene ligand redox states and relevant bond distances in Å**.** Bond lengths for the singly and doubly reduced states were determined from $[Ni(Me_2C_2S_2)_2]^n$ (n = 0 or 2–, respectively),[7-8] while $[Ni(Me_2pipdt)_2]^{2+}$ was used for the neutral state.[7, 9]

Table 6.1. Selected crystallographic bond distances for 1–8 highlighting the C–C bond distances of the 1,2,-dithioketone.

Bond (Å)	1[a]		2	3	4	5	6[b]	7	8	Average
	CO_{ap}	CO_{eq}	CO_{ap}	CO_{ap}	CO_{ap}	CO_{ap}	CO_{ap}	CO_{eq}	CO_{eq}	
C(2)–C(3)	1.350	1.359	1.357	1.359	1.354	1.356	1.343	1.347	1.350	1.353
C(2)–S(1)	1.735	1.718	1.728	1.727	1.735	1.733	1.762	1.732	1.741	1.735
C(3)–S(2)	1.726	1.717	1.741	1.737	1.740	1.737	1.756	1.737	1.727	1.735

[a]Values were adapted from previously published structures.[3-5]
[b]Crystals were ground from acetonitrile solutions and the structure was found to contain a coordinating acetonitrile molecule.

that **7** and **8** readily crystalize into the $CO_{equatorial}$ isomer as previous studies indicated it is the thermodynamically un-favorable isomer.[1-2] Nevertheless, this does however reveal the initial effects of phosphine substitution, and suggests that increased ligand sterics favor the sterically less incombered $CO_{equatorial}$ isomer.[3]

While minor variations in the bonding parameters are observed (Table 6.1), suggesting a similar electronic structure for all complexes. Most importantly, comparison of the C–C and C–S bond distances of the 1,2-dithioketone ligand allow determination of the dithioketone (and metal) oxidation state (Figure 6.4).[7-8, 10] For complexes **1**–**8**, average C–C and C–S bond distances of 1.354 Å and 1.733 Å respectively, are in excellent agreement with a doubly reduced dithietene ligand (C-C: 1.337 Å and C-S: 1.761 Å),[8, 10] and suggests a formal Ru(II), 16 e^- complex. Additional support for this assignment is found by isolation of the hexa-coordinate, trisphosphine complex, $Ru((CF_3)_2C_2S_2)(CO)(P(Ph)_2(Me))_3$ (**9**, Figure 6.1).

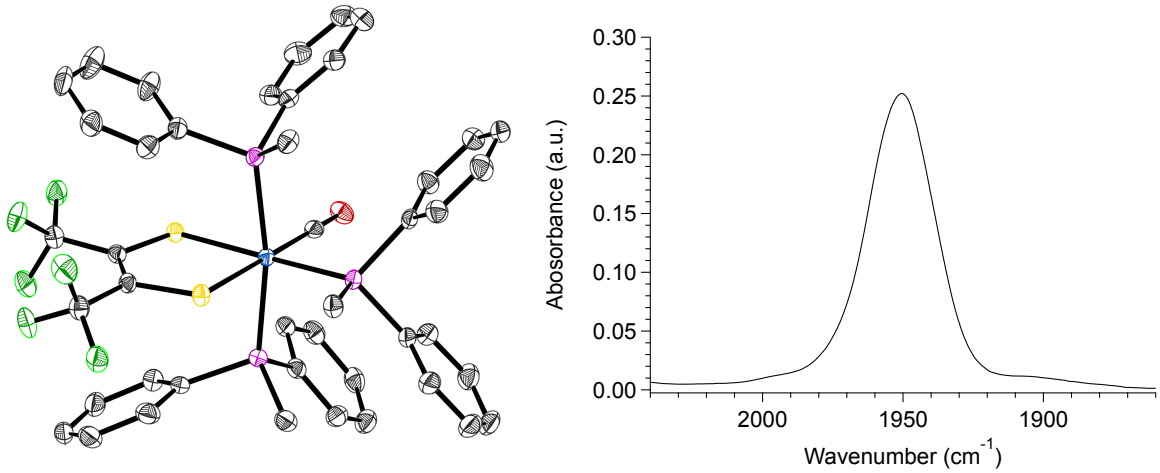

Figure 6.5. (left) ORTEP structure of **9** shown at 50% probability ellipsoids with hydrogen atoms omitted for clarity. (right) FTIR of **9** in DCM.

Based upon simple principles of electron counting, complex **9** is expected to have a doubly reduced dithietene ligand, giving the 18 e^-, Ru(II) complex. This is in excellent agreement with observed C–C and C–S bond distances of 1.350 Å and 1.765/1.752 Å respectively, supporting a Ru(II) assignment for **9**, and **1**–**8** as well. It is important to note that the trisphosphine adduct has only been isolated for complex **4**, where the relatively small cone angle (θ = 135°) is believed to allow the coordination of an additional phosphine ligand. Interestingly, while complex **9** is not expected to undergo dynamic exchange on the vibrational timescale (as judged by the narrow ν(CO) band, Figure 6.5), significantly broadened, partially coalesced NMR signals suggests a dynamic structure on the NMR timescale ($k_{ex} < 10^4$ s^{-1}, see appendix 6.5, Figure 6.31 and Figure 6.32). While additional studies are required, this remains outside of the scope of the current investigation and **9** aids only in determination of the metal oxidation state.

Upon dissolution of **2**–**8** into dichloromethane (DCM) a unique, significantly broadened ν(CO) band is observed for each complex, this behavior is indicative of exchange dynamics occurring on the vibrational timescale (Figure 6.6).[1, 11-20] Owing to the similar line shapes observed for complexes **1**–**3** (Figure 6.6) phosphine electronic effects are likely to have little impact on the isomerization reaction. Variation of the phosphine cone angles however, is observed to have an

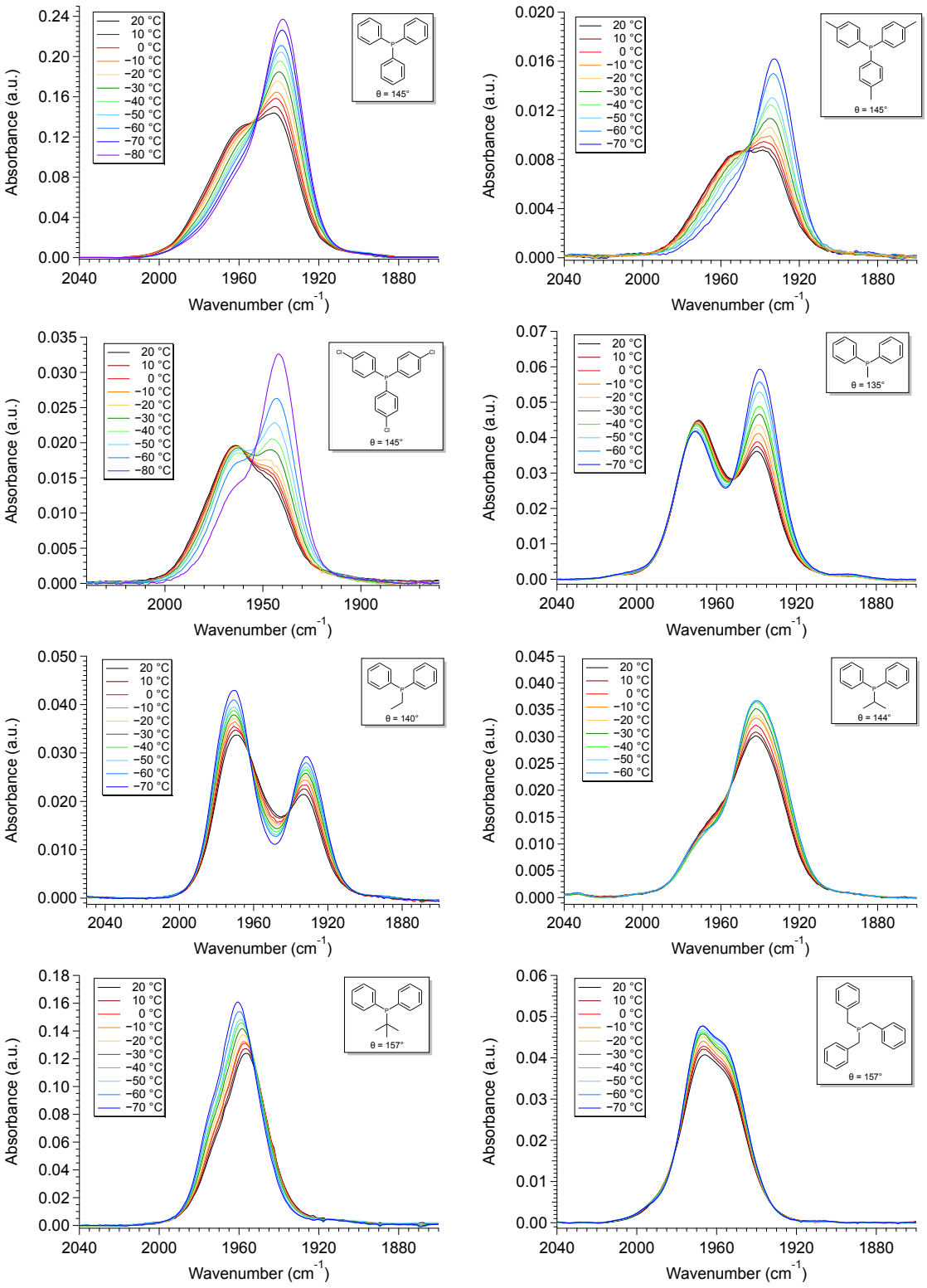

Figure 6.6. Variable temperature Fourier transform infrared (VT-FTIR) spectra of complexes **1**–**8** in DCM across a temperature range of 20 °C to –70 °C.

extensive impact. At small ligand cone angles (θ < 145°, **4** and **5**) two significantly broadened, partially coalesced ν(CO) bands are observed in the vicinity of 1936 and 1970 cm^{-1}. In comparison to complex **1** the ν(CO) bands for **4** and **5** are in excellent agreement with the $CO_{equatorial}$ (**1a**: ν(CO) ≈ 1960 cm^{-1}) and CO_{axial} (**1c**: ν(CO) ≈ 1940 cm^{-1}) isomers and the partial coalescences suggests relatively slow exchange dynamics (in comparison to the highly coalesced ν(CO) bands for **1**–**3** and **6**–**8**). Interestingly, two-component spectral deconvolutions are less than sufficient to reproduce the observed FTIR line shape (Figure 6.7 and Figure 6.8) and instead, at-least three Voigt functions are required to fit the ν(CO) bands in the vicinity of 1975 cm^{-}, 1965 cm^{-1}, and 1932 cm^{-1}. These findings are again in excellent agreement with the reported frequencies for the three isomers of complex **1** (Figure 6.1, ν(CO) ≈ **1a**:1950 cm^{-1}, **1b**: 1980 cm^{-1}, **1c**:1960 cm^{-1}),[1] and suggests the presence of the CO_{TBP} intermediate in **4** and **5**.

As the ligand cone angle is increased (θ ≈ 145°, **2**, **3**, and **6**), the ν(CO) band is observed to coalesce into a broad absorbance (FWHM ≈ 50 cm^{-1}) centered near 1958 cm^{-1}, where the nearly identical ν(CO) line shapes (in comparison to **1**) suggest very similar solution state dynamics. This however is not surprising, as similar sized phosphine ligands would be expected to display similar isomerization dynamics. These observations are confirmed through spectral deconvolution, where again, at least three Voigt functions in the vicinity of 1978 cm^{-1}, 1960 cm^{-1}, and 1940 cm^{-1} are required to fit the experimental line shape (Figure 6.7 and Figure 6.8). These findings in addition to the a nearly identical variable temperature response (Figure 6.6) support identical solution state dynamics for complexes **1**–**3** and **6**.

At large cone angles (θ > 145°, **7** and **8**), a near complete coalescence of the ν(CO) band is observed, and unlike complexes **1**–**6**, only two-component deconvolutions were required (Figure 6.7 and Figure 6.8). While this behavior would initially indicate faster rates of exchange in comparison to complexes **1**–**6**, a more likely explanation is inhibition of an isomerization pathway. Here, the deconvoluted center line frequencies (ν(CO) ≈ 1960 cm^{-1} and 1975 cm^{-1}) are in

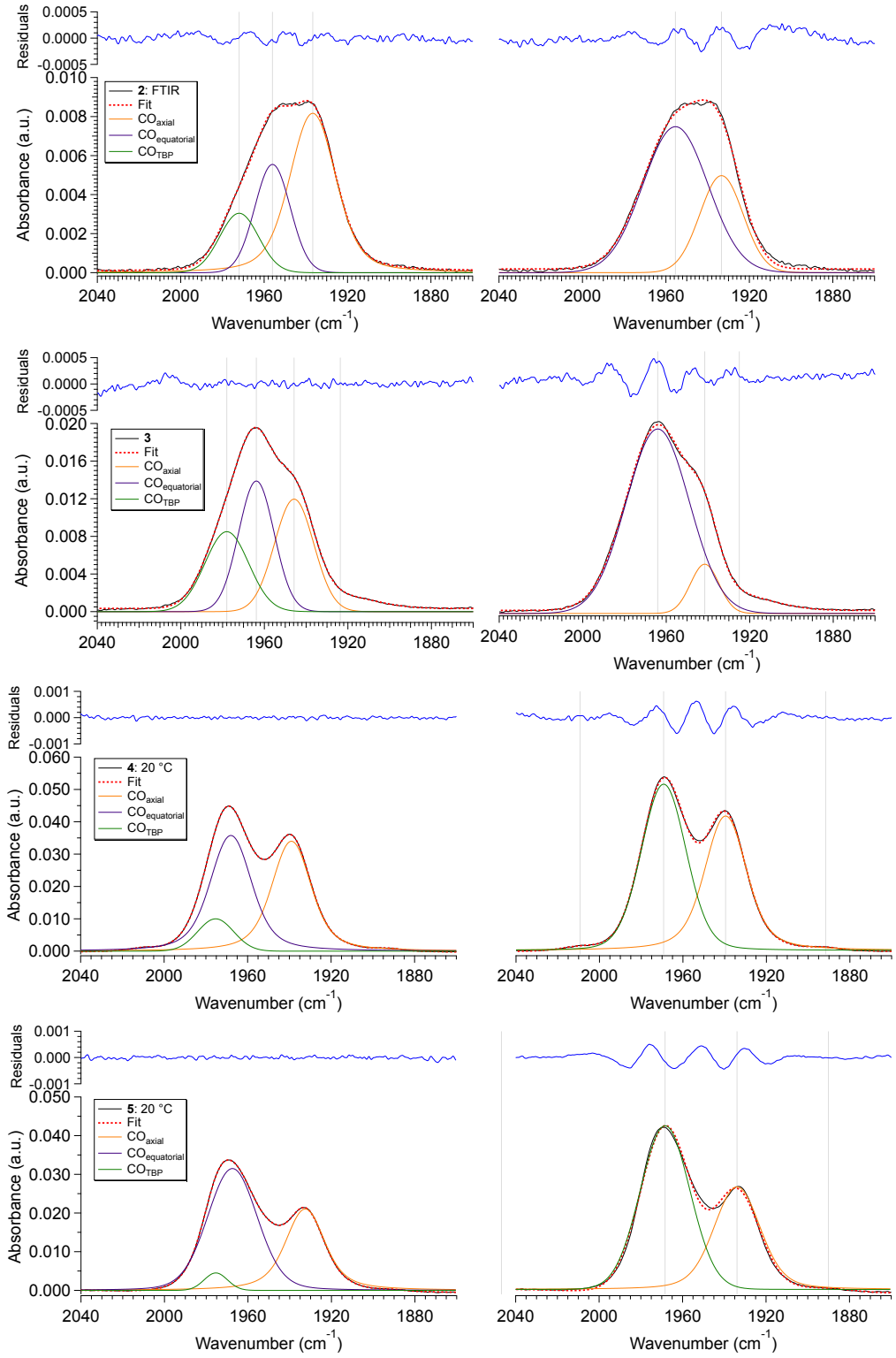

Figure 6.7. Three (left) and two (right) component spectral deconvolutions of the ν(CO) line shapes for **2**–**5** at 20 °C.

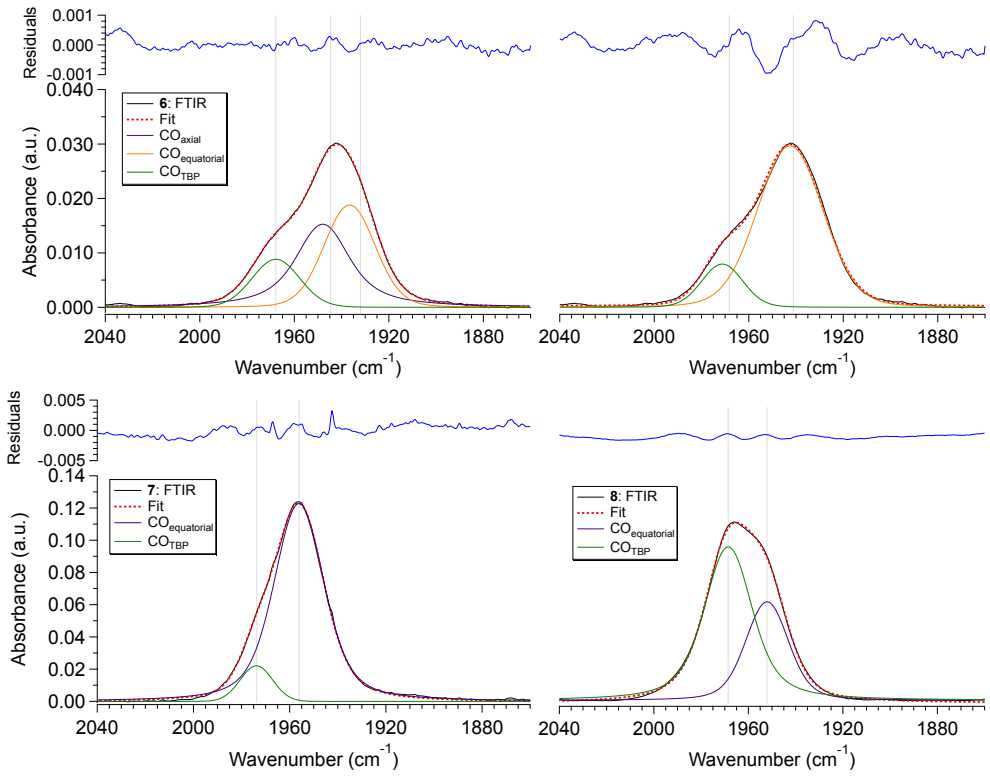

Figure 6.8. Three (left) and two (right) component spectral deconvolutions of the ν(CO) line shapes for **2**–**5** at 20 °C.

excellent agreement with observation of the $CO_{equatorial}$ and CO_{TBP} isomers and the notable lack of intensity in the vicinity of 1940 cm^{-1} suggests an absence of the CO_{axial} isomer. These findings are well supported by crystallographic and density function theory (DFT) studies (*vide infra*), where the CO_{axial} isomer is believed to be too sterically encumbered to form when exceedingly large phosphine ligands are used.

The thermodynamics of the isomerization reaction were investigated through the use of variable temperature Fourier transform infrared (VT-FTIR) spectroscopy. The VT-FTIR spectra of complexes **2**–**8** (Figure 6.6) were recorded using a SPECAC flow-through optical cryostat (Model: GS21525-C) and a Bruker Equinox 55 FTIR spectrometer. The samples were enclosed in a CaF_2 crystal windowed FTIR flow cell, contained in a vacuum jacketed housing, that was cooled using a liquid nitrogen/ethanol slurry to within 1 °C of the desired temperature using a built-in temperature controller. FTIR spectra for each complex were collected across a 100 °C span from

20 °C to –70 °C. After solvent subtraction, the VT-FTIR line shapes for each complex were fit using constrained Voigt functionals in accord with the aforementioned spectral deconvolutions (see appendix 6.5, Figure 6.13–Figure 6.16). The Voigt functionals were constrained by ± 5 cm^{-1} about the isomers center line frequencies, with FWHM constraints of 1–20 cm^{-1}, and peak heights of 0.001–0.05 a.u. Using the determined spectral areas (see appendix 6.5, Table 6.3 – Table 6.6), the population ratios of the isomers for complexes **4**–**8** were then determined (see appendix 6.5, Table 6.7–Table 6.9), allowing application of a Van 't Hoff analysis (Figure 6.9). While isomerization between the $CO_{equatorial}$ and CO_{TBP} isomers was observed for complexes **7** and **8**; interestingly, the isomerization from $CO_{equatorial}$ to CO_{TBP} in **8** was found to be exergonic, suggesting an entropically driven isomerization.

While ligand sterics likely play a major role in the thermal isomerization process, the changes in entropy across the entire series would suggest that solvation dynamics may also contribute to the overall reaction. While solvent studies are currently underway, this concept is not surprising as the reordering of solvent about each isomer would be expected to play a key role. This is especially true for an isomerization reaction occurring on the same dynamic timescale as solvent reorientation.[21-25] It is important to note however, that the thermochemical values are highly dependent on the peak locations of the spectral deconvolutions, and therefore should be only taken as estimates. While it is clear that higher ordered spectroscopy is required, two dimensional infrared spectroscopic measurements on complexes **2**–**8** are currently underway to better resolve the systems at hand.

Table 6.2. Thermochemical data obtained from the Van 't Hoff analysis of the isomerization reaction observed in complexes **4**–**8**.

Complex	Pathway	$\Delta G°_i$ (kcal mol^{-1})	ΔH_i (kcal mol^{-1})	ΔS_i (e.u.)
4	CO_{eq} to CO_{TBP}	0.9 (0.2)	1.4 (0.3)	1.9 (0.6)
	CO_{TBP} to CO_{ax}	–0.8 (0.2)	–2.2 (0.2)	4.7 (0.9)
	CO_{eq} to CO_{ax}	0.094 (0.007)	–0.76 (0.08)	–2.9 (0.4)
5	CO_{eq} to CO_{TBP}	1.6 (0.2)	1.96 (0.09)	1.1 (0.4)
	CO_{TBP} to CO_{ax}	–1.4 (0.2)	–2.1 (0.1)	–2.2 (0.5)
	CO_{eq} to CO_{ax}	0.26 (0.01)	–0.08 (0.04)	–1.2 (0.2)
7	CO_{eq} to CO_{TBP}	1.29 (0.04)	0.95 (0.03)	–1.2 (0.1)
8	CO_{eq} to CO_{TBP}	–0.40 (0.01)	0.62 (0.03)	3.4 (0.1)

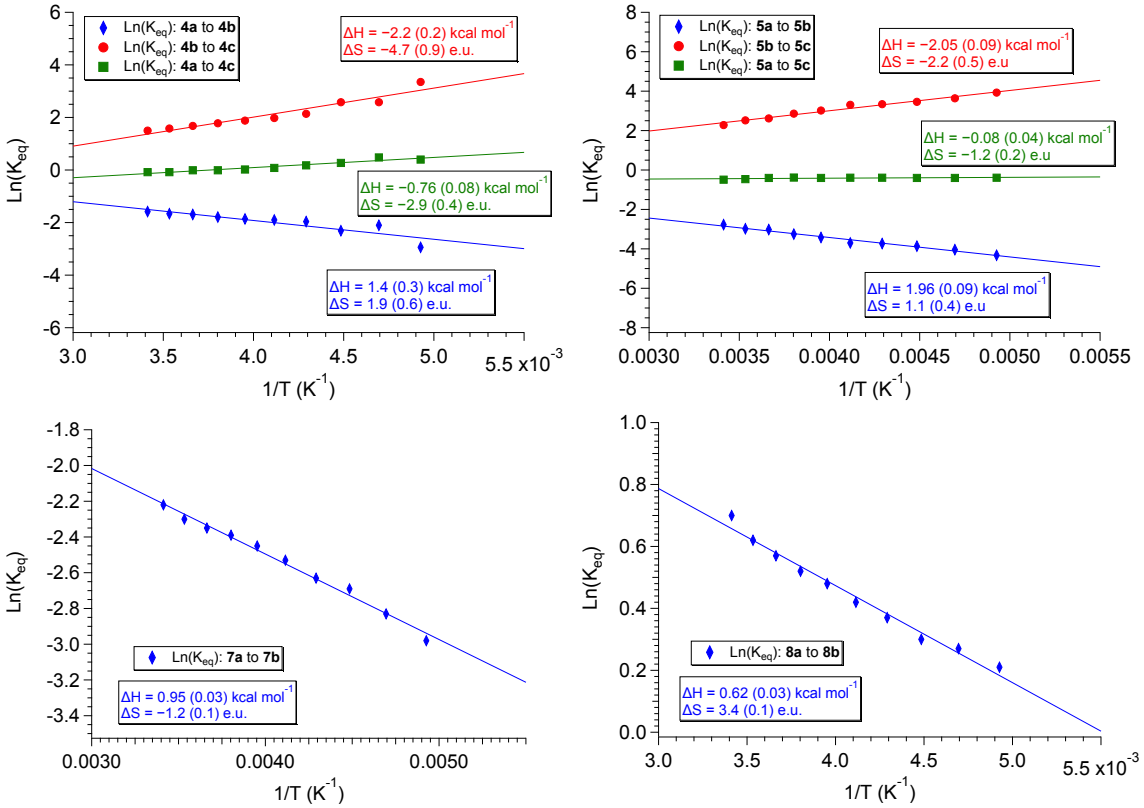

Figure 6.9. Van 't Hoff plots for complex **4** (top left), **5** (top right), **7** (bottom left), and **8** (bottom right) as determined from population ratios of the ν(CO) bands in the VT-FTIR. Equilibrium constants for isomerization from $CO_{equatorial}$ to CO_{axial} are shown as red traces, CO_{TBP} to CO_{axial} are shown as green traces, and $CO_{equatorial}$ to CO_{TBP} are shown as blue traces.

Despite the limitations of linear spectroscopy, additional support for these observations are obtained through the use of density functional theory (DFT). Due to computational time constraints DFT calculations were performed only on complexes **5** and **7** using the ORCA computational software package (version 3.0.3).[26-30] At the BP86 level of theory, all hydrogen, carbon, and fluorine atoms were treated with Alrich's def2-SVP basis set while all sulfur, phosphorous, oxygen, and ruthenium atoms were treated with the def2-TZVP basis set.[31-39] Relativistic effects were applied through the zero-order regular approximation (ZORA), dispersion corrections through a Becke-Johnson damping scheme (D3BJ), and solvation was accounted for using the conductor like screening model (COSMO) in DCM.[40-42] Initial geometries were adapted from the reported crystal structures and geometry optimizations were confirmed to be minima by frequency calculations performed at the same level of theory.

In agreement with previous studies, all three isomers for **5** were found to be minima while only the $CO_{equatorial}$ and CO_{TBPl} isomers were favorable for **7** (Figure 6.10). Interestingly, the CO_{axial}

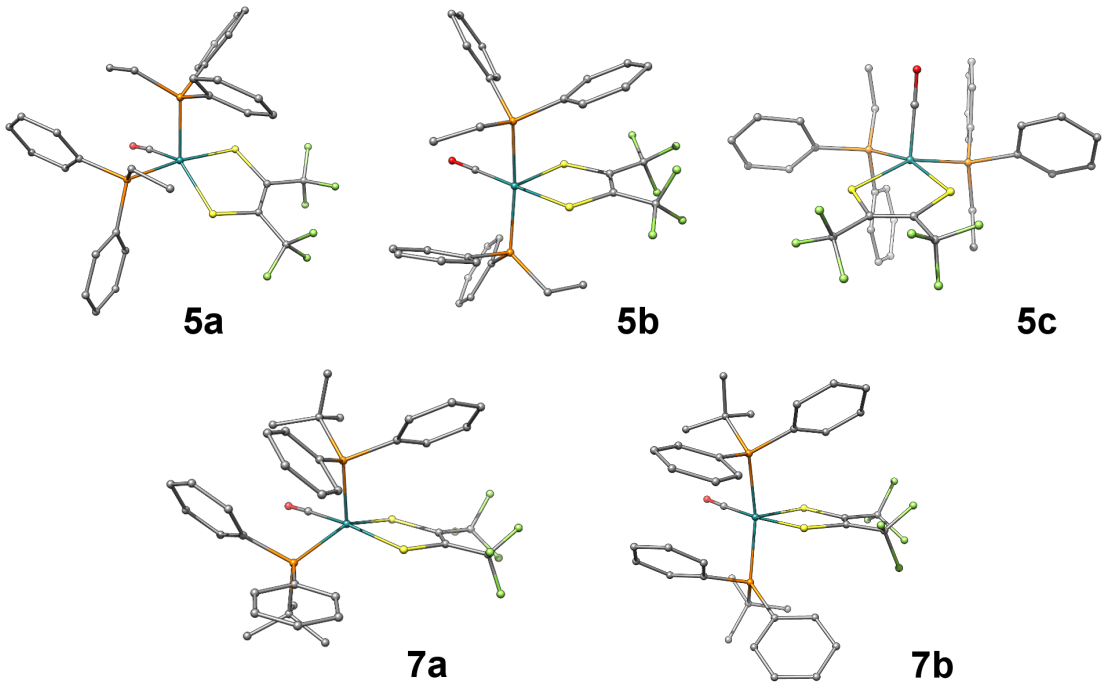

Figure 6.10. DFT optimized structures for complex **5** and **7**. All three isomers were found to be stable structures for **5** while only the $CO_{equatorial}$ and CO_{TBP} were observed to converge for **7**.

isomer for complex **7** consistently converged to a structure matching the $CO_{equatorial}$ isomer (Figure 6.11). These findings support that the CO_{axial} isomer is too sterically encumbered at large cone angles and are in agreement with experimental observations. Upon comparison of the bonding parameters from crystallography to DFT, only minor variations are observed, suggesting DFT well represents the electronic structure complexes **5** and **7** (Table 6.10). This is further confirmed by comparison of the DFT predicted FTIR with experiment (Figure 6.12). Here the DFT calculated ν(CO) bands are in excellent agreement with experiment suggesting the DFT calculated structures match those observed experimentally. This is well supported by previous studies,[1] and offers further support for the presence of the described isomers in these systems.

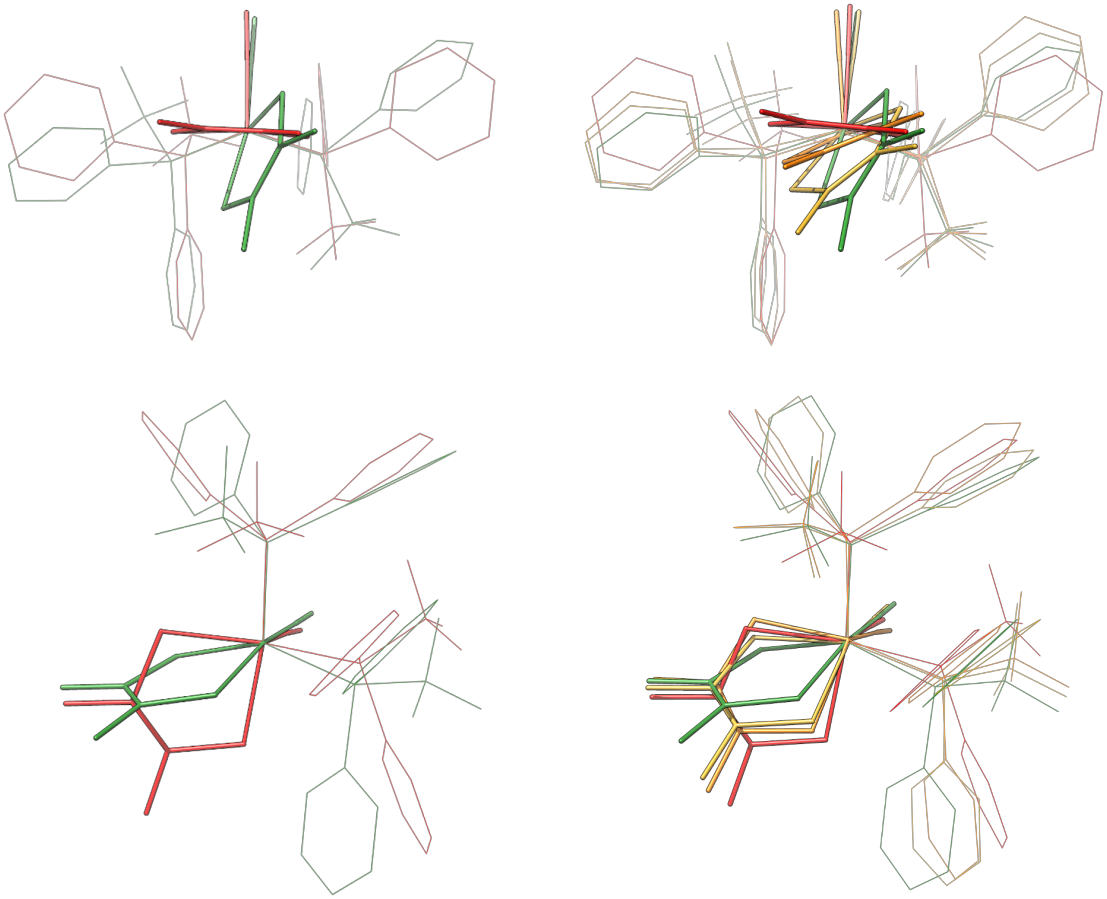

Figure 6.11. DFT optimization trajectory for isomer **7c** illustrating the transition from the starting coordinates of the CO_{axial} isomer (**7c**, red) to the ending coordinates matching the $CO_{equatorial}$ isomer (**7a**, green).

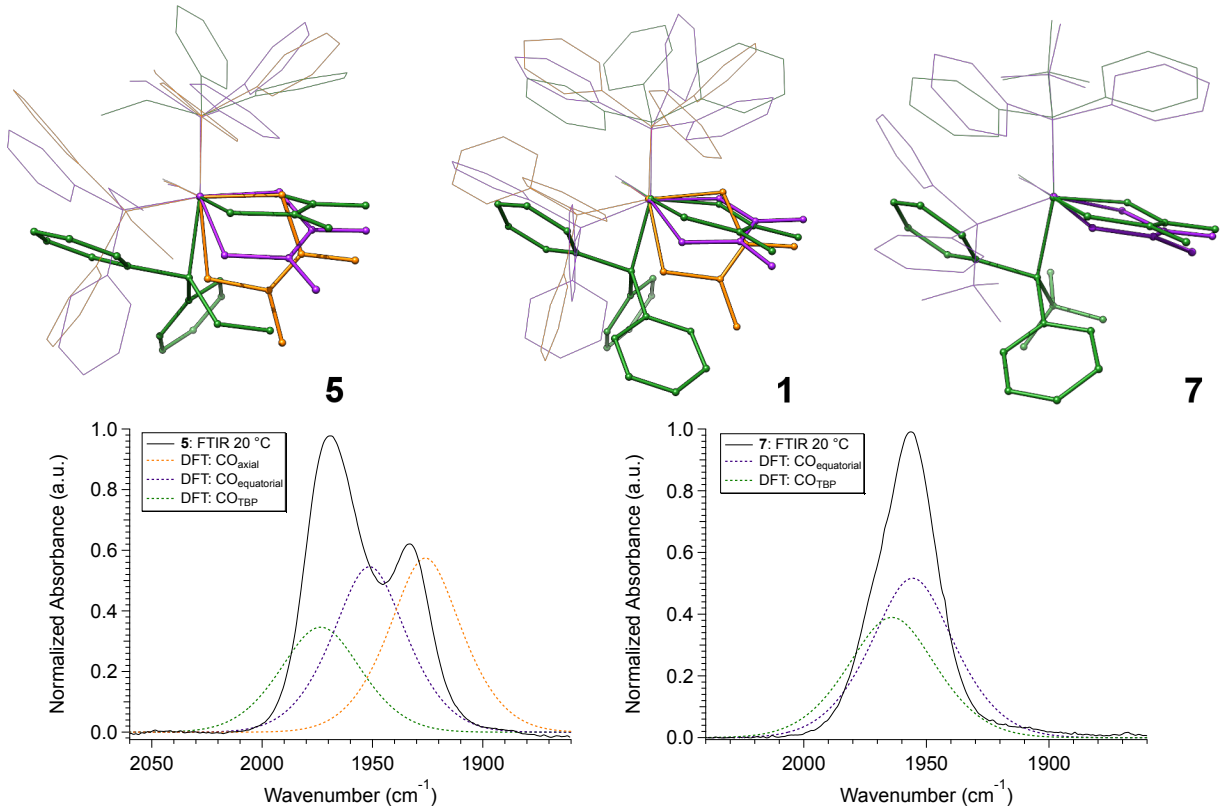

Figure 6.12. (top) Superimposed optimized structures of the CO_{axial} (orange), $CO_{equatorial}$ (violet) and CO_{TBP} (green) isomers for complexes 5 (left), 1 (middle), and 7 (right). Major differences between the structures have been highlighted in addition to the removal of H and F atoms for clarity. (bottom) Variable temperature Fourier transform infrared (VT-FTIR) spectra of 1–8 in DCM across a temperature range of 20 °C to –70 °C. (bottom) DFT predicted FTIR in comparison to experimental for **5** (left) and **7** (right).

While previous studies have proposed the isomerization shown in Figure 6.1, where isomerization is mediated by the trigonal bipyramidal intermediate, the direct isomerization between CO_{axial} and $CO_{equatorial}$ could not be ruled out.[1] Owing to the scope of the current investigation, this question is partly answered through superposition of the DFT structures (Figure 6.12). When the Ru, CO, and P atoms of each isomer are superimposed, one isomerization pathway is clearly revealed. Starting from the CO_{axial} isomer shown in orange, structural rearrangement between the CO_{axial} (orange) and $CO_{equatorial}$ (violet) occurs by a slight, 45° twist of the dithietene ligand. From here, isomerization between the $CO_{equatorial}$ (violet) and CO_{TBP} (green) isomers occurs by a second dithietene twist (< 35°), which opens a coordination site on the

ruthenium atom that was formerly occupied by the dithietne sulfur atom. This newly opened coordination site allows the phosphine ligand to "slide" into place forming the CO_{TBP} isomer (green). This would suggest that the CO_{TBP} isomer cannot be accessed directly from the CO_{axial} isomer without a complete dithietene twist. While the thermochemical data initially suggests that the CO_{TBP} is acting as an intermediate, this is only one slice along a multi-dimensional reaction pathway, and all three isomers may in fact be interconverting together. Interestingly, the magnitude required for the second dithietene twist ($CO_{equatorial}$ to CO_{TBP}) decreases with increasing phosphine cone angle is increased. This is most clearly in complex **7**, where almost no movement of the dithietene ligand is needed. This isomerization pathway is supported by the identification of several low-frequency normal modes (ν < 1000 cm^{-1}) whose nuclear displacements align with these proposed rearrangement pathways.

6.3 Conclusion

While higher ordered spectroscopy will be required to fully understand the isomerization dynamics in these systems, it remains clear that relatively large transition metal complexes can have remarkably low barriers to structural rearrangement. These findings clearly show the impact of ligand sterics and their large influence over equatorial–axial ligand exchange in and raise new questions about the role of solvent dynamics. The ability to influence isomerization pathways by steric tuning further suggests potential molecular device applications based on switching between three distinct states in systems that exhibit electronic tri-stability on the ps time scale.

6.4 Experimental

Preparation and Purification: The 2,3-hexafluorobutyne was used as received from Oakwood Chemicals, the triruthenium doedecacarbonyl was used as received from Acros Organics, and the methyldiphenylphosphine was used as received from Alfa aesar. The cyclohexane stabilized dichloromethane (DCM), was purchased from VWR International LLC, deoxygenated and dried over alumina columns on a custom built solvent system under an argon atmosphere and stored over activated 4 Å molecular sieves in a nitrogen filled glove box. The 2,3-dithiolene and $Ru(S_2C_2(CF_3)_2)(CO)(L)_2$ were prepared following modified literature reported procedures.[1-2]

$Ru(S_2C_2(CF_3)_2)(CO)(L)_2$ (2–8): Under an inert atmosphere a 100 mL Schlenk flask was charged with 200 mg (0.32 mmol, 1 eq.) triruthenium dodecacarbonyl, 325 mg (1.44 mmol, 4.5 eq) of bis(perfluoromethyl)-1,2-dithietene, and approximately 40 mL of *n*-heptane. After refluxing for one hour, a stoichiometeric amount of the phosphine ligand (L = P((*p*-Me)Ph)$_3$: 187 mg (**2**), P((*p*-Cl)Ph)$_3$: 231.1 mg (**3**), $P(Ph)_2Me$: 179.6 mg (**4**), $P(Ph)_2Et$: 186.3 mg (**5**), $P(Ph)_2{}^iPr$: 109.2 mg (**6**), $P(Ph)_2{}^tBu$: 218.1 mg (**7**), $P(CH_2Ph)_3$: 223.2 mg (**8**)) was added under a nitrogen stream followed by an additional 12 hour reflux. The solvent was then removed under vaccum to yield an orange/red solid and the ruthenium complexes were isolated by column chromatography. Using 7:3 Hexanes:DCM as the elutant, the complexes were isolated as the second red band (green for **7**) using an elutant of 7:3 Hexanes:DCM.

$Ru(S_2C_2(CF_3)_2)(CO)P((p\text{-}Me)Ph)_3$ (**2**). The complex, $Ru(S_2C_2(CF_3)_2)(CO)(P((p\text{-}Me)Ph)_3)_2$, was recrystallized at –30 °C by layering a saturated DCM solution with pentane, affording bright yellow/orange crystals identified as the axial iosomer (**2c**) of $Ru(S_2C_2(CF_3)_2)(CO)(P((p\text{-}Me)Ph)_3)_2$. Yield: 187.0 mg (62%). ^{1}H NMR (DCM-d_2, 500 MHz): δ (ppm) = 6.97 (m, 12H, C*H*), 6.90 (m, 12H, C*H*), 2.31 (s, 18H, CH_3). ^{13}C {^{1}H} NMR (DCM-d_2, 500 MHz): δ (ppm) = 230.6 (t, *C*O, J = 5 Hz), 144.89 (m, S*CC*S), 140.94 (s, *C*CH_3), 134.1 (t, *C*H, J = 5 Hz), 130.8 (m, P*C*), 129.04 (t, *C*H, *J* = 4 Hz), 123.2 (q, *C*F_3, J = 276 Hz), 21.36 (s, *C*H_3). ^{19}F NMR (DCM-d_2, 500 MHz): δ (ppm) = -53.94.

31P NMR (DCM-d_2, 500 MHz): δ (ppm) = 46.91. Anal. Calc for $C_{47}H_{42}F_6OS_2P_2Ru$: C, 58.56 %; H, 4.39 %; S, 6.65%; Found: C, 58.80 %; H, 4.24%; S, 6.19%; FTIR (CH_2Cl_2, cm^{-1}): 1944 cm^{-1} (br). UV-Vis (nm) 389, 465, 554.

Ru($S_2C_2(CF_3)_2$)(CO)P((*p*-Cl)Ph)$_3$ (**3**). The complex, Ru($S_2C_2(CF_3)_2$)(CO)(P((*p*-Cl)Ph)$_3$)$_2$, was recrystallized at –30 °C by layering a saturated DCM solution with pentane, affording bright yellow/orange crystals identified as the axial iosomer (**3c**) of Ru($S_2C_2(CF_3)_2$)(CO)(P((*p*-Cl)Ph)$_3$)$_2$. Yield: 231.1 mg (68%). ^{1}H NMR (DCM-d_2, 500 MHz): δ (ppm) = 7.24 (dd, 12H, C*H*, J = 8.6, 1.5 Hz), 6.94 (m, 12H, C*H*). ^{13}C {^{1}H} NMR (DCM-d_2, 500 MHz): δ (ppm) = 202.11 (t, *C*O, J = 15 Hz), 146.48 (m, S*CC*S), 137.9 (s, *C*Cl), 135.2 (t, *C*H, J = 15 Hz), 131.5 (P*C*, m), 130.7 (*C*Cl), 129.1 (t, *C*H, J = 5 Hz), 122.7 (q, *C*F_3, J = 276 Hz). ^{19}F NMR (DCM-d_2, 500 MHz): δ (ppm) = -54.25. ^{31}P NMR (DCM-d_2, 500 MHz): δ (ppm) = 49.14. Anal. Calc for $C_{41}H_{24}F_6Cl_6OS_2P_2Ru$: C, 45.33 %; H, 2.23 %; S, 5.90 %; Found: C, 45.23 %; H, 2.36 %; S, 6.21%; FTIR (CH_2Cl_2, cm^{-1}): 1963 (br). UV-Vis (nm) 389, 473, 554.

Ru($S_2C_2(CF_3)_2$)(CO)($PPh_2(Me)$)$_2$ (4). The complex, Ru($S_2C_2(CF_3)_2$)(CO)($PPh_2(Me)$)$_2$, was recrystallized at –30 °C by layering a saturated DCM solution with pentane, affording bright yellow/orange crystals identified as the axial iosomer (**4c**) of Ru($S_2C_2(CF_3)_2$)(CO)(PPh_2Me)$_2$. Yield: 179.6 mg (76%). ^{1}H NMR (DCM-d_2, 500 MHz): δ (ppm) = 7.38 (m, 4H, C*H*), 7.28 (m, 8H, C*H*), 7.11 (m, 8H, C*H*), 1.75 (d, 6H, PCH_3, J = 9 Hz). ^{13}C {^{1}H} NMR (DCM-d_2, 500 MHz): δ (ppm) = 201.57 (t, *C*O, J = 15 Hz), 144.62 (m, S*CC*S), 135.7 (m, P*C*), 132.2 (dt, *C*H, J = 118, 5 Hz), 130.8 (d, *C*H, J = 41 Hz), 128.8 (dt, *C*H, J = 27, 6 Hz), 123.22 (q, *C*F_3, 276 Hz), 17.68 (dt, *C*H_3, J = 34, 12 Hz). ^{19}F NMR (DCM-d_2, 500 MHz): δ (ppm) = -52.87 (C*F*$_3$). ^{31}P NMR (DCM-d_2, 500 MHz): δ (ppm) = 33.95 (*P*Ph_2Me). Anal. Calc for $C_{31}H_{26}F_6OS_2P_2Ru$: C, 49.27 %; H, 3.47 %; S, 8.49 %; Found: C, 49.42 %; H, 3.43 %; S, 8.33 %; FTIR (CH_2Cl_2, cm^{-1}): 1969 (s), 1940 (s). UV-Vis (nm) 370, 450, 522.

$Ru(S_2C_2(CF_3)_2)(CO)(PPh_2(Et))_2$ (**5**). The complex, $Ru(S_2C_2(CF_3)_2)(CO)(PPh_2(Et))_2$, was recrystallized at –30 °C by layering a saturated DCM solution with pentane, affording bright orange crystals identified as the axial iosomer (**5c**) of $Ru(S_2C_2(CF_3)_2)(CO)(PPh_2Me)_2$. Yield: 186.3 mg (76%). ^{1}H NMR (DCM-d_2, 500 MHz): δ (ppm) = 7.41 (dt, 4H, C*H*, J = 31.3, 7.2 Hz), 7.30 (dt, 8H, C*H*, J = 22.4, 7.2 Hz), 7.07 (dt, 8H, C*H*, J = 63, 8.1 Hz), 2.11 (dseptet, 4H, CH_2, J = 74.3, 7.3 Hz), 0.63 (dt, 6H, CH_3, J = 16.9, 7.3 Hz). ^{13}C {^{1}H} NMR (DCM-d_2, 500 MHz): δ (ppm) = 201.5 (t, CO, J = 14 Hz), 144.1 (m, S*CC*S), 133.5 (m, P*C*), 133.0 (m, *C*H), 130.6 (d, *C*H, J = 8 Hz), 128.6 (dt, *C*H, J = 15, 5 Hz), 123.3 (q, *C*F_3, J = 276 Hz), 24.7 (m, *C*H_2), 9.0 (s, *C*H_3). ^{19}F NMR (DCM-d_2, 500 MHz): δ (ppm) = –52.7 (C*F*$_3$). ^{31}P NMR (DCM-d_2, 500 MHz): δ (ppm) = 46.20 (*P*Ph_2Me). Anal. Calc for $C_{33}H_{30}F_6OS_2P_2Ru$: C, 50.57 %; H, 3.86 %; S, 8.18 %; Found: C, 50.92 %; H, 4.29 %; S, 7.81 %; FTIR (CH_2Cl_2, cm^{-1}): 1970 (s), 1933 (s). UV-Vis (nm) 370, 454, 530.

$Ru(S_2C_2(CF_3)_2)(CO)(PPh_2(^iPr))_2$ (**6**). The complex, $Ru(S_2C_2(CF_3)_2)(CO)(PPh_2(^iPr))_2$, was recrystallized at –30 °C by from acetonitrile, affording bright yellow/orange crystals identified as the axial iosomer (**6c**) of $Ru(S_2C_2(CF_3)_2)(CO)(PPh_2(t\text{-}Bu))_2$. The coordinated acetonitrile can be removed under vacuum, where crystals are observed to transition from yellow/orange to a deep red. Yield: 109.2 mg (43%). ^{1}H NMR (DCM-d_2, 500 MHz): δ (ppm) = 7.38 (dt, 4H, C*H*, J = 39.1, 7.5 Hz), 7.29 (dt, 8H, C*H*, J = 17.2, 8.5 Hz), 7.04 (dt, 8H, C*H*, J = 116, 8.6 Hz), 2.60 (m, 2H, C*H*$(CH_3)_2$), 0.72 (ddd, 12H, CH(C$H_3)_2$, J = 109, 16.2, 6.8 Hz). ^{13}C {^{1}H} NMR (DCM-d_2, 500 MHz): δ (ppm) = 203.7 (t, *C*O, J = 14 Hz), 143.2 (m, S*CCS*), 133.9 (dt, *C*H, J = 51, 4 Hz) 131.4 (m, P*C*), 130.1 (d, *C*H, J = 54 Hz), 127.9 (dt, *C*H, J = 34, 5 Hz), 122.9 (q, *C*F_3, J = 276 Hz), 31.7 (dt, *C*H$(CH_3)_2$, J = 28.7, 7.2 Hz), 18.3 (d, CH(*C*$H_3)_2$, J = 27.4 Hz). ^{19}F NMR (DCM-d_2, 500 MHz): δ (ppm) = -52.86. ^{31}P NMR (DCM-d_2, 500 MHz): δ (ppm) = 57.07. Anal. Calc for $C_{35}H_{34}F_6OS_2P_2Ru$•ACN: C, 52.11 %; H, 4.37 %; N, 1.64 %; S, 7.52 %; Found: C, 51.86 %; H, 4.54 %; N, 2.23 %; S, 7.55 %; FTIR (cm^{-1}): 1942 (br). UV-Vis (nm) 386, 455, 554.

$Ru(S_2C_2(CF_3)_2)(CO)(PPh_2(^tBu))_2$ (**7**). The complex, $Ru(S_2C_2(CF_3)_2)(CO)(PPh_2(^tBu))_2$, was recrystallized at –30 °C by layering a saturated DCM solution with pentane, affording dark red/violet crystals identified as the equatorial iosomer (**7a**) of $Ru(S_2C_2(CF_3)_2)(CO)(PPh_2(t\text{-}Bu))_2$. Yield: 218.1 mg (83%). ^{1}H NMR (DCM-d_2, 500 MHz): δ (ppm) = 7.35 (m, 6H, C*H*), 7.28 (m, 2H, C*H*), 7.11 (m, 12H, C*H*), 0.76 (d, 18H, CH_3, J = 15 Hz). ^{13}C {^{1}H} NMR (DCM-d_2, 500 MHz): δ (ppm) = 202.26 (t, *C*O, 15 Hz), 144.77 (m, S*CC*S), 134.3 (d, CH, J = 217 Hz), 132.7 (dd, P*C*, J = 275 Hz), 129.8 (d, *C*H, J = 55 Hz), 127.35 (d, *C*H, J = 65 Hz), 123.06 (q, *C*F_3, J = 275 Hz), 36.1 (*C*$(CH_3)_3$, m), 28.15 (s, C(*C*$H_3)_3$). ^{19}F NMR (DCM-d_2, 500 MHz): δ (ppm) = -53.44. ^{31}P NMR (DCM-d_2, 500 MHz): δ (ppm) = 74.47. Anal. Calc for $C_{37}H_{38}F_6OS_2P_2Ru$: C, 52.92 %; H, 4.56 %; S, 7.63 %; Found: C, 53.32 %; H, 4.53 %; S, 7.84 %; FTIR (CH_2Cl_2, cm^{-1}): 1956 (br). UV-Vis (nm) 377, 468, 594.

$Ru(S_2C_2(CF_3)_2)(CO)(P(CH_2Ph)_3)_2$ (**8**). The complex, $Ru(S_2C_2(CF_3)_2)(CO)(P(CH_2Ph)_3)_2$, was recrystallized at –30 °C by layering a saturated DCM solution with pentane, affording dark red/violet crystals identified as the axial iosomer (**8a**) of $Ru(S_2C_2(CF_3)_2)(CO)(P(CH_2Ph)_3)_2$. Yield: 223.2 mg (74%). ^{1}H NMR (DCM-d_2, 500 MHz): δ (ppm) = 7.24 (m, 18H, C*H*), 6.92 (m, 12H, C*H*), 3.07 (m, 12H, CH_2). ^{13}C {^{1}H} NMR (DCM-d_2, 500 MHz): δ (ppm) = 199.78 (t, *C*O, J = 15 Hz), 143.12 (m, S*CC*S), 133.9 (P*C*), 130.71 (*C*H), 129.19 (*C*H), 127.56 (*C*H), 123.38 (q, CF_3, J = 272 Hz), 38.28 (m, *C*H_2). ^{19}F NMR (DCM-d_2, 500 MHz): δ (ppm) = -53.32. ^{31}P NMR (DCM-d_2, 500 MHz): δ (ppm) = 51.07. Anal. Calc for $C_{47}H_{42}F_6OS_2P_2Ru$: C, 58.56 %; H, 4.39 %; S, 6.65 %; Found: C, 58.35 %; H, 4.72 %; S, 6.36 %; FTIR (CH_2Cl_2, cm^{-1}): 1966 (br). UV-Vis (nm) 525, 448, 367.

$Ru(S_2C_2(CF_3)_2)(CO)(P(Ph)_2(Me))_3$ (**9**). The complex, $Ru(S_2C_2(CF_3)_2)(CO)(P(Ph)_2(Me))_3$, was synthesized by dissolution of 100.0 mgs (0.132 mmol) of complex **4** into DCM, followed by the addition of 29.1 mg (0.146 mmol) of diphenylmethylphosphine. The complex was recrystallized at

–30 °C by layering a saturated DCM solution with pentane, affording bright yellow crystals identified as the trisphosphine adduct $Ru(S_2C_2(CF_3)_2)(CO)(P(Ph)_2(Me))_3$ (**9**). Yield: 103.7 mg (82 %). ^{1}H NMR (DCM-d_2, 500 MHz): δ (ppm) =7.35 (s, 12H, C*H*), 7.25 (s, 6H, C*H*), 7.15 (s, 12H, C*H*), 1.82 (s, 9H, PCH_3,). ^{13}C {^{1}H} NMR (DCM-d_2, 500 MHz): δ (ppm) = 202.76 (s, *C*O), 150.24 (m, S*CC*S) 136.09 (s, P*C*), 132.12 (s, *C*H), 129.37 (s, *C*H), 128.23 (*C*H), 123.05 (q, *C*F_3, J = 272 Hz), 11.61 (s, P*C*H_3). ^{19}F NMR (DCM-d_2, 500 MHz): δ (ppm) = –54.61. ^{31}P NMR (DCM-d_2, 500 MHz): δ (ppm) = 8.95, –6.15; Anal. Calc for $C_{44}H_{39}F_6OS_2P_3Ru$: C, 55.29 %; H, 4.11 %; S, 6.71 %; Found: C, 55.39 %; H, 4.11 %; S, 7.13 %; FTIR (CH_2Cl_2, cm^{-1}): 1948 (s). UV-Vis (nm) 343, 457.

Infrared Data Collection and Analysis. Infrared spectra were collected on a Bruker Equinox 55 FTIR spectrometer using a SPECAC flow through optical cryostat (model, 21525) with a 1.12 mm path length (determined from infringing pattern), CaF_2 windowed cell enclosed in a vacuum jacketed housing. Solutions were prepared in a nitrogen filled glove box using pre-dried DCM and *pure* orange crystals. Cell temperature (± 1 °C) was regulated by addition of liquid nitrogen/methanol to the cooling compartment while heating the cell compartment to the desired temperature with a computer controlled thermocouple/heating coil system. Both solutions of the complex and solvent blanks were recorded at temperatures ranging from 30 °C to –68 °C to ensure accurate solvent subtraction. To obtain the integrated spectral areas for the exchanging species, spectral curve fitting was carried out in IGOR Pro (WaveMetrics Inc., version 7.05).

Density Functional Theory Analysis. Calculations were performed in the ORCA software suite (version 3.0.3) at the BP86 level of theory with the RIJCOSX approximation.[26-30] Ruthenium, phosphorous, sulfur, and oxygen atoms were treated with the DEF2-TZVP basis sets while DEF2-SVP was used for all other atoms.[31-39] Dispersion corrections were applied using the atom-pairwise dispersion correction with a Becke-Johnson damping scheme (D3BJ), relativistic effects with the ZORA model, and solvation was accounted for using the COSMO solvation model in

methylene chloride.[40-42] Analytical frequency calculations were performed at the same level of theory. Molecular graphics were constructed with the UCSF Chimera package.[43]

NMR Data Collection and Analysis. NMR spectra were recorded on a JEOL 500 MHz NMR spectrometer and analyzed using iNMR software. Samples were prepared in dichloromethane-d_2 and referenced to solvent residuals for ^{1}H and ^{13}C, trifluoroethanol for ^{19}F, and phosphoric acid for ^{31}P NMR. A total of 16 scans of 32768 data points from –2 to 14 ppm were collected for ^{1}H NMR, 16 scans of 65536 data points from –220 to 20 ppm for ^{19}F NMR, and 64 scans of 32768 data points from –250 to 150 ppm for ^{31}P NMR.

6.5 Appendix

Chapter 6: This chapter is currently being prepared for submission for publication. "Phosphine Steric-Electronic Effects of an Ultrafast Isomerization," by Tyler M. Porter, Andrew L. Osterircher, and Clifford P. Kubiak. The dissertation author is the primary author.

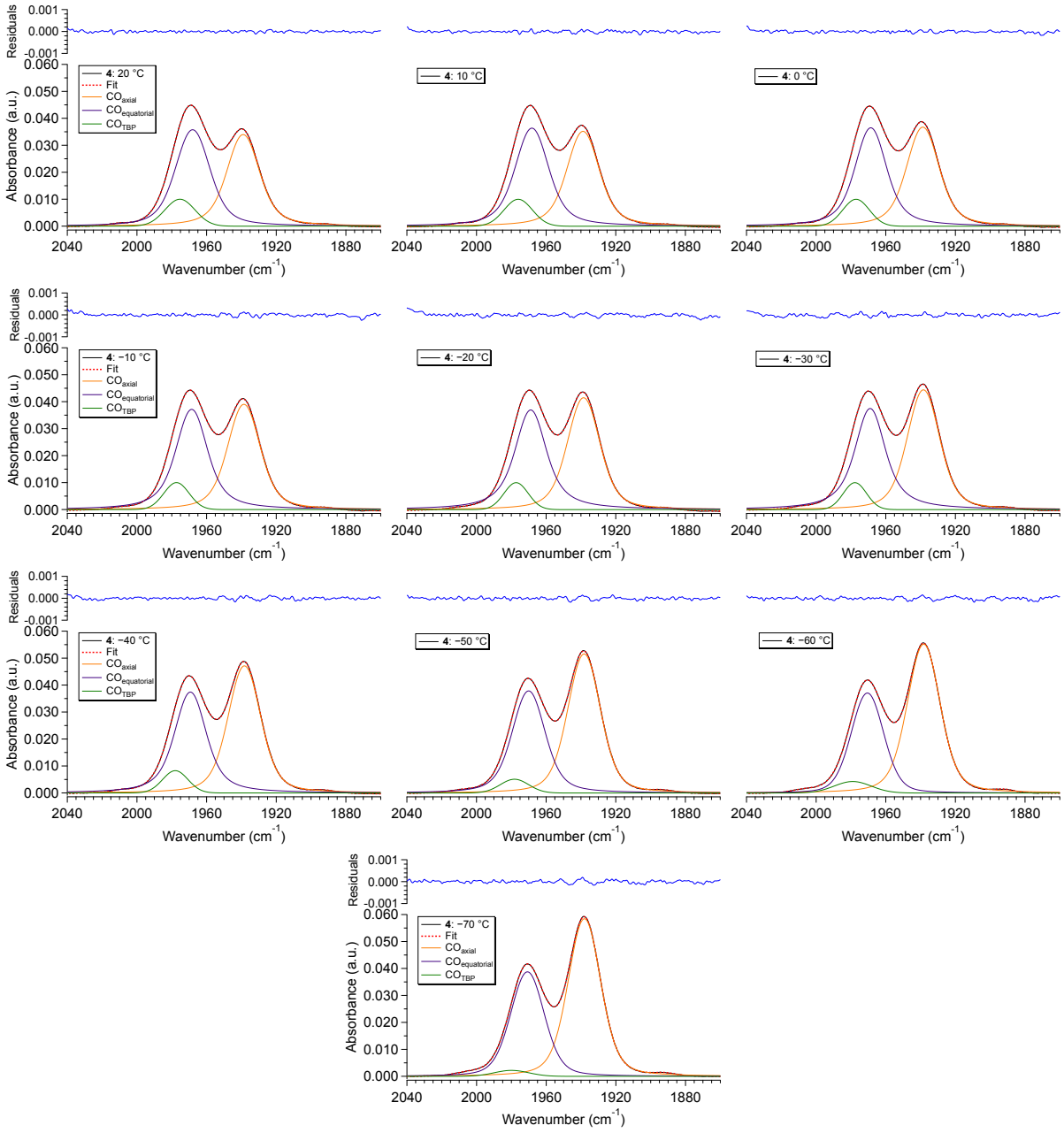

Figure 6.13. Spectral deconvolution of the variable temperature FTIR (VT-FTIR) spectra for complex **4** in DCM from 20 °C to –70 °C.

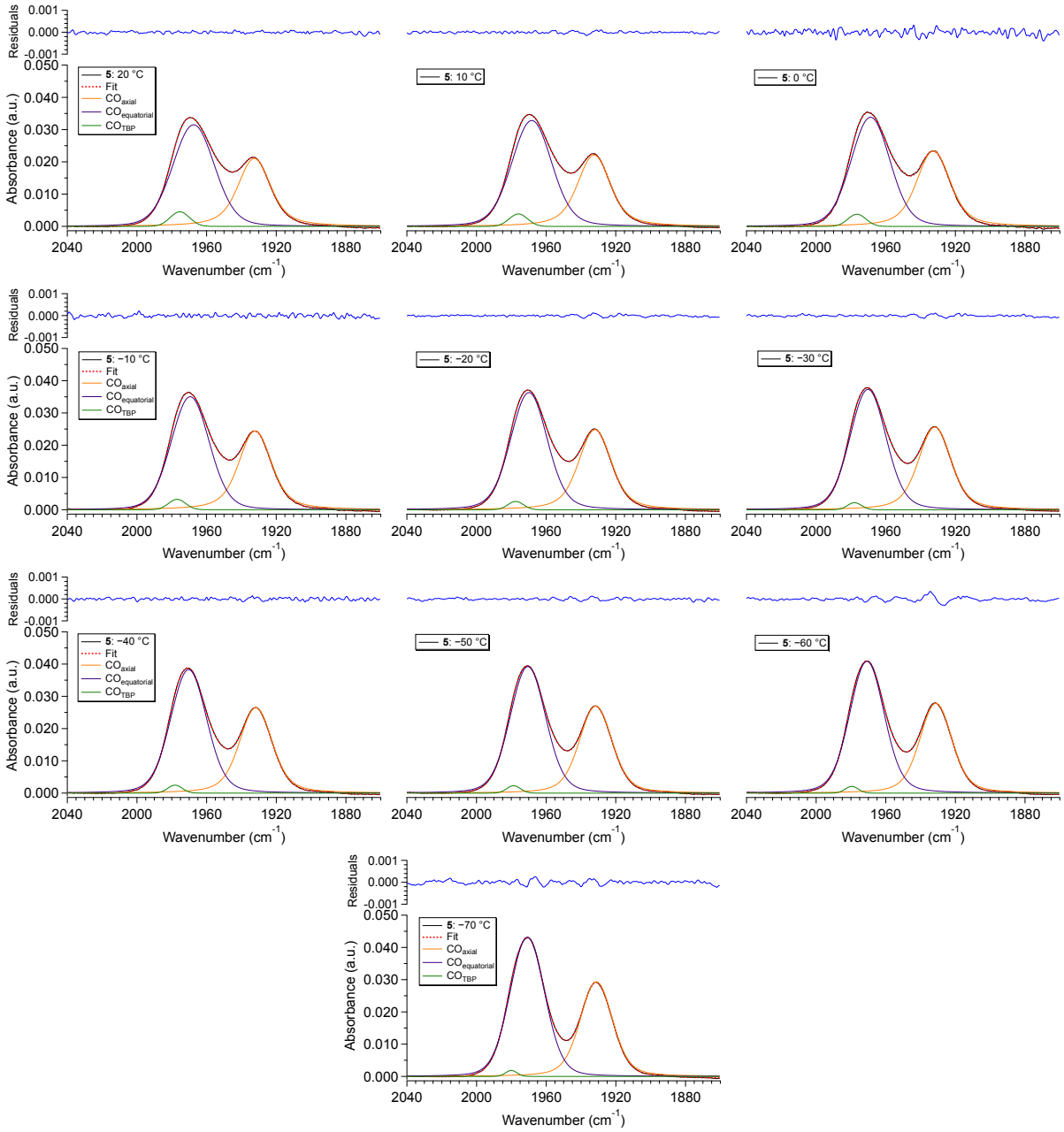

Figure 6.14. Spectral deconvolution of the variable temperature FTIR (VT-FTIR) spectra for complex **5** in DCM from 20 °C to –70 °C.

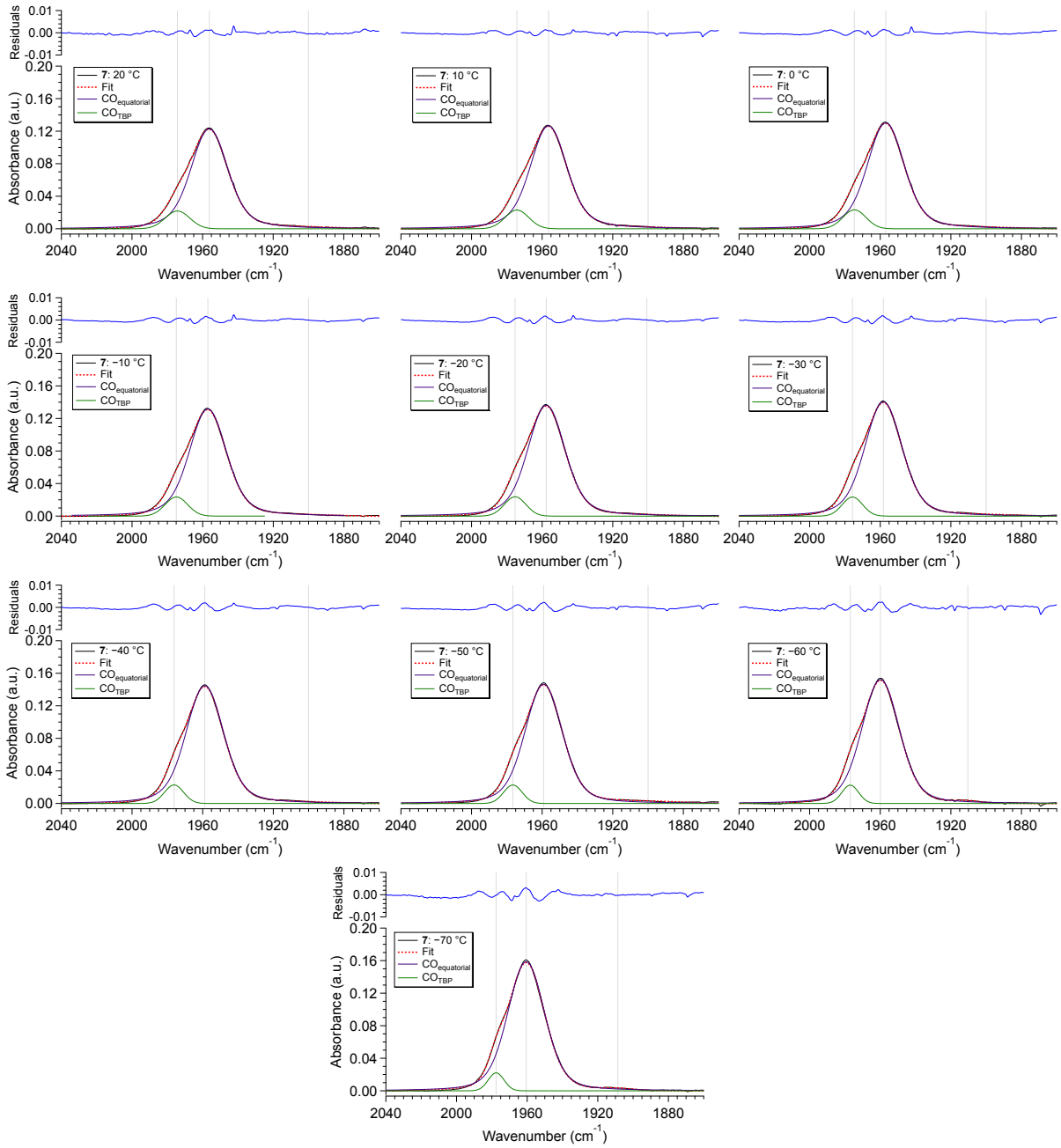

Figure 6.15. Spectral deconvolution of the variable temperature FTIR (VT-FTIR) spectra for complex **7** in DCM from 20 °C to –70 °C.

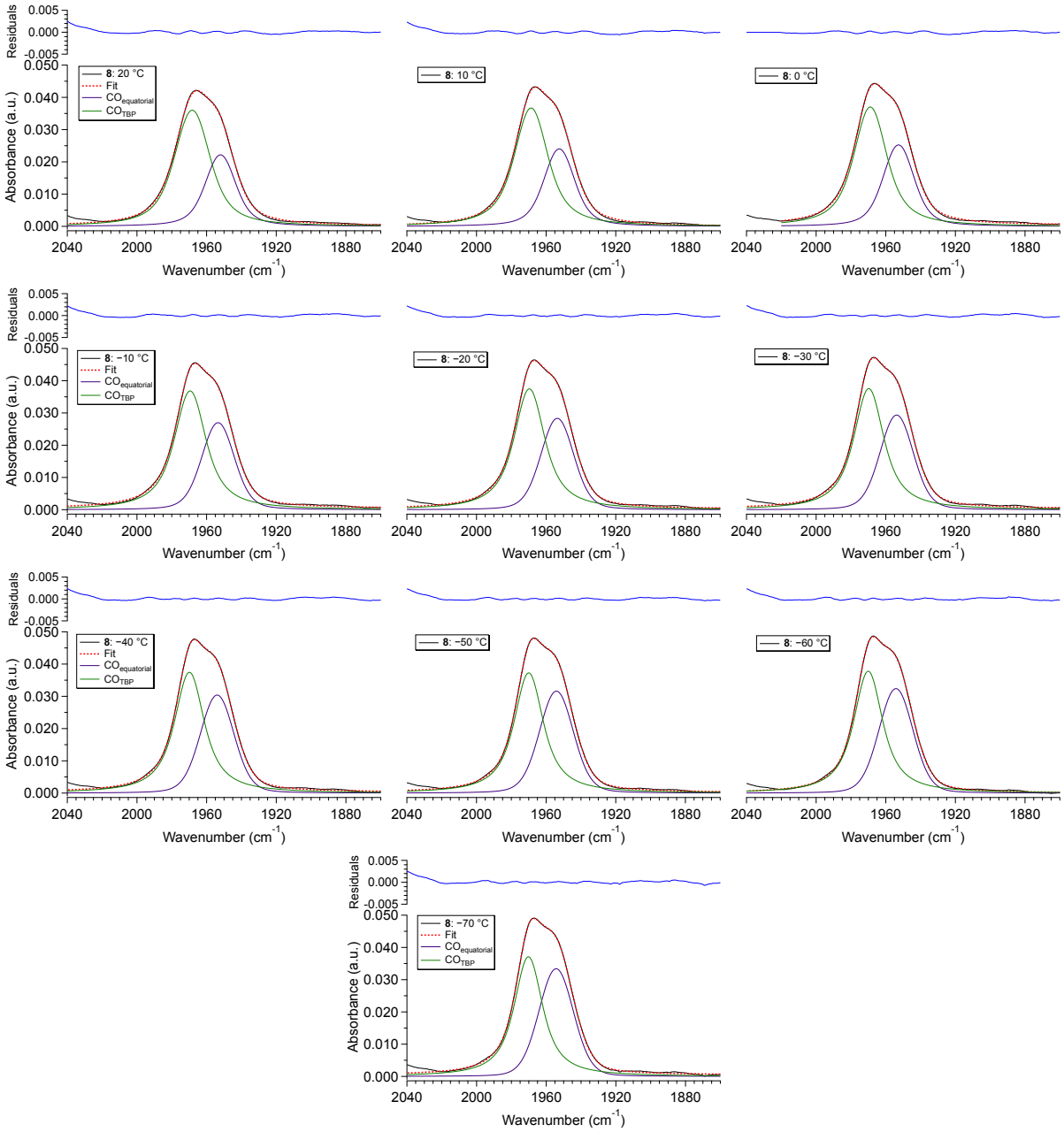

Figure 6.16. Spectral deconvolution of the variable temperature FTIR (VT-FTIR) spectra for complex **8** in DCM from 20 °C to –70 °C.

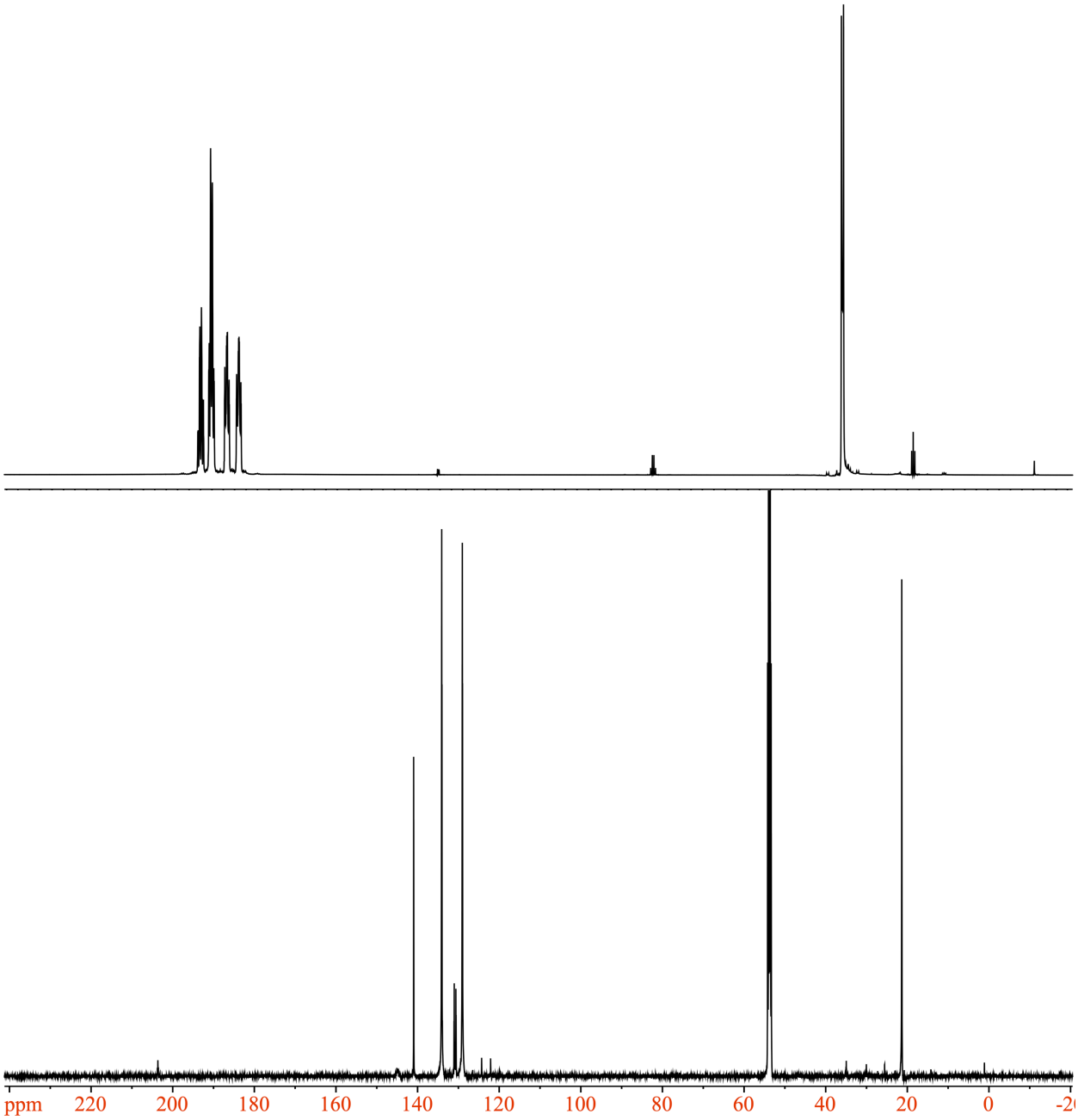

Figure 6.17. ^{1}H NMR (top) and ^{13}C NMR (bottom) of **2** in DCM-d_2 at 20 °C.

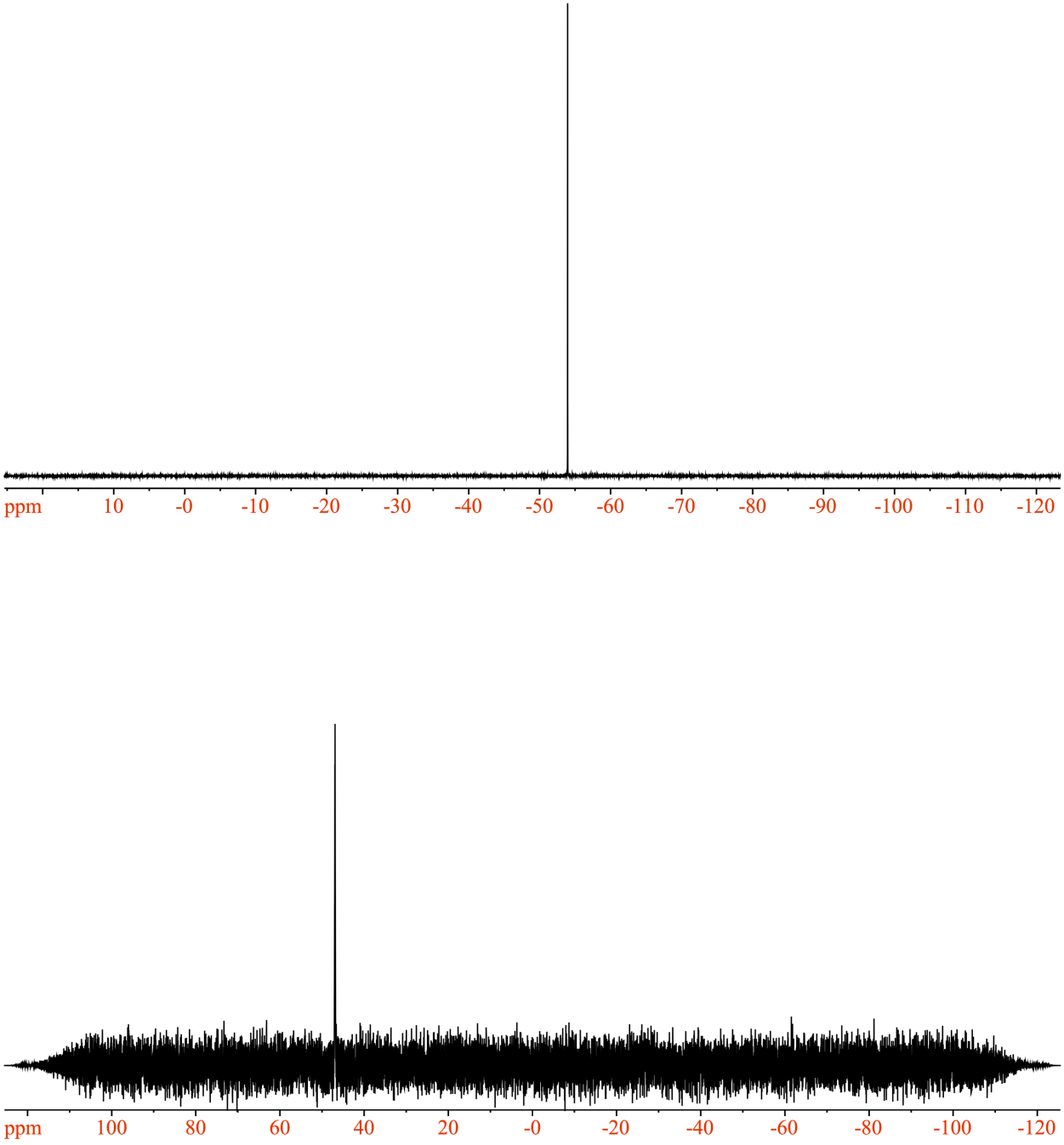

Figure 6.18. ^{19}F NMR (top) and ^{31}P (bottom) NMR of **2** in DCM-d_2 at 20 °C.

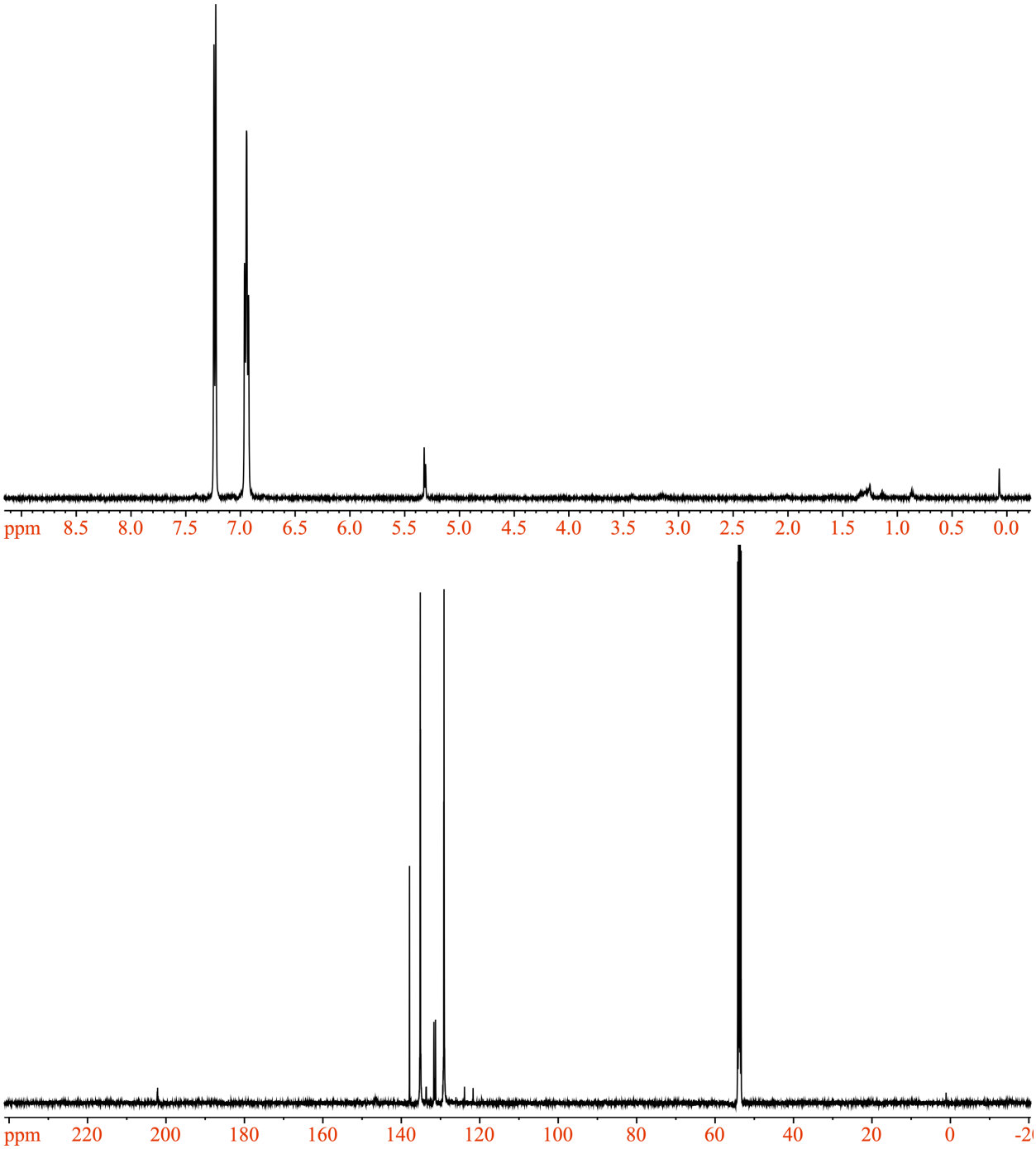

Figure 6.19. ^{1}H NMR (top) and ^{13}C NMR (bottom) of **3** in DCM-d_2 at 20 °C.

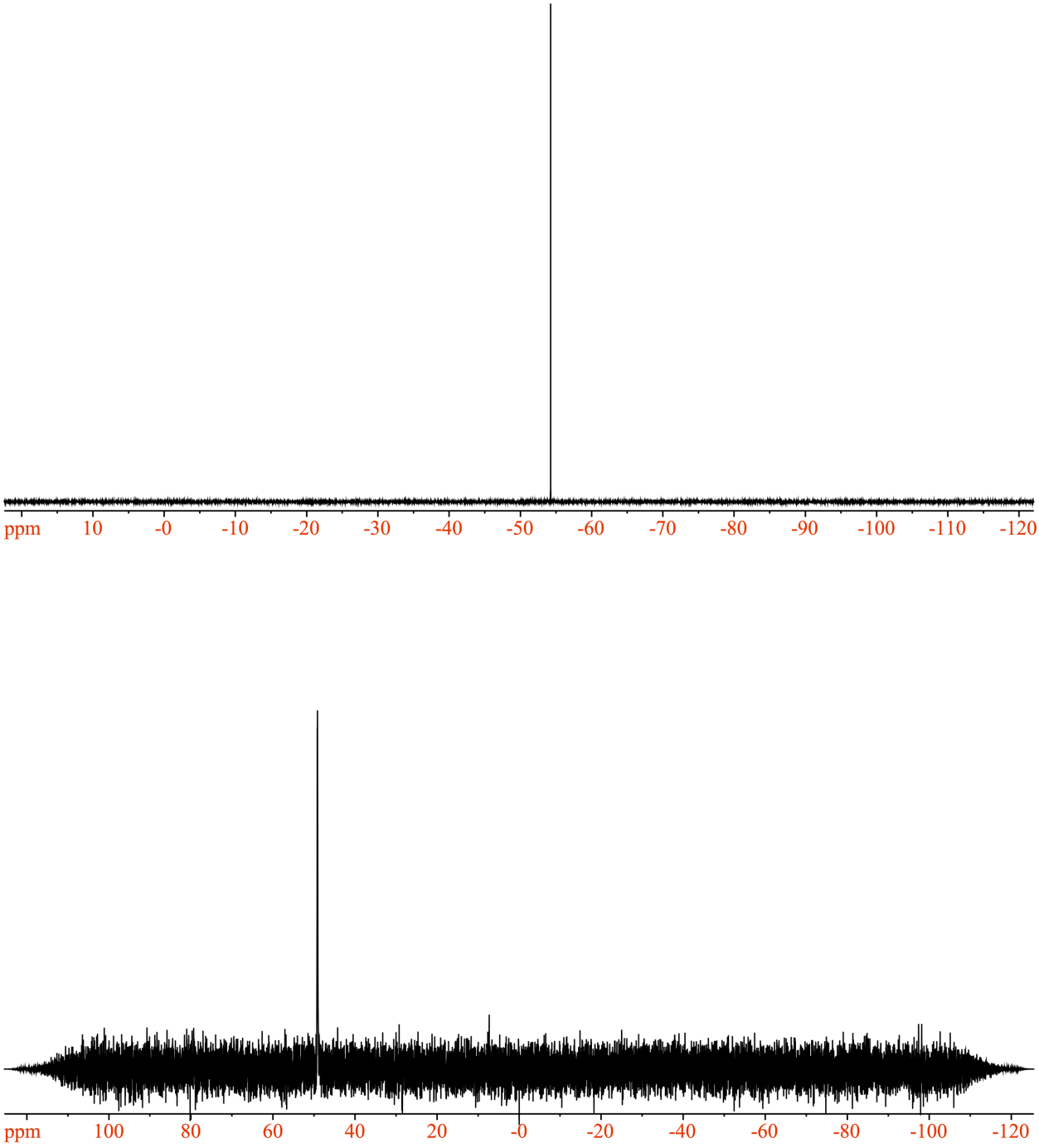

Figure 6.20. ^{19}F NMR (top) and ^{31}P (bottom) NMR of **3** in DCM-d_2 at 20 °C.

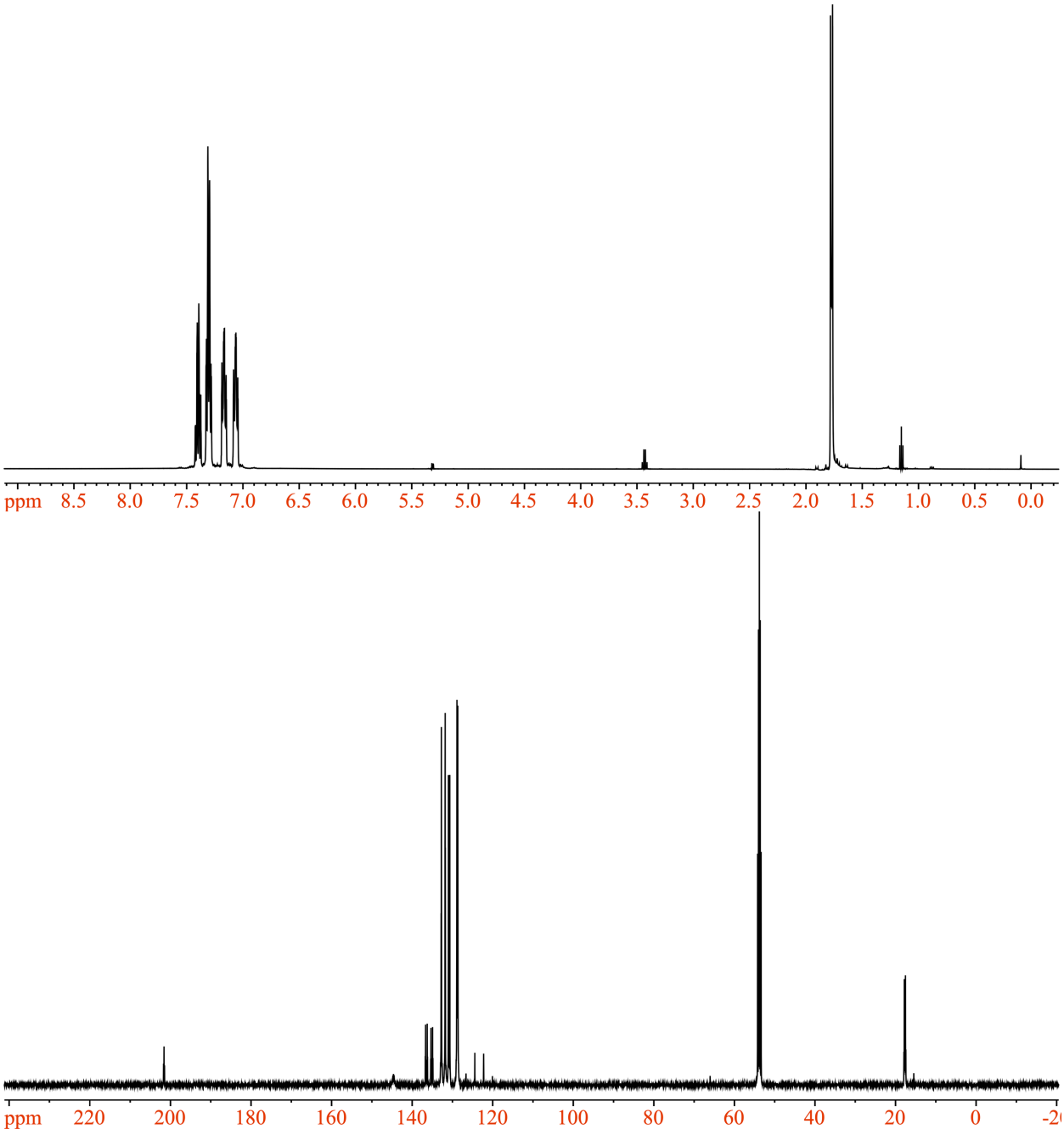

Figure 6.21. ^{1}H NMR (top) and ^{13}C NMR (bottom) of **4** in DCM-d_2 at 20 °C.

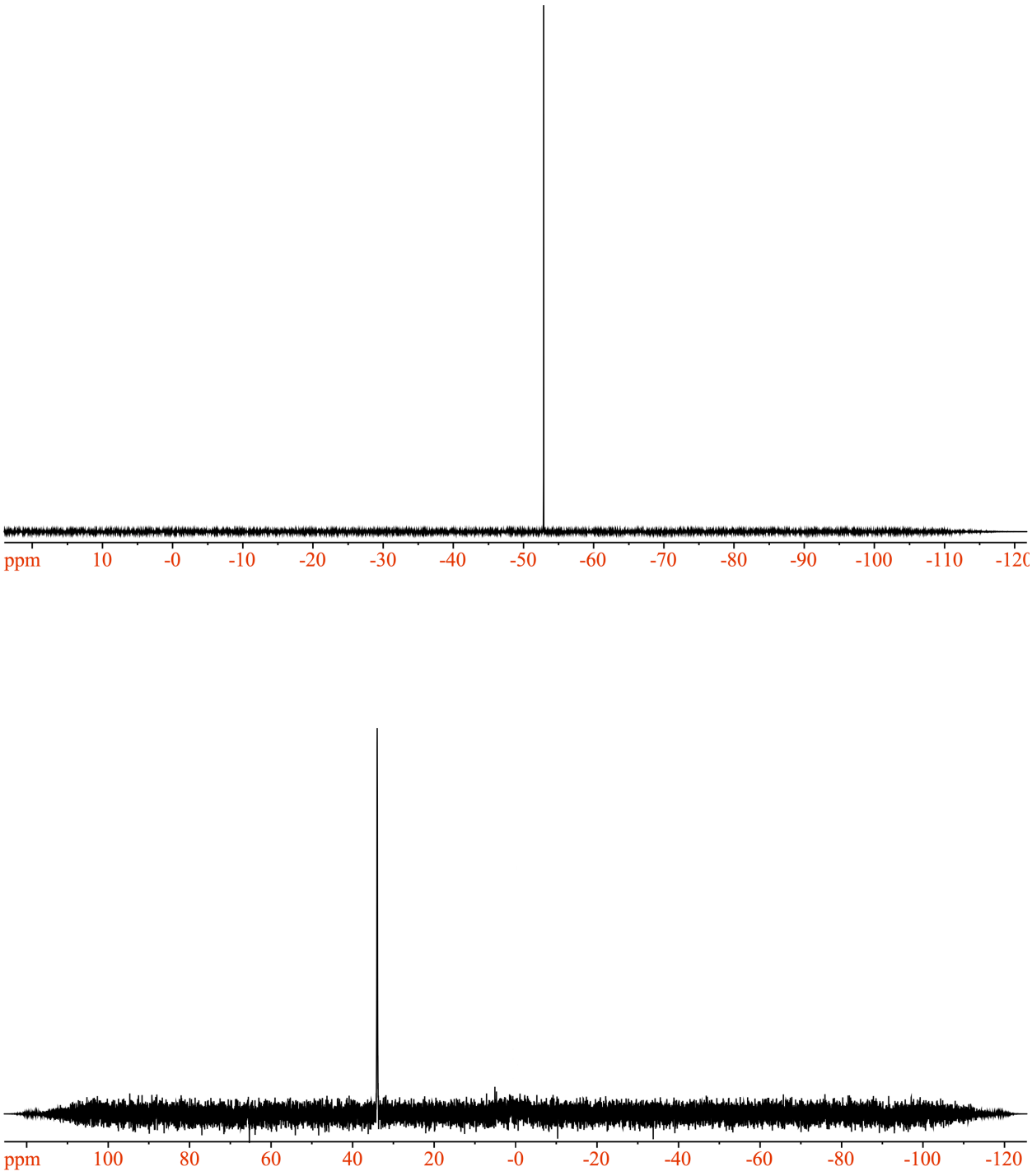

Figure 6.22. ^{19}F NMR (top) and ^{31}P (bottom) NMR of **4** in DCM-d_2 at 20 °C.

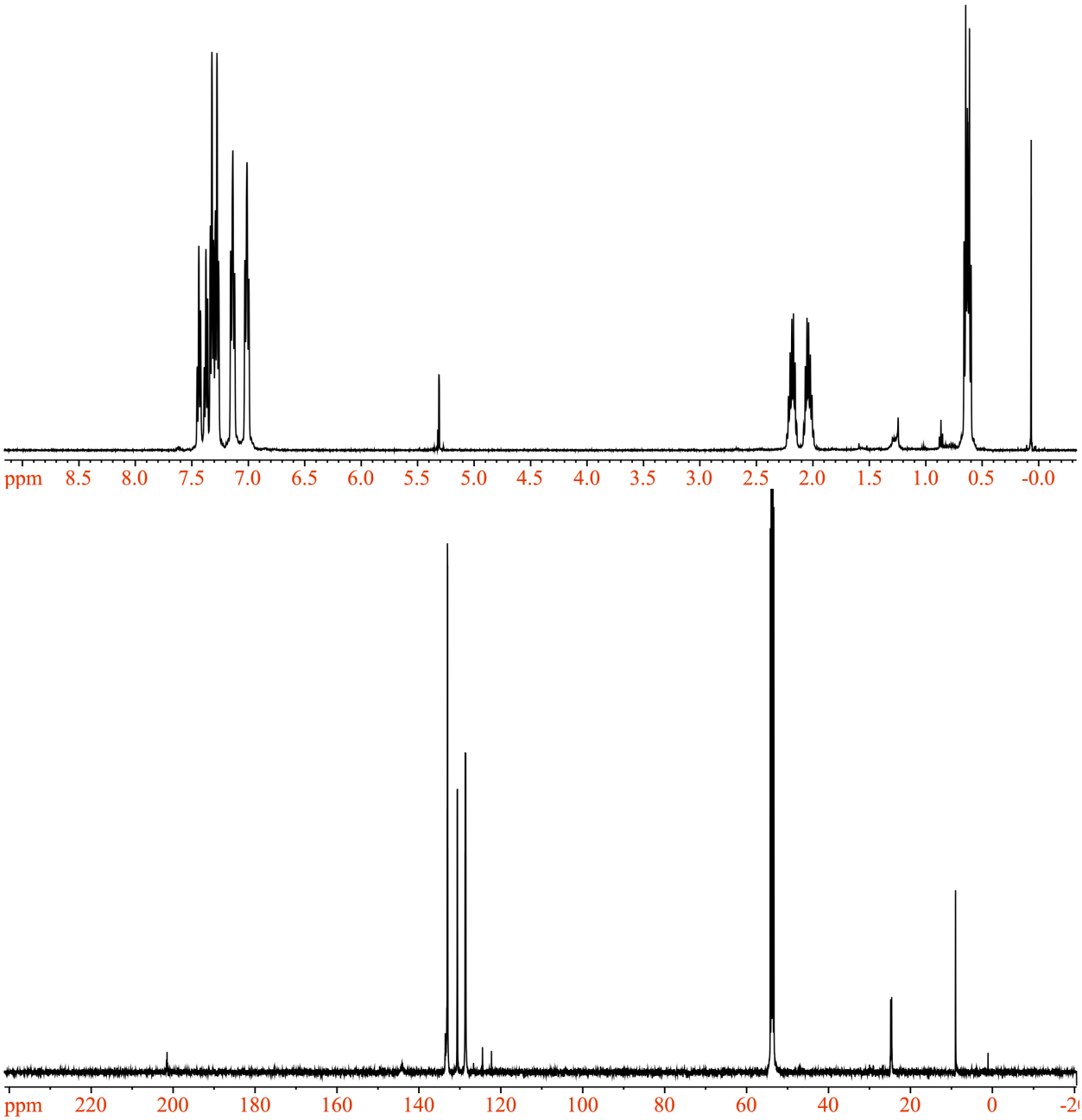

Figure 6.23. ^{1}H NMR (top) and ^{13}C NMR (bottom) of **5** in DCM-d_2 at 20 °C.

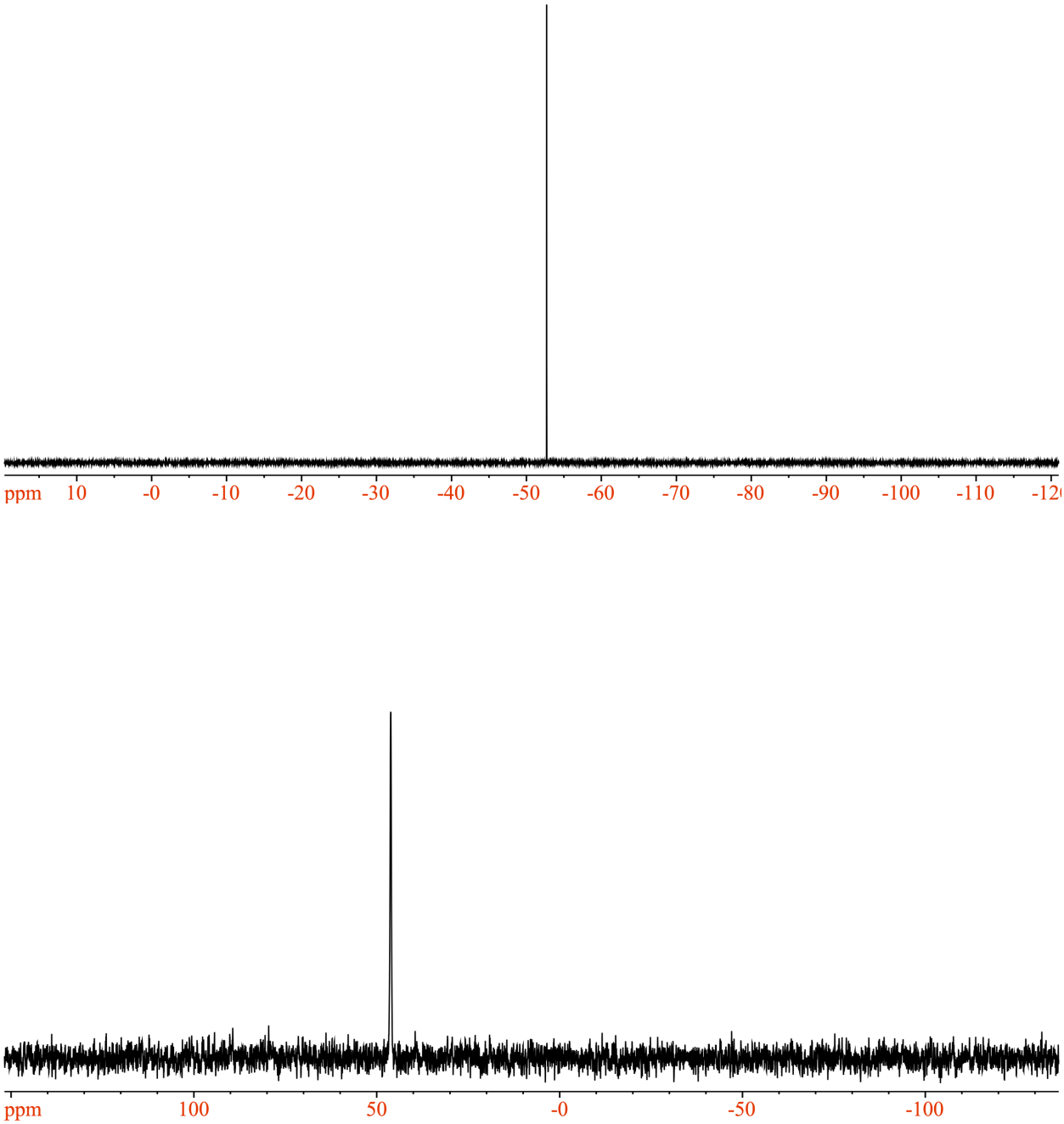

Figure 6.24. ^{19}F NMR (top) and ^{31}P (bottom) NMR of **5** in DCM-d_2 at 20 °C.

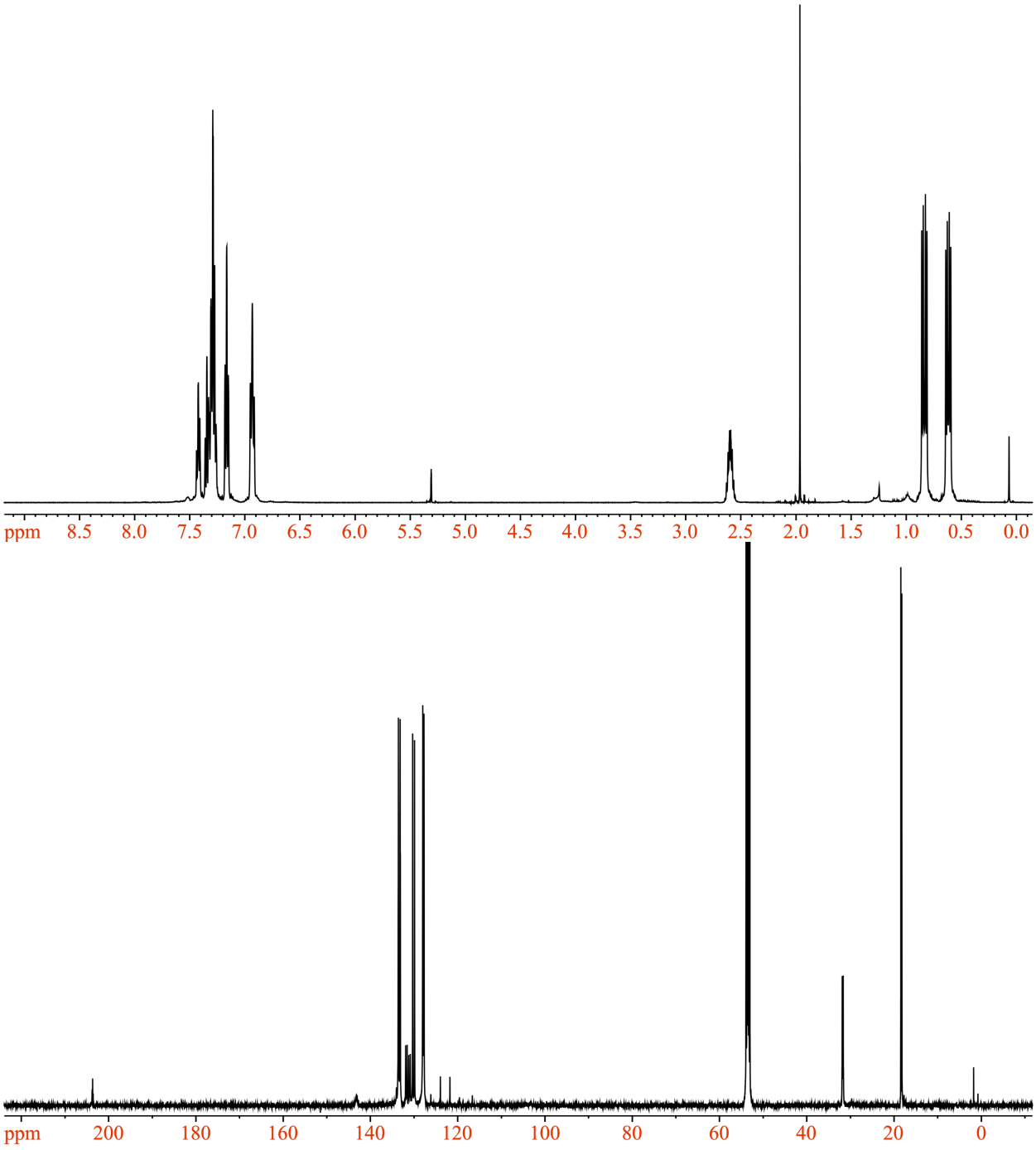

Figure 6.25. ^{1}H NMR (top) and ^{13}C NMR (bottom) of **6** in DCM-d_2 at 20 °C.

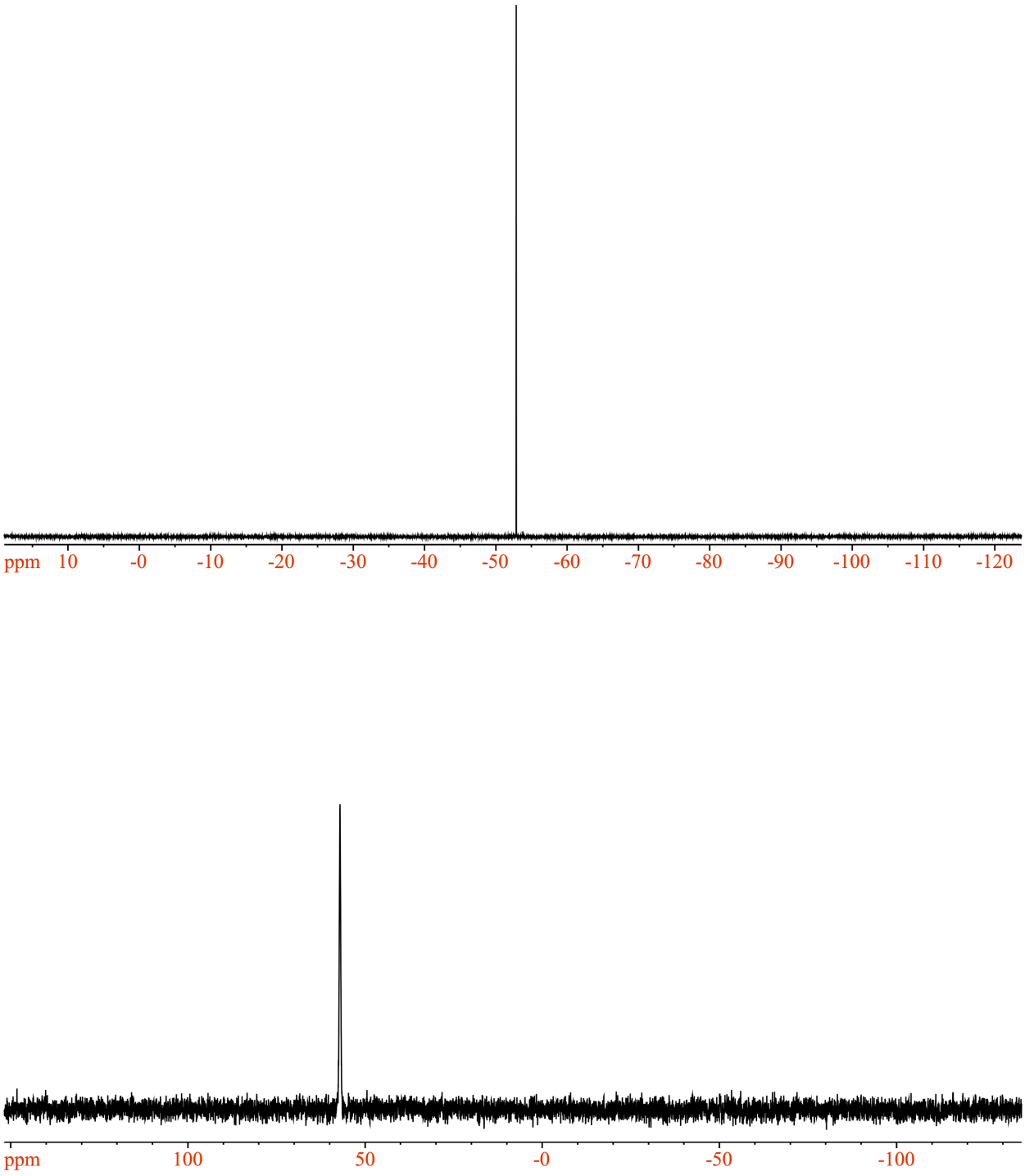

Figure 6.26. ^{19}F NMR (top) and ^{31}P (bottom) NMR of **6** in DCM-d_2 at 20 °C.

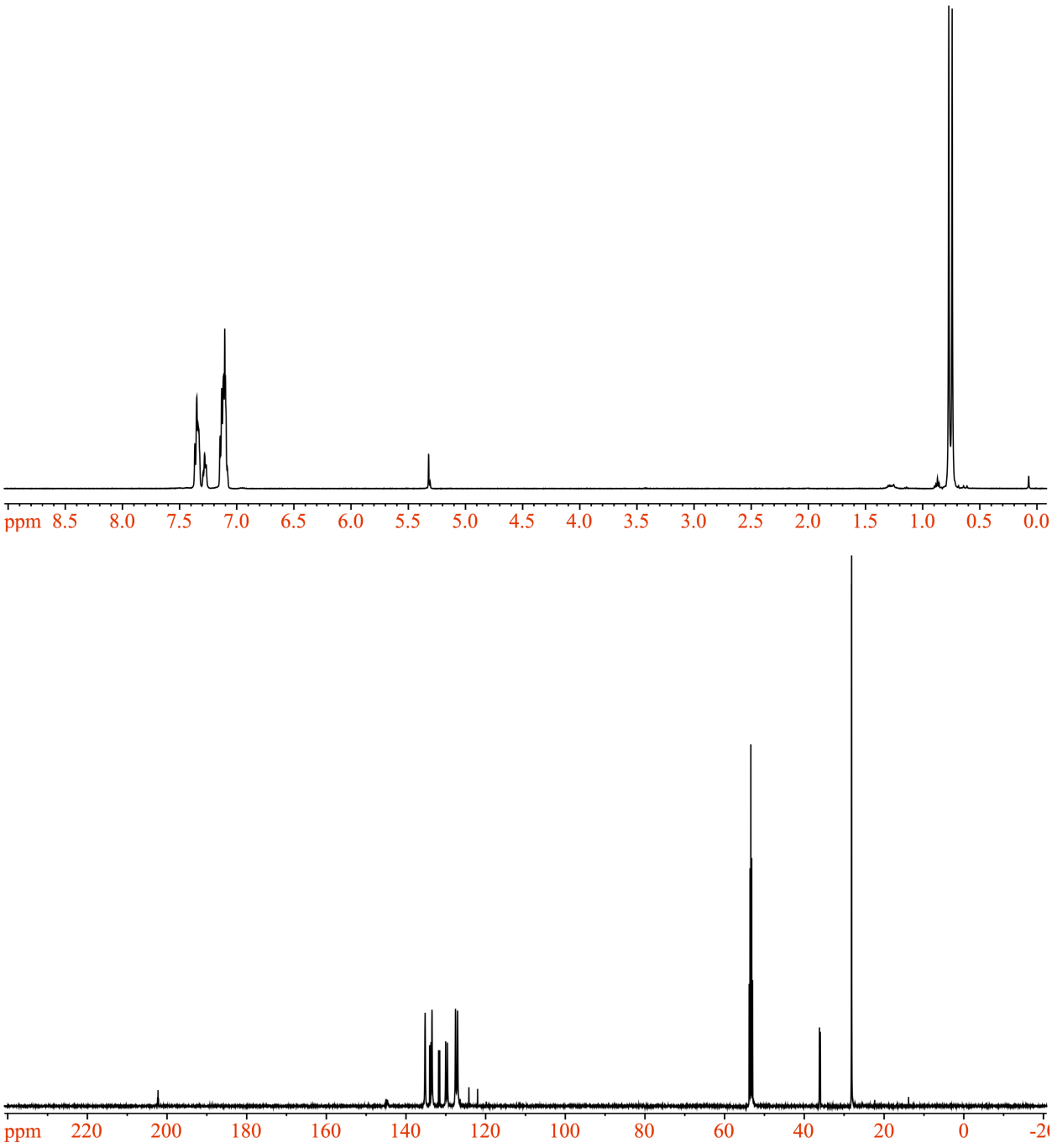

Figure 6.27. ^{1}H NMR (top) and ^{13}C NMR (bottom) of **7** in DCM-d_2 at 20 °C.

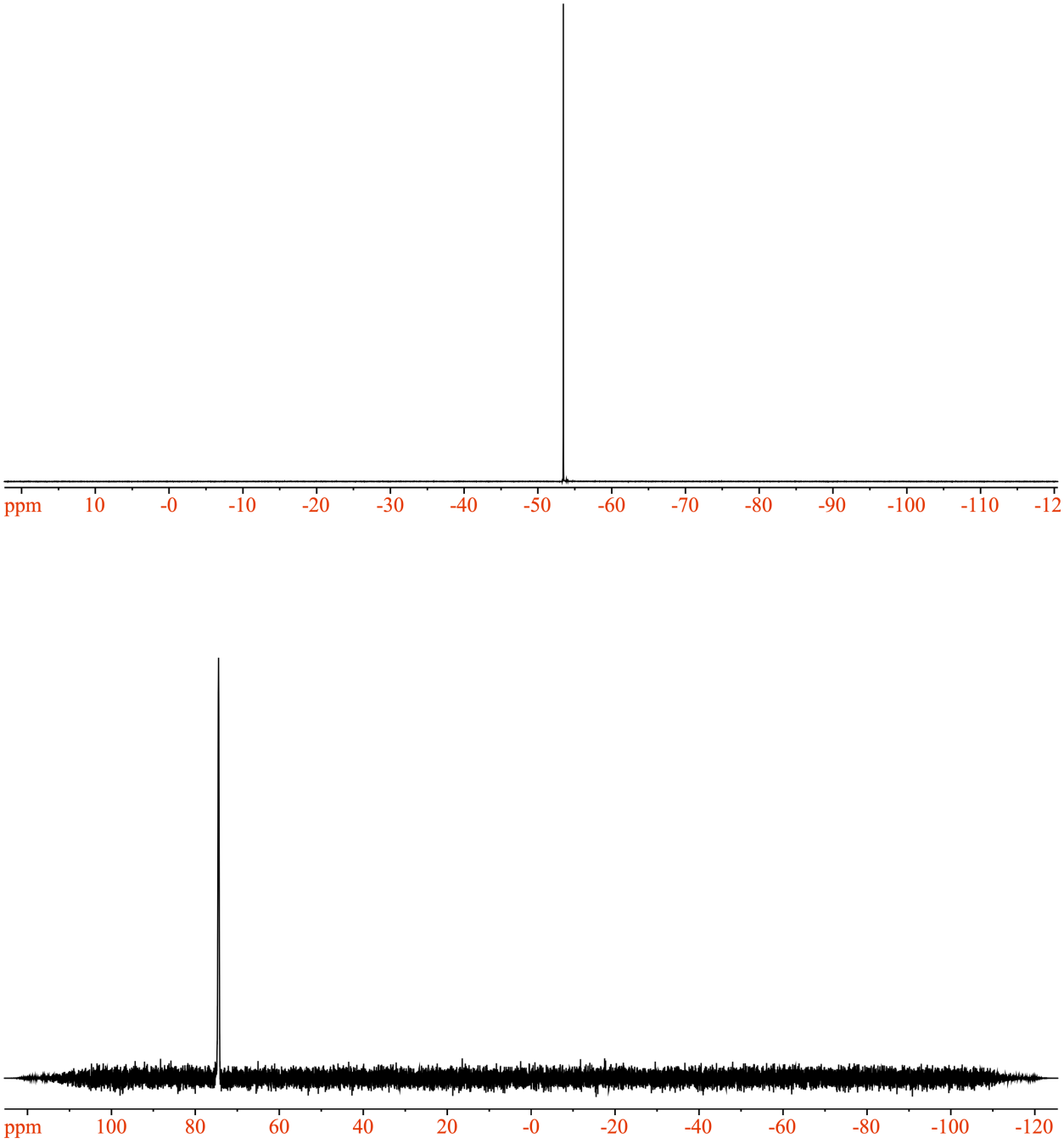

Figure 6.28. ^{19}F NMR (top) and ^{31}P (bottom) NMR of **7** in DCM-d_2 at 20 °C.

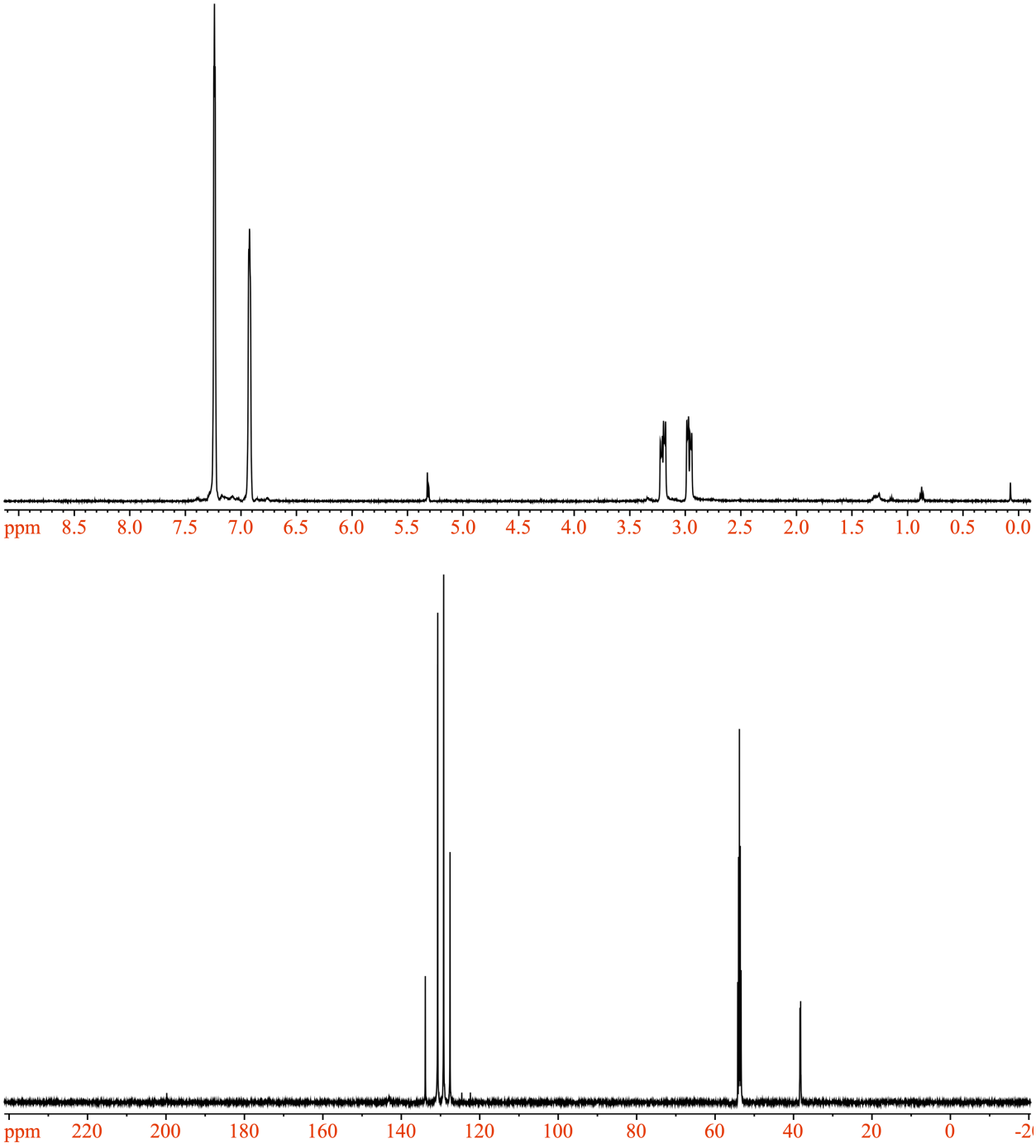

Figure 6.29. ^{1}H NMR (top) and ^{13}C NMR (bottom) of **8** in DCM-d_2 at 20 °C.

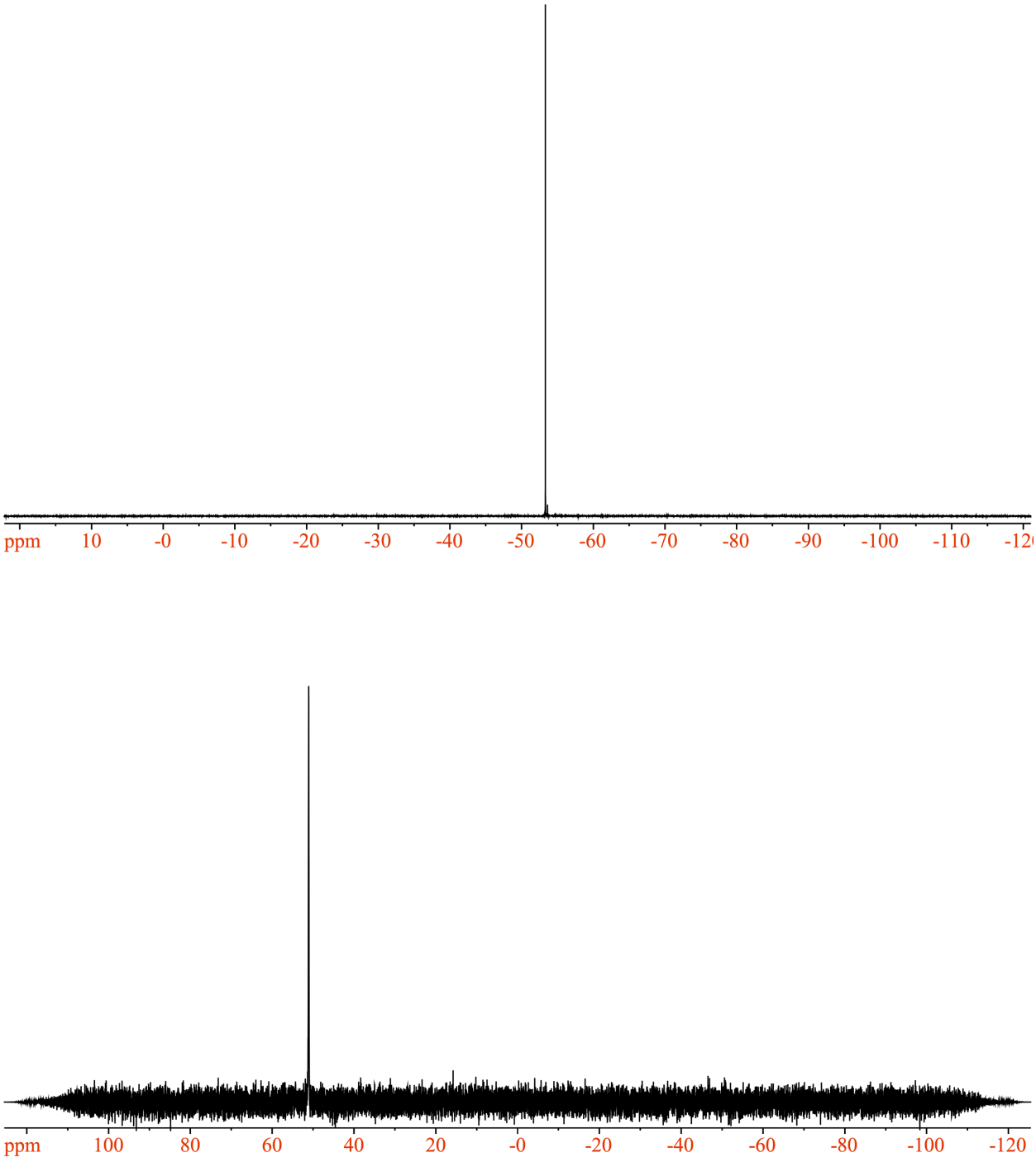

Figure 6.30. ^{19}F NMR (top) and ^{31}P (bottom) NMR of **8** in DCM-d_2 at 20 °C.

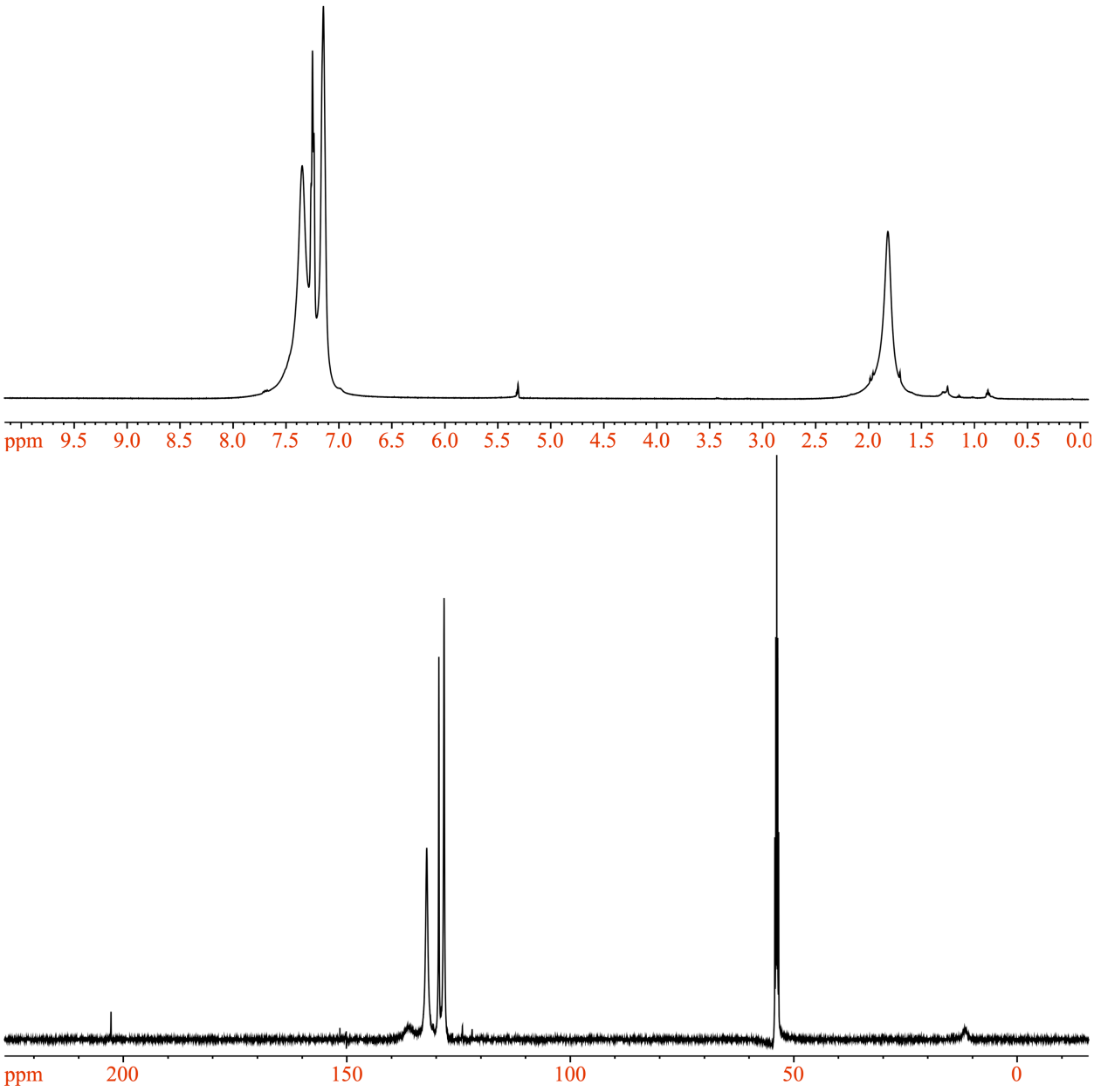

Figure 6.31. ^{1}H NMR (top) and ^{13}C NMR (bottom) of **9** in DCM-d_2 at 20 °C.

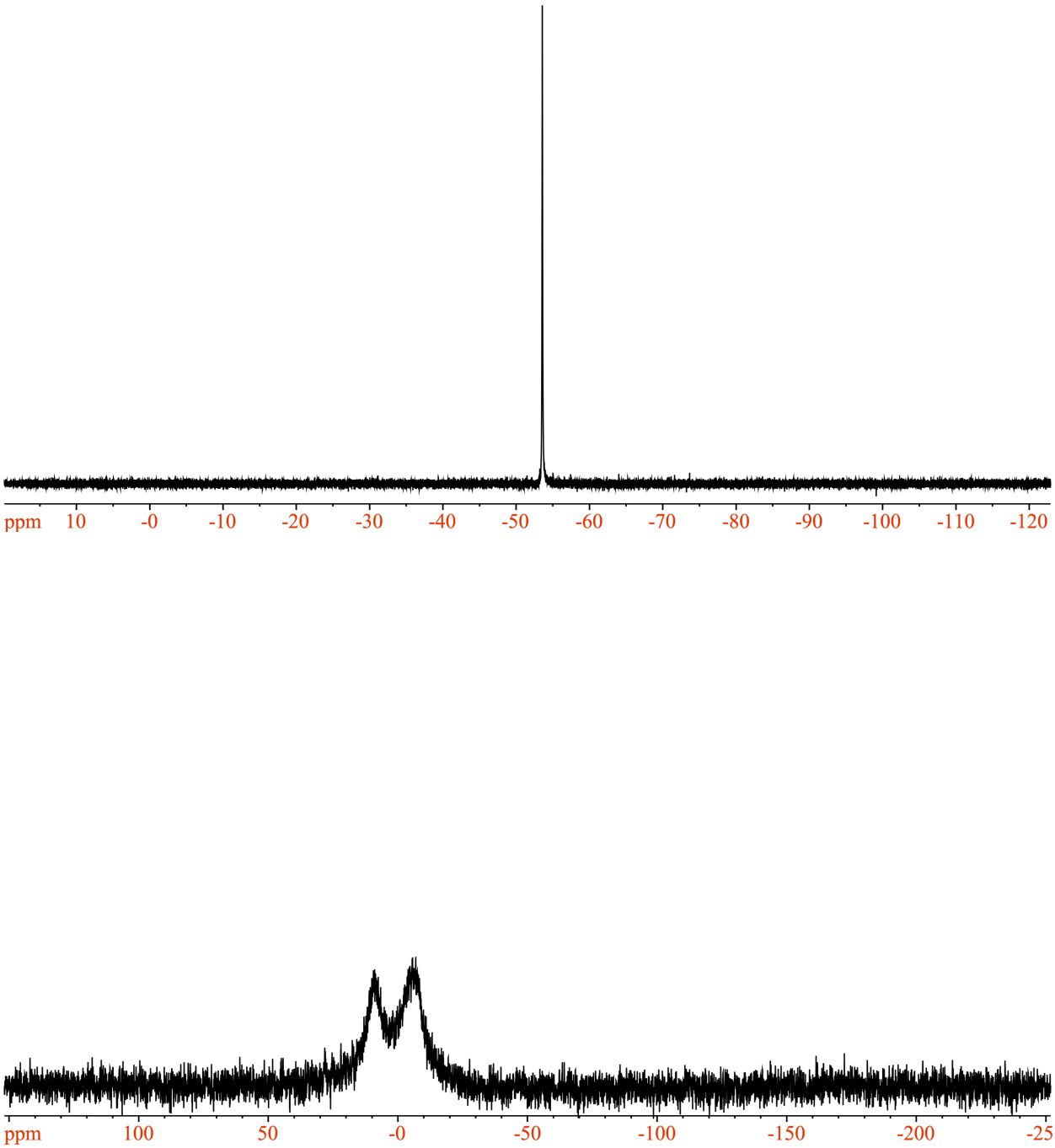

Figure 6.32. ^{19}F NMR (top) and ^{31}P (bottom) NMR of **9** in DCM-d_2 at 20 °C.

Table 6.3. Location and peak areas for three-component Gaussian deconvolutions of the VT-FTIR for complex **4** in DCM.

Temperature (°C)	Location (cm^{-1})	Area
	1939.0	0.968
20	1968.0	1.050
	1975.3	0.216
	1938.8	0.989
10	1968.2	1.074
	1976.1	0.203
	1938.7	1.031
0	1968.6	1.038
	1977.1	0.192
	1938.6	1.080
–10	1968.6	1.089
	1977.3	0.182
	1938.5	1.139
–20	1968.9	1.120
	1977.3	0.174
	1938.4	1.210
–30	1969.0	1.116
	1977.7	0.167
	1938.3	1.276
–40	1969.3	1.071
	1978.0	0.150
	1938.2	1.381
–50	1970.1	1.051
	1978.2	0.104
	1938.2	1.490
–60	1970.6	0.923
	1979.0	0.113
	1938.1	1.551
–70	1970.8	1.040
	1980.0	0.055

Table 6.4. Location and peak areas for three-component Gaussian deconvolutions of the VT-FTIR for complex **5** in DCM.

Temperature (°C)	Location (cm^{-1})	Area
	1932.6	0.613
20	1967.5	1.000
	1975.4	0.063
	1932.5	0.637
10	1968.3	1.019
	1976.2	0.051
	1932.6	0.677
0	1968.8	1.009
	1976.6	0.050
	1932.1	0.693
–10	1969.4	1.017
	1977.0	0.040
	1931.9	0.703
–20	1969.9	1.046
	1977.5	0.034
	1931.8	0.713
–30	1970.2	1.050
	1978.0	0.029
	1937.1	0.728
–40	1970.3	1.069
	1978.2	0.026
	1931.5	0.726
–50	1970.5	1.082
	1978.7	0.023
	1931.2	0.740
–60	1970.8	1.106
	1979.6	0.019
	1931.2	0.770
–70	1970.9	1.143
	1980.1	0.015

Table 6.5. Location and peak areas for two-component Gaussian deconvolutions of the VT-FTIR for complex **7** in DCM.

Temperature (°C)	Location (cm^{-1})	Area
20	1956.2	3.77
	1974.2	0.41
10	1956.4	3.88
	1974.3	0.39
0	1956.9	3.99
	1974.7	0.38
–10	1957.1	4.03
	1974.9	0.38
–20	1957.6	4.16
	1975.3	0.36
–30	1958.2	4.28
	1975.8	0.34
–40	1958.8	4.43
	1976.2	0.31
–50	1959.2	4.42
	1976.6	0.30
–60	1959.9	4.56
	1977.0	0.27
–70	1960.6	4.71
	1977.6	0.24

Table 6.6. Location and peak areas for two-component Gaussian deconvolutions of the VT-FTIR for complex **8** in DCM.

Temperature (°C)	Location (cm^{-1})	Area
20	1952.0	0.591
	1968.3	1.198
10	1952.5	0.640
	1968.7	1.198
0	1952.7	0.669
	1968.9	1.184
–10	1953.4	0.697
	1969.5	1.175
–20	1953.6	0.729
	1969.6	1.173
–30	1953.8	0.761
	1969.8	1.158
–40	1954	0.790
	1969.9	1.145
–50	1954.1	0.830
	1970.0	1.118
–60	1954.2	0.841
	1970.1	1.123
–70	1954.3	.871
	1970.3	1.07

Table 6.7. Equilibrium constants for the isomerization of complex **4** using the peak areas from Table 6.3 as the population ratios to determine K_{eq}.

Temperature (°C)	K_{eq}: CO_{TBP}/CO_{eq}	K_{eq}: CO_{ax}/CO_{TBP}	K_{eq}: CO_{eq}/CO_{ax}
20	0.206	4.479	0.922
10	0.190	4.850	0.921
0	0.185	5.374	0.993
-10	0.167	5.943	0.991
-20	0.155	6.547	1.017
-30	0.149	7.255	1.085
-40	0.140	8.485	1.192
-50	0.099	13.246	1.314
-60	0.123	13.155	1.614
-70	0.053	28.410	1.497

Table 6.8. Equilibrium constants for the isomerization of complex **5** using the peak areas from Table 6.4 as the population ratios to determine K_{eq}.

Temperature (°C)	K_{eq}: CO_{TBP}/CO_{eq}	K_{eq}: CO_{ax}/CO_{TBP}	K_{eq}: CO_{eq}/CO_{ax}
20	0.063	9.739	0.613
10	0.051	12.407	0.631
0	0.049	13.671	0.668
-10	0.039	17.510	0.682
-20	0.033	20.504	0.672
-30	0.025	27.419	0.679
-40	0.024	28.347	0.680
-50	0.021	31.963	0.671
-60	0.018	38.036	0.669
-70	0.013	50.750	0.674

Table 6.9. Equilibrium constants for the isomerization of complexes **7** and **8** using the peak areas from Table 6.5 and Table 6.6 as the population ratios to determine K_{eq}.

Temperature (°C)	K_{eq}: CO_{eq}/CO_{TBP} (7)	K_{eq}: CO_{eq}/CO_{TBP} (8)
20	0.109	2.02
10	0.101	1.86
0	0.095	1.77
-10	0.092	1.69
-20	0.087	1.61
-30	0.079	1.52
-40	0.072	1.45
-50	0.068	1.35
-60	0.059	1.31
-70	0.051	1.23

Table 6.10. Selected DFT bonding parameters for complexes **5** and **7**.

Bond	**5**			**7**	
	$CO_{equatorial}$	CO_{Axial}	CO_{TBP}	$CO_{equatorial}$	CO_{TBP}
C(1)–C(2)	1.38	1.38	1.37	1.38	1.37
C(1)–S(1)	1.74	1.74	1.76	1.73	1.75
C(2)–S(2)	1.73	1.74	1.76	1.74	1.76
C(5)–O(1)	1.20	1.20	1.19	1.19	1.19

Table 6.11. DFT optimized XYZ coordinates for the CO_{axial} isomer of complex **5**.

Atom	X	Y	Z
Ru	4.57142492	4.24036581	6.80652118
S	4.73353223	6.11731425	5.49878568
S	4.99284319	3.05590463	4.8704231
P	4.70689708	5.67467879	8.63189521
P	5.61619662	2.51269244	7.90759067
F	5.97690266	6.46001943	1.88538802
F	3.8321932	6.7397907	2.15607215
F	5.23992009	7.87411577	3.35751515
O	1.7618265	3.33362323	7.30124698
F	5.10506554	2.33558874	2.15617984
C	6.19074975	-1.3279468	6.45067632
H	7.01096143	-2.0548086	6.39916937
C	5.14827468	2.21956596	9.64925779
C	4.10826116	0.550794	6.57642502
H	3.29613463	1.28477682	6.59957256
C	4.06740598	7.3496321	8.26287081
C	6.40738917	-0.0785752	7.05472437
H	7.39532011	0.14179142	7.47393312
C	4.92989252	-1.6435275	5.91498007
H	4.76104386	-2.6184209	5.44178782
C	3.88879015	-0.7019632	5.98400268
H	2.90342261	-0.9355229	5.56328034
C	5.01328351	6.66180379	2.81221357
C	6.47727791	5.91494833	9.02651343
C	5.62207386	2.21206842	12.0438985
H	6.33659923	2.3382041	12.8662783
C	5.36850341	0.87135017	7.12595711
C	3.91341724	5.30189787	10.257782
H	4.36545431	4.36802077	10.6274764
H	4.21008369	6.12032071	10.940128
C	6.05951525	2.35918251	10.715316
H	7.11014187	2.60235547	10.5255999
C	3.80102655	1.90073628	9.92978807
H	3.08032917	1.80056333	9.11006699
C	4.76848883	8.51479687	8.62817277
H	5.73471198	8.43587075	9.14059833
C	2.39336328	5.17440574	10.1844229
H	2.08318147	4.37175095	9.49792868
H	1.92139998	6.11378658	9.84756643
H	1.99193811	4.93622631	11.1847634
C	4.99954055	5.5728171	3.86412955
C	7.33617316	6.30007698	7.97132242

Table 6.11 Continued. DFT optimized XYZ coordinates for the CO_{axial} isomer of complex **5**.

Atom	X	Y	Z
H	6.90430922	6.51325727	6.98476945
C	4.2778849	1.90780917	12.3160593
H	3.93768211	1.79697494	13.3527974
C	7.02495578	5.62263978	10.2919303
H	6.37954773	5.32827681	11.1255223
C	5.08632094	4.22557348	3.59037751
C	2.83044572	7.46461975	7.59170262
H	2.29642592	6.55993103	7.27907403
C	2.29519913	8.73024794	7.30947029
H	1.33206602	8.80940835	6.79168672
C	4.23749175	9.78171356	8.33315378
H	4.79351208	10.6836257	8.61651806
F	4.60345724	4.2484397	1.26138159
C	3.00008563	9.89099078	7.67481655
H	2.58783205	10.8802001	7.44089055
C	8.71981223	6.37994066	8.1772351
H	9.37519973	6.67805051	7.35021687
C	9.26516422	6.05771654	9.43506091
H	10.3501322	6.10026513	9.59182565
F	6.65724453	3.82141517	1.85789337
C	3.36921473	1.74114913	11.2537998
H	2.31955095	1.49849675	11.4575059
C	7.44231512	2.78170374	7.93687895
H	7.60498261	3.62562653	8.62963913
H	7.92691575	1.89530654	8.38498919
C	8.41576518	5.68569591	10.4908466
H	8.83401261	5.44034133	11.4746882
C	8.01349858	3.11053679	6.55710091
H	7.7668375	2.33265936	5.81325315
H	9.11083286	3.21282923	6.61718875
H	7.59506245	4.05893941	6.1801872
C	5.36201416	3.657493	2.21102657
C	2.90153688	3.68914376	7.18048218

Table 6.12. DFT optimized XYZ coordinates for the $CO_{equatorial}$ isomer of complex **5**.

Atom	X	Y	Z
Ru	4.59381182	4.35349639	7.03125611
S	4.03000066	6.09059398	5.59872012
S	6.15608883	3.79273173	5.44601229
P	5.02393104	5.84591419	8.65780201
P	5.45283567	2.5429265	8.21060297
F	6.19841812	7.693729	2.95473504
F	4.49586093	6.64271861	2.08426246
F	4.18734506	8.09906314	3.661791
O	1.72667376	3.86060313	7.86429939
F	7.81799958	3.77501037	3.15969379
C	6.45025187	-1.1714866	6.64817683
H	7.17218405	-1.9703146	6.85924252
C	4.46828564	1.96540955	9.64747617
C	4.61577127	0.88675754	6.10910642
H	3.91911554	1.70459734	5.88643576
C	4.09541664	7.41862118	8.5248042
C	6.44572429	-0.0101933	7.43868472
H	7.158458	0.07388109	8.26807838
C	5.53165365	-1.3087357	5.59172819
H	5.53510221	-2.216373	4.97536902
C	4.61112703	-0.2792526	5.32699816
H	3.89350542	-0.3782286	4.50312173
C	5.00768001	7.11758895	3.24050495
C	6.78046161	6.29965978	8.43826655
C	4.12075144	1.62595895	12.0419829
H	4.50348411	1.68201748	13.06853
C	5.52876225	1.0271852	7.17531508
C	4.81378848	5.40397344	10.4335991
H	5.46269262	4.53400474	10.632596
H	5.19951791	6.25760825	11.0228838
C	4.94563256	2.01639393	10.9726569
H	5.96163586	2.36297985	11.1905071
C	3.16637302	1.47524459	9.40671944
H	2.78881843	1.40764648	8.3806022
C	4.73997534	8.65017261	8.7545187
H	5.80688711	8.67161883	9.00732788
C	3.36432799	5.08564839	10.7985743
H	2.97053845	4.25003692	10.1989296
H	2.70852805	5.95963511	10.6435018
H	3.30212661	4.79388467	11.8604764
C	5.15688935	6.02372089	4.28197212
C	7.18873279	6.68875228	7.14183597

Table 6.12 Continued. Optimized XYZ coordinates for the $CO_{equatorial}$ isomer of complex 5.

Atom	X	Y	Z
H	6.43835176	6.7849038	6.34902655
C	2.81719232	1.16469342	11.7962241
H	2.17238773	0.86393192	12.6305829
C	7.74243712	6.17100803	9.45920201
H	7.44819166	5.88421137	10.4749988
C	6.10289782	5.02331182	4.2146318
C	2.72524995	7.40432154	8.1895585
H	2.21694269	6.45376135	7.99588393
C	2.00910702	8.60663382	8.09641357
H	0.94498663	8.58384109	7.83282407
C	4.02276766	9.85417822	8.65391041
H	4.53521802	10.8079964	8.82975374
F	6.8249952	5.28499014	1.95849517
C	2.65689945	9.83463617	8.32309485
H	2.09819317	10.7748008	8.23755476
C	8.54149049	6.91321846	6.86388282
H	8.84147642	7.17879073	5.84412141
C	9.50362673	6.761884	7.88086113
H	10.5660149	6.92295518	7.66022809
F	8.20727264	5.87823668	3.53586823
C	2.34564553	1.08151395	10.4730302
H	1.3345336	0.70986873	10.2693635
C	7.15933002	2.74203107	8.89577428
H	7.08829025	3.56800296	9.62602033
H	7.41240487	1.83087847	9.4692819
C	9.1015124	6.40095428	9.17774846
H	9.84572857	6.28802889	9.97535638
C	8.23040843	3.06742914	7.85611588
H	8.3230398	2.26651993	7.10185295
H	9.20742248	3.19351207	8.35332568
H	7.9934302	3.99789433	7.31718074
C	7.23355859	4.98747644	3.21124647
C	2.87289082	4.07958426	7.60345835

Table 6.13. DFT optimized XYZ coordinates for the CO_{TBP} isomer of complex **5**.

Atom	X	Y	Z
Ru	3.96980197	4.33102779	6.6696818
S	4.72788646	5.67179706	4.97221931
S	6.16265685	3.42511312	6.88768247
P	4.63314841	5.88381938	8.28148137
P	3.42210149	2.50142422	5.38483733
F	8.39939523	6.31167397	4.01252812
F	7.13425536	5.26854729	2.57544286
F	6.48140502	7.15011342	3.44362009
O	1.14203045	5.44139224	6.42460142
F	8.6896522	2.64674062	6.02542824
C	0.15654754	1.68915148	2.98436048
H	-0.5377892	0.86139561	2.79351404
C	2.81587216	1.79697473	6.9555507
C	1.93450697	3.81854166	3.47763203
H	2.6481168	4.63027839	3.6757436
C	3.63043716	7.41103966	8.37973118
C	1.17883296	1.53836209	3.93492314
H	1.28366117	0.59292804	4.48266087
C	0.02628154	2.89951122	2.27738034
H	-0.7729712	3.01519205	1.5344766
C	0.9187796	3.9595347	2.51907732
H	0.82137752	4.90069411	1.96419929
C	7.12084782	5.98984104	3.72681182
C	6.33603042	6.50005569	8.0687795
C	3.3537257	1.02111627	9.2183674
H	4.09904143	0.69524346	9.95317324
C	2.06533203	2.60598726	4.18883812
C	4.54814179	5.0852264	9.93911583
H	5.26691455	4.24678376	9.87874786
H	4.89662447	5.77365523	10.7306317
C	3.76830083	1.37284137	7.92312924
H	4.8320395	1.33603567	7.6590004
C	1.4506361	1.8939457	7.33093424
H	0.71271455	2.2584271	6.6068514
C	3.32350955	8.03593509	9.60566352
H	3.68783435	7.61547984	10.5502094
C	3.13352968	4.55290059	10.190654
H	2.83517191	3.84352331	9.39746202
H	2.38544965	5.36541675	10.2056541
H	3.08066926	4.02006486	11.1559596
C	6.43419762	5.25220441	4.84801652
C	6.59107348	7.49804202	7.1031406

Table 6.13 Continued. DFT optimized XYZ coordinates for the CO_{TBP} isomer of complex **5**.

Atom	X	Y	Z
H	5.76219357	7.93327523	6.53678824
C	1.99634621	1.09972423	9.57059163
H	1.67460429	0.82920188	10.5830973
C	7.4188578	5.91901465	8.76106872
H	7.24568425	5.12845326	9.49868993
C	7.01776273	4.27020532	5.60646421
C	3.16072398	7.98252873	7.17670335
H	3.4094207	7.49966732	6.22380036
C	2.40511198	9.1644814	7.20140463
H	2.05367002	9.60201233	6.25921487
C	2.55435113	9.21153482	9.62941711
H	2.31680213	9.68574512	10.5894412
F	8.78226934	3.68813006	4.12444752
C	2.09511598	9.77911042	8.42766901
H	1.49959716	10.6999988	8.44711693
C	7.90663534	7.90276137	6.83176372
H	8.09139746	8.66281344	6.0631234
C	8.97952103	7.32253105	7.52723362
H	10.0087184	7.63171562	7.3079587
F	9.3440073	4.71165009	5.96434882
C	1.04893367	1.54325816	8.62622749
H	-0.0092534	1.62078787	8.90389336
C	4.69772636	1.4141673	4.63964322
H	5.49387924	1.34624155	5.4033277
H	4.26504336	0.41390801	4.4573344
C	8.73271293	6.33273587	8.49311875
H	9.56705156	5.86703319	9.03092718
C	5.24997609	2.06602267	3.36587525
H	4.46132818	2.21242799	2.60645838
H	6.03281272	1.42475959	2.92381367
H	5.70420623	3.04625786	3.58488121
C	8.45650991	3.83925902	5.43256791
C	2.24993123	5.02168711	6.52622512

Table 6.14. DFT optimized XYZ coordinates for the CO_{axial} isomer of complex **7**.

Atom	X	Y	Z
Ru	4.44923757	4.19404094	7.04063475
S	5.8510056	5.65502076	5.91767431
S	3.74621585	3.64392047	4.93412174
P	4.61301588	5.7995343	8.81247144
P	5.71056338	2.42465404	7.77300394
F	7.21583047	5.40777341	2.43912536
F	5.89447785	7.1009945	2.67004411
F	7.5248129	6.8125393	4.03136438
O	1.99406189	2.76437554	8.03885078
F	3.39900811	3.4391696	2.16535137
C	5.16604578	-1.6455469	7.52295926
H	5.50452111	-2.5099754	8.0820754
C	5.73197718	2.09700377	9.57487671
C	4.31035229	0.57953635	6.12497998
H	3.97281173	1.43501223	5.55830067
C	4.12063413	7.42535479	8.12062492
C	5.54820391	-0.3796923	7.92991548
H	6.16953464	-0.2815527	8.80984309
C	4.34971613	-1.8064818	6.4124047
H	4.04350929	-2.7973283	6.09784685
C	3.92470422	-0.6889515	5.71645552
H	3.28450414	-0.7937773	4.84835621
C	6.57939458	6.16551306	3.34101619
C	6.2857653	6.14263566	9.46503853
C	6.72385196	2.12038208	11.7779306
H	7.56016108	2.37817933	12.4179394
C	5.12705255	0.75912937	7.23417068
C	3.43535027	5.7246156	10.2906476
C	6.7826144	2.42458773	10.4242619
H	7.66339677	2.91696407	10.0427324
C	4.61338321	1.46222895	10.1224136
H	3.78233409	1.19041178	9.48315815
C	4.58167088	8.62949071	8.64723683
H	5.31559482	8.62804747	9.44334975
C	2.02240225	5.96186153	9.75537855
H	1.77411116	5.29714384	8.92739135
H	1.87901144	6.99008215	9.42512863
H	1.31225396	5.75942355	10.562265
C	5.68274161	5.34650294	4.24360495
C	7.17292261	6.90130942	8.69613173
H	6.84548122	7.33502659	7.76097095
C	5.61326552	1.48354183	12.3052023

Table 6.14 Continued. DFT optimized XYZ coordinates for the CO_{axial} isomer of complex **7**.

Atom	X	Y	Z
H	5.57136589	1.24030251	13.3603675
C	6.75062195	5.60419756	10.6630695
H	6.10032345	5.01052547	11.2865337
C	4.76562357	4.44038624	3.80844114
C	3.18715517	7.46291865	7.08720716
H	2.83049359	6.5364933	6.65126747
C	2.72152202	8.67017336	6.59672441
H	1.99826348	8.67718304	5.7897319
C	4.12611442	9.83989393	8.14724026
H	4.50657285	10.7665457	8.56077531
F	4.71847119	4.98788337	1.49313565
C	3.19242859	9.86361356	7.12351629
H	2.83874289	10.8092089	6.72988059
C	8.47712238	7.1074221	9.11280914
H	9.14521448	7.69626207	8.49521357
C	8.92519134	6.56663928	10.3085569
H	9.94467808	6.73228547	10.6361295
F	5.51305655	3.06276744	2.05273915
C	4.55466236	1.15575664	11.4687668
H	3.67703341	0.66008414	11.8670297
C	7.48867208	2.42157102	7.14331613
C	8.05498361	5.81690085	11.082643
H	8.38706318	5.3946504	12.0241336
C	7.3892741	2.31726223	5.62088712
H	6.92334153	1.38103749	5.30986051
H	8.39862399	2.34590585	5.20117006
H	6.82487936	3.1429007	5.18981478
C	4.59781243	3.99281755	2.37552173
C	2.94881687	3.31094407	7.71001506
C	8.28372154	1.22216388	7.65576312
H	7.87630094	0.27956627	7.29283588
H	8.34491086	1.17990231	8.74365674
H	9.3034519	1.30826056	7.27023373
C	3.74271254	6.80940441	11.3179915
H	3.68940005	7.80637609	10.880286
H	4.71958943	6.69097815	11.7868722
H	2.98678025	6.75735237	12.1081412
C	3.46274379	4.35129193	10.9460202
H	3.07849301	3.58777662	10.2742104
H	2.81508235	4.36937085	11.8276224
H	4.4514596	4.03269624	11.2707117
C	8.22332326	3.70853797	7.50434539

Table 6.14 Continued. DFT optimized XYZ coordinates for the CO_{axial} isomer of complex **7**.

Atom	X	Y	Z
H	7.73808799	4.58078708	7.07267019
H	9.23312019	3.6511421	7.08863131
H	8.32123376	3.87716912	8.57566026

Table 6.15. DFT optimized XYZ coordinates for the $CO_{equatorial}$ isomer of complex **7**.

Atom	X	Y	Z
Ru	4.67971752	8.17199316	10.097693
S	5.58430583	10.272366	9.95097883
S	5.77042708	8.0421056	12.143588
P	4.87627754	5.88370779	9.64137026
P	2.62129794	8.27937666	11.0565
F	8.06140925	12.0501951	12.3461465
F	6.01844578	12.7969632	12.1852914
F	7.23076315	12.5375476	10.403418
F	6.65304453	8.87061657	14.676941
F	6.6530203	11.0141546	14.3363221
F	8.38738702	9.81224404	13.7789742
O	3.82885862	8.61767448	7.21004579
C	6.42096342	10.5753081	11.4463915
C	6.94128847	11.9872814	11.5994474
C	6.43299909	9.61387635	12.4349201
C	7.03604164	9.82801025	13.8112438
C	3.48606083	5.30498636	8.59532227
C	2.35143215	4.73965258	9.2192201
H	2.36660942	4.53507325	10.2931308
C	1.19785361	4.43738276	8.48081404
H	0.32928855	4.00488976	8.99277422
C	1.15552589	4.69293444	7.09955504
H	0.25224441	4.46298204	6.52126432
C	2.28331107	5.24088308	6.46459644
H	2.26830458	5.44012538	5.38610897
C	3.43996647	5.53821364	7.20323088
H	4.29809594	5.96960971	6.68294655
C	6.52736071	5.68215753	8.68129691
C	6.5601979	4.32496265	7.96270276
H	5.78626357	4.24282024	7.18089304
H	6.42405738	3.48917107	8.67063283
H	7.54580271	4.19568872	7.47691396
C	7.65648489	5.76405155	9.72674991
H	7.67905753	4.88371905	10.3898058
H	7.56125716	6.6715954	10.3515676
H	8.62601049	5.81513794	9.19731968
C	6.73098238	6.84714717	7.69372831
H	7.68937964	6.69306063	7.16336509
H	6.78896325	7.81181583	8.22887084
H	5.93993738	6.93804605	6.93293261
C	5.05240288	4.54731027	10.8967174
C	5.72274311	4.80544938	12.1114057

Table 6.15 Continued. DFT optimized XYZ coordinates for the $CO_{equatorial}$ isomer of complex **7**.

Atom	X	Y	Z
H	6.06994033	5.81865276	12.3298214
C	5.93639086	3.78533765	13.0492094
H	6.45571922	4.01733866	13.9868183
C	5.47700181	2.48192053	12.7929889
H	5.63260865	1.68505209	13.5307729
C	4.8219756	2.20703402	11.5806278
H	4.46761176	1.1925132	11.3610873
C	4.62183091	3.22765384	10.637079
H	4.11875386	2.98562677	9.69487947
C	4.10050324	8.40104969	8.3515035
C	2.69821396	9.36224301	12.5490077
C	3.39676593	10.5854921	12.4943138
H	3.8907353	10.8772124	11.5623281
C	3.49798193	11.4063903	13.626726
H	4.08153157	12.3297616	13.5630897
C	2.8968345	11.0165677	14.8349853
H	2.99060384	11.6479048	15.7273974
C	2.18022954	9.80892631	14.895449
H	1.7002141	9.49802849	15.8315361
C	2.08195727	8.98552005	13.7620006
H	1.52469265	8.04572199	13.8294019
C	1.25558607	9.07211316	10.0107589
C	0.03184463	9.37723599	10.9006572
H	-0.7709645	9.79703872	10.2660045
H	0.28027846	10.1251898	11.6720355
H	-0.374698	8.49072599	11.4117686
C	1.79179391	10.4111611	9.4662688
H	2.66683788	10.2810988	8.81349732
H	2.06406102	11.1043835	10.2788442
H	0.99126821	10.8893614	8.8713212
C	0.90052968	8.14159972	8.83602203
H	0.48986935	7.17276419	9.15256312
H	1.77249836	7.9338266	8.19888374
H	0.14147855	8.64102296	8.20455168
C	1.98560141	6.71601105	11.7845644
C	2.88601668	6.05939093	12.6531273
H	3.86100474	6.52148931	12.8468946
C	2.54842939	4.84226023	13.2576027
H	3.27550404	4.34402877	13.9086981
C	1.29714768	4.25381646	13.0033323
H	1.03736366	3.29073789	13.458313
C	0.38126531	4.91002607	12.1644058

Table 6.15 Continued. DFT optimized XYZ coordinates for the $CO_{equatorial}$ isomer of complex **7**.

Atom	X	Y	Z
H	-0.6014851	4.46675223	11.964219
C	0.72119411	6.13302594	11.5619985
H	-0.0113934	6.60597398	10.9057657

Table 6.16. DFT optimized XYZ coordinates for the CO_{TBP} isomer of complex **7**.

Atom	X	Y	Z
Ru	4.87617465	8.43521056	9.95123136
S	5.66063282	10.5609437	10.3648476
S	5.56105731	7.85096429	12.179417
P	6.93566108	7.66628005	9.09185474
P	2.71753479	8.56561067	10.8953229
F	8.17264009	11.587246	13.1091642
F	6.19375124	12.505706	13.1080195
F	7.39687679	12.4986657	11.3005149
F	6.41113416	8.19366778	14.8156614
F	6.62649978	10.3509806	14.8577028
F	8.25294475	9.10210391	14.1129979
O	3.97388925	9.26692633	7.16229748
C	6.43682375	10.4413347	11.943639
C	7.05278472	11.7478542	12.3738561
C	6.31985658	9.32343459	12.7336588
C	6.89725921	9.24413085	14.1281989
C	5.92171601	6.34861127	8.31717626
C	5.10948348	5.64600353	9.26399056
H	5.37633365	5.6665073	10.3302194
C	3.99155023	4.909157	8.83427511
H	3.36600401	4.39952806	9.5753998
C	3.68696169	4.83258041	7.46623598
H	2.8116965	4.26476287	7.12855773
C	4.51158746	5.48020547	6.52588973
H	4.28384715	5.40577205	5.45535695
C	5.61262263	6.24328605	6.94379256
H	6.21370443	6.77241186	6.19727331
C	8.0192979	8.63031112	7.90362648
C	8.95774853	7.68538158	7.13718438
H	8.40706881	6.99063974	6.47910418
H	9.5785046	7.0853778	7.82593706
H	9.63887275	8.28306576	6.5014359
C	8.81803782	9.59516376	8.80798365
H	9.52053091	9.06030401	9.46904394
H	8.13490249	10.207863	9.42509674
H	9.40945791	10.2740735	8.16484797
C	7.14353906	9.4685182	6.95894217
H	7.80596612	10.0353368	6.27778663
H	6.54251371	10.1952275	7.52898635
H	6.45905217	8.86686167	6.34107331
C	8.08584505	6.78240696	10.1912954
C	8.574914	7.4294765	11.3463983

Table 6.16 Continued. DFT optimized XYZ coordinates for the CO_{TBP} isomer of complex **7**.

Atom	X	Y	Z
H	8.28068176	8.46130757	11.5621276
C	9.43574922	6.75309021	12.2231945
H	9.790725	7.263696	13.1250269
C	9.80635403	5.42189184	11.9624503
H	10.4723173	4.89173989	12.6549687
C	9.31519472	4.76763665	10.8186807
H	9.60078154	3.72983731	10.6090305
C	8.45251415	5.44423138	9.93944852
H	8.06481586	4.92734289	9.05326892
C	4.31729392	8.93517277	8.25411141
C	2.65888977	9.26048363	12.5900387
C	3.38700187	10.4399152	12.8521814
H	3.96823139	10.8965441	12.0430557
C	3.40863831	10.9915288	14.140494
H	4.01907709	11.8808867	14.3273932
C	2.69168011	10.3772032	15.1816687
H	2.71893005	10.7993828	16.1940738
C	1.94351261	9.21472341	14.9227612
H	1.37812106	8.73206096	15.7296023
C	1.92683437	8.65753558	13.6333611
H	1.35192829	7.74333966	13.4473618
C	1.39389617	9.52103845	9.94335184
C	0.08828405	9.59725685	10.7562112
H	-0.6737214	10.1488107	10.1740508
H	0.23954459	10.1307442	11.7101176
H	-0.3183783	8.59733196	10.987029
C	1.96807829	10.9415595	9.7622221
H	2.91797276	10.9334537	9.20437599
H	2.14676131	11.4369814	10.7313491
H	1.23964105	11.5531846	9.19787902
C	1.16849642	8.85597035	8.55652295
H	0.16956839	8.39227919	8.49468273
H	1.91285222	8.07761811	8.32156789
H	1.23567568	9.60920412	7.75395399
C	2.13592996	6.83060851	11.1226544
C	2.87059758	6.02269082	12.0251999
H	3.71243547	6.47009175	12.5683125
C	2.54176312	4.67416459	12.2174613
H	3.1282439	4.07150644	12.9218337
C	1.46757392	4.09972319	11.5119347
H	1.20779227	3.04469619	11.6610769
C	0.7287087	4.89193165	10.6182206

Table 6.16 Continued. DFT optimized XYZ coordinates for the CO_{TBP} isomer of complex **7**.

Atom	X	Y	Z
H	-0.1143394	4.46018506	10.065303
C	1.05835379	6.24562253	10.425849
H	0.46084693	6.83034179	9.72388526

Table 6.17. Structural and refinement data for complex **2**.

Empirical formula	$C_{48}H_{44}Cl_2F_6OP_2RuS_2$
Formula weight	1048.86
Temperature/K	100.0
Crystal system	monoclinic
Space group	$P2_1/n$
a/Å	22.0285(3)
b/Å	10.09770(10)
c/Å	22.3884(3)
α/°	90
β/°	108.0770(10)
γ/°	90
Volume/Å^3	4734.20(11)
Z	4
ρ_{calc}g/cm^3	1.472
μ/mm^{-1}	0.659
F(000)	2136.0
Crystal size/mm^3	0.2 × 0.2 × 0.2
Radiation	MoKα (λ = 0.71073)
2Θ range for data collection/°	2.266 to 50.7
Index ranges	-26 ≤ h ≤ 26, -12 ≤ k ≤ 12, -26 ≤ l ≤ 25
Reflections collected	51983
Independent reflections	8669 [R_{int} = 0.0324, R_{sigma} = 0.0213]
Data/restraints/parameters	8669/17/575
Goodness-of-fit on F^2	1.046
Final R indexes [I>=2σ (I)]	R_1 = 0.0367, wR_2 = 0.0955
Final R indexes [all data]	R_1 = 0.0419, wR_2 = 0.1012
Largest diff. peak/hole / e Å^{-3}	2.77/-0.73

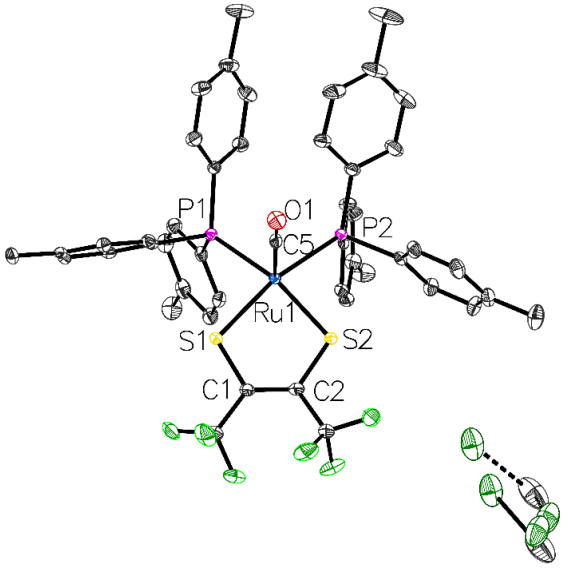

Notes on refinement: One molecule of dichloromethane exhibits significant positional disorder in the unit cell. This was treated as two-site disorder, modeled and refined anisotropically with carbon-chlorine and chlorine-chlorine distances constrained.

Table 6.18. Structural and refinement data for complex **3**.

Empirical formula	$C_{43}H_{28}Cl_{10}F_6OP_2RuS_2$
Formula weight	1256.28
Temperature/K	100.0
Crystal system	triclinic
Space group	P-1
a/Å	11.3432(4)
b/Å	12.7836(5)
c/Å	17.7908(7)
α/°	82.7760(10)
β/°	78.0010(10)
γ/°	75.6050(10)
Volume/Å^3	2436.72(16)
Z	2
ρ_{calc}g/cm^3	1.712
μ/mm^{-1}	1.080
F(000)	1248.0
Crystal size/mm^3	0.2 × 0.2 × 0.1
Radiation	MoKα (λ = 0.71073)
2Θ range for data collection/°	3.3 to 52.904
Index ranges	-14 ≤ h ≤ 14, -15 ≤ k ≤ 15, -22 ≤ l ≤ 22
Reflections collected	34329
Independent reflections	10022 [R_{int} = 0.0319, R_{sigma} = 0.0332]
Data/restraints/parameters	10022/0/586
Goodness-of-fit on F^2	1.040
Final R indexes [I>=2σ (I)]	R_1 = 0.0445, wR_2 = 0.1104
Final R indexes [all data]	R_1 = 0.0525, wR_2 = 0.1166
Largest diff. peak/hole / e Å^{-3}	2.52/-1.97

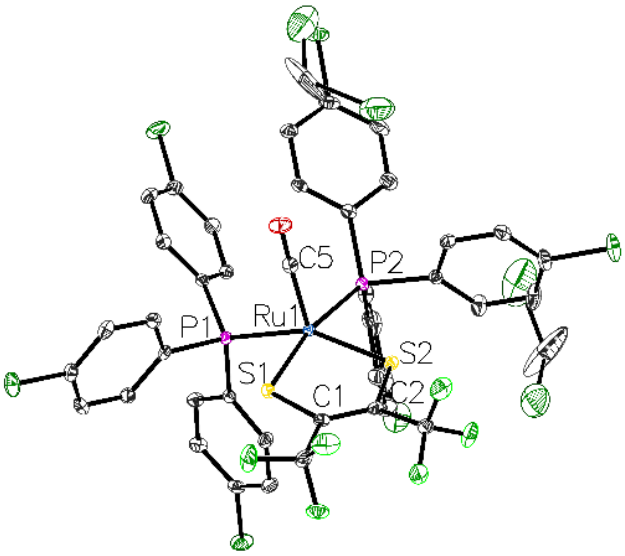

Table 6.19. Structural and refinement data for complex **4**.

Empirical formula	$C_{31}H_{26}F_6OP_2RuS_2$
Formula weight	755.65
Temperature/K	100.0
Crystal system	monoclinic
Space group	$P2_1/n$
a/Å	9.9248(5)
b/Å	14.4285(7)
c/Å	22.0349(12)
α/°	90
β/°	93.158(2)
γ/°	90
Volume/Å^3	3150.6(3)
Z	4
ρ_{calc}g/cm^3	1.593
μ/mm^{-1}	0.792
F(000)	1520.0
Crystal size/mm^3	0.2 × 0.2 × 0.1
Radiation	MoKα (λ = 0.71073)
2Θ range for data collection/°	3.376 to 52.768
Index ranges	-12 ≤ h ≤ 12, -17 ≤ k ≤ 18, -27 ≤ l ≤ 27
Reflections collected	12342
Independent reflections	6439 [R_{int} = 0.0231, R_{sigma} = 0.0334]
Data/restraints/parameters	6439/0/412
Goodness-of-fit on F^2	1.033
Final R indexes [I>=2σ (I)]	R_1 = 0.0355, wR_2 = 0.0759
Final R indexes [all data]	R_1 = 0.0463, wR_2 = 0.0801
Largest diff. peak/hole / e Å^{-3}	0.91/-0.75

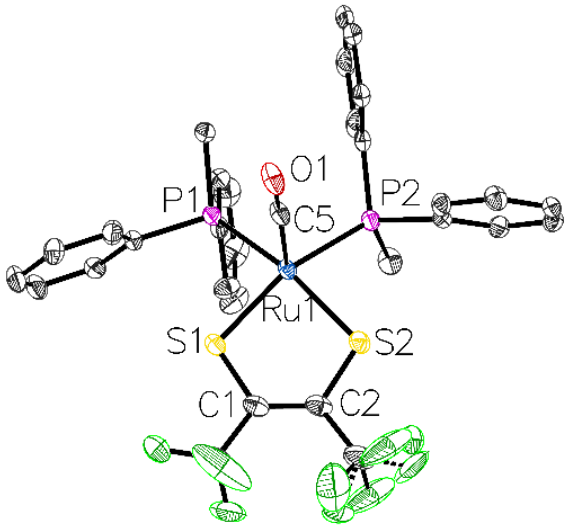

Notes on refinement: Rotational disorder exists about the C3 axis of one of the CF_3 of the dithiolene ligand; this was treated as two-site positional disorder, modeled and refined anisotropically.

Table 6.20 Structural and refinement data for complex **5**.

Empirical formula	$C_{33}H_{30}F_6OP_2RuS_2$
Formula weight	783.70
Temperature/K	100.0
Crystal system	monoclinic
Space group	$P2_1/n$
a/Å	10.1017(13)
b/Å	14.5492(18)
c/Å	22.325(3)
α/°	90
β/°	92.279(2)
γ/°	90
Volume/Å^3	3278.5(7)
Z	4
ρ_{calc}g/cm^3	1.588
μ/mm^{-1}	0.764
F(000)	1584.0
Crystal size/mm^3	0.3 × 0.1 × 0.1
Radiation	MoKα (λ = 0.71073)
2Θ range for data collection/°	3.342 to 51.432
Index ranges	-12 ≤ h ≤ 12, -17 ≤ k ≤ 17, -27 ≤ l ≤ 27
Reflections collected	31464
Independent reflections	31464 [R_{int} = ?, R_{sigma} = 0.0384]
Data/restraints/parameters	31464/0/437
Goodness-of-fit on F^2	1.067
Final R indexes [I>=2σ (I)]	R_1 = 0.0294, wR_2 = 0.0676
Final R indexes [all data]	R_1 = 0.0328, wR_2 = 0.0689
Largest diff. peak/hole / e Å^{-3}	0.49/-0.37

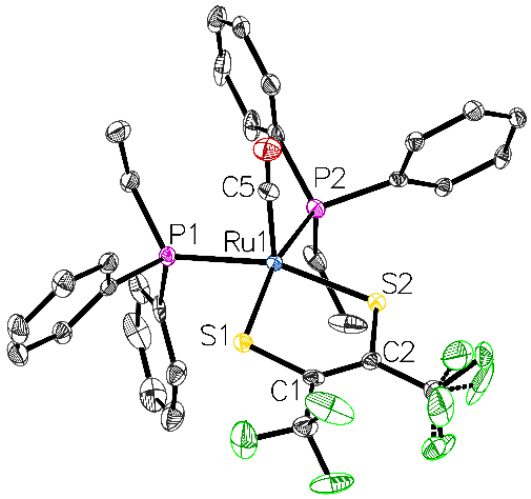

Notes on refinement: Two contributing twin components exist and were treated with the PLATON routine Twin.Rot.Mat and subsequently refined within the Olex2 software. Rotational disorder exists about the C3 axis of one of the CF_3 of the dithiolene ligand; this was treated as two-site positional disorder, modeled and refined anisotropically.

Table 6.21. Structural and refinement data for complex **6**.

Empirical formula	$C_{39}H_{40}F_6N_2OP_2RuS_2$
Formula weight	893.86
Temperature/K	100.0
Crystal system	triclinic
Space group	P-1
a/Å	11.3418(6)
b/Å	12.3720(6)
c/Å	15.6817(8)
α/°	82.532(2)
β/°	88.038(2)
γ/°	87.632(2)
Volume/Å^3	2179.01(19)
Z	2
ρ_{calc}g/cm^3	1.362
μ/mm^{-1}	0.585
F(000)	912.0
Crystal size/mm^3	0.2 × 0.2 × 0.1
Radiation	MoKα (λ = 0.71073)
2Θ range for data collection/°	4.49 to 51.388
Index ranges	-13 ≤ h ≤ 10, -15 ≤ k ≤ 14, -19 ≤ l ≤ 19
Reflections collected	29765
Independent reflections	8242 [R_{int} = 0.0391, R_{sigma} = 0.0464]
Data/restraints/parameters	8242/0/540
Goodness-of-fit on F^2	1.022
Final R indexes [I>=2σ (I)]	R_1 = 0.0347, wR_2 = 0.0684
Final R indexes [all data]	R_1 = 0.0497, wR_2 = 0.0728
Largest diff. peak/hole / e Å^{-3}	0.52/-0.64

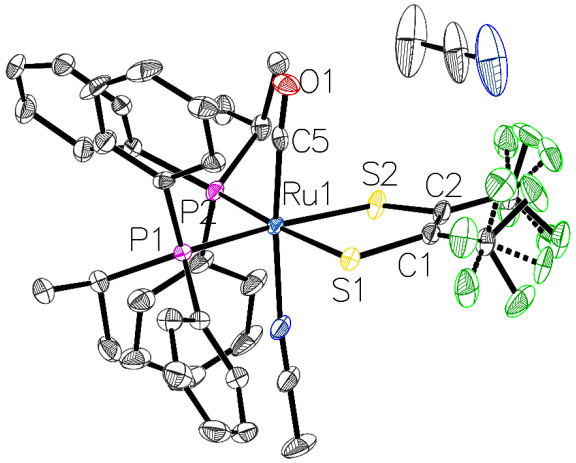

Notes on refinement: Rotational disorder exists about the C3 axis of one of the CF_3 groups of the dithiolene ligand; this was treated as two-site positional disorder, modeled and refined anisotropically. Density attributed to a second highly disordered molecule of uncoordinated acetonitrile was omitted from the unit cell using the PLATON routine SQUEEZE.

Table 6.22. Structural and refinement data for complex **7**.

Empirical formula	$C_{38}H_{40}Cl_2F_6OP_2RuS_2$
Formula weight	924.73
Temperature/K	100.0
Crystal system	triclinic
Space group	P-1
a/Å	9.6923(10)
b/Å	13.9409(13)
c/Å	15.7231(15)
α/°	69.532(3)
β/°	89.543(3)
γ/°	80.855(3)
Volume/Å^3	1962.5(3)
Z	2
ρ_{calc}g/cm^3	1.565
μ/mm^{-1}	0.783
F(000)	940.0
Crystal size/mm^3	0.3 × 0.1 × 0.1
Radiation	MoKα (λ = 0.71073)
2Θ range for data collection/°	2.768 to 52.742
Index ranges	-12 ≤ h ≤ 12, -17 ≤ k ≤ 17, -19 ≤ l ≤ 19
Reflections collected	49727
Independent reflections	8021 [R_{int} = 0.0588, R_{sigma} = 0.0448]
Data/restraints/parameters	8021/0/475
Goodness-of-fit on F^2	1.019
Final R indexes [I>=2σ (I)]	R_1 = 0.0308, wR_2 = 0.0607
Final R indexes [all data]	R_1 = 0.0460, wR_2 = 0.0664
Largest diff. peak/hole / e Å^{-3}	0.70/-0.58

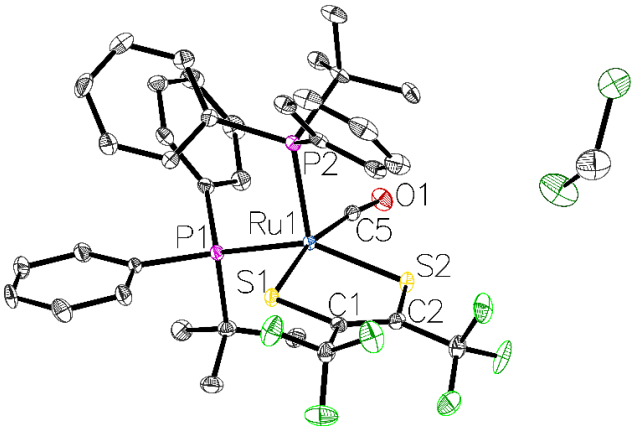

Table 6.23. Structural and refinement data for complex **8**.

Empirical formula	$C_{47}H_{42}F_6OP_2RuS_2$
Formula weight	963.93
Temperature/K	100.0
Crystal system	monoclinic
Space group	$P2_1/n$
a/Å	19.0916(12)
b/Å	13.4073(8)
c/Å	20.9793(11)
α/°	90
β/°	116.859(2)
γ/°	90
Volume/Å^3	4790.7(5)
Z	4
ρ_{calc}g/cm^3	1.336
μ/mm^{-1}	0.537
F(000)	1968.0
Crystal size/mm^3	0.3 × 0.2 × 0.1
Radiation	MoKα (λ = 0.71073)
2Θ range for data collection/°	3.736 to 50.7
Index ranges	-22 ≤ h ≤ 22, -16 ≤ k ≤ 16, -21 ≤ l ≤ 25
Reflections collected	55591
Independent reflections	8759 [R_{int} = 0.0577, R_{sigma} = 0.0481]
Data/restraints/parameters	8759/130/585
Goodness-of-fit on F^2	1.071
Final R indexes [I>=2σ (I)]	R_1 = 0.0587, wR_2 = 0.1326
Final R indexes [all data]	R_1 = 0.0858, wR_2 = 0.1445
Largest diff. peak/hole / e Å^{-3}	3.42/-0.73

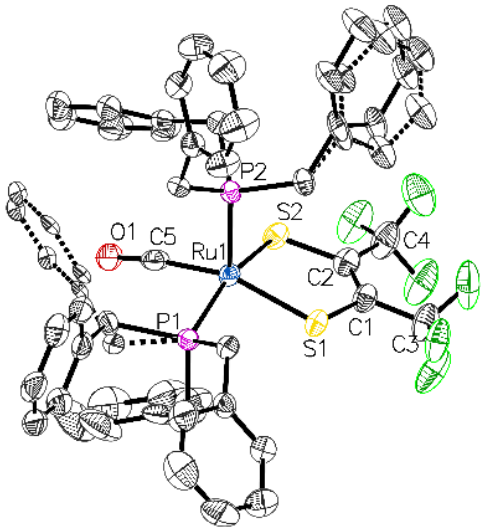

Notes on refinement: Two orientations exist at two of the benzyl moieties. This results in significant disorder which was treated as two-site positional disorder with RIGU and EADP constraints on the benzyl rings. Furthermore, density attributed to a highly disordered molecule of dichloromethane was omitted from the unit cell using the PLATON routine SQUEEZE.

Table 6.24. Structural and refinement data for complex **9**.

Empirical formula	$C_{45}H_{41}Cl_2F_6OP_3RuS_2$
Formula weight	1040.78
Temperature/K	100.0
Crystal system	monoclinic
Space group	$P2_1/c$
a/Å	11.4007(3)
b/Å	23.5110(5)
c/Å	17.6024(4)
α/°	90
β/°	108.7530(10)
γ/°	90
Volume/Å^3	4467.71(18)
Z	4
ρ_{calc}g/cm^3	1.547
μ/mm^{-1}	6.350
F(000)	2112.0
Crystal size/mm^3	0.2 × 0.2 × 0.2
Radiation	CuKα (λ = 1.54178)
2Θ range for data collection/°	6.5 to 140.554
Index ranges	-13 ≤ h ≤ 13, -27 ≤ k ≤ 28, -21 ≤ l ≤ 21
Reflections collected	32908
Independent reflections	8476 [R_{int} = 0.0493, R_{sigma} = 0.0410]
Data/restraints/parameters	8476/0/544
Goodness-of-fit on F^2	1.022
Final R indexes [I>=2σ (I)]	R_1 = 0.0350, wR_2 = 0.0854
Final R indexes [all data]	R_1 = 0.0476, wR_2 = 0.0919
Largest diff. peak/hole / e Å^{-3}	0.93/-0.87

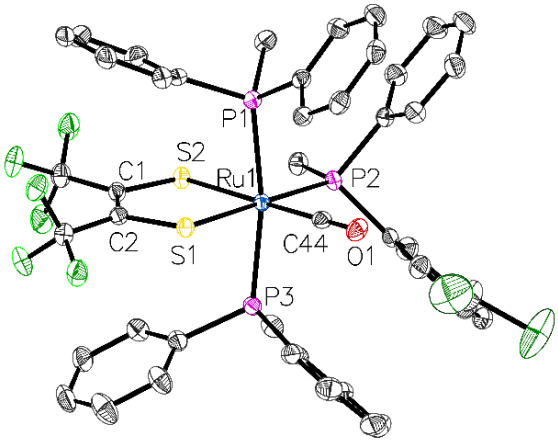

6.6 References

1. Porter, Tyler M.; Wang, J.; Li, Y.; Xiang, B.; Salsman, C.; Miller, J. S.; Xiong, W.; Kubiak, C. P., Direct observation of the intermediate in an ultrafast isomerization. *Chem. Sci.* **2019,** *10* (1), 113-117.
2. Balch, A. L.; Miller, J., 1,2-Dithiolene complexes of ruthenium and iron. *Inorg. Chem.* **1971,** *10* (7), 1410-1415.
3. Bernal, I.; Clearfield, A.; Epstein, E. F.; Ricci, J. S.; Balch, A.; Miller, J. S., Isomeric conformations in a pentaco-ordinated ruthenium compound; crystal and molecular structures of the orange and violet isomers of $(Ph_3P)_2[(CF_3)_2C_2S_2]Ru(CO)$. *Chem. Commun.* **1973,** (2), 39-40.
4. Bernal, I.; Clearfield, A.; Ricci, J. S., Crystal structure of the orange isomer of $[(C_6H_5)_3P]_2[C_2S_2(CF_3)_2]RuCO$. *J. Cryst. Mol. Struct.* **1974,** *4* (1), 43-54.
5. Clearfield, A.; Epstein, E. F.; Bernal, I., The Crystal and Molecular Structure of the Violet Isomer of $Ru(S_2C_2(CF_3)_2)(CO)(PPh_3)_2$. *J. Coord. Chem.* **1977,** *6* (4), 227-240.
6. Tolman, C. A., Steric effects of phosphorus ligands in organometallic chemistry and homogeneous catalysis. *Chem. Rev.* **1977,** *77* (3), 313-348.
7. Yan, Y.; Keating, C.; Chandrasekaran, P.; Jayarathne, U.; Mague, J. T.; DeBeer, S.; Lancaster, K. M.; Sproules, S.; Rubtsov, I. V.; Donahue, J. P., Ancillary Ligand Effects upon Dithiolene Redox Noninnocence in Tungsten Bis(dithiolene) Complexes. *Inorg. Chem.* **2013,** *52* (11), 6743-6751.
8. Lim, B. S.; Fomitchev, D. V.; Holm, R. H., Nickel Dithiolenes Revisited: Structures and Electron Distribution from Density Functional Theory for the Three-Member Electron-Transfer Series $[Ni(S_2C_2Me_2)_2]^{0,1-,2}$. *Inorg. Chem.* **2001,** *40* (17), 4257-4262.
9. Bigoli, F.; Chen, C.-T.; Wu, W.-C.; Deplano, P.; Mercuri, M. L.; Pellinghelli, M. A.; Pilia, L.; Pintus, G.; Serpe, A.; Trogu, E. F., [Ni(R2pipdt)2](BF4)2 (R_2pipdt = 1,4-disubstituted-piperazine-3,2-dithione) as useful precursors of mixed–ligand dithiolenes of interest for non-linear optics. *Chem. Commun.* **2001,** (21), 2246-2247.
10. Eisenberg, R.; Gray, H. B., Noninnocence in Metal Complexes: A Dithiolene Dawn. *Inorg. Chem.* **2011,** *50* (20), 9741-9751.
11. Cohen, B.; Weiss, S., IR lines broadened by chemical exchange. *J. Chem. Phys.* **1980,** *72* (12), 6804-6804.
12. Grevels, F.-W.; Jacke, J.; Klotzbücher, W. E.; Krüger, C.; Seevogel, K.; Tsay, Y.-H., Dynamic Processes on the IR Time Scale: Coalescence of CO Stretching Vibrational Bands in [(η^4-Diene)$Fe(CO)_3$] Complexes. *Angew. Chem. Int. Ed.* **1987,** *26* (9), 885-887.
13. Grevels, F.-W.; Kerpen, K.; Klotzbücher, W. E.; McClung, R. E. D.; Russell, G.; Viotte, M.; Schaffner, K., The Very Low Barrier of CO Site Exchange in Tricarbonyl(η^4-1,5-cyclooctadiene)iron: Picosecond Kinetics in Solution Investigated by Line Shape Simulation of the v(CO) IR Bands and Complementary Evidence from the Course of 13CO Incorporation in a Low-Temperature Matrix. *J. Am. Chem. Soc.* **1998,** *120* (40), 10423-10433.
14. Nilsen, I. A.; Osborne, D. G.; White, A. M.; Anna, J. M.; Kubarych, K. J., Monitoring equilibrium reaction dynamics of a nearly barrierless molecular rotor using ultrafast vibrational echoes. *J. Chem. Phys.* **2014,** *141* (13), 134313.
15. Giordano, A. N.; Lear, B. J., Comparing the Energetic and Dynamic Contributions of Solvent to Very Low Barrier Isomerization Using Dynamic Steady-State Vibrational Spectroscopy. *J. Phys. Chem. A* **2015,** *119* (15), 3545-3555.
16. Eckert, P. A.; Kubarych, K. J., Dynamic Flexibility of Hydrogenase Active Site Models Studied with 2D-IR Spectroscopy. *J. Phys. Chem. A* **2017,** *121* (3), 608-615.

17. Turner, J. J.; Bühl, M., Infrared Dynamics of Iron Carbonyl Diene Complexes. *J. Phys. Chem. A* **2018,** *122* (14), 3497-3505.

18. Ito, T.; Hamaguchi, T.; Nagino, H.; Yamaguchi, T.; Washington, J.; Kubiak, C. P., Effects of Rapid Intramolecular Electron Transfer on Vibrational Spectra. *Science* **1997,** *277* (5326), 660-663.

19. Londergan, C. H.; Kubiak, C. P., Electron transfer and dynamic infrared-band coalescence: It looks like dynamic NMR spectroscopy, but a billion times faster. *Chem. Eur. J.* **2003,** *9* (24), 5962-5969.

20. Porter, T. M.; Heim, G. P.; Kubiak, C. P., Stable Mixed-Valent Complexes Formed by Electron Delocalization Across Hydrogen Bonds of Pyrimidinone-Linked Metal Clusters. *J. Am. Chem. Soc.* **2018,** *140* (40), 12756-12759.

21. Horng, M. L.; Gardecki, J. A.; Papazyan, A.; Maroncelli, M., Subpicosecond Measurements of Polar Solvation Dynamics: Coumarin 153 Revisited. *J. Phys. Chem.* **1995,** *99* (48), 17311-17337.

22. Horng, M. L.; Dahl, K.; Jones, G.; Maroncelli, M., Electron transfer in a donor-substituted acridinium dye: evidence for dynamical solvent control. *Chem. Phys. Lett.* **1999,** *315* (5), 363-370.

23. Zheng, J.; Kwak, K.; Asbury, J.; Chen, X.; Piletic, I. R.; Fayer, M. D., Ultrafast Dynamics of Solute-Solvent Complexation Observed at Thermal Equilibrium in Real Time. *Science* **2005,** *309* (5739), 1338.

24. Lear, B. J.; Glover, S. D.; Salsman, J. C.; Londergan, C. H.; Kubiak, C. P., Solvent dynamical control of ultrafast ground state electron transfer: implications for class II-III mixed valency. *J. Am. Chem. Soc.* **2007,** *129* (42), 12772-12779.

25. Kubiak, C. P., Inorganic Electron Transfer: Sharpening a Fuzzy Border in Mixed Valency and Extending Mixed Valency across Supramolecular Systems. *Inorg. Chem.* **2013,** *52* (10), 5663-5676.

26. Neese, F., An improvement of the resolution of the identity approximation for the formation of the Coulomb matrix. *Journal of Computational Chemistry* **2003,** *24* (14), 1740–1747.

27. Kossmann, S.; Neese, F., Comparison of two efficient approximate Hartee–Fock approaches. *Chem. Phys. Lett.* **2009,** *481* (4–6), 240–243.

28. Neese, F.; Wennmohs, F.; Hansen, A.; Becker, U., Efficient, approximate and parallel Hartree–Fock and hybrid DFT calculations. A 'chain-of-spheres' algorithm for the Hartree–Fock exchange. *Chem. Phys.* **2009,** *356* (1–3), 98–109.

29. Izsák, R.; Neese, F., An overlap fitted chain of spheres exchange method. *J. Chem. Phys.* **2011,** *135* (14), 144105.

30. Neese, F., The ORCA program system. *Wiley Interdisciplinary Reviews: Computational Molecular Science* **2012,** *2* (1), 73–78.

31. Huzinaga, S.; Andzelm, J.; Radzio-Andzelm, E.; Sakai, Y.; Tatewaki, H.; Klobukiwski, M., *Gaussian Basis Sets for Molecular Calculations*. Elsevier Science: 1983; Vol. 16, p 434.

32. Andrae, D.; Häußermann, U.; Dolg, M.; Stoll, H.; Preuß, H., Energy-adjustedab initio pseudopotentials for the second and third row transition elements. *Theor. Chem. Acc.* **1990,** *77* (2), 123–141.

33. Schäfer, A.; Horn, H.; Ahlrichs, R., Fully optimized contracted Gaussian basis sets for atoms Li to Kr. *The Journal of Chemical Physics* **1992,** *97* (4), 2571–2577.

34. Schäfer, A.; Huber, C.; Ahlrichs, R., Fully optimized contracted Gaussian basis sets of triple zeta valence quality for atoms Li to Kr. *J. Chem. Phys.* **1994,** *100* (8), 5829–5835.

35. Weigend, F., Accurate Coulomb-fitting basis sets for H to Rn. *Physical Chemistry Chemical Physics* **2006,** *8* (9), 1057–1065.

36. Pantazis, D. A.; Neese, F., All-electron scalar relativistic basis sets for the 6p elements. *Theoretical Chemistry Accounts* **2012,** *131* (11), 1292.

37. Pantazis, D. A.; Neese, F., All-Electron Scalar Relativistic Basis Sets for the Actinides. *Journal of Chemical Theory and Computation* **2011,** *7* (3), 677-684.

38. Pantazis, D. A.; Neese, F., All-Electron Scalar Relativistic Basis Sets for the Lanthanides. *Journal of Chemical Theory and Computation* **2009,** *5* (9), 2229-2238.

39. Pantazis, D. A.; Chen, X.-Y.; Landis, C. R.; Neese, F., All-Electron Scalar Relativistic Basis Sets for Third-Row Transition Metal Atoms. *J. Chem. Theory Comput.* **2008,** *4* (6), 908-919.

40. Sinnecker, S.; Rajendran, A.; Klamt, A.; Diedenhofen, M.; Neese, F., Calculation of Solvent Shifts on Electronic g-Tensors with the Conductor-Like Screening Model (COSMO) and Its Self-Consistent Generalization to Real Solvents (Direct COSMO-RS). *The Journal of Physical Chemistry A* **2006,** *110* (6), 2235–2245.

41. Grimme, S.; Ehrlich, S.; Goerigk, L., Effect of the damping function in dispersion corrected density functional theory. *Journal of Computational Chemistry* **2011,** *32* (7), 1456–1465.

42. Grimme, S.; Antony, J.; Ehrlich, S.; Krieg, H., A consistent and accurate ab initio parametrization of density functional dispersion correction (DFT-D) for the 94 elements H-Pu. *The Journal of Chemical Physics* **2010,** *132* (15), 154104.

43. Pettersen, E. F.; Goddard, T. D.; Huang, C. C.; Couch, G. S.; Greenblatt, D. M.; Meng, E. C.; Ferrin, T. E., UCSF Chimera–a visualization system for exploratory research and analysis. *J. Comput. Chem.* **2004,** *25* (13), 1605–1612.